Isotopic characterisation of atmospheric nitrous oxide fourier transform infrared spectroscopy

Federico Turatti
University of Wollongong

Isotopic Characterisation of Atmospheric Nitrous Oxide by Fourier Transform Infrared Spectroscopy

A thesis submitted in fulfilment of the

requirements for the award of the degree

DOCTOR OF PHILOSOPHY

from

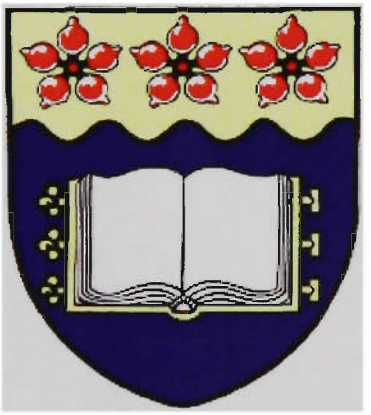

UNIVERSITY OF WOLLONGONG

by

FEDERICO TURATTI, BSc (Hons.)

Department of Chemistry, 2001

Certification

I, Federico Turatti, declare that this thesis, submitted in fulfilment of the requirements for the award of Doctor of Philosophy, in the Department of Chemistry, University of Wollongong, is wholly my own work unless otherwise referenced or acknowledged. The document has not been submitted for qualifications at any other academic institution.

Federico Turatti

Acknowledgments

Many people have helped me complete this work and all deserve my sincere thanks and acknowledgement:

- *My academic supervisors, Associate Professor David Griffith, Dr Stephen Wilson and Dr Paul Steele, for their many suggestions, their scientific encouragement and for their constructive advice and criticisms.*
- *The University of Wollongong and CSIRO Atmospheric Research for financial and scientific support, and CSIRO Land and Water for scientific support.*
- *Fellow team members of the Atmospheric Chemistry and Spectroscopy Group for their companionship, especially David Hsu for many cups of tea and many absorbing discussions about politics, current affairs and authentic Szechwan food. Joanne Menegazzo and Jerker Samuelsson also deserve my thanks for their invaluable help in the atrocious and unforgettable conditions of the Corowa field trip.*
- *Steve Cooper, Geoffrey Hurt and John Bourke of the Faculty of Science Workshop for constructing crucial pieces of hardware used in this work.*

I reserve my deepest and most heartfelt gratitude for my wife Justine, for my dearest friends and for my family, whose support made progress through a painful journey possible. Those who complete works of substance inevitably face doubts, but courage is found in the support of one's closest confidants.

Publications

Sections of this work described in this thesis have been reported in the following publications:

- Turatti, F., D.W.T. Griffith, S.R. Wilson, M.B. Esler, T. Rahn, H. Zhang, and G.A. Blake, Positionally dependent ^{15}N fractionation factors in the photolysis of N_2O determined by high resolution FTIR spectroscopy, *Geophysical Research Letters*, *27* (16), 2489-2492, 2000.
- Turatti, F., D.W.T. Griffith, S.R. Wilson, M.B. Esler, L.P. Steele, T. Rahn, and H. Zhang, Isotopic analysis of atmospheric N_2O by FTIR spectroscopy: ^{15}N, ^{18}O and ^{15}N positional dependence, in *Cape Grim Baseline Air Pollution Station Annual Meeting*, edited by N. Tindale, CSIRO Atmospheric Research, Aspendale, 1999.
- Esler, M.B., D.W.T. Griffith, F. Turatti, S.R. Wilson, and T. Rahn, N_2O concentration and flux measurements and complete isotope analysis using FTIR spectroscopy, *Chemosphere: Global Change Science*, *2*, 445-454, 2000.
- Griffith, D.W.T., S.R. Wilson, F. Turatti, M.B. Esler, and I.M. Jamie, Isotopomeric Analysis of Environmental Trace Gases by FTIR spectrometry: N_2O, CH_4, CO_2 and H_2O, in *1st International Symposium on Isotopomers*, edited by N. Yoshida, Yokohama, Japan, 2001.
- Wilson, S.R., D.W. Griffith, F. Turatti, and J. Menegazzo, Characterisation of agricultural N_2O emission sources using isotopic labelling studies, in *Gape Grim Baseline Air Pollution Station Annual Scientific Meeting*, edited by N. Tindale, and N. Derek, Aspendale, Vic, Australia, 2000.

Abstract

Nitrous oxide is the third most important anthropogenic greenhouse gas after CO_2 and CH_4 and contributes 6% of the total terrestrial radiative forcing due to greenhouse gases. It is closely involved in the depletion of stratospheric ozone by providing one of the main sources of NO radicals. Biological processes such as nitrification and denitrification are primarily responsible for N_2O production. Despite its importance and years of research, the estimates of the global size of N_2O sources and sinks remain highly uncertain, and its budget is not yet fully balanced.

Analysis of N_2O isotopes can aid in reducing the large uncertainties in source and sink estimates by providing information that is complementary to the N_2O mixing ratio. Analysis of the mean $\delta^{15}N$ and mean $\delta^{18}O$ has already lead to some insight on the N_2O budget. Until very recently the intramolecular ^{15}N positional isotopes $^{14}N^{15}N^{16}O$ and $^{15}N^{14}N^{16}O$ were not measurable by any analytical technique. The intramolecular difference $\delta^{14}N^{15}N^{16}O$-$\delta^{15}N^{14}N^{16}O$ is an additional isotopic discriminator than the mean $\delta^{15}N$ alone, as it directly describes the processes forming the N-N bond in N_2O production processes such as nitrification and denitrification.

This thesis describes the development of a high resolution Fourier transform infrared technique for the measurement of the N_2O isotopomers $^{14}N^{15}N^{16}O$, $^{15}N^{14}N^{16}O$, $^{14}N^{14}N^{18}O$ and $^{14}N^{14}N^{17}O$. The FTIR technique utilises 0.012 cm^{-1} resolution FTIR spectroscopy, a 2.4 m optical pathlength, 120 mL sample cell, with precise control of sample temperature and pressure. The typical analytical precision of the $^{14}N^{15}N^{16}O$ and $^{15}N^{14}N^{16}O$ isotopomers is of the order of 1-2 ‰, and approximately 3-4 ‰ for the oxygen isotopomers $^{14}N^{14}N^{18}O$ and $^{14}N^{14}N^{17}O$. Two independent chemometric multivariate analytical methods were developed for determination of high resolution N_2O spectra: multi-micro-window classical least squares, and non-linear least squares. The strengths and limitations of the FTIR technique are analysed and compared to those of the complementary isotope ratio mass spectrometry technique. The FTIR technique is analytically robust and serves as an independent and complementary technique to N_2O analysis by isotope ratio mass spectrometry.

The FTIR technique was used to analyse N_2O from several contexts. The isotopic fractionation factors in the laboratory photolysis of N_2O at three wavelengths were determined by analysis of the unphotolysed N_2O fraction. Samples of nitrous oxide were extracted from whole air at an urban location over the period of approximately one year and isotopically characterised. The emissions of N_2O from a pig effluent fertilised crop field have been isotopically characterised. In each of the three contexts, results are interpreted in relation to the processes involved.

TABLE OF CONTENTS

LIST OF FIGURES

LIST OF TABLES

Chapter 1 Introduction

Nitrous oxide (N_2O) is the third most important anthropogenic greenhouse gas after carbon dioxide and methane based on its greenhouse warming potential. It is chemically inert in the troposphere but is chemically active in the stratosphere, where it is a key component in the chemistry of ozone destruction. Nitrous oxide was first discovered in the atmosphere as an infrared absorption feature in the solar spectrum by *Adel* [1938]. Its current atmospheric mixing ratio is 314 nmol mol^{-1} (ppb) and rising at approximately 0.25 % per year from a pre industrial revolution mixing ratio of approximately 270 nmol mol^{-1} [*Albritton et al.*, 2001]. This has implications for both the terrestrial radiative balance and ozone atmospheric chemistry.

This chapter will give an account of the available information about nitrous oxide. The significance of N_2O will be examined in terms of its effects on the atmospheric radiative balance and stratospheric chemistry. The latest estimates of the global N_2O source and sink processes will be discussed. The idea of stable isotopic analysis of N_2O as an aid to constraining the N_2O budget will be discussed. The currently available N_2O isotopomer analysis methods will be introduced and discussed, and the analysis method developed during this work will be introduced. A summary of the project major aims will be given.

1.1 The significance of atmospheric N_2O

1.1.1 The atmospheric radiative balance

The incoming solar radiation averaged over the earth's surface is approximately 342 W m^{-2}, but approximately 107 W m^{-2} is reflected from clouds, aerosol, the atmosphere and the Earth's surface due to the terrestrial albedo. The net solar radiation absorbed by the terrestrial system is therefore approximately 235 W m^{-2} [*Brasseur et al.*, 1999]. A simple calculation using the Stefan-Boltzmann constant shows that the Earth, in the absence of an atmosphere, should re-emit this radiation as a black body radiator at approximately 255 K, or –18 °C [*Brasseur et al.*, 1999]. This is clearly not the real case.

The re-radiated 235 W m^{-2} is partially absorbed by clouds and atmospheric gases, primarily water vapour and carbon dioxide CO_2 in the lower layers of the atmosphere. The net effect of these gases is to raise the average global temperature from 255 K to a habitable 288 K (+15 °C) [*Brasseur et al.*, 1999]. This is the so-called "greenhouse effect": a natural and normal feature of the Earth's atmosphere that maintains global average temperature warmer than would be otherwise expected, providing a habitable environment.

The 830 to 1250 cm^{-1} region is often called the atmospheric window as terrestrial radiation escapes to space through this region because of the relatively weak absorption in this region of the spectrum. Therefore, any gas with strong absorption features in this spectral region will be efficient in trapping terrestrial radiation. Gases that absorb in this region are often called "greenhouse gases" or "radiatively active". They include

water, CO_2, CH_4, N_2O, and several gases with anthropogenic origins, such as the chlorofluorocarbons (CFCs), hydrofluorocarbons (HFCs), some fully fluorinated species (eg SF_6) and some ethers and halogenated ethers. The net effect of these gases is to reduce the amount of radiative energy emitted to space and increase the energy re-radiated back to the troposphere and the earth's surface – the "enhanced greenhouse effect" [*Brasseur et al.*, 1999].

Industrial and agricultural activities of the world are increasing the concentrations of most greenhouse gases, which, compared to their pre-industrial levels and their geological records, are extremely rapid [*Albritton et al.*, 2001]. As the concentration of greenhouse gases increases, so does the amount of outgoing terrestrial radiation that is trapped, leading to an increase in the radiative forcing of the atmosphere. For example, a doubling of the pre-industrial CO_2 concentration, with no other changes, will lead to a global radiative forcing change of +4 W m^{-2} (according to one model) due to the trapping of more outgoing infrared radiation, directly warming the Earth's surface by at least 1°C on average [*Prather et al.*, 1995].

The relative strengths of greenhouse gases can be assessed using greenhouse warming potentials (GWPs) which are based on the atmospheric lifetime of the various greenhouse gases and their ability to absorb infrared radiation. The GWP of a well mixed gas is defined as the time-integrated change in the radiative forcing due to the instantaneous release of 1 kg of a trace gas *i* relative to that from the release of 1 kg of CO_2 [*Houghton et al.*, 1990], so that

$$GWP = \frac{\int_0^T \Delta F_{R,i}(t)dt}{\int_0^T \Delta F_{R,CO_2}(t)dt} \qquad (1.1)$$

where ΔF_R is the change in radiative forcing and T is the time horizon over which the calculation is performed. Estimating GWPs for greenhouse gases requires estimates of the radiative forcing for the gas i and for the reference gas CO_2, the lifetimes of the gas i and of CO_2, and the definition of the time horizon, T. The choice of T depends on the type of climate impact to be studied. For example, when estimating the maximum change in temperature a typical T is approximately 100 years, but to estimate the rate of change in temperature a typical T is 20 to 50 years [*Brasseur et al.*, 1999]. The GWPs for some greenhouse gases are given in Table 1.1.

Table 1.1 Global Warming Potentials for several greenhouse gases[a]

Species	Formula	Lifetime (yrs)	Global Warming Potential		
			T = 20 years	100 years	500 years
Carbon dioxide	CO_2		1	1	1
Methane	CH_4	12-18 [b]	48-90	20-43	8-15
Nitrous oxide	N_2O	121	290	330	180
CFC-11	$CFCl_3$	50	5000	4000	1400
CFC-12	CF_2Cl_2	102	7900	8500	4200
Halon-1301	CF_3Br	65	6200	5600	2200
Sulfur hexaflouride	SF_6	3200	15100	22200	32400

a. Modified from *Brasseur et al.* [1999]
b. Includes the effect of the variable hydroxyl radical methane sink

Nitrous oxide is the third most important anthropogenic greenhouse gas after CO_2 and CH_4 in terms of its annual emissions, and is estimated to contribute 6 % of the radiative forcing due to greenhouse gases. It has a relatively long lifetime of approximately 120 years and over the 100 year time horizon its GWP is more than 300 times that of CO_2 and between 7 and 16 times that of methane.

1.1.2 The N_2O stratospheric chemistry

No gas phase tropospheric sinks of N_2O are known, therefore leading to its long atmospheric lifetime. *Crutzen* [1971; 1970] and *McElroy and McConnell* [1971] were the first to become aware of the important role of nitrous oxide in the stratospheric ozone balance. Nitrous oxide is destroyed in the stratosphere under the influence of ultraviolet radiation between 180 and 215 nm forming singlet oxygen,

$$N_2O + h\nu \rightarrow N_2 + O(^1D)\ (\lambda \approx 180\text{-}215\ nm) \qquad (1.2)$$

or by reaction with singlet oxygen, $O(^1D)$, so that

$$N_2O + O(^1D) \rightarrow N_2 + O_2 \qquad (1.3)$$

$$N_2O + O(^1D) \rightarrow 2\ NO \qquad (1.4)$$

Reaction 1.2 is responsible for the destruction of 90 % of the stratospheric N_2O, with equations 1.3 and 1.4 the destroying the remainder (4 and 6 %, respectively). The last of these reactions (reaction 1.4) is the primary source of the nitric oxide radical, NO, which is involved in the catalytic destruction of ozone. Approximately 20 % of ozone destruction, averaged over the whole stratosphere, is via

$$O_3 + O \rightarrow O_2 + O_2 \qquad (1.5)$$

and the remainder through a catalytic route [for example *Brasseur et al.*, 1999; *Warneck*, 2000; *Wayne*, 2000] so that

$$O_3 + X \rightarrow XO + O_2 \qquad (1.6)$$

$$XO + O \rightarrow X + O_2 \qquad (1.7)$$

$$\textit{Net}: O + O_3 \rightarrow O_2 + O_2 \qquad (1.8)$$

X is a catalytic species that is either H, OH, NO, Cl or Br. Nitric oxide radicals are responsible for more than 50 % of the ozone destruction in the 25 km to 40 km region of the stratosphere – the middle stratosphere.

1.2 The N_2O budget

Albritton et al. [2001] provides the most recent review of the scientific literature on greenhouse gases. The latest available figure for the global average N_2O mixing ratio is 314 ppb. The rate of change of N_2O concentration, averaged over 1980-1999 is 0.8 ppb yr^{-1} (0.25% yr^{-1}), and the latest estimate of its atmospheric lifetime is 114 years. Its pre-industrial concentration was approximately 270 ppb. Substantial changes in the annualised growth rate of N_2O have been observed. For example, between 1991 and 1993 the annual growth rate was approximately 0.4 ppb yr^{-1} (0.13% yr^{-1}). Several suggestions exist for this anomaly, namely a decrease in nitrogen-based fertilizer usage, lower biogenic emissions and larger stratospheric losses due to volcanic eruptions [*Albritton et al.*, 2001]. The growth rate of N_2O has returned to 0.8 ppb yr^{-1} (0.25% yr^{-1}) since 1993 [*Albritton et al.*, 2001]. While the full Third Assessment of the Intergovernmental Panel on Climate Change (IPCC) is not available at this time, the Technical Summary of Working Group 1 [*Albritton et al.*, 2001] concludes several important points:

- "*The global budget of nitrous oxide is in better balance than in the Second Assessment Report, but uncertainties in the emissions from individual sources are still quite large*", and

- *"...the predictive understanding associated with this significant, long-lived greenhouse has not improved significantly since the last assessment".*

There are many small sources of N_2O contributing to the global N_2O budget, and each of these sources are relatively small in size, making and accurate determination of the N_2O budget difficult. The latest and most comprehensive summary of the sources of N_2O is still *Bouwman et al.* [1995], who compiled a $1° \times 1°$ gridded global inventory of N_2O sources and their errors. More recent works have concentrated on specific N_2O sources. Table 1.2 is a summary of the state of knowledge of the N_2O budget starting with *Bouwman et al.* [1995] and augmented with the latest available studies, in units of Tg N_2O-N yr^{-1} (1 Tg = 10^{12} g = 1 million tonnes). Sections 1.2.1, 1.2.2 and 1.2.3 describe the natural N_2O sources, the anthropogenic N_2O sources and the N_2O sink, respectively.

Table 1.2 Source and sink estimates for N_2O

Sources	*Bouwman et al. [1995]*	IPCC 1995 range [a]	Likely size (from IPCC 1995)	Latest estimates [b]
	Tg N_2O-N yr^{-1}	*Tg N_2O-N yr^{-1}*	*Tg N_2O-N yr^{-1}*	*Tg N_2O-N yr^{-1}*
Natural				
Oceans	2.8-5.7	1-5	3.0	7-11 [c]
Soils				
Tropical soils	3.3	2.7-5.7	4.0	3.55-4.85 [d]
Temperate forests	0.5	0.1-2.0	1.0	
Grasslands	1.4-1.5	0.5-2.0	1.0	
NH_3 oxidation (?)	0.3-1.2			
Total natural	8.3-12.2	4.3-14.7	9	
Anthropogenic				
Arable land	0.4-1.9	1.8-5.3	3.5	0.8-3.7 [e]
Tropical forest conversion	0.4			
Industrial sources				
Fossil fuels	0.1-0.6			
Adipic acid production	0.2-0.4	0.7-1.8	1.3	
Nitric acid production	0.1-0.3			
Animal excreta	1	0.2-0.5	0.4	
Biomass burning	0.1	0.2-1.0	0.5	0.6 [f]
Eutrophication of aquatic systems by human waste	0.01-1.6			
Total anthropogenic	2.3-6.3	2.9-8.6	5.7	
Total identified sources	**10.6-18.5**	**7.2-23.3**	**14.7**	
Atmospheric increase		**2.2-7.2**	**2.4**	
Sinks				
Stratospheric photochemistry		9-16	12.3	12.2 [g]
Soil uptake	?	?	?	1.5-3 [h]
Total sinks		**9-16**	**12.3**	

a. [*Prather et al.*, 1995]
b. Where no latest estimate is quoted, the latest estimate is from *Bouwman et al.* [1995] or *Prather et al.* [1995]
c. [*Bange et al.*, 1996]
d. [*Breuer et al.*, 2000]
e. [*Dobbie et al.*, 1999]
f. [*Kroeze et al.*, 1999]
g. [*Minschwaner et al.*, 1993]
h. [*Cicerone*, 1989], highly speculative
? Speculative

1.2.1 Natural sources

1.2.1.1 Oceans

Oceans are the largest natural source of N_2O. Nitrous oxide fluxes from oceans are very difficult to measure directly and fluxes are generally estimated from N_2O supersaturation in water near the ocean surface and the water-air gas transfer coefficient [*Bouwman et al.*, 1995]. *Bouwman et al.* [1995] estimate this source to be between 2.8-5.7 Tg N_2O-N yr^{-1}, while the 1995 IPCC report quotes a range of 1-5 Tg N_2O-N yr^{-1}. There have been several important developments in estimating the size of the oceanic N_2O flux since 1995. Nitrous oxide has been measured in water deeper than 2000 m of waters of several oceans [*Bange and Andreae*, 1999]. Despite the fact that ocean waters deeper than 2000 m comprise approximately 95% of the total ocean volume, this source is estimated to contribute no more than 3-16 % of the total oceanic source flux. *Bange and Andreae* [1999] also find, interestingly, that N_2O production from deep waters does not supply all the N_2O that is emitted from the near-surface oceanic waters, and propose a previously undescribed source of 2.4 Tg N_2O-N yr^{-1} attributed to nitrification in the 0-2000 m of the oceanic water column to balance the oceanic N_2O budget. Other recent works have measured large N_2O sources from subtropical North Pacific waters [*Dore et al.*, 1998] and determined the budgetary and biological implications of the isotopic signatures of N_2O emitted from the Arabian Sea [*Naqvi et al.*, 1998]. *Nevison et al.* [1995] quote a range for the oceanic source strength of 1.2-6.8 Tg N_2O-N yr^{-1} with a probable size of 4 Tg N_2O-N yr^{-1}. There is not unanimous agreement on the magnitude of the oceanic N_2O source. For example, *Bange et al.*, [1996] claim that the size of the oceanic N_2O source has been greatly underestimated, and suggest an annual global sea to air flux of 7-11 Tg N_2O-N yr^{-1}.

1.2.1.2 Soils under natural vegetation

Nitrification and denitrification processes by bacteria contribute the largest proportion of N_2O emissions. Soils under natural vegetation are a source of N_2O and include closed and open tropical forests, temperate forests and grasslands. *Bouwman et al.* [1993] developed a model for N_2O production from soils based on five major regulators: (1) input of organic matter into the soil, (2) the quality and N content of the organic matter, (3) the effects of soil moisture and (4) temperature, and (5) soil oxygen status. They calculated global emission from soils under natural vegetation as 4.3-4.5 Tg N yr^{-1}. Natural grasslands are calculated to emit 1.4-1.5 Tg N yr^{-1}. *Bouwman et al.* [1995] estimates that tropical forest soils contribute approximately 2.3 Tg N yr^{-1}. Very recent measurements of N_2O emissions from soils in the Australian Northern Territory [*Breuer et al.*, 2000] conclude that the annual tropical soil emissions might be as high as 3.55 Tg N yr^{-1}. *Bouwman et al.* [1995] point out that

> "*There is a lack of flux measurement data for a number of important ecosystems that have not been sampled...*".

1.2.2 Anthropogenic sources

1.2.2.1 Arable land

Arable land is defined as the N_2O emission from fertilised cultivated fields. *Bouwman* [1996] estimates that the direct N_2O emission from fertilizer application to arable land is 1.25 ± 1% of the applied N loading and quotes an annual emission of 0.4-1.9 Tg N yr^{-1}, while more a more recent work by *Dobbie* [1999] quotes an annual emission of 0.8-3.7 Tg N yr^{-1}. The IPCC report of 1995, [*Prather et al.*, 1995], quotes a range of 1.8-5.3 Tg N_2O-N yr^{-1} from arable land.

1.2.2.2 Animal excreta

Khalil and Rasmussen [1992] first identified animal excreta as a source of N_2O and quantified it between 0.2-0.6 Tg N yr^{-1} from cattle sheds and barns. Bouwman assumes that this emission is approximately 1% of the N from animal excreta, and estimates a strength of approximately 1 Tg N_2O-N yr^{-1}. The 1995 IPCC report quotes a range of 0.2-0.5 Tg N_2O-N yr^{-1}.

1.2.2.3 Biomass burning

Biomass burning is a small but significant source of N_2O. *Bouwman* [1995] quotes a potential source strength of 0.1 Tg N_2O-N yr^{-1}, with some estimates showing a range of 0.5-2.2 Tg N_2O-N yr^{-1} [*Andreae*, 1991]. The 1995 IPCC report quotes a range from this source of 0.2-1.0 Tg N_2O-N yr^{-1}, while *Kroeze et al.* [1999] quotes 0.6 Tg N_2O-N yr^{-1}.

1.2.2.4 Industrial sources of N_2O

Industrial sources of N_2O can be broadly grouped in three: Fossil fuel combustion, adipic acid production and nitric acid production. Fossil fuel combustion by cars equipped with catalytic converters is an important N_2O source. Emissions from this source are difficult to estimate due to the decreasing efficiency (and therefore increased N_2O production) with catalytic converter age [*Bouwman et al.*, 1995]. Bouwman *et al.* estimate this source to contribute 0.1-0.6 Tg N_2O-N yr^{-1}. Approximately 99% of the global N_2O emission from this source is from the northern hemisphere, as the bulk of the world's cars with catalytic converters are in northern hemisphere countries [*Bouwman et al.*, 1995].

Adipic acid (hexanedioic acid, HOOC-$CH_2CH_2CH_2CH_2$-COOH) is an intermediary in the production of 6,6 nylon. A mixture of cyclohexanone and cyclohexanol is oxidised

with nitric acid to produce adipic acid. Nitrous oxide is an intrinsic by-product of this reaction. The calculated emission strength of this source is 0.2-0.4 Tg N_2O-N yr^{-1} [*Bouwman et al.*, 1995]. Nitric acid (HNO_3) is the main feedstock in fertilizer production. Production of nitric acid itself is also a source of N_2O emissions, estimated at 0.1-0.3 Tg N_2O-N yr^{-1} [*Bouwman et al.*, 1995]. The 1995 IPCC report combines all industrial N_2O sources into one estimated emission of 0.7-1.8 Tg N_2O-N yr^{-1}.

1.2.2.5 Tropical forest conversion

Forest clearing for arable land or pasture can cause an enhanced "pulse" of N_2O emissions from soils due to the enhanced decomposition and mineralization of organic plant and soil matter in the first few years after deforestation. *Bouwman* [1995] estimates this N_2O pulse to be approximately 0.4 Tg N_2O-N yr^{-1}, while the 1995 IPCC report includes this term in its estimate of emissions from cultivated soils.

1.2.2.6 Other potential N_2O sources

There are several potential N_2O sources for which no estimates exist in the literature. Potentially any process which involves nitrogen oxidation in overall reducing conditions [*Bouwman et al.*, 1995] could be a source of N_2O. Examples include uses of nitric acid outside of fertilizer production, production of diodic acids (similar in structure to adipic acid), production of coke from coal, chlorination of water, cement manufacturing and metal treatment processes [*Oliver*, 1993]. Other potential sources are the production and use of explosives and use of N_2O in anaesthesia. Formation of N_2O in the atmosphere from the oxidation of NH_3 by OH may be in the range of 0.3-1.2 Tg N_2O-N yr^{-1}.

Eutrophication of aquatic systems may cause N_2O production [*Bouwman et al.*, 1995] with estimates of N_2O emissions from water systems contaminated by human waste from 0.01 to 1.6 Tg N_2O-N yr^{-1}. An example of this source is sewage and waste water treatment plants.

1.2.3 Sinks

Early attempts to balance the N_2O budget often had a surplus of N_2O on the source side of the equation by approximately 30 % [*Watson et al.*, 1990], leading to speculation about a missing N_2O sink. More recent attempts at estimating N_2O sources and sinks [*Mosier et al.*, 1998; *Prather et al.*, 1995] have moved closer to a balanced budget within the large uncertainties, primarily due to revision in estimates of the size of oceanic and agricultural N_2O sources. There is only one quantified N_2O sink: stratospheric photochemistry as described in section 1.1.1. *Minschwaner et al.* [1993] modelled the absorption of solar radiation by O_2 in the stratosphere and combined this with vertical profile measurements of N_2O to approximately 40 km to estimate the size of the stratospheric N_2O sink. The size of the sink they derived is 12.2 Tg N_2O-N yr^{-1}, which is still the most commonly accepted value. The 1995 IPCC report states a range for the stratospheric N_2O sink of 9-16 Tg N_2O-N yr^{-1}. *Nevison et al.* [1999] use the recently discovered stratospheric isotopic enrichment in N_2O (described in detail in section 1.3.2.3 below) and stratospheric tracer correlations (NO_y, CH_4 and others) to constrain the N_2O sink. The authors quote

> "*...the generally good agreement between modelled and observed correlation slopes does not support the existence of an undiscovered N_2O sink that accounts for a major fraction of the total sink.*".

The authors leave open the possibility of small new sink which might be disguised in the uncertainties of their study, accounting for less than 20 % of the total sink, but they consider it unlikely as it would require an enrichment factor of –60 ‰ in the mean ^{15}N of N_2O.

Suggestions of additional tropospheric N_2O sinks have been proposed [for example *Prasad*, 1994; *Prasad*, 1997; *Prasad et al.*, 1997]. It is known that under specific conditions soils can indeed act as N_2O sinks [*Castro et al.*, 1993; *Keller et al.*, 1986; *Schmidt et al.*, 1988], even though they are net annual N_2O sources. The possibility of an N_2O sink arises as a result of microbial denitrification. Denitrification involves the reduction of nitrate, NO_3^- to N_2 under anaerobic conditions (see section 1.3.2.3 below and Chapter 7). Nitrous oxide is formed in denitrification and is both a product and an intermediate in the process, as it can be denitrified to N_2. If the denitrification process proceeds strongly to completion (by generating primarily N_2), a net N_2O deficit can occur in the denitrification reaction chain. Under these specific circumstances it is possible that the required N_2O intermediary would be taken from the atmosphere, creating a localised N_2O sink. It is unlikely that soils would exist in such a state long enough to sustain a net N_2O sink, although *Ryden* [1981; 1983] observed a net annual N_2O consumption by grassland soils. *Cicerone* [1989] speculates that a possible soil sink of 1.5-3 Tg N_2O-N yr^{-1} would have serious implications for the atmospheric lifetime of N_2O, leading to a reduction of as much as 20%.

1.3 The isotopomers of N_2O

Nitrogen exists in two stable isotopic forms of ^{14}N and ^{15}N with natural abundance 99.64 % and 0.36 %, respectively, and oxygen exists in three stable isotopic forms ^{16}O, ^{17}O, ^{18}O with natural abundances of 99.763, 0.0375 and 0.1905 %, respectively [*Bowen*, 1991]. This gives rise to 12 possible isotopic isomers for the N_2O molecule, for convenience named isotopomers. These are described in Table 1.3.

Table 1.3 Isotopomers of N_2O and their natural abundances

Isotopomer	Shorthand [(a)]	Natural average abundance (%)
$^{14}N^{14}N^{16}O$	446	99.046
$^{14}N^{15}N^{16}O$	456	0.3579
$^{15}N^{14}N^{16}O$	546	
$^{14}N^{14}N^{18}O$	448	0.1891
$^{14}N^{14}N^{17}O$	447	0.03723
$^{15}N^{15}N^{16}O$	556	0.001293
$^{14}N^{15}N^{18}O$	458	6.833×10^{-4}
$^{15}N^{14}N^{18}O$	548	
$^{14}N^{15}N^{17}O$	457	1.345×10^{-4}
$^{15}N^{14}N^{17}O$	547	
$^{15}N^{15}N^{18}O$	558	2.469×10^{-6}
$^{15}N^{15}N^{17}O$	557	4.86×10^{-7}

(a) Shorthand notation used in this thesis for the respective N_2O isotopomers, derived by taking the second digit of the atomic mass for the individual NNO atoms in the respective N_2O isotopomer. For example $^{14}N^{15}N^{16}O$ has shorthand notation 456 (atomic masses 14, 15, 16).

The first five N_2O isotopomers are sufficiently abundant to be typically detected in almost all sources of N_2O. Doubly substituted N_2O, isotopomer 556, ($^{15}N^{15}N^{16}O$) is normally only observed in studies where the source nitrogen is heavily enriched in ^{15}N [*Nedwell*, 2001, personal communication and N2O samples]. Isotopomers less

abundant than 556 are not seen in ordinary processes, and are extremely difficult if not impossible to measure with current methods because of their extremely low abundance.

Isotope measurements are expressed as relative deviations from a standard of known isotopic composition. These deviations (δ) are quoted as parts per thousand or per mille (‰) relative to a standard. For example $\delta^{18}O$ is the calculated isotopic deviation in ‰ relative to a standard via

$$\delta^{18}O = \left(\frac{R^{18}O_{sample}}{R^{18}O_{standard}} - 1 \right) \times 1000 \qquad (1.9)$$

where $R^{18}O$ is the measured or known ratio of $^{18}O/^{16}O$ in either the sample or standard. Internationally accepted isotopic standards exist for the measurement of common isotopic deviations. For example, the standard used when measuring $\delta^{13}C$ in CO_2 or CH_4 is V-PDB (Vienna Peedee Belemnite). This standard is maintained by the International Atomic Energy Agency and is originally derived from Peedee Belemnite, a $CaCO_3$ deposit whose C and O isotopic ratios have been well characterised [*Craig*, 1957]. Similarly, V-SMOW (Vienna Standard Mean Ocean Water) [*Craig*, 1961] is the reference used when determining $\delta^{18}O$ in water. Measurements of the mean $\delta^{15}N$ of N_2O (the mean of δ^{456} and δ^{546}) are commonly made referenced to atmospheric nitrogen, and δ^{448} is measured relative to atmospheric O_2 or occasionally V-SMOW. Currently no internationally accepted standard exists for measuring the intramolecular ^{15}N difference δ^{456} - δ^{546} or the individual δ^{456} and δ^{546}.

Section 1.2 shows that large uncertainties exist in the N_2O budget. Analysis of N_2O isotopomers has potential to provide constraints that are not available from measuring

the mixing ratio alone. Source and sink processes fractionate between the isotopomeric form in distinct ways, including fractionating between the mass-identical but symmetry different $^{14}N^{15}N^{16}O$ and $^{15}N^{14}N^{16}O$. This will be discussed in more detail in the next section.

1.3.1 Budget implications of N_2O isotopomer analysis

The isotopomeric signature of N_2O can be utilised to help constrain the global N_2O budget and this, so some extent, has been recently carried out [*Kim and Craig*, 1993; *Naqvi et al.*, 1998; *Perez et al.*, 2001; *Rahn and Wahlen*, 2000; *Yoshida and Toyoda*, 2000]. The following description is similar to that by *Yoshida and Toyoda* [2000]. A simple mass balance of N_2O in the troposphere is

$$\sum F_{sources} = F_{trop \rightarrow strat} + \Delta T - F_{strat \rightarrow trop} \tag{1.10}$$

where F represents global N_2O fluxes, specifically from all oceanic and terrestrial natural and anthropogenic sources ($F_{sources}$), from the troposphere to stratosphere and vice versa ($F_{trop \rightarrow strat}$ and $F_{strat \rightarrow trop}$ respectively), and ΔT is the annual tropospheric increase. In this simple analysis N_2O tropospheric sinks are neglected.

If N_2O oceanic sinks are ignored, the equation for the bulk $\delta^{15}N$ isotope is:

$$\sum {}^{15}\alpha_{sources}\, {}^{15}R_{sources} F_{sources} = {}^{15}R_{trop}\left(F_{trop \rightarrow strat} + \Delta T\right) - {}^{15}R_{strat} F_{strat \rightarrow trop} \tag{1.11}$$

where ${}^{15}\alpha_{sources}$ is the fractionation factor for ^{15}N in N_2O production processes and R is the isotope ratio of sources and of N_2O in the troposphere and stratosphere. An analogous equation can be written for the $N_2{}^{18}O$ and $N_2{}^{17}O$ isotopes.

Equation 1.11 can be improved by including the positional ^{15}N isotopomers of N_2O. Two equations result:

$$\sum {}^{15}\alpha^{456}{}_{sources}\,{}^{15}R^{456}{}_{sources}F_{sources} = {}^{15}R^{456}{}_{trop}\left(F_{trop\rightarrow strat}+\Delta T\right)-{}^{15}R^{456}{}_{strat}F_{strat\rightarrow trop} \quad (1.12)$$

$$\sum {}^{15}\alpha^{546}{}_{sources}\,{}^{15}R^{546}{}_{sources}F_{sources} = {}^{15}R^{546}{}_{trop}\left(F_{trop\rightarrow strat}+\Delta T\right)-{}^{15}R^{546}{}_{strat}F_{strat\rightarrow trop} \quad (1.13)$$

where the subscripts 456 and 546 are the commonly accepted shorthand notation for $^{14}N^{15}N^{16}O$ and $^{15}N^{14}N^{16}O$ respectively. The δ^{456}-δ^{546} difference varies significantly depending on the source of the N_2O [*Menegazzo*, 2000, Chapters 5, 6 and 7 of this thesis; *Perez et al.*, 2000; *Yoshida and Toyoda*, 2000], and varies significantly more than the mean $\delta^{15}N$ of N_2O. This implies that the use of equations 1.12 and 1.13 allows the N_2O budget to be more tightly constrained than is possible using only the bulk (or average) $\delta^{15}N$ signature alone. Intramolecular ^{15}N analysis adds a fifth constraint to the N_2O isotopic budget, along with mean $\delta^{15}N$ analysis and analysis of the oxygen isotopomers.

1.3.2 Isotopomer effects of nitrification and denitrification

Nitrification and denitrification are microbially mediated processes that run in tandem in soils. Both processes form nitrogen trace gas species as intermediates. At the simplest level, these two processes are described by the "leaky pipe" model of *Firestone and Davidson* [1989], shown in Figure 1.1. The pipes represent the processes through which N "flows" and the holes represent the reactions through which trace N-gases "leak". Nitrous oxide is both a product and intermediary in denitrification.

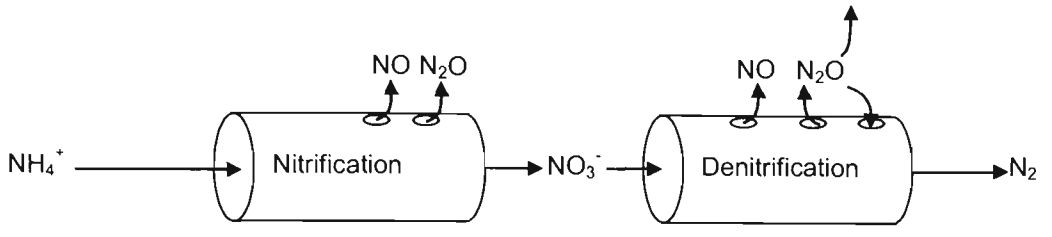

Figure 1.1 A conceptual model of nitrification and denitrification

In this simplistic model, factors that control the rate of the overall process determine the movement of N through the "pipes", and factors that determine the oxidative state of N or the partitioning to NO and N_2O control the rate of NO and N_2O release from the "holes". Therefore, a low rate of denitrification and nitrification will lead to a low emission of trace gas nitrogen species, regardless of the relative proportions of the end products. Nitrous oxide is also emitted by some processes that are not strictly denitrification or nitrification [*Robertson and Tiedje*, 1987; *Tiedje*, 1988] whose global significance, mechanisms and regulating variables are poorly known. Examples of these are chemical nitrification and denitrification.

Kaye [1987] gives a thorough review on the mechanisms for isotopic fractionation of molecular gaseous species in planetary atmospheres. Mechanisms for isotopic fractionation, amongst others, include atmospheric escape, the effect of isotopic substitution on nuclear motion, thermal equilibrium effects, phase change effects and chemical reaction rates. Nitrification and denitrification are microbial mechanisms and therefore the potential exists for ^{15}N fractionation of the emitted N_2O, as the light (or parent) ^{14}N is preferentially consumed [*Kaye*, 1987]. Discrimination between $^{14}N^{15}N^{16}O$ and $^{15}N^{14}N^{16}O$ (δ^{456}-δ^{456}), independent of the mean $\delta^{15}N$, can also exists depending on how the N-N bond is formed in the denitrification and nitrification

mechanisms. The hypothesis is that the δ^{456}-δ^{546} of N_2O from soils can act as a more sensitive marker for nitrification and denitrification than $\delta^{15}N$ alone. The next section describes the mechanisms of nitrification and denitrification and highlights the potential for isotopic discrimination.

1.3.2.1 The denitrification mechanism

Denitrification is a microbial enzymatic reduction reaction of NO_3^- and NO_2^- to N_2O and eventually N_2. There has been a significant debate in the literature over the mechanism of denitrification [*Garber and Hollocher*, 1981; *Garber and Hollocher*, 1982a; *Garber and Hollocher*, 1982b; *Kim and Hollocher*, 1983; *Mariotti et al.*, 1982; *Shearer and Kohl*, 1988; *Weeg-Aerssens et al.*, 1987; *Weeg-Aerssens et al.*, 1988]. This debate is important as the two competing mechanisms have different methods of N-N bond formation in the N_2O molecule, and will therefore have different effects on the isotopic composition of N_2O, particularly in the $^{14}N^{15}N^{16}O$ and $^{15}N^{14}N^{16}O$ isotopomers. The two competing mechanisms are known as the sequential [*Weeg-Aerssens et al.*, 1987; *Weeg-Aerssens et al.*, 1988] and the parallel [*Garber and Hollocher*, 1981; *Garber and Hollocher*, 1982a; *Garber and Hollocher*, 1982b] mechanisms. The reaction mechanisms for each are detailed in Figure 1.2 and Figure 1.3.

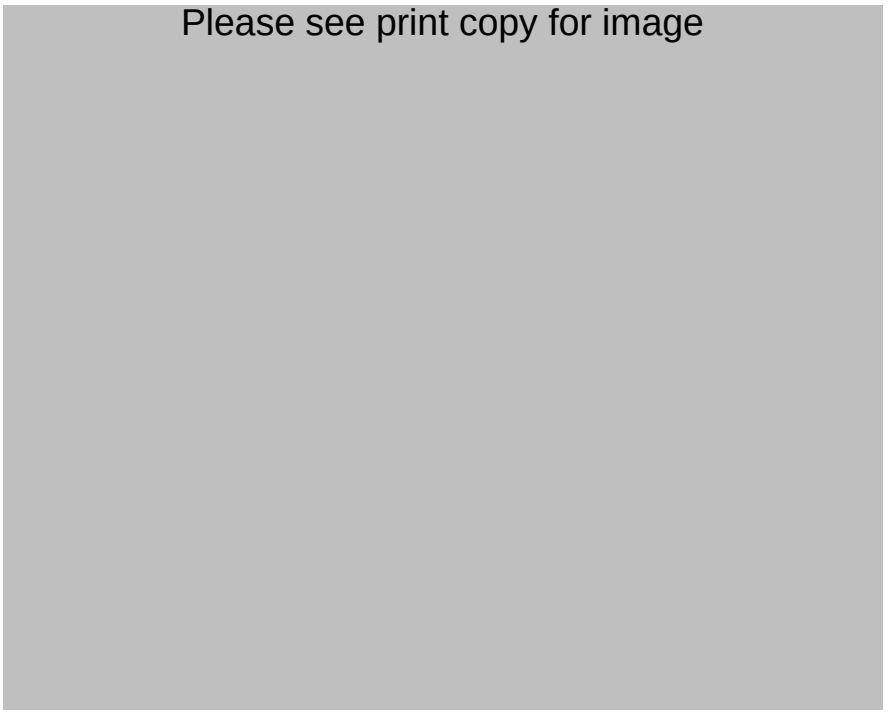

Figure 1.2 The parallel mechanism for denitrification
E represents free enzyme, Rr and Ro represent reduced and oxidised forms of a reductant [*Shearer and Kohl*, 1988].

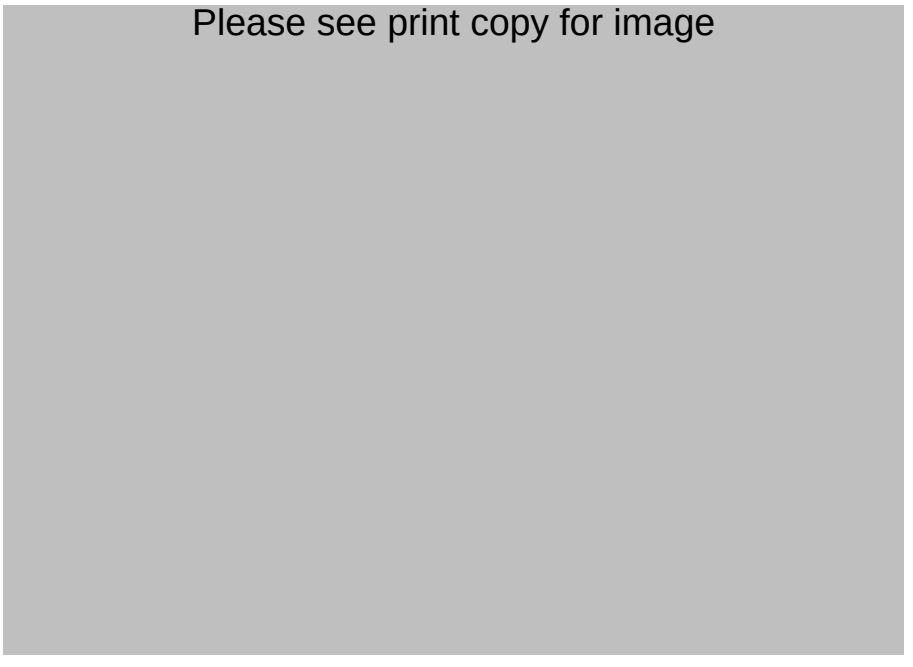

Figure 1.3 The sequential mechanism for denitrification
E represents free enzyme, Rr and Ro represent reduced and oxidised forms of a reductant [*Shearer and Kohl*, 1988].

Both mechanisms can potentially discriminate $\delta^{15}N$, but δ^{456}-δ^{546} depends on the N-N bond formation process which is different in the two mechanisms. The parallel mechanism forms two equivalent NO^- ions which then join to form N_2O. Discrimination between $^{14}N^{15}N^{16}O$ and $^{15}N^{14}N^{16}O$ is possible depending on which N-O bond breaks in the transition state O=N-N=O molecule. The sequential mechanism forms the N-N bond in N_2O in a linear (sequential), rather than parallel, path from NO_2^- to N_2O. A δ^{456}-δ^{546} signal is possible in the $E\text{-}NO^+ + NO_2^-$ step, as the N-N bond is formed from different N substrates. A further δ^{456}-δ^{546} signal is possible depending on which N-O bond is cleaved in the $E\bullet N_2O_3^-$ intermediate. A further δ^{456}-δ^{546} signal can be imparted on the N_2O as it is reduced by denitrification to N_2 gas. A different δ^{456}-δ^{546} signal is expected from the parallel and sequential denitrification mechanisms, as the mechanisms for N_2O production are different. The scientific consensus has swung in favour of the sequential mechanism [*Shearer and Kohl*, 1988; *Weeg-Aerssens et al.*, 1987; *Weeg-Aerssens et al.*, 1988]. In particular, *Shearer and Kohl* [1988] found several experimental inconsistencies in the works of *Garber and Hollocher* [1981; 1982a; 1982b].

1.3.2.2 Nitrification

Nitrification is the enzymatic oxidation of ammonium (NH_4^+) to nitrate (NO_3^-) by bacteria. It is represented by the following reaction scheme:

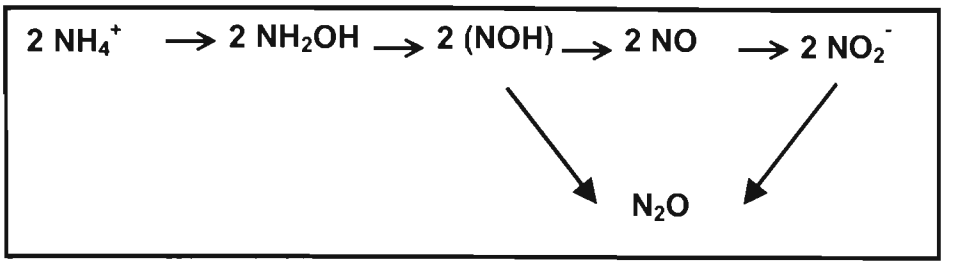

Figure 1.4 Schematic diagram of the nitrification mechanism

Both NO and N_2O gases are produced as an intermediate in the step oxidising NH_2OH to NO_2^-, but the exact reaction mechanism for N-N bond formation in N_2O is not known [*Mosier and Schimel*, 1993]. The bulk $\delta^{15}N$ of N_2O exclusively nitrification has been measured and is very depleted with respect to atmospheric N_2, with *Yoshida* [1988] quoting a $\delta^{15}N$ value of – 66 ‰ for N_2O from nitrification by a pure culture of the nitrifying bacteria *Nitorsomonas europaea*.

1.3.2.3 Isotopic fractionation during sink processes

Stratospheric photolysis is the main N_2O sink as has been described in section 1.1.2 and section 1.2.3. Stratospheric enrichment in the N_2O heavy isotopes ^{15}N and ^{18}O was first measured by *Rahn and Wahlen* [1997] and *Kim and Craig* [1993]. A theory was proposed by *Yung and Miller* [1997] to explain the heavy isotopomer enrichment under photolysis. According to this theory the photolysis rates are proportional to the size of the zero point energy shift of the heavy isotopomers to the parent $^{14}N^{14}N^{16}O$ (a first approximation), such that photolysis rates are predicted to increase in the order $^{14}N^{14}N^{16}O > ^{14}N^{14}N^{17}O > ^{15}N^{14}N^{16}O > ^{14}N^{14}N^{18}O > ^{14}N^{15}N^{16}O$. A substantially expanded version of this theory [*Johnson et al.*, 2001] gives a more detailed explanation of the reasons for isotopomer enrichment and its predictions agree very well with laboratory

photolysis studies and stratospheric N_2O measurements. Chapter 5 describes this in more detail. Enrichment in the positional ^{15}N isotopomers has been directly measured by balloon flights of an FTIR spectrometer [*Griffith et al.*, 2000], and by cryogenic sampling of stratospheric air and analysis by isotope ratio mass spectrometry (IRMS) in the laboratory [*Yoshida and Toyoda*, 2000]; [*Röckmann et al.*, 2001a]. Figure 1.5 shows a plot of the intramolecular difference δ^{546}-δ^{456} as a function of tangent altitude of the FTIR balloon flights (top) and logarithm of the fraction *f* of N_2O in the slant column relative to the unphotolysed tropospheric value (bottom). Balloon flights are fully described by *Griffith et al.* [2000].

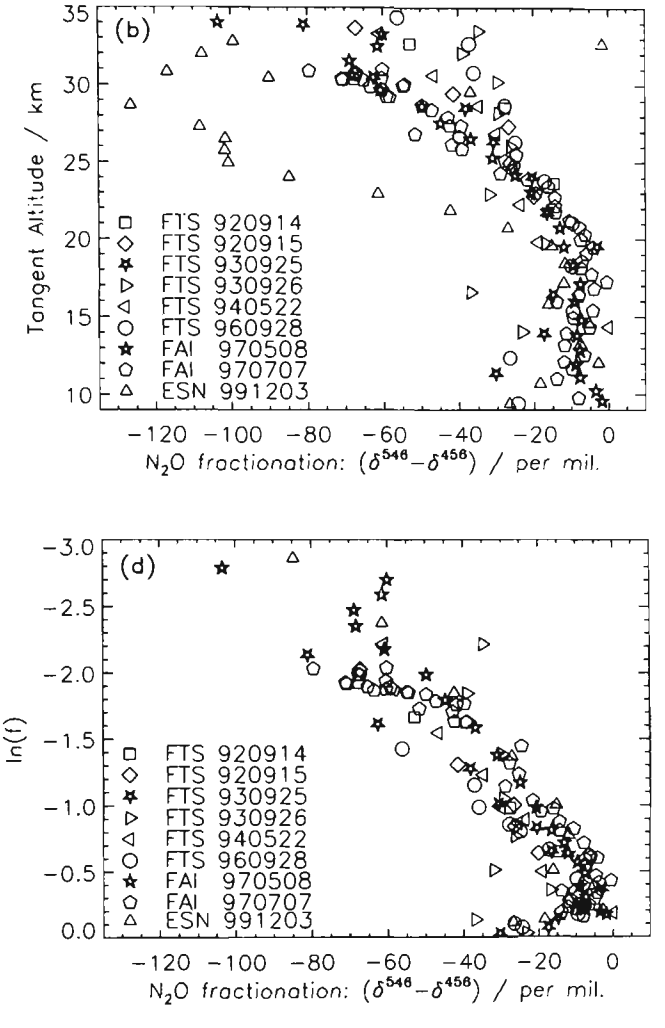

Figure 1.5 Vertical profiles of δ^{546}-δ^{456} of N_2O from FTIR balloon flights as described by *Griffith et al.* [2000]

Top panel is for tangent altitude, bottom panel is for ln(f) where f is the fraction of N_2O concentration to the tropospheric (unphotolysed) concentration. Balloon flights are from: FTS = Fort Sumner (34°N), FAI = Fairbanks (65°N), ESN = Esrange (68°N). The six digit code is the date in yymmdd format.

The δ^{546}-δ^{456} difference gets larger by 50-100 ‰ with altitude up to 35 km. The scatter above 35 km is due to the low concentration of N_2O (less than 10 % of the tropospheric N_2O) and the high relative measurement errors. The important point is that the δ^{546}-δ^{456} difference varies as a function of height and consequently as a function of ln(f) where f

is the ratio of the N_2O concentration to the tropospheric (unphotolysed) N_2O concentration.

1.4 Gas isotopomer measurement methods

1.4.1 Isotope Ratio Mass Spectrometry

The most established technique for measuring isotopic signatures is isotope ratio mass spectrometry (IRMS). Isotope ratio mass spectrometers are different from standard mass spectrometers because they are optimised for measuring typically three to six mass to charge ratios (*m/z*) rather than the complete *m/z* spectrum of molecular fragments.

An IRMS consists of an ion source, accelerating electrodes, a magnet and Faraday collector cup detectors for the *m/z* being measured. For the example, measuring the isotopomers of CO_2 requires Faraday collector cups for *m/z* 44 ($^{12}C^{16}O_2$), 45 ($^{13}C^{16}O_2$) and 46 ($^{12}C^{18}O^{16}O$). Figure 1.6 shows the schematic configuration of an IRMS optimised for measuring $\delta^{15}N$ of N_2.

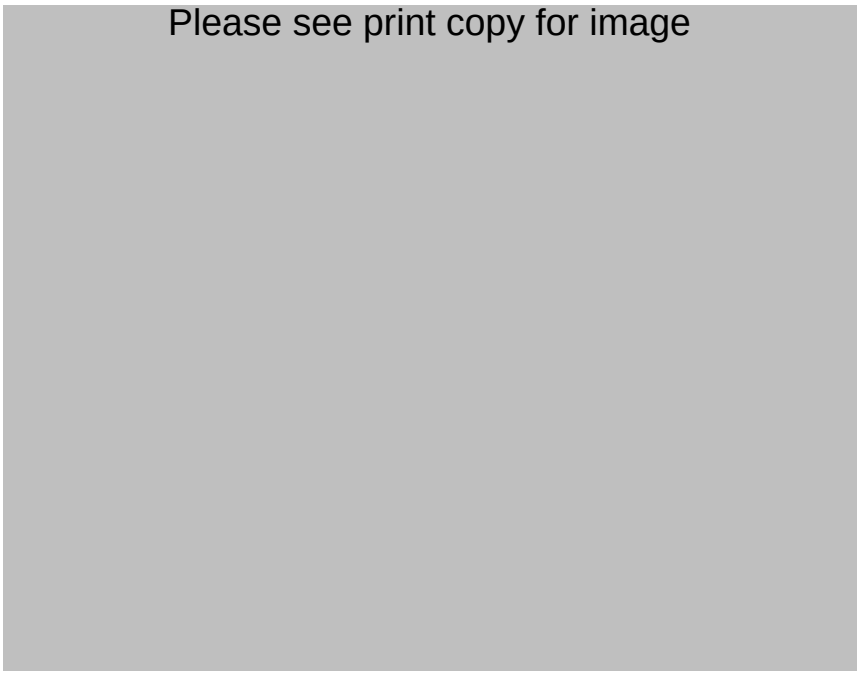

Figure 1.6 Schematic diagram of an isotope ratio mass spectrometer optimised for measuring $\delta^{15}N$ [*Mulvaney*, 1993].
m/e is the mass to charge ratio, described in this thesis as *m/z*

The major limitation that IRMS faces is that it measures mass and therefore cannot easily discriminate between molecules with identical mass but with different structures, for example CO_2 and N_2O which both have *m/z* 44. In the case of N_2O isotopomers a paper published in 1950 by *Friedman and Bigeleisen* [1950] first described the use of a modified IRMS technique to measure the positional isotopomers $^{14}N^{15}N^{16}O$ and $^{15}N^{14}N^{16}O$, and a paper by *Garber and Hollocher* [1982a] also described a similar technique. This technique was further developed by *Brenninkmeijer and Röckmann* [1999] and *Toyoda and Yoshida* [1999].

The five significant N_2O isotopomers, $^{14}N^{14}N^{16}O$, $^{14}N^{15}N^{16}O$, $^{15}N^{14}N^{16}O$, $^{14}N^{14}N^{18}O$ and $^{14}N^{14}N^{17}O$ have *m/z* ratios of 44, 45, 45, 46 and 45 respectively. Nitrous oxide ionises in the IRMS source, forming ions of *m/z* 44, 45 and 46. Fragmentation also occurs,

forming ions $^{14}N^{16}O^+$, $^{15}N^{16}O^+$, $^{14}N^{17}O^+$ and $^{14}N^{18}O^+$, with *m/z* of 30, 31, 31 and 32 respectively. If R is defined as the ratio of the isotopically heavy species to the unsubstituted species, then the following relationships apply [*Yoshida and Toyoda*, 2000]:

$$I^{45} = R^{456} + R^{546} + R^{447} \tag{1.14}$$

$$I^{46} = R^{448} + \left(R^{456} + R^{546}\right) \cdot R^{447} + R^{456} \cdot R^{546} \tag{1.15}$$

$$I^{31} = R^{456} + R^{447} \tag{1.16}$$

$$I^{32} = R^{448} + R^{456} \cdot R^{447} \tag{1.17}$$

where I^x is the ion beam intensity ratio for species of mass x to the most abundant species and the shorthand N_2O isotopomer notation (Table 1.3) is used. The isotopic ratios R^{456}, R^{546}, R^{448} and R^{447} can in theory be obtained by substituting observed measurements into equations 1.14 to 1.17. In practice, the signal from *m/z* 32 is very unreliable because of interference from O_2 [*Brenninkmeijer and Röckmann*, 1999; *Toyoda and Yoshida*, 1999] and therefore the R^{447}/R^{448} ratio is assumed to simplify calculations. In most naturally occurring samples R^{447}/R^{448} is very close to 0.515 because the great majority of reactions fractionate the heavy isotopes of a molecule strictly according to their mass [*Kaye*, 1987], but evidence has emerged to show that there is a mass independent fractionation component in some N_2O samples [*Cliff et al.*, 1999; *Cliff and Thiemens*, 1997; *Röckmann et al.*, 2001a; *Röckmann et al.*, 2001b]. As the measured size of the mass independent fractionation anomaly is about 1 ‰ for δ^{447}, a small overestimation in δ^{456} and $\delta^{15}N$ of 0.1 and 0.05 ‰ respectively results. By measuring N_2O and NO, $\delta^{15}N$, δ^{448} and δ^{456} can be obtained. However δ^{546} is calculated from equations 1.14 and 1.15 using the assumptions outlined above.

The IRMS has two significant advantages over any other existing technique: precision and sample size. *Yoshida and Toyoda* [2000] claim that with a sample of more than 1 μmol the precision of each isotopomer determination is better than 0.05 ‰, while that of the bulk isotope is close to 0.02 ‰. For samples of N_2O from ambient background air, passed through a GC for pre-concentration, the N_2O isotopomer precision is between 0.4 and 0.7 ‰. Aliquots of 100-150 mL of air provided enough N_2O for analysis with the IRMS technique. Continuos flow IRMS uses nano molar amounts of N_2O [*Yoshida and Toyoda,* [2000].

This technique has some complications. Firstly, the $\delta^{447}/\delta^{448}$ ratio is assumed to be mass-dependent. Secondly, scrambling of the isotopes occurs in the ion beam and must be calibrated. The fundamental assumption made in this technique is that the ions assumed in the calculations are the ones formed solely from N_2O in the direct dissociation to only N and NO in the ion source. The third complication is that δ^{546} is calculated and not measured directly. Compensating these limitations is that no other current technique can match IRMS for sample size requirements and precision.

1.4.2 Optical emission spectroscopy

Optical emission spectroscopy has been used for measuring $\delta^{15}N$ of N_2, with *Naudé* [1929] the first to discoverer ^{15}N, by using a form of this technique. If gas at low pressure is placed in a discharge tube and excited by absorbing energy from an external radio-frequency (RF) source, the emitted UV-VIS radiation as the gas relaxes to the ground state can be used to ascertain its isotopic composition. In the case of nitrogen, the ^{15}N enrichment is determined from the relative intensities for the $^{14}N_2$, $^{14}N^{15}N$ and

$^{15}N_2$ lines of the 2 → 0 vibrational transition of the $C\left(^3\Pi_u\right) \rightarrow B\left(^3\Pi_g\right)$ electronic transition [*Preston*, 1993].

Figure 1.7, adapted from *Preston* [1993] shows schematically the components for analysis of ^{15}N by optical emission spectroscopy.

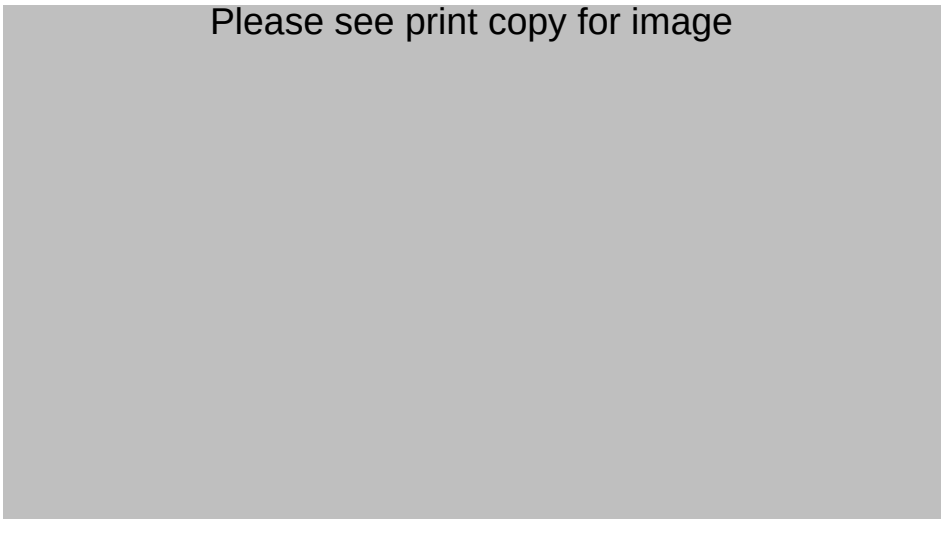

Figure 1.7 Basic components of an optical emission ^{15}N analyser [*Preston*, 1993]

The light emitted by the sample is focused by a quartz lens onto a grating monochromator and the intensity of the emitted light as a function of wavelength is recorded. For routine analysis of biological samples at natural abundance, precision and accuracy are both approximately ± 0.1-0.2 ‰ ^{15}N. This technique does not feature prominently in the literature for nitrogen isotopic analysis beyond approximately 1991. It was originally developed as a low cost alternative to IRMS, but has since been superseded by cheaper isotope ratio mass spectrometers, and has not been used to measure N_2O isotopomers.

1.4.3 Tunable diode laser spectroscopy

Much work has been invested in developing tunable diode laser (TDL) spectroscopy for measuring stable isotopes. TDL spectroscopy has been used for measuring, for example, $^{13}CH_4/^{12}CH_4$ and $^{14}N^{15}N^{16}O/^{15}N^{14}N^{16}O/^{14}N^{14}N^{16}O$ [*Uehara et al.*, 2001], $^{12}CH_3D/^{12}CH_4$ [*Bergamaschi and Harris*, 1995] and the D/H, $^{17}O/^{16}O$ and $^{18}O/^{16}O$ ratios in water [*Kerstel et al.*, 1999]. The emission of a TDL is used to measure a pair of closely spaced and adjacent rotational-vibrational lines in the gas sample, one from each isotopomers of interest, chosen so that they are of similar strength. For example, when measuring $^{13}CO_2$ and $^{12}CO_2$, *Becker et al.* [*Becker et al.*, 1992] chose the *R(10)* line of $^{13}CO_2$ at 2291.681 cm^{-1} and the *P(60)* line of $^{12}CO_2$ at 2291.542 cm^{-1}. Their narrow separation of only 0.139 cm^{-1} enables their resolution by using a TDL.

There are several common points in the experiments listed above. The single mode laser beam is typically split and passed through a sample and reference gas cell, and indium antimonide or mercury cadmium telluride detector measures the infrared radiation absorbed by the analyte gas. The sample cell can either be of the single pass design [*Becker et al.*, 1992] or of the multipass Herriot design [*Uehara et al.*, 2001], where pathlengths of 100 m are common. This technique can be very accurate and precise (± 0.3 ‰), primarily due to the high signal to noise ratio achieved by using high volume to pathlength Herriot cells to contain the sample. The main disadvantage of using TDLs for isotopic measurements is that a different laser is normally required for measuring each gaseous species as the laser frequency is tunable only over a very limited range.

1.4.4 Fourier transform infrared spectroscopy

Fourier transform infrared spectroscopy (FTIR) spectroscopy has been used for measuring $\delta^{13}C$ of CO_2 [*Esler*, 1997; *Esler et al.*, 2000c; *Kindness and Marr*, 1996; *Kindness and Marr*, 1997]. *Kindness and Marr* [1996] used 0.25 cm^{-1} resolution spectroscopy to analyse pure CO_2 samples to a reported $\delta^{13}C$ precision of ± 12 ‰. *Kindness and Marr* [1997] used 1 cm^{-1} resolution FTIR and approximately 10 bar sample pressures to achieve a $\delta^{13}C$ precision of ± 8 ‰. *Esler* [1997] and *Esler et al.* [2000b; 2000c] used low resolution (1 cm^{-1}) FTIR spectroscopy to measure $\delta^{13}C$ during a six-week continuous measurement campaign at the Cape Grim Baseline Air Pollution Station, and also from a tower during an intensive experimental investigation of the biosphere-atmosphere exchange of energy, water, CO_2, N_2O, CH_4 and stable isotopes – the OASIS (Observations at Several Interacting Scales) experiment. The precision of a single $\delta^{13}C$ CO_2 analysis was ± 0.19 ‰. A typical experimental configuration for FTIR analysis of $\delta^{13}C$ and trace gases is shown in Figure 1.8.

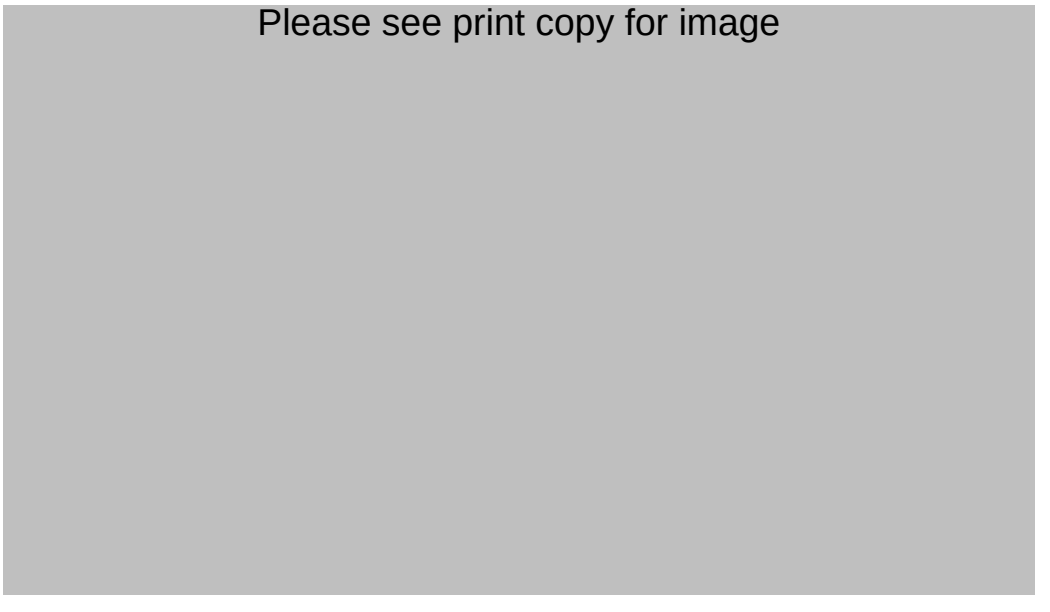

Figure 1.8 Schematic diagram of an FTIR instrument for analysis of $\delta^{13}C$ and trace gases [*Esler et al.*, 2000a]

The key components are a Bomem MB100 FTIR spectrometer with maximum resolution of $1cm^{-1}$, an indium antimonide infrared detector cooled by liquid nitrogen, and a multi-pass White cell [*White*, 1942]. The spectrometer is temperature controlled and purged with dry CO_2-free N_2. *Esler* [1997] and *Esler et al.* [2000b; 2000c] describe the experimental method in great detail.

1.5 Introduction to this work

Nitrous oxide is an extremely important atmospheric gas due to its key role in the chemistry of stratospheric ozone destruction, its role in the global radiative balance and its long atmospheric lifetime. It is the least understood of the major greenhouse gases and its budget is poorly known. Isotopomer analysis could prove a very useful tool in narrowing the uncertainty in the global N_2O cycle, in the same way that isotopomer analysis has proved successful in constraining the CO_2 budget. In particular, analysis of the intramolecular ^{15}N position of the N_2O molecule could provide unique information

that is not provided in analysis of the mean $\delta^{15}N$. Thus, intramolecular $\delta^{15}N$ analysis can be used as an additional independent constraint on the N_2O budget.

This project has several foci. High resolution Fourier transform infrared (FTIR) spectroscopy is developed as an independent technique for measuring the complete isotopic composition of N_2O. This includes developing the quantitative methods for analysis of high resolution N_2O spectra. The technique is compared to other existing N_2O isotope techniques. The FTIR technique is used to quantify isotopic processes occurring in an N_2O source (nitrification and denitrification from soils), an N_2O sink (stratospheric photolysis) and to monitor the tropospheric N_2O isotopic composition.

Chapters 2 reviews the spectroscopy theory of the high resolution N_2O spectrum and FTIR spectroscopy, describes the development of quantitative analytical techniques for the analysis of high resolution N_2O FTIR spectra. Chapter 3 describes the design, construction and operation of the experimental hardware that was constructed for N_2O isotopomer analysis, describes the selection of an N_2O working standard and describes the procedures for sample handling and measurement. Chapter 4 describes in detail the derivation of the theoretical optimum spectroscopic conditions, describes the method validation, describes in detail the limits to the precision of the method and provides a comprehensive summary of the FTIR method. Chapter 5 describes the measurement of the isotopic fractionation factors for the laboratory photolysis of N_2O by the FTIR method and compares the results to other experimental studies and to N_2O photolysis theories. Chapter 6 discusses the tropospheric N_2O isotopomer composition as measured over the course of approximately one year. Chapter 7 describes the isotopomeric measurement of N_2O emissions from a pig-effluent fertilized crop field

Chapter 8 concludes the thesis. Detailed procedures for assembly and dismantling the experimental equipment are given in the Appendix.

1.6 References

Adel, A., Further detail in the rock-salt prismatic solar spectrum, *Journal of Astrophysics*, *88* (186-188), 1938.

Albritton, D.L., L.G. Meira Filho, U. Cubasch, X. Dai, Y. Ding, D.J. Griggs, B. Hewitson, J.T. Houghton, I. Isaksen, T. Karl, M. McFarland, V.P. Meleshko, J.F.B. Mitchell, M. Noguer, B.S. Nyenzi, M. Oppenheimer, J.E. Penner, S. Pollonais, T. Stocker, and K.E. Trenberth, Technical Summary of the Working Group 1 Report, pp. 21-83, Intergovernmental Panel on Climate Change Third Assessment Report, 2001.

Andreae, M.O., Biomass burning: Its history, use and distribution and its impact on environmental quality and global climate, in *Global biomass burning*, edited by J.S. Levine, pp. 3-28, MIT Press, Cambridge, Mass., 1991.

Bange, H.W., and M.O. Andreae, Nitrous oxide in the deep waters of the world's oceans, *Global Biogeochemical Cycles*, *13* (4), 1127-1135, 1999.

Bange, H.W., S. Rapsomanikis, and M.O. Andreae, Nitrous Oxide in Coastal Waters, *Global Biogeochemical Cycles*, *10* (1), 197-207, 1996.

Becker, J.F., T.B. Sauke, and M. Lowenstein, Stable isotope analysis using tunable diode laser spectroscopy, *Applied Optics*, *31* (12), 1921-1927, 1992.

Bergamaschi, P., and G.W. Harris, Measurements of stable isotope ratios $^{13}CH_4/CH_4$, CH_3D/CH_4 in landfill methane using a Tunable Diode Laser absorption spectrometer, *Global Biogeochemical Cycles*, *9* (4), 439-447, 1995.

Bouwman, A.F., Direct emissions of nitrous oxide from agricultural soils, *Nutrient Cycling in Agroecosystems*, *46*, 53-70, 1996.

Bouwman, A.F., I. Fung, Matthews, and J. J, Global analysis of the potential for N_2O production in natural soils, *Global Biogeochemical Cycles*, *7* (3), 557-597, 1993.

Bouwman, A.F., K.W.v.d. Hoek, and J.G.J. Olivier, Uncertainties in the global source distribution of nitrous oxide, *Journal of Geophysical Research-Atmospheres*, *100* (D2), 2785-2800, 1995.

Bowen, R., *Isotopes and climates*, Elsevier, 1991.

Brasseur, G.P., J.J. Orlando, and G.S. Tyndall, *Atmospheric Chemistry and Global Change*, Oxford University Press, Oxford, 1999.

Brenninkmeijer, C.A.M., and T. Röckmann, Mass spectrometry of the intramolecular nitrogen isotope distribution of environmental nitrous oxide using fragment-ion analysis, *Rapid Communications in Mass Spectrometry*, *13* (20), 2028-2033, 1999.

Breuer, L., H. Papen, and K. Butterbach-Bahl, N_2O emission from tropical forest soils of Australia, *Journal of Geophysical Research-Atmospheres*, *105* (D21), 26353-26367, 2000.

Castro, M.S., P.A. Steudler, J.M. Melillo, J.D. Aber, and S. Millham, Exchange of N_2O and CH_4 between the atmosphere and soils in spruce-fir forests in the north eastern United States, *Biogeochemistry*, *18*, 119-135, 1993.

Cicerone, R., Analysis of sources and sinks of atmospheric nitrous oxide (N_2O), *Journal of Geophysical Research-Atmospheres*, *94*, 18265-18271, 1989.

Cliff, S.S., C.A.M. Brenninkmeijer, and M.H. Thiemens, First measurement of the $^{18}O/^{16}O$ and $^{17}O/^{16}O$ ratios in stratospheric nitrous oxide: A mass-independent anomaly, *Journal of Geophysical Research-Atmospheres*, *104* (D13), 16171-16175, 1999.

Cliff, S.S., and M.H. Thiemens, The $^{8}O/^{16}O$ and $^{17}O/^{16}O$ ratios in atmospheric nitrous oxide: a mass-independent anomaly, *Science*, *278*, 1774-1776, 1997.

Craig, H., Isotopic standards for carbon and oxygen and correction factors for mass spectrometric analysis of carbon dioxide, *Geochimica et Cosmochimica Acta*, *12*, 133-149, 1957.

Craig, H., Standards for reporting concentrations of deuterium and oxygen-18 in natural waters, *Science*, *133*, 1833-1834, 1961.

Crutzen, P., Ozone production rates in an oxygen-nitrogen-hydrogen oxide atmosphere, *Journal of Geophysical Research-Atmospheres*, *76*, 7311-7327, 1971.

Crutzen, P.J., The influence of nitrogen oxides on the atmospheric ozone content, *Quarterly Journal of the Royal Meteorological Society*, *96*, 320-325, 1970.

Dobbie, K.E., I.P. McTaggart, and K.A. Smith, Nitrous oxide emissions from intensive agricultural systems: Variations between crops and seasons, key driving variables, and mean emission factors, *Journal of Geophysical Research-Atmospheres*, *104* (D21), 26,891-26,899, 1999.

Dore, J.E., B.N. Popp, D.M. Karl, and F.J. Sansone, A large source of atmospheric nitrous oxide from subtropical North Pacific surface waters, *Nature*, *396*, 63-66, 1998.

Esler, M.B., High precision measurement of atmospheric trace gases using Fourier transform infrared spectroscopy, PhD thesis, University of Wollongong, Wollongong, 1997.

Esler, M.B., D.W.T. Griffith, F. Turatti, S.R. Wilson, and T. Rahn, N_2O concentration and flux measurements and complete isotope analysis using FTIR spectroscopy, *Chemosphere: Global Change Science*, *2*, 445-454, 2000a.

Esler, M.B., D.W.T. Griffith, S.R. Wilson, and L.P. Steele, Precision trace gas analysis by FT-IR spectroscopy. 1. Simultaneous analysis of CO_2, CH_4, N_2O, and CO in air, *Analytical Chemistry*, *72* (1), 206-215, 2000b.

Esler, M.B., D.W.T. Griffith, S.R. Wilson, and L.P. Steele, Precision trace gas analysis by FT-IR spectroscopy. 2. The $^{13}C/^{12}C$ isotope ratio of CO_2, *Analytical Chemistry*, *72* (1), 216-221, 2000c.

Firestone, M.K., and D.S. Schimel, Microbiological Basis of NO and N_2O Production and Consumption in Soil, in *Exchange of Trace Gases between Terrestrial Ecosystems and the Atmosphere*, edited by M.O. Andreae, and D.S. Schimel, John Wiley & Sons, New York, 1989.

Friedman, L., and J. Bigeleisen, Oxygen and isotope effects in the decomposition of ammonium nitrate, *Journal of Chemical Physics*, *18* (10), 1325-1331, 1950.

Garber, E.A.E., and T.C. Hollocher, ^{15}N Tracer Studies on the Role of NO in Denitrification, *Journal of Biological Chemistry*, *256* (11), 5459-5465, 1981.

Garber, E.A.E., and T.C. Hollocher, ^{15}N, ^{18}O Tracer Studies on the Activation of Nitrite by Denitrifying Bacteria, *Journal of Biological Chemistry*, *257* (14), 8091-8097, 1982a.

Garber, E.A.E., and T.C. Hollocher, Positional isotopic equivalence of nitrogen in N_2O produced by the denitrifying bacterium Pseudomonas stutzeri, *Journal of Biological Chemistry*, *257* (9), 4705-4708, 1982b.

Griffith, D.W.T., G.C. Toon, B. Sen, J.F. Blavier, and R.A. Toth, Vertical profiles of nitrous oxide isotopomer fractionation measured in the stratosphere, *Geophysical Research Letters*, *27* (16), 2485-2488, 2000.

Houghton, J.T., C.J. Jenkins, and J.J. Ephraums, Climate Change: The IPCC Scientific Assessment, Intergovernmental Panel on Climate Change, Cambridge University Press, Cambridge, UK, 1990.

Johnson, M.S., G. Due-Billing, A. Gruodis, and M.H.M. Janssen, Photolysis of nitrous oxide isotopomers studied by time-dependent Hermite propagation, *Journal of Physical Chemistry*, *105* (38), 8672-8680, 2001.

Kaye, J.A., Mechanisms and observations for isotopic fractionation of molecular species in planetary atmospheres, *Reviews of Geophysics*, *28* (8), 1609-1658, 1987.

Keller, M., W.A. Kaplan, and S.C. Wofsy, Emission of N_2O, CH_4, and CO_2 from tropical forest soils, *Journal of Geophysical Research*, *91*, 11791-11802, 1986.

Kerstel, E.R.T., R. van Trigt, N. Dam, J. Reuss, and H.A.J. Meijer, Simultaneous determination of the $^{2}H/^{1}H$, $^{17}O/^{16}O$, and $^{18}O/^{16}O$ isotope abundance ratios in water by means of laser spectroscopy, *Analytical Chemistry*, *71* (5297-5303), 1999.

Khalil, M.A.K., and R.A. Rasmussen, The global sources of nitrous oxide, *Journal of Geophysical Research*, *97*, 14651-14660, 1992.

Kim, C.H., and T.C. Hollocher, ^{15}N Tracer Studies on the Reduction of Nitrite by the Purified Dissimilatory Nitrite Reductase of *Pseudomonas aeruginosa*, *Journal of Biological Chemistry*, *258* (8), 4861-4863, 1983.

Kim, K.R., and H. Craig, Nitrogen-15 and Oxygen-18 Characteristics of Nitrous Oxide - a Global Perspective, *Science*, *262* (5141), 1855-1857, 1993.

Kroeze, C., A. Mosier, and L. Bouwman, Closing the global N_2O budget: A retrospective analysis 1500-1994, *Global Biogeochemical Cycles*, *13* (1), 1-8, 1999.

Mariotti, A., J.C. Germon, and A. Leclerc, Nitrogen isotope fractionation associated with the $NO_2^- \rightarrow N_2O$ step of denitrification in soils, *Canadian Journal of Soil Science*, *62*, 227-241, 1982.

McElroy, M.B., and J.C. McConnell, Nitrous oxide: a natural source of stratospheric NO., *Journal of Atmospheric Science*, *29*, 1095-1098, 1971.

Menegazzo, J., Isotopic signature of nitrous oxide emitted from agricultural soils, Honours thesis, University of Wollongong, Wollongong, 2000.

Minschwaner, K., R.J. Salawitch, and M.B. McElroy, Absorption of solar radiation by O_2: Implications for O3 and lifetimes of N2O, CFCl3, and CF2Cl2, *Journal of Geophysical Research*, *98* (D6), 10543-10561, 1993.

Mosier, A., C. Kroeze, C. Nevison, O. Oenema, S. Seitzinger, and O. Vancleemput, Closing the global N_2O budget - nitrous oxide emissions through the agricultural nitrogen cycle - OECD/IPCC/IEA phase ii development of IPCC guidelines for national greenhouse gas inventory methodology, *Nutrient Cycling in Agroecosystems*, *52* (2-3), 225-248, 1998.

Mosier, A.R., and D.S. Schimel, Nitrification and Denitrification, in *Nitrogen isotope techniques*, edited by R. Knowles, and H. Blackburn, Academic Press, 1993, 1993.

Mulvaney, R.L., Mass Spectrometry, in *Nitrogen isotope techniques*, edited by R. Knowles, and H. Blackburn, Academic Press, San Diego, 1993.

Naqvi, S.W.A., T. Yoshinari, D.A. Jayakumar, M.A. Altabet, P.V. Narvekar, A.H. Devol, J.A. Brandes, and L.A. Codispoti, Budgetary and biogeochemical implications of N_2O isotope signatures in the Arabian Sea, *Nature*, *394*, 462-464, 1998.

Naudé, S.M., An isotope of nitrogen, mass 15, *Physical Review*, *34*, 1498-1499, 1929.

Nedwell, D., N_2O emissions from laboratory controlled nitrification and denitrification conditions, 2001.

Nevison, C.D., E.R. Keim, S. Solomon, D.W. Fahey, J.W. Elkins, M. Loewenstein, and J.R. Podolske, Constraints on N_2O sinks inferred from observed tracer correlations in the lower stratosphere, *Global Biogeochemical Cycles*, *13* (3), 737-742, 1999.

Nevison, C.D., R.F. Weiss, and D.J. Erickson, Global oceanic emissions of nitrous oxide, *Journal of Geophysical Research-Oceans*, *100* (C8), 15809-15820, 1995.

Oliver, J.G.J., Working group report, Nitrous oxide emissions from fuel combustion and industrial processes. A draft methodology to estimate national inventories, in Proceedings of the International Workshop "Methane and Nitrous Oxide: Methods in National Emission Inventories and Options for Control", in *Technical Report 481507003*, edited by A.R. van Amstel, pp. 347-361, National Institute of Public Health and Environmental Protection, Bilthoven, The Netherlands, 1993.

Perez, T., S.E. Trumbore, S.C. Tyler, E.A. Davidson, M. Keller, and P.B. de Camargo, Isotopic variability of N_2O emissions from tropical forest soils, *Global Biogeochemical Cycles*, *14* (2), 525-535, 2000.

Perez, T., S.E. Trumbore, S.C. Tyler, P.A. Matson, I. Ortiz-Monasterio, T. Rahn, and D.W.T. Griffith, Identifying the agricultural imprint on the global N_2O budget using stable isotopes, *Journal of Geophysical Research-Atmospheres*, *106* (D9), 9869-9878, 2001.

Prasad, S.S., Natural atmospheric sources and sinks of nitrous oxide. 1. An evaluation based on 10 laboratory experiments, *Journal of Geophysical Research*, *99*, 5285-5294, 1994.

Prasad, S.S., Potential Atmospheric Sources and Sinks of Nitrous Oxide .2. Possibilities From Excited O_2, Embryonic O_3, and Optically Pumped Excited O_3, *Journal of Geophysical Research-Atmospheres*, *102* (D17), 21527-21536, 1997.

Prasad, S.S., E.C. Zipf, and X.P. Zhao, Potential Atmospheric Sources and Sinks of Nitrous Oxide .3. Consistency With the Observed Distributions of the Mixing Ratios, *Journal of Geophysical Research-Atmospheres*, *102* (D17), 21537-21541, 1997.

Prather, M., R. Derwent, D. Ehhalt, P. Fraser, E. Sanhueza, and X. Zhou, Other trace gases and atmospheric chemistry, in *Climate Change 1994: Radiative Forcing of Climate Change and An Evaluation of the IPCC IS92 Emission Scenarios (IPCC 94)*, edited by J.T. Houghton, L.G.M. Filho, J. Bruce, H. Lee, B.A. Callender, E. Haites, N. Harris, and K. Maskell, pp. 73-126, Cambridge University Press, Cambridge, 1995.

Preston, C.M., Optical emission spectrometry, in *Nitrogen isotope techniques*, edited by R. Knowles, and H. Blackburn, Academic Press, San Diego, 1993.

Rahn, T., and M. Wahlen, Stable isotope enrichment in stratospheric nitrous oxide, *Science*, *278*, 1776-1778, 1997.

Rahn, T., and M. Wahlen, A reassessment of the global isotopic budget of atmospheric nitrous oxide, *Global Biogeochemical Cycles*, *14* (2), 537-543, 2000.

Robertson, G.P., and J.M. Tiedje, Nitrous oxide sources in aerobic soils: Nitrification, denitrification and other biological processes, *Soil Biol. Biochem.*, *19*, 187-193, 1987.

Röckmann, T., J. Kaiser, R. Crowley, R. Borchers, W.A. Brand, and P.J. Crutzen, The isotopic enrichment of nitrous oxide ($^{15}N^{14}NO$, $^{14}N^{15}NO$, $^{14}N^{14}N^{18}O$) in the stratosphere and in the laboratory, *Journal of Geophysical Research-Atmospheres*, 10403-10410, 2001a.

Röckmann, T., J. Kaiser, R. Crowley, R. Borchers, W.A. Brand, and P.J. Crutzen, The isotopic enrichment of nitrous oxide ($^{15}N^{14}NO$, $^{14}N^{15}NO$, $^{14}N^{14}N^{18}O$) in the stratosphere and in the laboratory, *Journal of Geophysical Research-Atmospheres*, 10403-10410, 2001a.

Röckmann, T., J. Kaiser, R. Crowley, C.A.M. Brenninkmeijer, and P.J. Crutzen, The Origin of the Anomalous or "Mass-Independent" Oxygen Isotope Fractionation in Atmospheric N_2O, in *1st International Symposium on Isotopomers*, edited by N. Yoshida, pp. 35-36, Yokohama, Japan, 2001b.

Ryden, J.C., N_2O exchange between a grassland soil and the atmosphere, *Nature*, *292* (235-237), 1981.

Ryden, J.C., Denitrification loss from a grassland soil in the field receiving different rates of nitrogen as ammonium nitrate, *Journal of Soil Science*, *34*, 355-365, 1983.

Schmidt, J., J.W. Seiler, and R. Conrad, Emission of nitrous oxide from temperate forest soils into the atmosphere, *Journal of Atmospheric Chemistry*, *6*, 95-115, 1988.

Shearer, G., and D.H. Kohl, Nitrogen Isotopic Fractionation and ^{18}O Exchange in Relation to the Mechanism of Denitrification of Nitrite by *Pseudomonas stutzeri*, *Journal of Biological Chemistry*, *263* (26), 13231-13245, 1988.

Tiedje, J.M., Ecology of denitrification and dissimilatory nitrate reduction to ammonium, in *Biology of Anaerobic Microorganisims*, edited by A.J.B. Zehnder, John Wiley, New York, 1988.

Toyoda, S., and N. Yoshida, Determination of Nitrogen Isotopomers of Nitrous Oxide on a Modified Isotope Ratio Mass Spectrometer, *Analytical Chemistry*, *71* (20), 4711-4718, 1999.

Uehara, K., K. Yamamoto, T. Kikugawa, and N. Yoshida, Isotope analysis of environmental substances by a new laser-spectroscopic methods utilizing different pathlengths, *Sensors and Actuators B - Chemical*, *74*, 173-178, 2001.

Warneck, P., *Chemistry of the Natural Atmosphere*, Academic Press, 2000.

Watson, R.T., G. Rodhe, H. Oeschger, and U. Siegenthaler, Greenhouse gases and aerosols, in *Climate Change: The IPCC scientific assessment*, Cambridge University Press, 1990.

Wayne, R.P., *Chemistry of Atmospheres*, Oxford University Press, 2000.

Weeg-Aerssens, E., J.M. Tiedje, and B.A. Averill, The mechanism of microbial denitrification, *Journal of the American Chemical Society*, *109*, 7214, 1987.

Weeg-Aerssens, E., J.M. Tiedje, and B.A. Averill, Evidence from isotope labelling studies for a sequential mechanism for dissimilatory nitrite reduction, *Journal of the American Chemical Society*, *110*, 6851-6856, 1988.

White, J.U., Long optical paths of large aperture, *Journal of the Optical Society of America*, *32*, 285-288, 1942.

Yoshida, N., 15N depleted N_2O as a product of nitrification, *Nature*, *335*, 528-529, 1988.

Yoshida, N., and S. Toyoda, Constraining the atmospheric N_2O budget from intramolecular site preference in N_2O isotopomers, *Nature*, *405* (18 May), 330-334, 2000.

Yung, Y.L., and C.E. Miller, Isotopic fractionation of stratospheric nitrous oxide, *Science*, *278*, 1778-1780, 1997.

Chapter 2 Experimental I: Infrared Spectroscopy and Quantitative Spectral Analysis

2.1 The infrared spectrum of the nitrous oxide molecule

Nitrous oxide (N_2O) is a linear non symmetrical triatomic molecule with the structure N=N=O. The theory of the combined rotational-vibrational infrared spectrum of N_2O and its isotopomers will be briefly explained.

2.1.1 The rotational energy levels of N_2O

The rotational energy levels for a linear molecule (a simple rotator) are described by

$$F(J) = BJ(J+1) - DJ^2(J+1)^2 + HJ^3(J+1)^3 + KJ^4(J+1)^4 + \ldots \qquad (2.1)$$

where *F(J)* is the rotational term value (in cm^{-1}), *J* is the rotational quantum number, *h* is Planck's constant, *B* is the rotational constant (in cm^{-1}) and *D* is the centrifugal distortion constant, related to *B*. Since *D* is positive, the spacing between successive rotational energy levels decreases slightly with increasing *J*. The constants *H*, *K*, etc., are negligibly small compared to *D* and most molecules are adequately described by the first two terms of equation 2.1.

The terms following $BJ(J+1)$ correct for the non-rigidity of the rotating molecule and increase relative to $BJ(J+1)$ with increasing *J*, making the rotational levels more closely spaced at higher *J* values. For the purposes of this description, non-rigidity effects can be neglected. Detailed definitions of each term in the rotational energy

equation are given in most molecular spectroscopy texts, for example *Herzberg* [1962] and *Barrow* [1962].

2.1.2 The vibrational spectrum of N_2O

The N_2O molecule exhibits three vibrational degrees of freedom which are illustrated molecule in Figure 2.1, each of which exhibits a changing dipole moment and is infrared active.

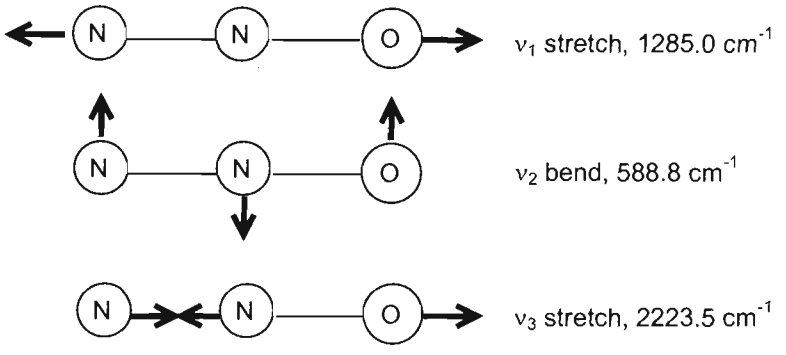

Figure 2.1 Normal vibrations and their fundamental frequencies for the N_2O molecule

To a first approximation, each vibrational mode behaves like an independent harmonic oscillator. The allowable energy levels for an oscillating molecule in wavenumbers are given by

$$G(\upsilon)=\left(\upsilon+\frac{1}{2}\right)\tilde{\nu}-\left(\upsilon+\frac{1}{2}\right)^2\tilde{\nu}x_e \qquad (2.2)$$

where υ is the vibrational quantum number and $\tilde{\nu}$ is the fundamental frequency in cm^{-1} of the vibration. The term x_e is the anharmonicity constant and is always positive,

making the separation between successive vibrational levels decrease with increasing υ.

2.1.3 The infrared spectrum of N_2O

The total energy of a molecule $T(\upsilon, J)$ is given by the sum of the rotational and vibrational energy components (equations 2.1 and 2.2) so that

$$T(\upsilon, J) = F(J) + G(\upsilon) \tag{2.3}$$

Each vibrational energy level contains a number of rotational energy levels giving rise to the high resolution structure in the N_2O spectrum. The infrared spectrum of N_2O results from transitions between vibrational and rotational energy levels subject to selection rules. For the linear asymmetric N_2O molecule in the harmonic oscillator approximation, the allowable transitions are when $\Delta\upsilon = \pm 1$ and when $\Delta J = \pm 1$. For perpendicular transitions such as the ν_2 bend, $\Delta J = 0$ is also allowed. At high resolution, the vibrational bands of N_2O show a large number of closely spaced lines which are due to rotational transitions.

Isotopically substituting one or more atoms in the N_2O molecule leads to a change in the reduced mass of the molecule, which in turn causes a shift in the fundamental vibrational frequency $\tilde{\nu}$ and therefore a spectral shift. The rotational constant B is dependent on the moment of inertia of a molecule [*Herzberg*, 1962] and therefore also changes slightly with isotopic substitution. Each isotopically substituted species therefore has a spectrum distinct from that of the parent molecule, both in the fundamental vibrational frequency and in the rotational spacings between the absorption lines. The measured infrared spectrum of an N_2O sample consists of contributions from

infrared spectra of each of its individual isotopomers. Providing the spectrum is measured with sufficient resolution, the individual isotopomer spectral lines are resolved and can be used as a basis for quantification. This principle is the basis of this work.

Figure 2.2 shows the synthetically calculated high resolution spectra of the $^{14}N^{14}N^{16}O$, $^{14}N^{15}N^{16}O$, $^{15}N^{14}N^{16}O$, $^{14}N^{14}N^{18}O$, $^{14}N^{14}N^{17}O$ and $^{15}N^{15}N^{16}O$ isotopomers of N_2O at natural abundances. Spectra were calculated using the computer program MALT, described in section 2.4. The shifted spectra of the N_2O isotopomers are clearly visible.

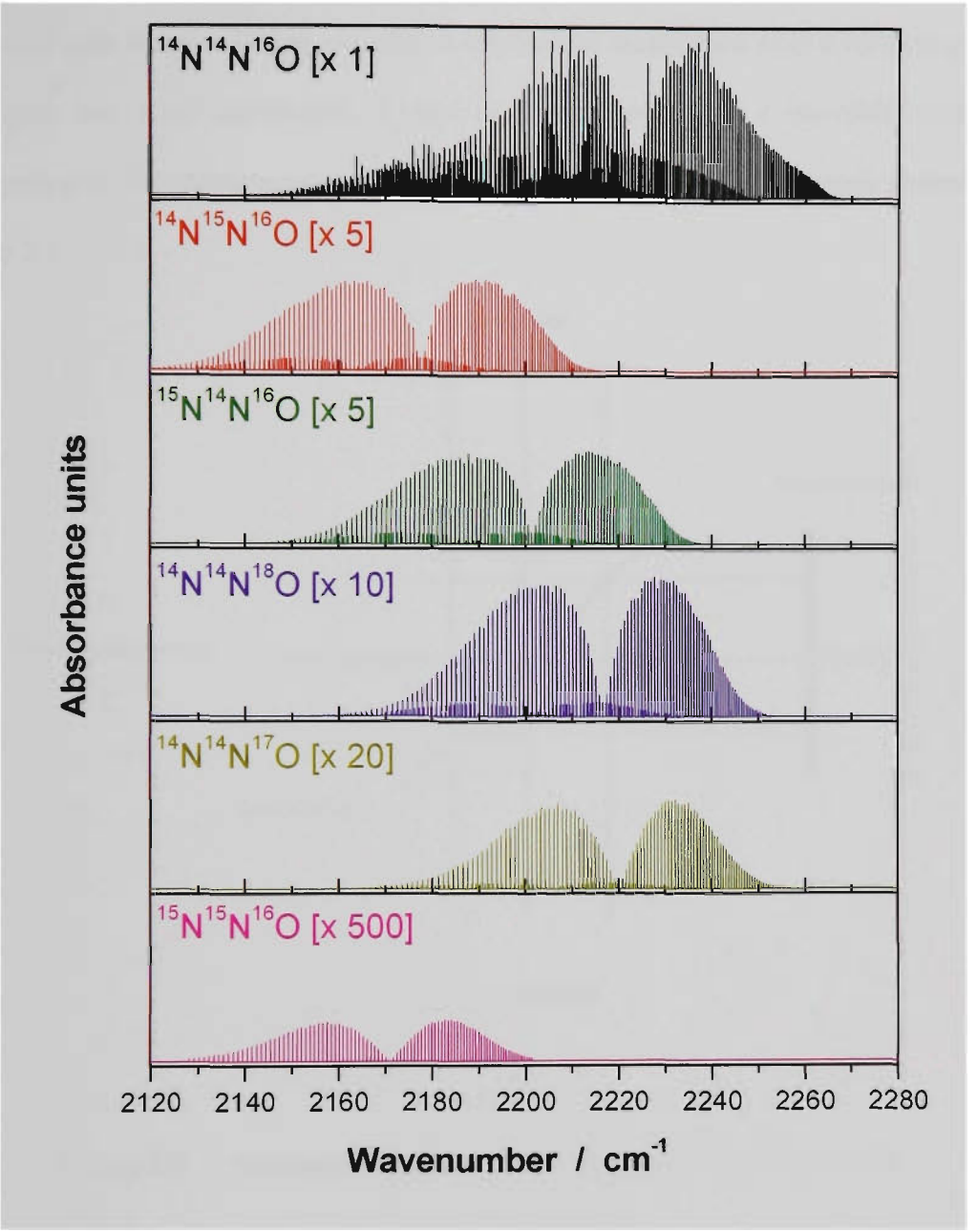

Figure 2.2 **Synthetically calculated FTIR spectra between 2120 and 2280 cm^{-1} of the six most naturally abundant N_2O isotopomers.**
Spectra are calculated using the computer program MALT (section 2.4), with N_2O line parameters provided by *Toth* [1991; 1993; 1999; 2000]

2.2 Fourier transform infrared (FTIR) spectroscopy

Fourier transform infrared (FTIR) spectrometers are based on the Michelson interferometer invented over 100 years ago [*Michelson*, 1891], which enables a beam of

light to be split into two beams via a beam splitter and recombined after a variable path difference has been introduced in one of those beams by a movable mirror. Schematically, the interferometer as used in a commercial FTIR spectrometer shown in Figure 2.3.

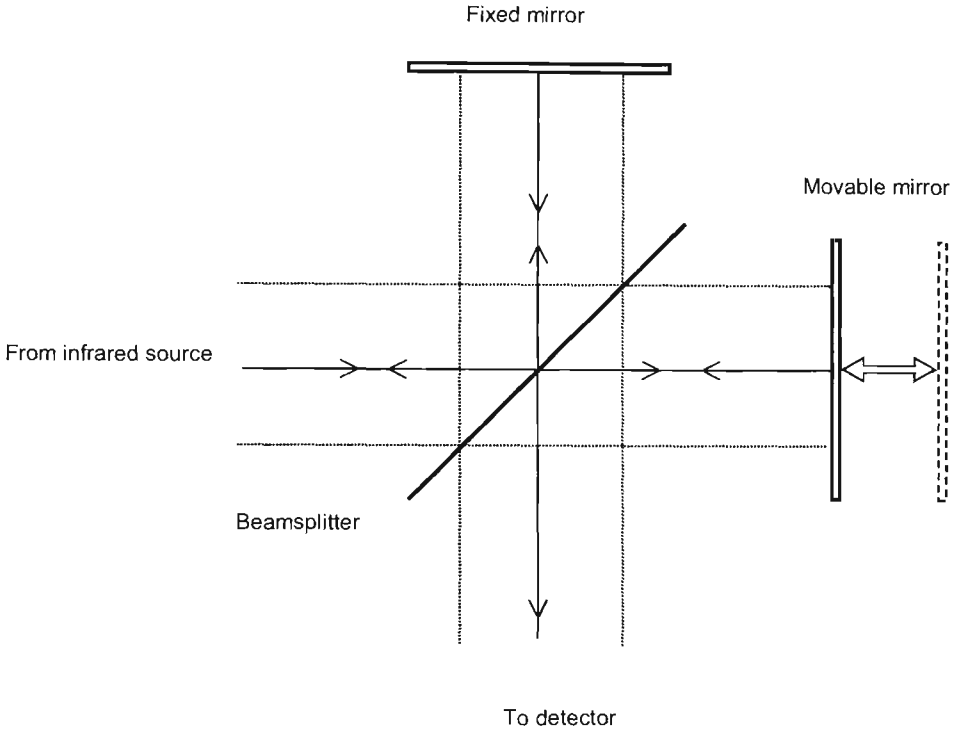

Figure 2.3 Schematic diagram of the Michelson interferometer

The beam of light from the source is partially reflected and partially transmitted by the beam splitter. The reflected beam reflects from the stationary mirror back to the beam splitter. The transmitted beam passes to a movable mirror and is then reflected back to the beam splitter where it recombines with the beam reflected from the fixed mirror. Because the movable mirror has introduced a variable path difference to the light beam, constructive or destructive interference occurs. This combined beam is partially reflected and transmitted by the beam splitter. One beam is measured by the detector

and another beam carrying the same spectral information as the first but 180° out of phase beam returns to the source. Modern spectrometers with corner cube mirror designs allow access to the "return beam" for analytical use. A thorough treatment of the FTIR spectrometer is given by *Griffiths and de Haseth* [1986].

2.2.1 Basic FTIR theory

The theoretical operation of an FTIR spectrometer can best be described by taking the very specific case of a perfectly monochromatic and collimated light source of wavelength λ cm and wavenumber $\tilde{\nu}$ ($=1/\lambda$) cm^{-1}. Let us assume the fixed and movable mirrors are equidistant from the beam splitter, so that the optical path difference (δ) is zero. If the movable mirror is moved a distance of $\lambda/4$ cm, the optical path difference between the two beams is now $\lambda/2$ cm. The beam from the fixed mirror and the beam from the movable mirror combine at the beam splitter. The distance they have travelled is exactly half a wavelength different and are therefore 180° out of phase, so destructive interference occurs. If the movable mirror is moved a further $\lambda/4$ cm, the total optical difference becomes λ cm. The beams are now in phase and constructively interfere at the beam splitter. Whenever the optical path difference is an integer multiple of λ, the two beams recombine at the beam splitter constructively in the output path. The beam returning to the source has the opposite phase as it has undergone two transmissions at the beam splitter, whereas the beam at the detector has undergone two reflections at the beam splitter.

For the ideal case of a perfectly collimated and monochromatic light source, the intensity seen at the detector, $I(\delta)$, is seen to vary sinusoidally so

$$I(\delta) = 0.5\, I_{source}\left(1 + \cos 2\pi\, \tilde{\nu}\delta\right) \tag{2.4}$$

where I_{source} is the infrared source intensity. This equation describes the interferogram – the relationship between intensity and mirror position. A real spectrometer does not contain a perfectly collimated monochromatic source, but a broad band infrared source with a divergent beam. The interferogram seen at the detector is the sum of the interferograms of each individual frequency emitted from the infrared source. Equation 2.4 becomes

$$I(\delta) = \int_{-\infty}^{+\infty} I(\tilde{\nu}) \cos 2\pi\, \tilde{\nu}\delta \cdot d\tilde{\nu} \tag{2.5}$$

if the spectroscopically insignificant constant term $0.5\, I_{source}$ is neglected and $I(\tilde{\nu})$ is set as the single beam spectral intensity. The single beam spectrum $I(\tilde{\nu})$ is calculated by taking the cosine Fourier transform of $I(\delta)$ such that

$$I(\tilde{\nu}) = 2 \int_{0}^{+\infty} I(\delta) \cos 2\pi\, \tilde{\nu}\delta \cdot d\delta \tag{2.6}$$

since $I(\delta)$ is an even function.

This description of $I(\tilde{\nu})$ is an approximation to the real measured spectrum. The interferogram cannot be measured between zero and infinite optical path difference. The measured interferogram is equivalent to the real interferogram multiplied by a truncation and weighting function (the apodisation function) to cope with a finite optical path difference. Therefore, spectral resolution is finite.

The infrared beam from the source passing through the spectrometer in reality is not perfectly collimated but diverges and has a finite field of view. This has the effect of limiting the maximum resolution achievable and shifting the wavenumber of a measured spectral line from its true value. Errors in sampling the x-axis of the spectrum (phase errors) also degrade the theoretical spectrum, and arise from either interferogram sampling errors or the effects of electronic filters designed to remove high frequency noise. Phase errors essentially add sine wave components to the cosine wave interferogram. All these effects and others combine to create the real measured spectrum from the theoretical one described by equation 2.6.

Take two identical spectra, $I_o(\tilde{\nu})$ and $I_{sample}(\tilde{\nu})$, with the second identical to the first except that it contains the sample to be measured, then the absorbance spectrum of the sample, $A(\tilde{\nu})$, is defined by

$$A(\tilde{\nu}) = \ln\left(\frac{I_o(\tilde{\nu})}{I_{sample}(\tilde{\nu})}\right) \tag{2.7}$$

Beer's law is a linear relationship between absorbance and sample concentration, so that at infinite spectral resolution

$$A(\tilde{\nu}) = \alpha(\tilde{\nu})Cl \tag{2.8}$$

where $\alpha(\tilde{\nu})$ is the absorption coefficient of the sample, C is its concentration and l is the distance infrared radiation traverses through the sample – the pathlength. Beer's law (equation 2.8) is an approximation in a real system where spectral resolution is finite. The transmission of the sample, $T(\tilde{\nu})$, is defined as

$$T(\tilde{\nu}) = \frac{I_{sample}(\tilde{\nu})}{I_o(\tilde{\nu})} \tag{2.9}$$

Since both single beam spectra have been collected under identical conditions, instrumental effects cancel out. Section 2.5 and section below describe in detail how this quantitative spectral information is extracted using the two above relationships. Absorbance spectra were analysed by classical least squares (CLS). Transmittance spectra, being non–linear with respect to component concentration, were analysed with non–linear least squares (NLLS).

2.2.2 Spectral signal to noise ratio (SNR)

The aim of this work is to retrieve quantitative isotopic information from samples of N_2O with the highest possible precision, for which high SNR is required. Several components act together to determine the overall SNR of a spectrum. Most of these components are "tradeable", so that increasing one component to increase SNR leads to a decrease in another component. *Griffiths and de Haseth* [1986] give an excellent and thorough treatment of FTIR signal to noise ratio trading rules.

The equation that summarises the contributions to the signal to noise ratio is given by:

$$SNR = \frac{U(\tilde{\nu},T)\cdot\Theta\cdot\Delta\tilde{\nu}\cdot t^{1/2}\cdot\xi\cdot D^{*}}{A_D^{1/2}} \qquad (2.10)$$

where

$U(\tilde{\nu},T)$ is the energy emitted by the infrared source at a specific wavenumber and temperature (W sr^{-1} cm^{-2} $(cm^{-1})^{-1}$),

Θ and ξ are the spectrometer throughput and efficiency respectively (cm^2.sr and unit less, respectively),

$\Delta\tilde{\nu}$ is the spectrometer resolution (cm^{-1}),

t is the spectrum averaging time (seconds),

D^* is the specific detectivity of the detector and is a measure of its sensitivity (cm $Hz^{1/2}$ W^{-1}), and

A_D is the detector surface area (cm^2).

For most experiments in FTIR spectroscopy, the source intensity, spectrometer efficiency, detector area and D^* are fixed, leaving resolution, averaging time and throughput as the levers available to the user to maximise the signal to noise ratio. Maximising SNR for N_2O spectra is discussed in the experimental section of the thesis.

2.3 Calculating spectra from first principles

This section is based on the spectroscopy theory outlined in *Griffith* [1996]. The total optical depth of a sample at each wavenumber is due to the absorption line of each molecule at that wavenumber. For each absorption line k of molecule i the contribution to the monochromatic optical depth τ at wavenumber $\tilde{\nu}$ is given by

$$\tau_i^k(\tilde{\nu}) = \sigma_i^k(\tilde{\nu}) \cdot a_i \tag{2.11}$$

where $\sigma_i^k(\tilde{\nu})$ is the absorption coefficient (cross section) at $\tilde{\nu}$, and a_i is the amount of component i, equal to the pathlength–concentration product. The usual units for $\sigma_i^k(\tilde{\nu})$ are cm^2 $molecule^{-1}$, and a_i has units of molecule cm^{-2}. The absorption coefficient is calculated from the integrated line strength by convolution with the true line shape. Two main broadening processes contribute to the true line shape, Doppler broadening and pressure broadening. Doppler broadening is due to the random molecular motion and leads to a Gaussian line shape

$$f_G(\tilde{\nu}) = \frac{1}{\alpha_G \sqrt{\pi}} \exp\left(-\frac{(\tilde{\nu} - \tilde{\nu}_0)^2}{\alpha_G^2} \right) \tag{2.12}$$

where α_G is the Gaussian half-width at half-height, expressed by

$$\alpha_G = 2\sqrt{\left(2\ln 2\frac{kT}{m}\right)}\frac{\tilde{\nu}}{c} \tag{2.13}$$

and m is the molecular mass, c is the speed of light, k is the Boltzmann constant and T is the temperature in Kelvin. Pressure broadening is due to collisions between gas molecules which perturb the energy levels and leads to a Lorentzian line shape described by

$$f_L(\tilde{\nu}) = \frac{\alpha_L / \pi}{(\tilde{\nu} - \tilde{\nu}_0)^2 + \alpha_L^2} \tag{2.14}$$

where α_L is the Lorentzian half-width at half height and is proportional to the total sample pressure. The Gaussian half-width is calculated from the sample temperature and molecular weight. Typical values at 1 atmosphere and 298 K for α_G and α_L are 0.002 cm^{-1} and 0.07 cm^{-1} atm^{-1}, respectively. The Lorentzian contribution dominates at pressures above approximately 45 torr. The combined line shape, a convolution of the Gaussian and Lorentzian line shapes, is known as the Voigt profile.

The absorption coefficient $\sigma_i^k(\tilde{\nu})$ is the convolution of the integrated line strength and the Gaussian and Lorentzian line shape contributions is given by

$$\sigma_i^k(\tilde{\nu}) = S_i^k \otimes [f_L(\tilde{\nu})]_i^k \otimes [f_G(\tilde{\nu})]_i^k \tag{2.15}$$

where $\otimes$ represents convolution.

The total monochromatic optical depth at frequency $\tilde{\nu}$ for a single homogeneous layer is the sum of the optical depth, $\tau_i^k(\tilde{\nu})$, over all absorption lines k of all molecules i in the sample and is given by

$$\tau(\tilde{\nu}) = \sum_i \sum_k \tau_i^k(\tilde{\nu}) \tag{2.17}$$

The true transmission spectrum of a sample without instrumental effects (infinite resolution) is given by

$$T(\tilde{\nu}) = \exp(-\tau(\tilde{\nu})) \tag{2.18}$$

and for absorbance

$$A(\tilde{\nu}) = \tau(\tilde{\nu}) \tag{2.19}$$

The intensity passing through the sample is

$$I(\tilde{\nu}) = I_o(\tilde{\nu})\exp(-\tau(\tilde{\nu})) \tag{2.20}$$

If the width of the instrumental line shape is much narrower than the true monochromatic line widths, then the above expressions for transmission (T) and absorbance (A) will be good approximations. A real spectrometer convolves the true spectrum intensity, $I(\tilde{\nu})$, with an instrumental line shape function to produce the measured spectrum. If $f_{ILS}(\tilde{\nu})$ is the instrument line shape, the measured spectrum is given by

$$I'(\tilde{\nu}) = I(\tilde{\nu}) \otimes f_{ILS}(\tilde{\nu}) \tag{2.21}$$

and the measured absorbance spectrum is

$$A'(\tilde{\nu}) = -\log\left(\frac{I(\tilde{\nu}) \otimes f_{ILS}(\tilde{\nu})}{I_0(\tilde{\nu}) \otimes f_{ILS}(\tilde{\nu})}\right) \tag{2.22}$$

Spectra $I'(\tilde{\nu})$ and $A'(\tilde{\nu})$ as calculated above should be identical to those obtained by an FTIR spectrometer if $f_{ILS}(\tilde{\nu})$ can be determined.

The instrument line shape function for a perfectly aligned spectrometer, $f_{ILS}(\tilde{\nu})$, is itself a convolution of an apodisation line shape which depends on a weighting (apodisation) applied to the raw interferogram, and a rectangular line shape, whose width depends on the divergence of the collimated beam in the interferometer due to the finite input aperture. The width of the rectangular divergence or field-of-view (FOV) contribution is given by $\tilde{\nu}\alpha^2/2$ where α is the divergence half angle and $\alpha = \phi/2f$, where ϕ is the entrance aperture diameter in the spectrometer and f is the collimator focal length. For and optimally chosen aperture $\tilde{\nu}_{\max}\alpha^2 = 1/L$, so that

$$\phi = 2f\sqrt{\frac{1}{\tilde{\nu}_{\max}L}} \tag{2.23}$$

2.4 Calculation of synthetic spectra with MALT

MALT (Multiple Atmospheric Layer Transmission) [*Griffith*, 1996] is a Fortran computer program that allows the calculation of the infrared spectra of gases from compilations of infrared line parameters according to the theoretical basis described above. One of the key uses of MALT is its ability to generate a synthetic calibration set of spectra with multiple components including distinct isotopomers. For the example of N_2O isotopomer analysis, a set of 50 calibration spectra with the partial pressures of $^{14}N^{14}N^{16}O$, $^{14}N^{15}N^{16}O$, $^{15}N^{14}N^{16}O$, $^{14}N^{14}N^{18}O$ and $^{14}N^{14}N^{17}O$ all independently varying can be generated. Manually generating this calibration set would require preparing 50 actual samples with independently varying N_2O isotopomer concentrations and measuring 50 consecutive high resolution spectra. In principle this calibration would have to be repeated whenever instrumental conditions changed and is clearly not

practicable. A synthetic set of calibration spectra that meets these criteria is easily generated in a matter of minutes.

The calculation of synthetic spectra by MALT starts from a compilation of absorption line parameters. The most commonly used line parameter compilation is the HITRAN database [*Rothman et al.*, 1998] and now available at http://www.hitran.com with regular updates. HITRAN contains line parameters for 31 common atmospheric gases and their isotopomers. For each absorption line of each molecule, the line frequency ν_0, integrated line strength S, lower state energy level E_0 and the Lorentzian half width α_L, the temperature dependence of S and the temperature and pressure dependence of α_L are included. For this work a subset of N_2O line parameters was used which was kindly provided by *Toth* [1991; 1993; 1999; 2000].

In line-parameter databases such as HITRAN the integrated line strengths are quoted for 296 K and are corrected to the temperature of the spectrum calculation. The correction arises because of the temperature dependence of the lower state energy level populations and the small contribution from spontaneous emission. This correction is given by

$$S(T) = S(296)\cdot\frac{Q(296)}{Q(T)}\cdot\frac{\exp\left(-\frac{c_2\tilde{\nu}_0}{T}\right)}{\exp\left(-\frac{c_2\tilde{\nu}_0}{296}\right)}\cdot\left(\frac{1-\exp\left(-\frac{c_2\tilde{\nu}_0}{T}\right)}{1-\exp\left(-\frac{c_2\tilde{\nu}_0}{296}\right)}\right) \qquad (2.24)$$

where Q is the partition function and c_2 is the second radiation constant (= hc/k = 1.439 cm K). The vibrational contributions to the partition functions are evaluated in the harmonic approximation, and the rotational contributions are proportional to T for linear molecules and $T^{1.5}$ for non-linear molecules.

MALT firstly calculates the monochromatic spectrum – the spectrum of the gas at unit concentration at infinite resolution without the distorting effect of the instrument. The line positions and intensities form a "stick" spectrum which is convolved with the Lorentzian and Gaussian line shape functions to obtain the monochromatic optical depth, $\tau_i(\tilde{\nu})$. The optical depth is then summed over all absorbing molecules and the monochromatic transmission calculated. This is linearly scaled by the amount of gas in the measurement without loss of accuracy. The final step is to convolve the monochromatic transmission spectrum with the instrument line shape function, which is calculated by taking into account the field of view, resolution, apodisation and empirical terms which mimic the line broadening and asymmetry effects of instrument misalignment. There are five of these empirical terms [*Griffith*, 1996]:

- FAPOD: eFfective APODisation (range 0-1), a trapezoidal apodisation function. When FAPOD = 0 the apodisation is a true boxcar shape, and when FAPOD = 1 the apodisation is a true triangular shape.
- MALIGN: The absolute misalignment of the spectrometer aperture in millimetres.
- SYM1 and SYM2: The imperfect line shape is parameterised by convolution with two functions, e^{-ax} or xe^{-ax}, as shown Figure 2.4. SYM1 and SYM2 are the constants a in the two parameterisation equations.
- PHASE: an empirical parameter which mimics phase errors in the real spectrum by adding sine components to the Fouricr transform.

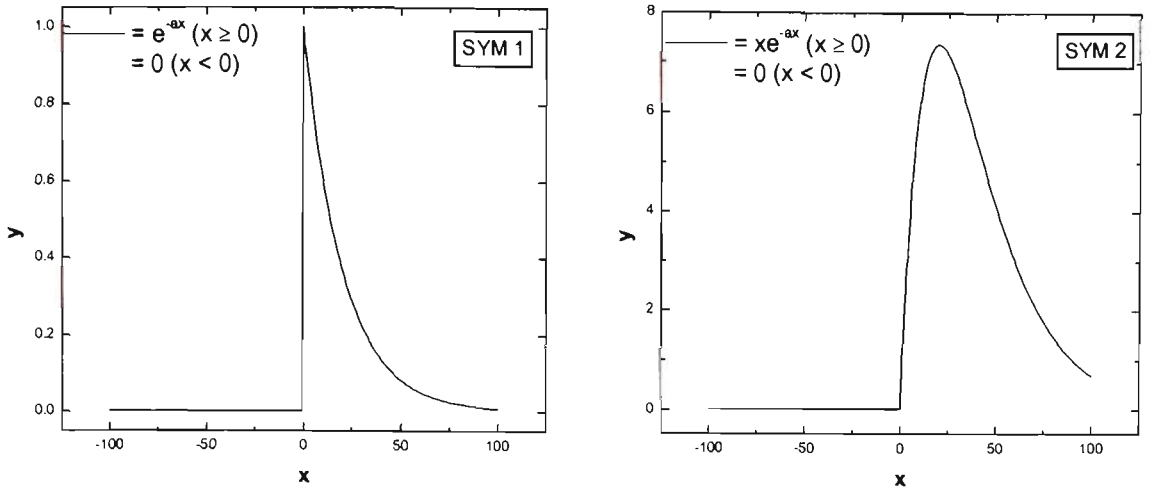

Figure 2.4 Functions e^{-ax} (SYM1) and xe^{-ax} (SYM2)

During this step the spectrum is converted to the required y-axis units (either transmittance or absorbance) and the point spacing is matched to that of a real spectrum. Detailed treatment of the algorithms used in MALT are given by *Griffith* [1996].

2.5 Classical Least Squares (CLS)

2.5.1 Theory

CLS is an example of a multivariate analysis technique – it uses information across the whole spectrum. Univariate techniques use absorbance information at a single wavelength, usually that of the most intense spectral peak. This ignores much of the spectral information. The CLS method employed here closely follows the work of *Haaland* [1987; 1990; 1992; 2000], *Haaland and Easterling* [1980; 1982] and *Haaland et al.* [2000; 1985]. This theory section summarises the theory of CLS analysis as discussed in the above publications.

The basis of CLS spectral analysis is the assumption inherent in Beer's Law that spectra behave linearly such that the total absorbance $A(\tilde{\nu})$ at a frequency $\tilde{\nu}$ is the linear sum of the absorptivity-pathlength product K_i times the component's concentration, C. For a sample containing m components, Beer's law can be expressed as:

$$A(\tilde{\nu}) = \sum_{i=1}^{m} K(\tilde{\nu})_i C_i \tag{2.25}$$

In the calibration phase of the CLS analysis, the absorbance spectra A and the concentrations C of a set of standards are known and $K(\tilde{\nu})_i$ is determined for each component. MALT is used in this work to generate a synthetic set of calibration standards. The range of concentrations for each absorbing component and number of calibration spectra required are given as input, and a set of spectra with random concentrations within the limits given is calculated. The spectra and concentration information are in a format for direct use by the calibration and prediction algorithm. The matrix of $K(\tilde{\nu})_i$ (the **K** matrix) is determined at each frequency $\tilde{\nu}$ via a least squares analysis. Each row of **K** represents the unit concentration spectrum of one component, and each column is the absorbances at one frequency, therefore the **K** matrix represents the pure component spectra at unit pathlength and concentration. Information describing the spectrum baseline behaviour can be added as additional rows in the **K** matrix. In the prediction part of the CLS analysis, the estimated pure component spectra (**K** matrix) and measured absorbance are used to determine in a least squares method the concentrations C_i for the individual spectral components for all frequencies simultaneously. In other words, a linear combination of pure-component spectra is selected that gives the best estimate of the unknown sample spectrum that

minimises the sum of the squares of the difference between the estimated spectrum and measured spectrum.

It is more useful to use matrix notation when dealing with multiple components of various concentrations at several frequencies. The Beer-Lambert law therefore can be expressed as

$$\mathbf{A} = \mathbf{CK} + \mathbf{E} \tag{2.26}$$

where

A is the $n \times p$ absorbance matrix of n spectra at p frequencies,

C is the $n \times m$ concentration matrix of the n spectra and m components,

K is the $m \times p$ matrix of absorption coefficients, and

E is the $n \times p$ matrix which describes spectral noise or model error.

In the calibration phase of a CLS determination, MALT is used to synthetically generate the matrix **A** and the matrix **C**. The square of the residual matrix **E** is minimised by finding the least squares estimate of the **K** matrix, $\hat{\mathbf{K}}$. In matrix notation

$$\hat{\mathbf{K}} = (\mathbf{C}'\mathbf{C})^{-1}\mathbf{C}'\mathbf{A} \tag{2.27}$$

where $\hat{\mathbf{K}}$ is the least squares estimate of the matrix **K** and $\mathbf{C}'$ is the transpose of **C**.. During the prediction phase of the CLS determination, the spectrum of an unknown sample is measured and can be represented by the 1 x p vector **a**, so that

$$\mathbf{a} = \mathbf{cK}' + \mathbf{e} \tag{2.28}$$

where $\mathbf{K}'$ is the transposed $\mathbf{K}$ matrix. A second least squares determination is carried out to estimate the individual component concentrations in the spectrum, $\hat{\mathbf{c}}$ from the previously least squares determined $\hat{\mathbf{K}}$:

$$\hat{\mathbf{c}} = (\hat{\mathbf{K}}\hat{\mathbf{K}}')^{-1}\mathbf{a}\hat{\mathbf{K}}' \tag{2.29}$$

where $\hat{\mathbf{K}}'$ is the (p x m) transposed least squares estimate of the matrix $\mathbf{K}$, determined in equation 2.27.

The software used for CLS determination was originally written by Galactic industries in Array Basic for use with the GRAMS spectral software. The CLS software was modified by us (Dr David Griffith, Fred Turatti) for use in analysing high resolution N_2O spectra.

2.5.2 Windows and regions

CLS is a whole spectrum technique which assumes Beer's law linearity. Under the measurement conditions in this work the spectrum of N_2O contains saturated lines from the parent isotope, $^{14}N^{14}N^{16}O$, and other, weaker lines from the other isotopomers. The saturated lines of the parent isotope dominate the spectrum. When measuring spectra in absorbance space, these spectral lines behave non-linearly due to finite spectral resolution, as there is insufficient spectral resolution to fully resolve these intense lines [*Anderson and Griffiths*, 1975]. The measured absorbance is not proportional to the concentration of N_2O and therefore the CLS assumptions break down. Spectral lines with absorbances less than approximately 0.8 units , between the saturated main parent isotopomer lines exhibit linear behaviour at resolutions better than or equal to 0.012

cm^{-1}. It is these small regions of the N_2O spectrum that are of interest for CLS determination as illustrated in Figure 2.5 and Table 2.1.

For the purpose of a CLS determination, the complete N_2O spectrum can be thought of as a series of suitable spectral "micro-windows" between saturated $^{14}N^{14}N^{16}O$ absorption lines. Regions in the N_2O spectrum between 2130 and 2270 cm^{-1} that were bound by N_2O spectral lines of 0.8 absorbance units or greater were selected. Therefore, each of these "micro-windows" contained N_2O spectral lines with absorbance less than 0.8. At a typical N_2O sample pressure of 1.0 torr and resolution of 0.012 cm^{-1}, this criterion resulted in a total of 81 micro-windows, most less than 1 cm^{-1} wide. The individual micro-windows selected are given in Table 2.1.

Table 2.1 Micro-windows used in CLS analysis of high resolution N_2O spectra

Window	Lower limit (cm-1)	Upper limit (cm-1)		Lower limit (cm-1)	Upper limit (cm-1)		Lower limit (cm-1)	Upper limit (cm-1)		Lower limit (cm-1)	Upper limit (cm^{-1})
1	2130.1	2160.07	*22*	2178.45	2178.53	*43*	2195.83	2196.05	*64*	2223.78	2224.07
2	2160.27	2161.27	*23*	2178.8	2179.09	*44*	2196.39	2196.5	*65*	2224.23	2224.45
3	2161.48	2162.57	*24*	2179.5	2179.6	*45*	2198.23	2198.49	*66*	2224.93	2225.24
4	2162.79	2163.8	*25*	2179.78	2180.17	*46*	2199.11	2199.53	*67*	2225.66	2225.95
5	2164.05	2164.93	*26*	2180.74	2181.08	*47*	2200.1	2200.25	*68*	2226.37	2226.85
6	2165.27	2166.03	*27*	2181.69	2181.82	*48*	2202.08	2202.49	*69*	2227.28	2227.46
7	2166.51	2167.24	*28*	2182.19	2182.36	*49*	2203	2203.4	*70*	2229.06	2229.27
8	2167.67	2168.35	*29*	2183.11	2183.38	*50*	2203.91	2204.07	*71*	2229.74	2230.06
9	2168.82	2169.44	*30*	2184.03	2184.35	*51*	2204.98	2205.17	*72*	2230.44	2230.79
10	2170.79	2171.02	*31*	2185.03	2185.25	*52*	2205.85	2206.04	*73*	2231.12	2231.37
11	2171.47	2171.69	*32*	2185.61	2185.74	*53*	2206.2	2206.4	*74*	2233.51	2233.84
12	2171.92	2172.23	*33*	2186.17	2186.39	*54*	2207.04	2207.14	*75*	2234.22	2234.46
13	2172.46	2172.76	*34*	2186.84	2187.0	*55*	2210.92	2211.12	*76*	2240.72	2240.94
14	2173.58	2173.78	*35*	2187.77	2188.01	*56*	2212.64	2212.75	*77*	2241.32	2241.52
15	2174.18	2174.34	*36*	2188.62	2189.1	*57*	2212.88	2213.03	*78*	2241.92	2242.28
16	2174.5	2174.57	*37*	2189.61	2190.02	*58*	2215.58	2215.79	*79*	2244	2244.21
17	2174.75	2174.9	*38*	2190.65	2191.21	*59*	2216.28	2216.67	*80*	2248.32	2248.52
18	2175.91	2176.03	*39*	2191.64	2192.22	*60*	2216.99	2217.38	*81*	2262.39	2269.9
19	2176.37	2176.74	*40*	2192.76	2193.28	*61*	2220.68	2221.02			
20	2177.36	2177.65	*41*	2193.65	2194.2	*62*	2221.46	2221.82			
21	2177.85	2178.02	*42*	2194.83	2195.18	*63*	2222.25	2222.53			

Each of these micro-windows contains lines from one or more of the N_2O isotopomers. Therefore, the CLS method and the synthetically generated calibration training set can be used to determine the isotopomers of N_2O from each of these 81 windows. The CLS software retrieves from every micro-window an amount and standard error (SE) for each isotopomer. The standard error for a spectrum is defined by

$$SE = \sqrt{\frac{\sum_{n} \left(S_{measured} - S_{fitted}\right)^2}{n}} \tag{2.30}$$

where n is the number of spectra in the calibration training set, $S_{measured}$ is the measured spectrum, and S_{fitted} is the best estimate (or fit) of the measured spectrum according to the classical least squares criteria described above.

The final determination of each isotopomer is the weighted mean of the determinations over the 81 windows, with the weights being the inverse squared standard error for each isotopomer and window, so that

$$\overline{C}_w = \frac{\sum_{j=1}^{m} \left(\left(C_{predicted}\right)_m \Big/ \left(SE\right)_m^2 \right)}{\sum_{j=1}^{m} \left(1 \Big/ \left(SE\right)_m^2 \right)} \tag{2.31}$$

where $\overline{C}_w$ is the weighted isotopomer concentration, $C_{predicted}$ is the CLS predicted isotopomer concentration, SE is as defined by equation 2.30 and m is the number of micro-windows (81 in this case). An example of two micro-window fits for window number 1 and 38 are shown in Figure 2.5 and Figure 2.6. Window 1 is a special case containing the weaker, high J lines at the lower edge of the 446 band.

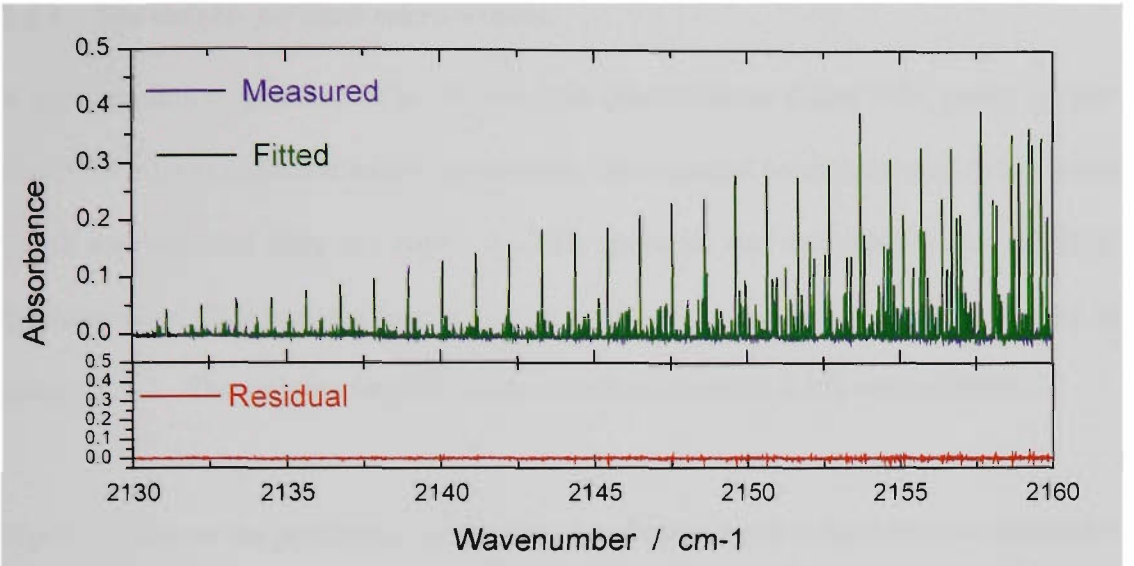

Figure 2.5 **Measured, Fitted and Residual spectrum for N_2O between 2130 and 2160 cm^{-1}, micro-window 1.**

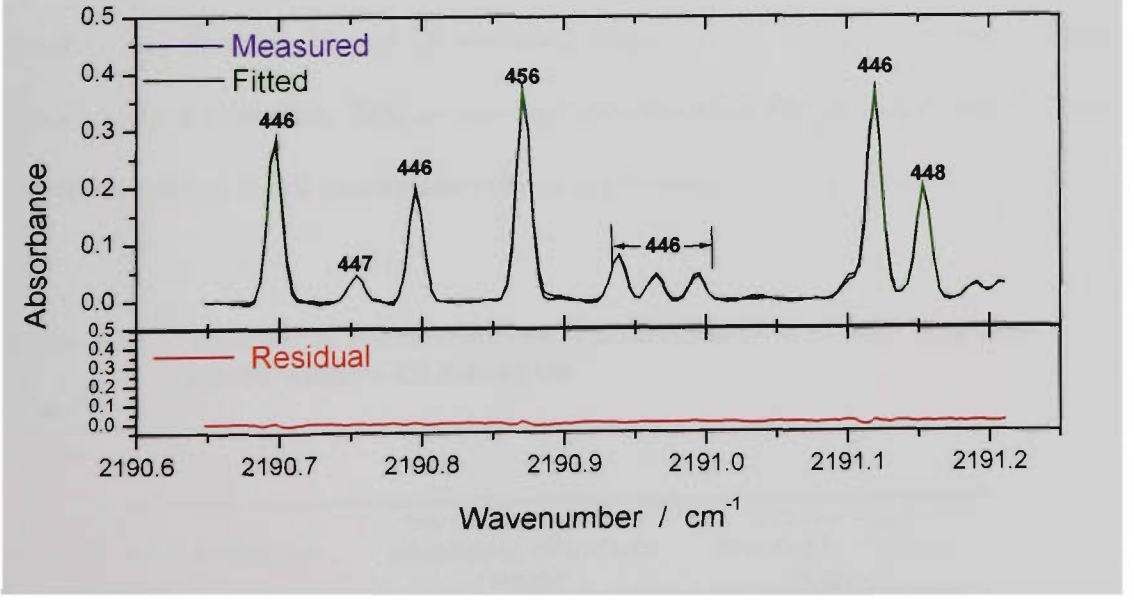

Figure 2.6 **Measured, Fitted and Residual spectrum for N_2O between 2190.65 and 2191.25 cm^{-1}, micro-window 38.**
446 = $^{14}N^{14}N^{16}O$, 456 = $^{14}N^{15}N^{16}O$, 448 = $^{14}N^{14}N^{16}O$ and 447 = $^{14}N^{14}N^{17}O$.

2.5.3 The weights for each micro-window

A high resolution spectrum of an N_2O sample (Scott-Marrin Gases N_2O, purity greater than 99.9 %) was collected under the standard experimental conditions used in this work which are described fully in Chapter 4. This spectrum was determined using multiple micro-window CLS analysis from a synthetic fifty-spectrum calibration as described in section 2.5.2. The weights for each micro-window (equation 2.30) were collated.

Figure 2.7 shows the percentage of the total weight attributed to each micro-window for each N_2O isotopomer for the above analysis, and Table 2.2 shows the number of windows required to describe 90% of the total weight for each isotopomer. Approximately 10 micro-windows contribute 90% or more to the final isotopomer determination for the isotopomers $^{14}N^{14}N^{16}O$, $^{14}N^{15}N^{16}O$, and $^{14}N^{14}N^{17}O$ (Table 2.2). For the isotopomers $^{15}N^{14}N^{16}O$ and $^{14}N^{14}N^{18}O$, 90% of the contribution to the final result is described by 33 and 20 windows, respectively. Using ten micro-windows describes, at a minimum, 54% of the final determination for all isotopomers. These results are typical for all spectra analysed by multi-window CLS analysis.

Table 2.2 Number of micro-windows contributing 90% of total weight in micro-window CLS analysis.

Isotopomer	No. of micro-windows contributing 90% of total weight	% of total weight described by 10 micro-windows
446	10	90
456	12	88
546	33	54
448	20	71
447	9	93

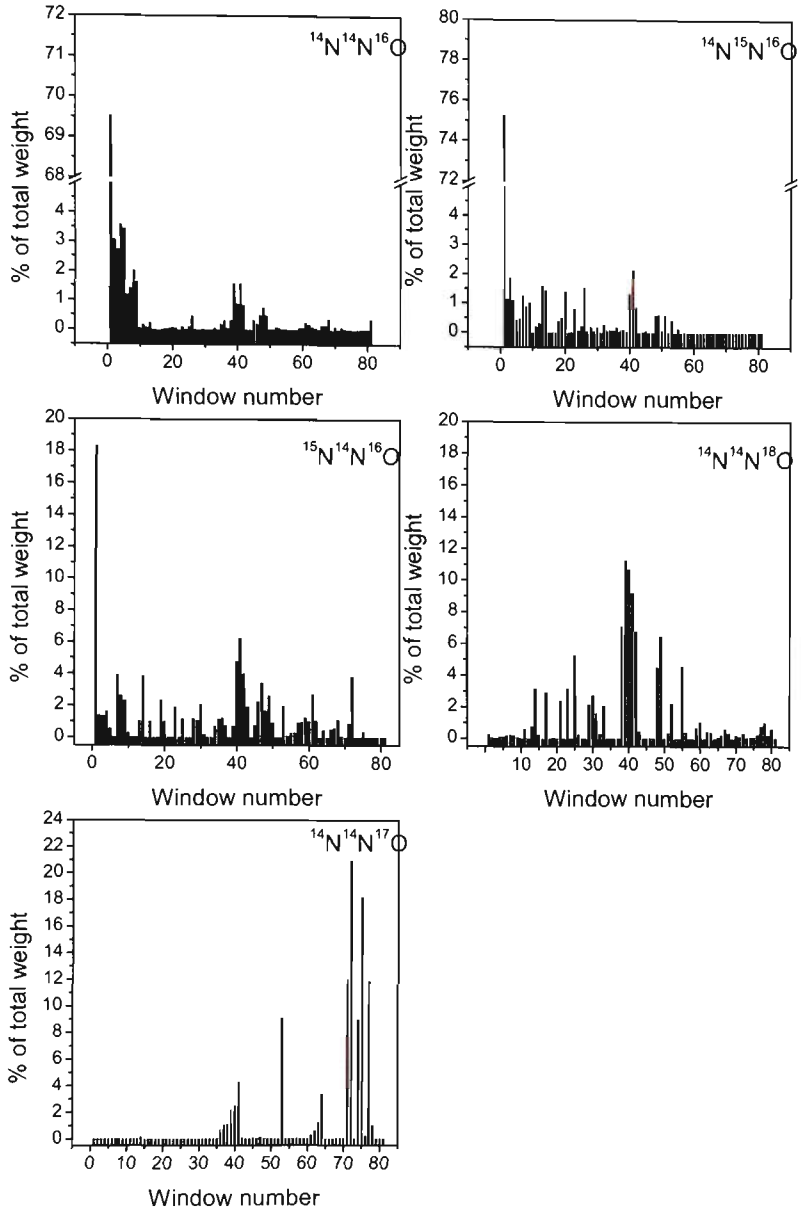

Figure 2.7 Weights as a function of micro-window for each N_2O isotopomer

The first window (Figure 2.7), between 2130 and 2160 cm^{-1}, on the edge of the main absorbance band, contributes approximately 70% of the weighed mean determination for both $^{14}N^{14}N^{16}O$ and $^{14}N^{15}N^{16}O$, and approximately 18% of the weighted mean determination of $^{15}N^{14}N^{16}O$. The determination for these three isotopomers is therefore almost completely governed by the determination of the first micro-window. The

properties of micro-window 1 which enable a good fit to the measured spectrum, and consequently low residual and high weight are:

- Its width is approximately 30 cm^{-1} wide compared to the 0.5 to 1 cm^{-1} width of most other micro-windows. Micro-window 1 therefore contains between 30 and 60 times more spectral data than other micro-windows,
- There is a very large number of high quality spectral lines present in the window for the isotopomers $^{14}N^{14}N^{16}O$, $^{14}N^{15}N^{16}O$ and $^{15}N^{14}N^{16}O$, and,
- There are no influences from the shoulders of intense peaks from the parent isotope.

The first micro-window is rich with high quality spectral information which is highly weighed by the CLS algorithm. There are some disadvantages to relying so much on this one window. Since it lies at the extreme of the P branch of the N_2O spectrum, it consist of transitions from high energy levels, or high J number. Absorptions from high J numbers are highly temperature dependent, as the ground-state population is highly temperature dependent. In order to minimise this, a set of spectral windows between 2170 and 2240 cm^{-1} was generated, thereby excluding high J number transitions. Predicting the same set of spectra with all windows and the 2170 to 2240 cm^{-1} subset shows that excluding the high J number transition lines decreases the isotopic determination precision by a factor of approximately 2, probably due to a lack of spectral information. Further, the experimental system is capable of controlling the temperature of the N_2O measured to ± 0.01 °C, which reduces the impact of high J number transitions negatively affecting determination precision.

2.5.4 Effect of the weights on determination precision

There are small systematic differences in the determination from each micro-window arising from baseline uncertainties and errors in line parameters. Variations in the weights between fitted spectra can cause variations in the final weighted determinations (section 2.5.3), effectively adding noise to the measurements. The following test was performed to determine if the weights used in the multi-window CLS determination affected the retrieved isotopomer δ values.

Three series of spectra were collected on 1 September 2000 (experiment SE01021m), 4 September 2000 (experiment SE04017m) and 25 September 2000 (experiment SE25033m), consisting of 21, 14 and 25 consecutive spectra, respectively. The sample was N_2O from BOC Gases Australia, with purity greater than 99.9 %, and spectra were collected under the standard experimental conditions which are described fully in Chapter 4. Isotopic determinations were calculated relative to the first spectrum in each series. Each spectrum set was predicted with multi-window CLS analysis using four separate weight sets:

1. Weights were calculated as $1/(SE)^2$ as described above, where SE is the standard error (equation 2.30) for each individual micro-window of each spectrum in the series. This weight set was abbreviated to "free weights".
2. Weights calculated as $1/(SE)^2$ from the multi-window fits to the first spectrum of the series of spectra being predicted. The weights were then fixed for all other spectra in that set. This weight set was abbreviated to "fixed weights".
3. Weights calculated as $1/(SE)^2$ from the multi-window fits to the first spectrum in a series of Scott-Marrin Gases N_2O working standard spectra. The weights

were then fixed for all determinations of other sets of spectra. This weight set was abbreviated to "Fixed Scott-Marrin N_2O weights".

4. Weights calculated as $1/(SE)^2$ from the multi-window fits to the first spectrum in a series of BOC Gases N_2O working standard spectra. The weights were then fixed for all determinations of other sets of spectra. This weight set was abbreviated to "Fixed BOC N_2O weights".

Figure 2.8 shows the retrieved δ $^{14}N^{15}N^{16}O$ for the spectrum series SE25033m, calculated relative to the first spectrum in the series. Twenty five consecutive spectra of the same sample of approximately 1.0 torr of BOC Gases N_2O working standard in a 2.4 m multiple reflection cell at 0.012 cm^{-1} apodised resolution were collected. Results for other N_2O isotopomers and experiment sets show very similar patterns.

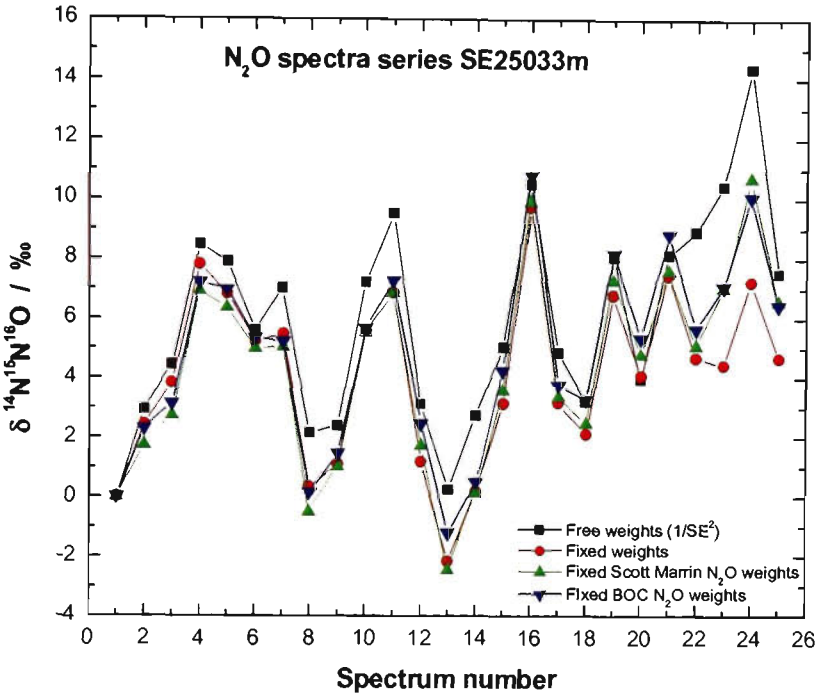

Figure 2.8 **$\delta^{14}N^{15}N^{16}O$ determinations for consecutive N_2O spectra series SE25033m determined with different sets of weights.**
δ is measured relative to the first spectrum

There are two patterns visible. The most obvious pattern is the scatter in δ for consecutive spectra determined with the same set of weights which is due to spectrometer instability and laboratory temperature drifts. The second pattern is the variation in δ for the same spectrum as retrieved by using different weight sets. Scatter in retrieved δ are most obvious when using the classical definition of inverse variance weighting, where the weights are calculated as $1/(SE)^2$ where SE is the standard error for each individual micro-window of each spectrum in the series – the "free weights" criterion. This is especially noticeable in the $\delta^{15}N^{14}N^{16}O$ determination. Using the "free weight" criterion when retrieving δ means the weights used are dominated by random spectrum to spectrum variation in the quality of the fit. Section 2.5.5 highlights

reasons for the spectrum to spectrum variation in weights. A fixed set of weights was therefore used for most isotopomer δ determinations, most often the Scott Marrin N_2O weights (point 3, section 2.5.4) in order to reduce some of this variability. The most statistically correct weighting method (point 1, section 2.5.4) leads directly to δ determinations results with the greatest scatter due to the random spectrum to spectrum variability.

2.5.5 The causes of weight variation and spectrum to spectrum variability

The $1/(SEP)^2$ weights for the same micro-window for consecutive spectra of the same N_2O sample from the experiments SE01021m, SE04017m and SE25033m show that the relative weights vary substantially between spectra of the same experimental series, occasionally by as much as 100%. Investigation of spectrum number 4 and spectrum number 22 of the SE25033m, having the lowest and highest weight respectively for the first micro-window, show that line shape asymmetry is primarily responsible for the variability in the weights. The more symmetric the line shape, the better the fit and therefore the higher the weight accorded to that micro-window. The cause of spectrum to spectrum variability is described in detail in Chapter 4 of this thesis.

2.6 Non-linear Least Squares (NLLS)

The assumption inherent in the Beer-Lambert law is that the calculated absorbance at any wavenumber is linearly proportional to the analyte concentration (equation 2.8). This assumption breaks down at moderately high absorbances because finite spectral resolution limits the accurate measurement of a strongly absorbing line [*Anderson and Griffiths*, 1975]. The CLS process assumes that the noise is the same at all spectral points, which is reasonable for low absorbances. In reality the noise is constant only in

the single beam spectrum. For regions where the single beam spectrum is approximately constant, this equates to constant noise in the transmission spectra. It is therefore more appropriate to fit spectra that have large absorbances as transmission spectra. This, and the convolution between the instrument line shape and spectrum intensity (equation 2.21) remove the linearity between absorbance and concentration. An alternative approach to spectral quantitative analysis is to assume that no linear relationship exists between analyte concentration and absorption and to determine the spectra in transmission with non-linear least squares (NLLS) analysis. This approach is described below.

2.6.1 Theory

The general form of the transmission equation is

$$I(\tilde{\nu}) = I_0(\tilde{\nu})\exp(-\tau(\tilde{\nu})) \tag{2.32}$$

where $I_o(\tilde{\nu})$ and $I(\tilde{\nu})$ are the intensities before and after passing through the sample, and $\tau(\tilde{\nu})$ is the total monochromatic optical depth of the measured sample. A real spectrometer convolves the spectrum intensity $I(\tilde{\nu})$ with an instrument line shape function to produce the real, or measured spectrum so that

$$I_{measured}(\tilde{\nu}) = [I_0(\tilde{\nu})\exp(-\tau(\tilde{\nu}))] \otimes f_{ILS}(\tilde{\nu}) \tag{2.33}$$

where $f_{ILS}(\tilde{\nu})$ is the instrument line shape function. The above equation is clearly non-linear with respect to the component concentration and cannot be solved using linear regression. However, it can be solved using standard non–linear minimisation techniques. Component concentration, resolution and field of view can be varied iteratively using, for example, the Levenberg-Marquardt method [*Press et al.*, 1991] to

obtain the best fit to the measured spectrum, $I_{measured}(\tilde{\nu})$. This is done by minimising the sum of the squares χ^2, where

$$\chi^2 = \sum_{i=1}^{N} [I_{measured}(\tilde{\nu}) - I_{calc}(\tilde{\nu})]^2 \quad . \tag{2.34}$$

This is the basis of the non-linear least squares (NLLS) algorithm used in this work. Studies by *Niple* [1980] and *Lin et al.* [1980a; 1980b] are early descriptions of the use of non-linear analysis in determination of atmospheric gas spectra.

2.6.2 The non-linear least squares algorithm

The NLLS algorithm used in this work was initially developed by Andreas R Reisinger at the University of Canterbury, New Zealand [*Reisinger*, 1998]. It is written in C++ and uses MALT as an external subroutine to generate the monochromatic spectra, following the theory described in sections 2.3 and 2.4. The algorithm was extensively modified (Fred Turatti, Dr David Griffith) to allow parameterisation of symmetric and asymmetric line broadening and called is referred to as Non-Linear MALT 3 (NLM3).

NLM3 allows iterative fitting of any of the following parameters: spectral shift, resolution, field of view, phase error, effective apodisation, SYM1, SYM2 and gas concentration. Parameters which simulate a non-ideal line shape, such as effective apodisation and additional symmetric and asymmetric line broadening parameters (SYM1 and SYM2, section 2.4) are also iteratively fitted. The process of quantitative spectral analysis by the NLM3 program can best be understood by way of a simplified program flow chart, shown in Figure 2.9

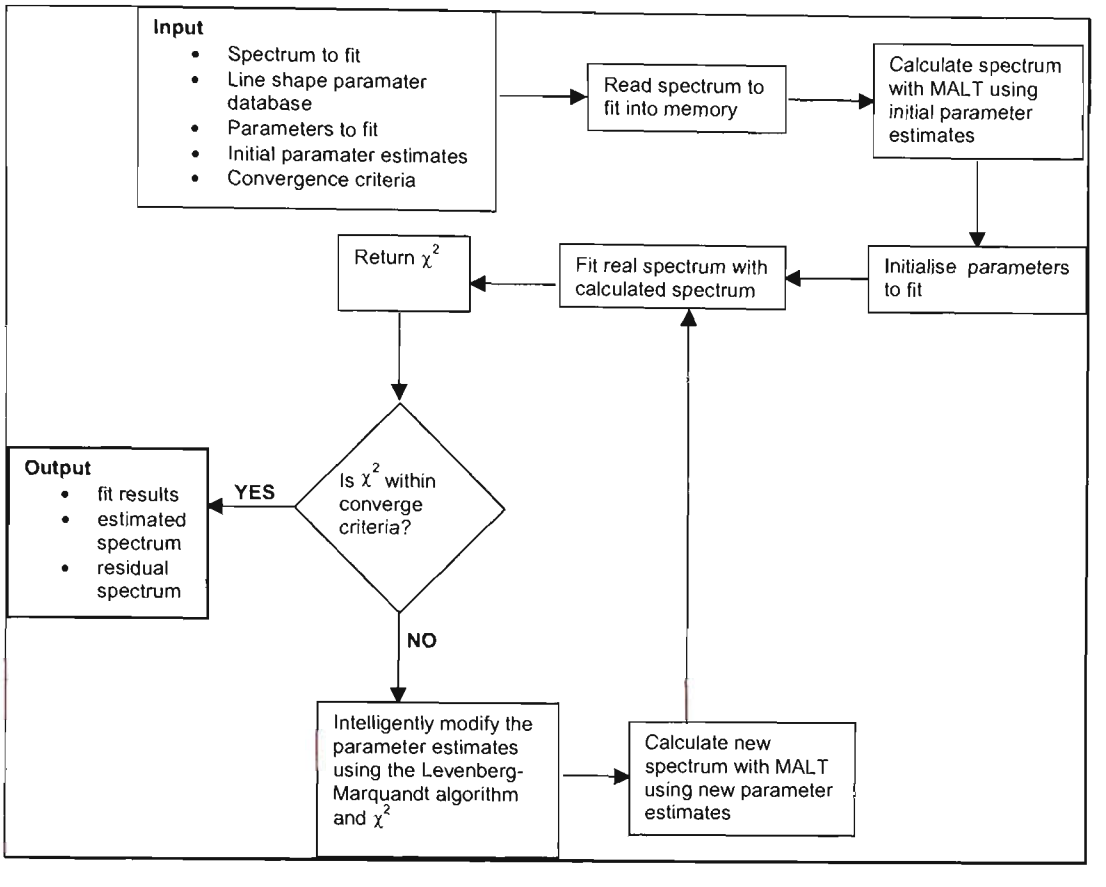

Figure 2.9 Flowchart for spectral analysis by non-linear least squares by the program NLM3.

NLM3 starts by reading from an input file standard information such as the spectrum name and format, the line parameter database and the initial estimates for the parameters to be fitted by the non-linear algorithm. The input file also contains the convergence criteria for χ^2. For example, the program can exit after a minium or maximum number of iterations, or when the difference between successive χ^2 are within a certain range. An initial synthetic spectrum is generated using the initial parameter estimates. This initial calculated spectrum is used to fit the measured spectrum and the parameter χ^2 is returned (equation 2.34). If χ^2 is within the convergence criteria, NLM3 ends. If χ^2 is outside the specified convergence criteria, the parameters to be fitted are intelligently

modified using a standard Levenberg-Marquandt algorithm [*Press et al.*, 1991] and the synthetic spectrum is recalculated. The fit cycle is repeated until the change in χ^2 meets the specified convergence criteria.

2.6.3 Optimum fitting regions

Non-linear least squares is capable of fitting very large spectral regions, for example the whole of the v3 stretch region of approximately 2110 cm^{-1} to 2280 cm^{-1}. This has advantages over multi-window CLS analysis in that only one window region is required to quantify all N_2O isotopomers, and that more spectral data are used. However, there are substantial advantages in determination precision to be gained by optimising the spectral regions which are used for isotopomer determination.

Twenty five consecutive spectra of 1.00 torr N_2O were collected with the DA-8 FTIR spectrometer using the standard measurement conditions fully described in Chapter 4. Quantitative determination of the N_2O isotopomers was performed with NLM3 with spectral regions of varying width between the upper and lower boundaries of 2160 and 2260 cm^{-1}. The combination band between 2400 and 2500 cm^{-1} was also investigated for determination of the parent $^{14}N^{14}N^{16}O$ isotopomer. Each fit to each collected spectrum can be characterised by the standard error in the individual isotopomer determinations. Therefore a three dimensional surface can be generated, with the left and right axes of the surface equivalent to the upper and lower boundary of the spectral window fitted, and the z axis as the average standard error from the quantitative fit to the 25 consecutive spectra. Using the average standard error from 25 spectra rather than one spectrum ensures that the standard error is a good representation of the real

experimental variation. Figure 2.10 shows the standard error surface for determination of the $^{14}N^{15}N^{16}O$ isotopomer.

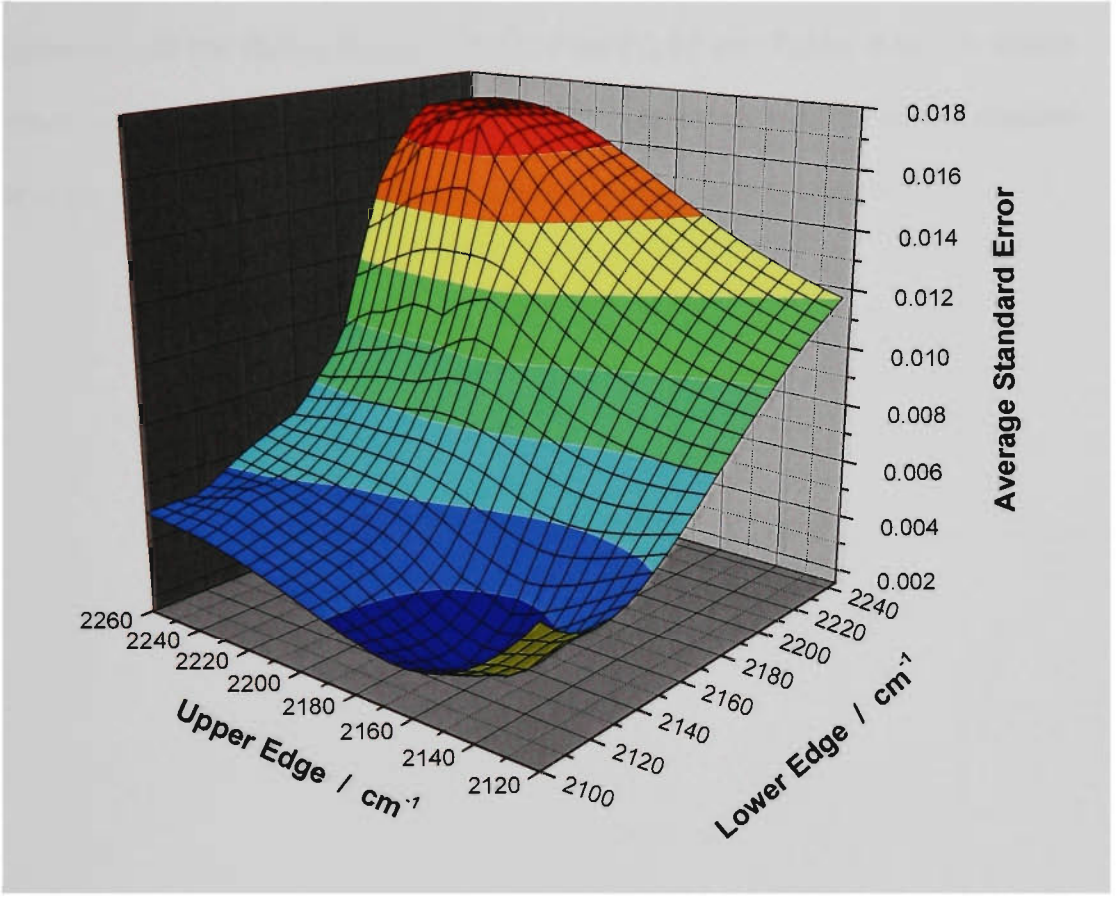

Figure 2.10 Standard error surface for $^{14}N^{15}N^{16}O$ isotopomer a function of upper and lower edge of the NLM3 fit window

Varying the left and right edge of the window used for NLLS quantification of the $^{14}N^{15}N^{16}O$ isotopomer leads to a large variation in the average standard error of the fit. Significant standard error advantages are gained by judicious choice of the region to used in the determination. Figure 2.10 shows the lowest standard error to be obtained with a window between 2120 and 2160 cm^{-1}. This corresponds to the far left portion of the P branch of the $^{14}N^{15}N^{16}O$ isotopomer spectrum, and therefore comprises many high *J* number lines. These lines are very temperature sensitive and are probably not the best

to rely on solely for quantitative analysis. A reasonable compromise between standard error and use of high J number lines is the 2120 – 2180 cm^{-1} region. Similar standard error surfaces were derived for analysis of the $^{15}N^{14}N^{16}O$, $^{14}N^{14}N^{18}O$ and $^{14}N^{14}N^{17}O$ isotopomers and are shown in Figure 2.11, Figure 2.12 and Figure 2.13. A similar approach can be used in modelling the effect of temperature variability on the standard error of the isotopomer determination, and this is carried out in Chapter 4.

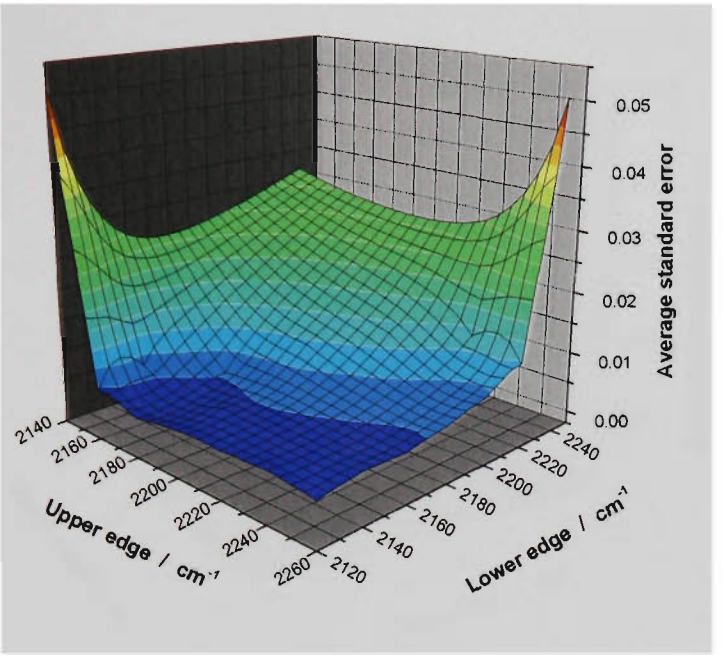

Figure 2.11 **Standard error surface for $^{15}N^{14}N^{16}O$ isotopomer a function of upper and lower edge of the NLM3 fit window**

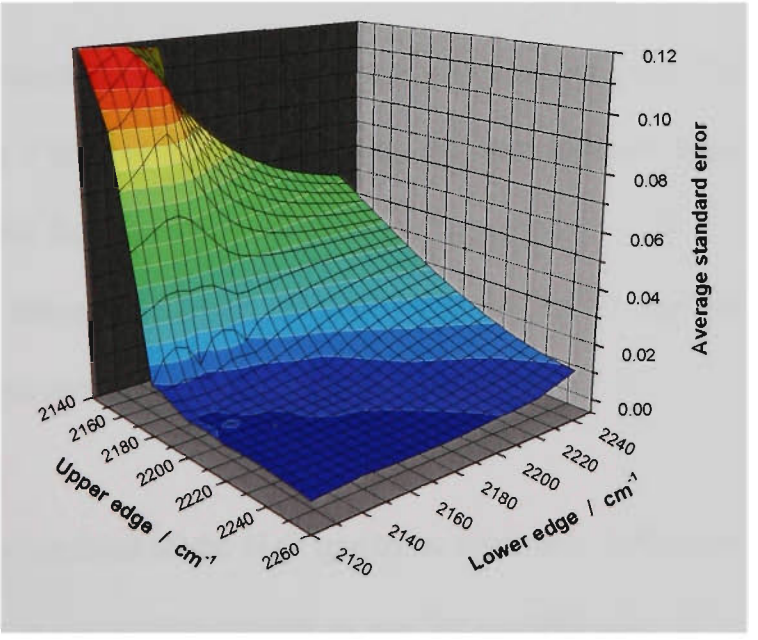

Figure 2.12 **Standard error surface for $^{14}N^{14}N^{18}O$ isotopomer as a function of upper and lower edge of the NLM3 fit window**

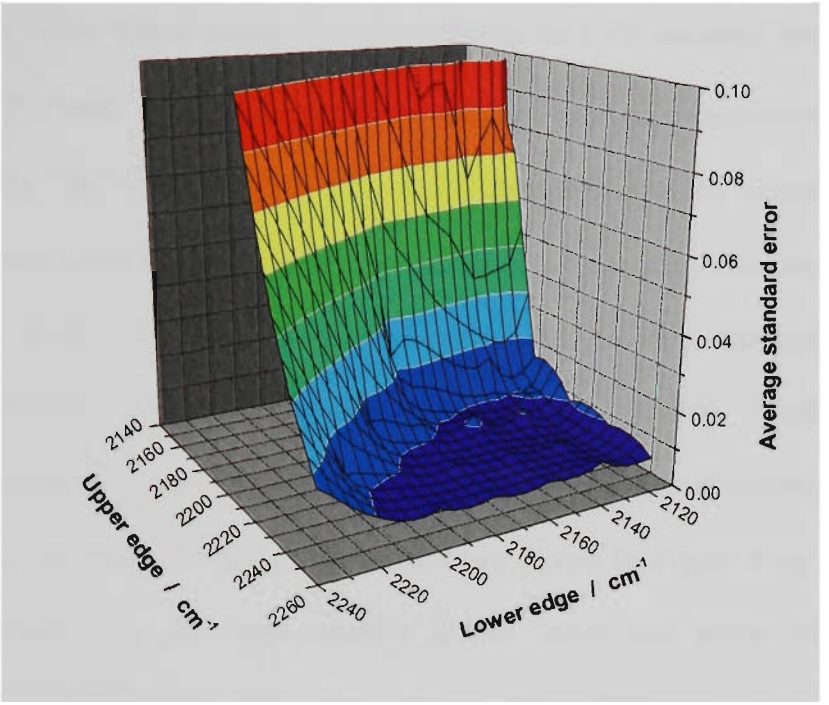

Figure 2.13 Standard error surface for $^{14}N^{14}N^{17}O$ isotopomer as a function of upper and lower edge of the NLM3 fit window

Analysing the results from the above standard error surfaces, and taking into account the influence of the high J number contribution lines in some windows leads to selecting two optimum windows for analysis of the enriched isotopomers: 2120 – 2180 cm^{-1} for analysis of the heavy nitrogen isotopes, $^{14}N^{15}N^{16}O$ and $^{15}N^{14}N^{16}O$; and 2160 – 2260 for analysis of the heavy oxygen isotopomers, $^{14}N^{14}N^{18}O$ and $^{14}N^{14}N^{17}O$.

The $\nu_1+ 2\nu_2$ combination band of the N_2O spectrum, centred at 2462.6 cm^{-1} is a strong infrared absorber. It is not strong enough to use for quantification of the heavy N_2O isotopomers, but it is quite adequate for analysis of the parent $^{14}N^{14}N^{16}O$ isotopomer. There is a substantial advantage in using this spectral region rather than the more obvious and much stronger ν_3 band for determination of the parent $^{14}N^{14}N^{16}O$. The absorption lines of $^{14}N^{14}N^{16}O$ are not saturated in the combination band as they are in the ν_3 band. Non-linear fits to the $\nu_1+ 2\nu_2$ combination band are more reliable than fits

to the ν_3 band, as under typical measurement conditions no N_2O saturated lines are present in the $\nu_1 + 2\nu_2$ band. The $\nu_1 + 2\nu_2$ combination band has similar transmission for $^{14}N^{14}N^{16}O$ as ν_3 for $^{14}N^{15}N^{16}O$ and $^{15}N^{14}N^{16}O$ and is therefore good for comparison since some systematic errors in the determination are minimised. Further, the maximum absorption in this combination band is approximately 50%, which is the optimum absorption for best determination with non-linear methods [*Niple*, 1980]. A standard error surface for quantitative analysis of $^{14}N^{14}N^{16}O$ in the $\nu_1 + 2\nu_2$ combination band was determined as described above and the results are shown in Figure 2.14. The $^{14}N^{14}N^{16}O$ determination is not very sensitive to the upper and lower window boundaries, therefore the whole $\nu_1 + 2\nu_2$ band between 2400 – 2520 cm^{-1} is used. An example of fits to N_2O spectra using NLM3 is shown in Figure 2.15.

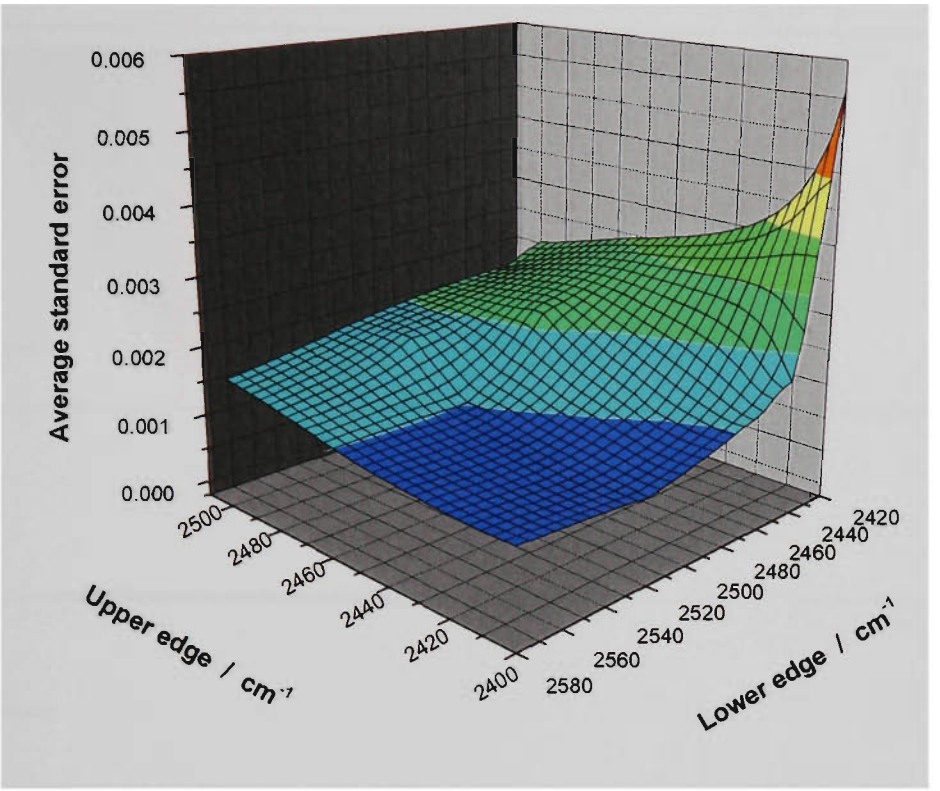

Figure 2.14 **Standard error surface for parent $^{14}N^{14}N^{16}O$ isotopomer as a function of upper and lower edge of the NLM3 fit window**

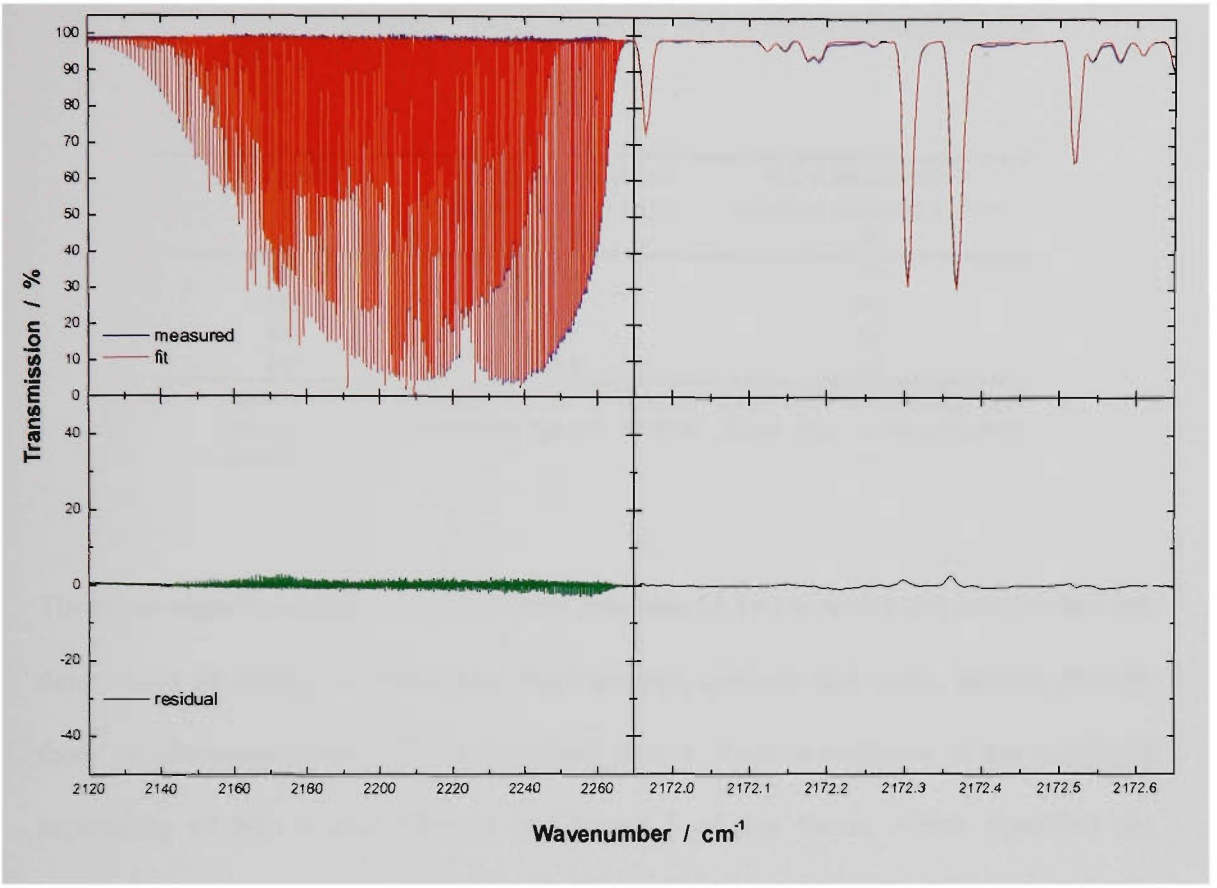

Figure 2.15 Non-linear least squares fit to the 2120 – 2270 cm^{-1} (left) and 2172.1–2172.6 cm^{-1} (right) regions of the N_2O spectrum
Spectrum is of N_2O at 0.5 torr, in a 2.4 m White cell at 0.012cm^{-1} resolution with 30 co added scans.

2.6.4 The advantages of non-linear least squares over classical least squares

The spectra series collected on 25 September 2000 (filename SE25033m, section 2.5.4) was re-analysed using the non-linear least squares technique. The standard deviation (± 1σ) of the isotopomer determination was compared between the NLLS analysis and the original CLS analysis. Results are shown in Table 2.3.

Table 2.3 Standard deviation of isotopomer determination for a series of spectra[a] determined by NLLS and CLS techniques

Isotopomer	NLLS determination standard deviation (± 1σ), ‰	CLS determination standard deviation (± 1σ), ‰
456	1.8	3.0
546	2.3	4.5
448	4.0	6.7
447	5.1	11

a. Spectra series collected on 25 September 2000 (file SE25033m) and consists of 25 consecutive spectra of BOC Gases N_2O as described in section 2.5.4.

There is a significant improvement in the precision (± 1σ) to which the isotopomers are determined by using the non-linear least squares analysis technique, arising directly from its advantages over CLS as described above. Further evidence of the analytical superiority of NLLS over CLS is in Chapter 5 of this thesis, which describes the determination of isotopic fractionation factors during the laboratory photolysis of N_2O. The N_2O spectra collected during this study were analysed by both classical least squares and non-linear least squares. Classical least squares data were previously published by *Turatti et al.* [2000]. A substantial increase in the precision to which the fractionation factors are determined is gained when the N_2O spectra are analysed with non-linear least squares.

NLLS analysis with the program NLM3 has substantial advantages over multi-window classical least squares analysis in the analysis of high resolution N_2O spectra. The main advantages are:

1. No assumption of linearity and ability to fit saturated lines and wide regions, thereby using more spectral data,
2. Much better fits to line shape imperfections than CLS analysis,

3. Speed and convenience – NLM3 is effectively a one step procedure as a calibration matrix is not required,
4. Use of a single spectral window removes dependence on the CLS micro-window "weights", which effectively add noise to the isotopomer determination (section 2.5.4), and
5. A significant increase in the precision of isotopomer determinations.

2.7 References

Anderson, R.J., and P.R. Griffiths, Errors in absorbance measurements in infrared Fourier transform spectrometry because of limited instrument resolution, *Analytical Chemistry*, *47*, 2339-2347, 1975.

Barrow, G.M., *Introduction to Molecular Spectroscopy*, 318 pp., McGraw-Hill, New York, 1962.

Griffith, D.W.T., Synthetic calibration and quantitative analysis of gas phase infrared spectra, *Applied Spectroscopy*, *50* (1), 59-70, 1996.

Griffiths, P.R., and J.A. de Haseth, *Fourier Transform Infrared Spectrometry*, 656 pp., John Wiley and Sons, New York, 1986.

Haaland, D.M., Methods to include Beer's Law non-linearities in quantitative spectral analysis, in *Computerised Quantitative Infrared Analysis, ASTM-STP-934*, edited by G.L. McClure, pp. 78-94, American Society for Testing and Materials, Philadelphia, 1987.

Haaland, D.M., Multivariate calibration methods applied to quantitative FTIR analyses, in *Practical Fourier Transform Infrared Spectroscopy*, edited by J.R. Ferraro, and K. Krishnan, Academic Press, San Diego, 1990.

Haaland, D.M., Multivariate calibration methods applied to the quantitative analysis of infrared spectra, in *Computer-enhanced analytical spectroscopy*, edited by P.C. Jurs, pp. 1-30, Plenum Press, New York, 1992.

Haaland, D.M., Synthetic multivariate models to accommodate unmodeled interfering spectral components during quantitative spectral analyses, *Applied Spectroscopy*, *54* (2), 246-254, 2000.

Haaland, D.M., W.B. Chambers, M.R. Keenan, and D.K. Melgaard, Multi-window classical least-squares multivariate calibration methods for quantitative ICP-AES analyses, *Applied Spectroscopy*, *54* (9), 1291-1302, 2000.

Haaland, D.M., and R.G. Easterling, Improved Sensitivity of Infrared Spectroscopy by the Application of Least Squares Methods, *Applied Spectroscopy*, *34*, 539-548, 1980.

Haaland, D.M., and R.G. Easterling, Application of new least squares methods for the quantitative infrared analysis of multicomponent samples, *Applied Spectroscopy*, *36* (6), 665-673, 1982.

Haaland, D.M., R.G. Easterling, and D.A. Vopika, Multivariate least squares methods applied to the quantitative spectral analysis of multicomponent samples, *Applied Spectroscopy*, *39*, 73-84, 1985.

Herzberg, G., *Molecular spectra and molecular structure II. Infrared and Raman spectra of polyatomic molecules*, 632 pp., D Van Nostrand Company, Princeton, 1962.

Lin, C.L., E. Niple, J.H. Shaw, and J.G. Calvert, The quantitative analysis of absorption spectra, *Applied Optics*, *33* (5), 481-487, 1980a.

Lin, C.L., E. Niple, J.H. Shaw, and J.G. Calvert, Retrieval of information from an absorption spectrum, *Applied Optics*, *3* (5), 487-491, 1980b.

Michelson, A.A., *Phil. Mag.*, *5* (31), 256, 1891.

Niple, E., Nonlinear least squares analysis of atmospheric absorption spectra, *Applied Optics*, *19* (20), 3481-3490, 1980.

Press, W.H., B.P. Flannery, S.A. Teukolsky, and W.T. Vetterling, *Numerical Recipies in C The Art of Scientific Computing*, Cambridge University Press, Cambridge, 1991.

Reisinger, A.R., Spectroscopic analysis of trace gas concentrations in the urban atmosphere, PhD thesis, University of Canterbury, Christchurch, New Zealand, 1998.

Rothman, L.S., C.P. Rinsland, A. Goldman, S.T. Massie, D.P. Edwards, J.M. Flaud, A. Perrin, C. Camy-Peyret, V. Dana, J.Y. Mandin, J. Schroeder, A. McCann, R.R. Gamache, R.B. Watson, K. Yoshino, K. Chance, K.W. Jucks, L.R. Brown, V. Nemtchinov, and P. Varanasi, The HITRAN molecular spectroscopic database and HAWKS (HITRAN Atmospheric Workstation): 1996 edition, *Journal of Quantitative Spectroscopy and Radiative Transfer*, *60*, 665-710, 1998.

Toth, R.A., Line-frequency measurements and analysis of N_2O between 900 and 4700 cm^{-1}, *Applied Optics*, *30* (36), 5289-5315, 1991.

Toth, R.A., Line strengths (900-3600 cm^{-1}), self-broadened linewidths, and frequency shifts (1800-2360 cm-1) of N_2O, *Applied Optics*, *32* (36), 7326-7365, 1993.

Toth, R.A., Line positions and strengths of N_2O between 3515 and 7800 cm^{-1}, *Journal of Molecular Spectroscopy*, *197* (2), 158-187, 1999.

Toth, R.A., N_2 and air-broadened linewidths and frequency-shifts of N_2O, *Journal of Quantitative Spectroscopy and Radiative Transfer*, *66*, 285-304, 2000.

Turatti, F., D.W.T. Griffith, S.R. Wilson, M.B. Esler, T. Rahn, H. Zhang, and G.A. Blake, Positionally dependent ^{15}N fractionation factors in the photolysis of N_2O determined by high resolution FTIR spectroscopy, *Geophysical Research Letters*, *27* (16), 2489-2492, 2000.

Chapter 3 Experimental II: Hardware, sample handling and measurement procedures

This chapter describes in detail the experimental hardware which was constructed for this work. Procedures for sample handling and measurement are detailed, as are procedures for the extraction of N_2O from sources. A description of the N_2O working standard is given.

3.1 The FTIR spectrometer and optical configuration

A Bomem DA8 spectrometer from Bomem Industries (Canada) was used for the high resolution N_2O isotopomer analysis. The DA8 has a maximum optical path difference of 250 cm, allowing a maximum apodised resolution of 0.004 cm^{-1}. The beam splitter was germanium on a KBr substrate, and a liquid nitrogen cooled InSb detector was used. A broad band optical filter with cut off limits of 1980 and 3310 cm^{-1} was used. The spectrometer was continuously purged with dried, CO_2 free air from a purge gas generator (Domnick Hunter model CO_2RP280).

Figure 3.1 shows the optical configuration of the analysis system. The N_2O samples were contained in a multiple reflection White cell [*White*, 1942] (Infrared Analysis model 2.4-PA) with a total optical path of 2.4 m, consisting of 24 passes of a base 0.1 m optical path, and a volume of 0.120 L. This cell had the highest pathlength to volume ratio of any on the market at the time of 20 m L^{-1}, which maximises sensitivity for a given amount of sample. A simple four mirror transfer optics system was constructed to direct the infrared beam into the cell and onto the InSb detector. The White cell was

mounted internally in the DA8 sample compartment, attached to the inside of the left sample compartment side-plate as is shown in Figure 3.1.

3.2 Sample handling and temperature control

Figure 3.2 shows an engineering drawing by Geoff Hurt (University of Wollongong Faculty of Science Workshop) of the spectrometer attachment which was built for this work. This attachment allows the White cell and a small sample handling manifold to be kept at a constant known temperature. The White cell (shaded blue in Figure 3.2) was attached to a 12 mm thick aluminium plate with a custom made o-ring compression seal, sealing onto the outside of the glass cell. The spectrometer attachment was mounted to the left sample compartment of the spectrometer, as shown in Figure 3.4. The infrared radiation entry and exit side of the cell was sealed with a 4mm thick CaF_2 window with an 0.5 degree wedge, sealed to the glass White cell with Apiezon "Black Wax". The leak rate of this system was less than 1.8×10^{-3} torr $hour^{-1}$. Procedures for attaching and removing the CaF_2 window to the White cell and procedures for dismantling and cleaning the White cell are given in full detail in the Appendix.

Accurate temperature control of the White cell and manifold is essential to minimise drifts in isotopic determination due to temperature variations. The White cell is mounted inside a thin copper cylinder, a few millimetres larger in diameter than the White cell, highlighted in red in Figure 3.2. A ¼" copper tube is tightly coiled and soldered around this can. A Julabo model F25 water circulator, capable of maintaining temperature to ± 0.01 °C circulates water at 25 °C around this coil. The coil outlet is connected to a channel milled in the aluminium plate protruding underneath the sample handling manifold. The channel is cut in a close "square wave" pattern, maximising the

surface area of the plate in contact with the temperature controlled water. The water returns to the circulator after exiting the plate. The copper coil and channel are shown in Figure 3.2 highlighted in pink. The sample handling manifold is attached above the plate and enclosed in a Perspex box. Convection from the plate, and air circulation by way of a small fan, maintain the vacuum manifold temperature at 25 °C.

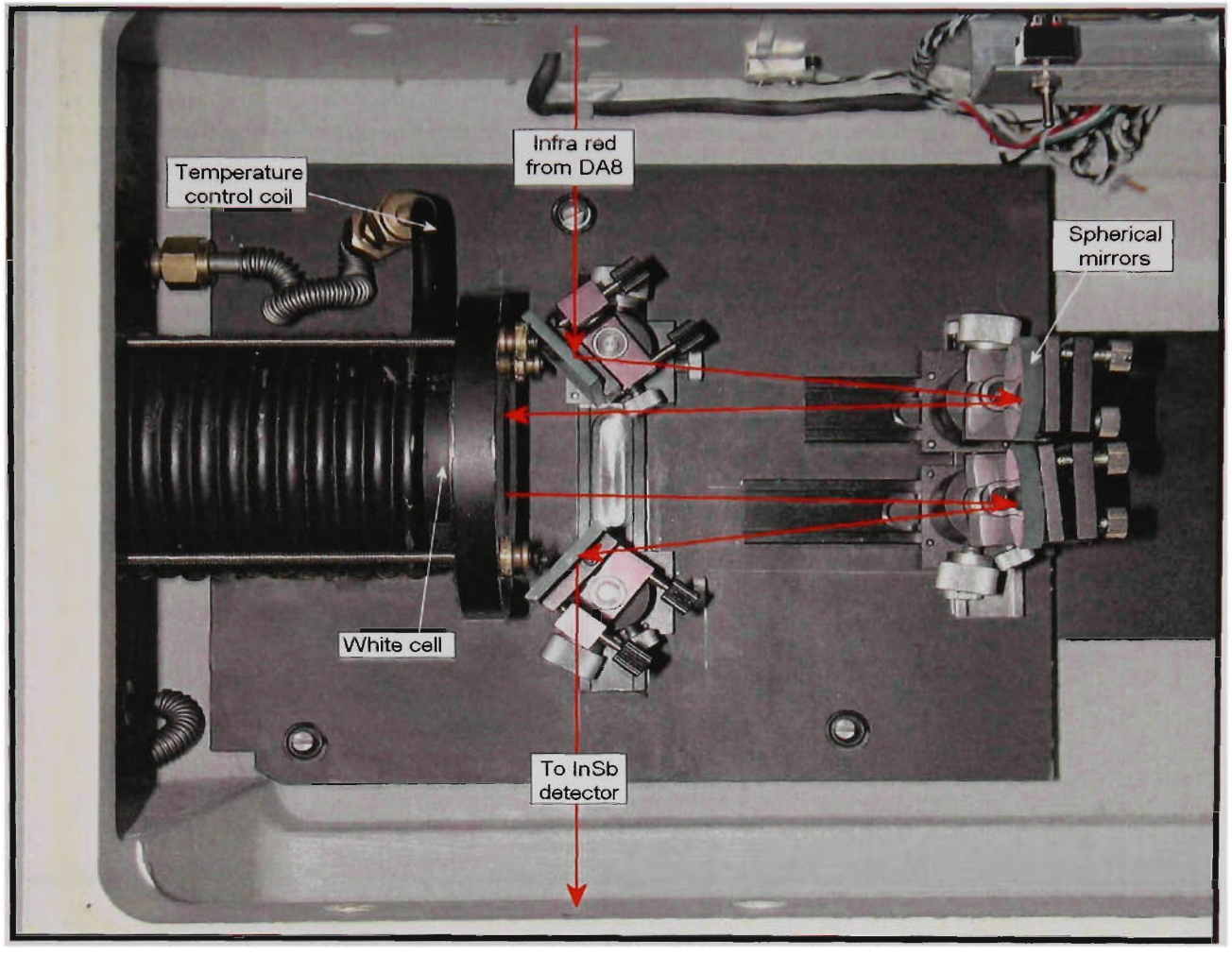

Figure 3.1 The infrared optical configuration

Figure 3.2 **Engineering drawing of the temperature control system and White cell**
Drawing by Geoffrey Hurt, Faculty of Science Workshop.

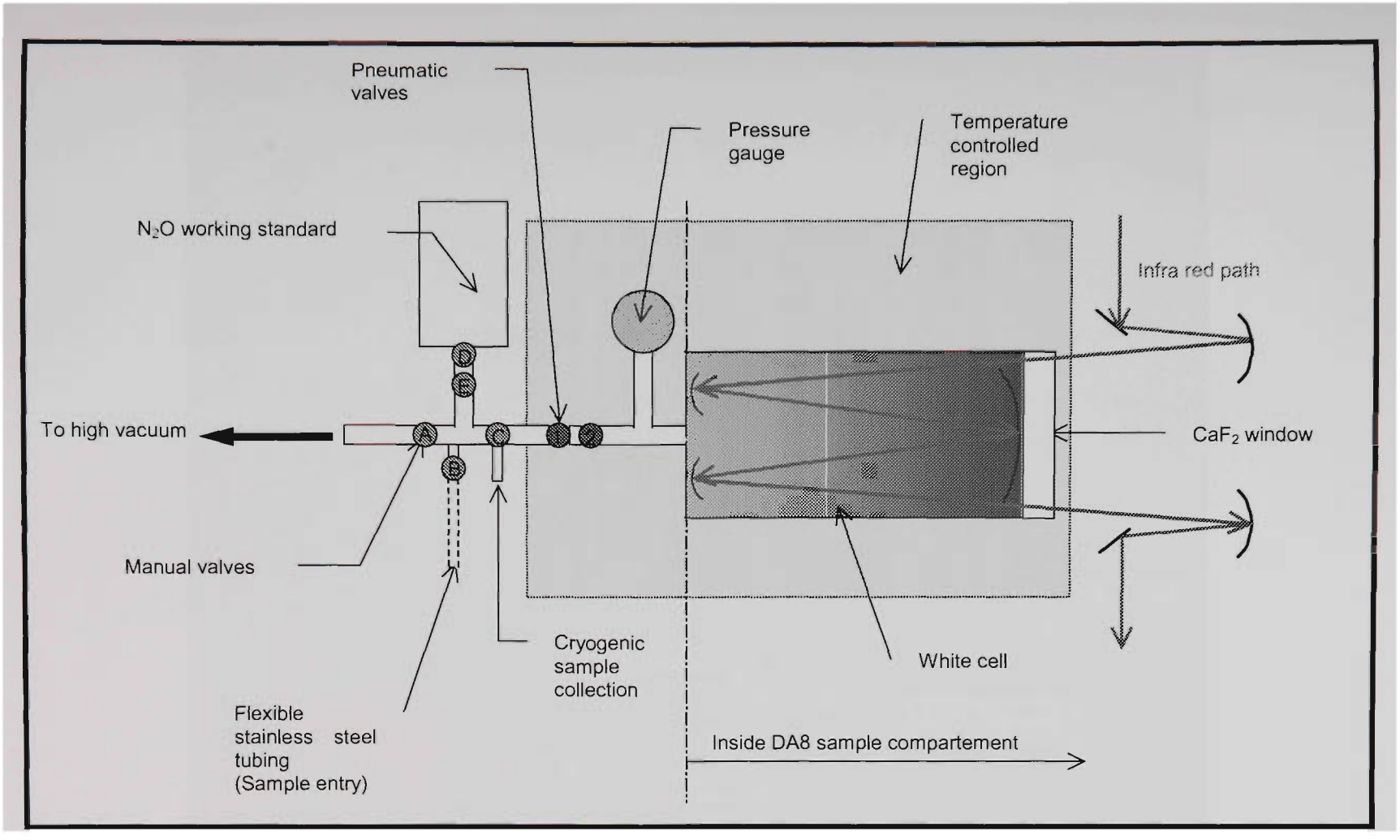

Figure 3.3 Schematic diagram of the sample handling manifold and White cell

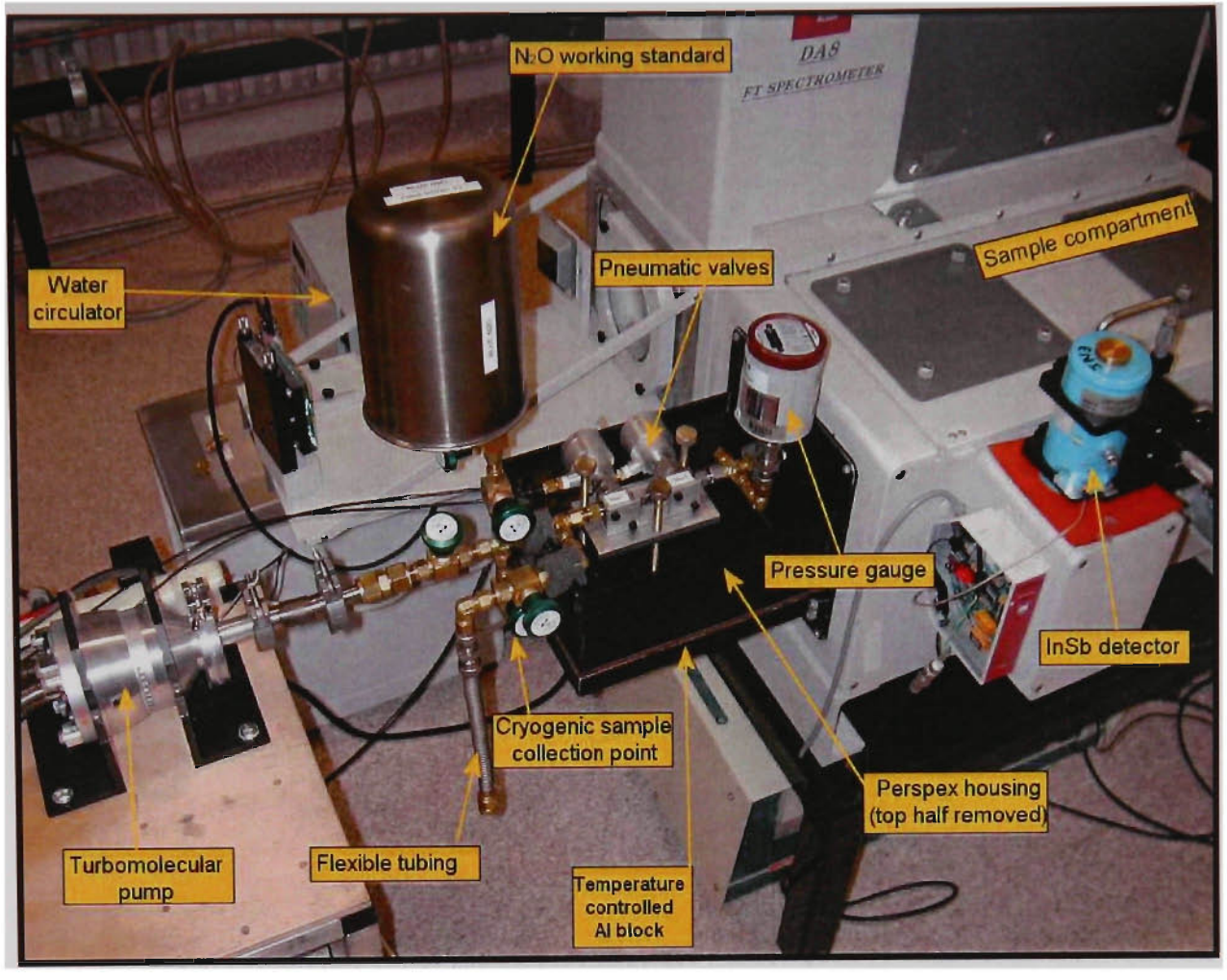

Figure 3.4 The sample handling manifold attached to the DA8 spectrometer

Figure 3.3 shows a schematic diagram of the sample handling manifold and Figure 3.4 shows a photograph of it as attached to the DA8 spectrometer. The manifold was constructed from ¼" Swagelock fittings and tubing and was connected to the White cell. An MKS Baratron (model 726A) was used as the pressure gauge, with a range of 0-100 torr. Two compressed-air actuated valves are used in tandem to lower the sample pressure in the White cell by sequentially withdrawing small (≈ 1 mL) aliquots of the gas being measured. This procedure minimises the risk of isotopically fractionating the N_2O sample by avoiding slow "bleeding" of the excess through the narrow orifice of a manually operated needle valve. The excess sample is either pumped away or collected cryogenically at the sample collection point. Vacuum is generated by an Alcatel ATH30 turbo molecular pump and a Neuberger N813.4ANE four stage diaphragm pump, with the ultimate vacuum achievable in the manifold at 4×10^{-2} torr. The N_2O working gas standard is contained in a stainless steel cylinder of approximately 2 L volume. The flexible stainless steel bellows is used to "crack", under vacuum, gas samples contained in flame-sealed 6 mm glass tubes. The design of the sample handling manifold is such that a sample can be introduced and trapped cryogenically at greater than 99.9 % efficiency. The collection efficiency was measured manometrically by cryogenically collecting and re-expanding an accurately known amount of N_2O. The total volume of the White cell, manifold and flexible stainless steel tubing is 143.5 ± 1 mL.

3.3 Sample measurement procedures

3.3.1 Sample introduction and measurement

This section describes the extraction of an N_2O sample from a flame sealed 6 mm diameter glass tube. The glass tube is scored across the middle with a small file and placed in the flexible stainless steel bellows discussed above (at valve B, Figure 3.3). A glass tube to cryogenically collect the sample after measurement is attached to the manifold at valve C, Figure 3.3. The manifold and White cell are evacuated. Precautions are taken which prevent the White cell coming into contact with ambient air thus contaminating the inside surface of the White cell with water vapour which is difficult to evacuate. Precautions are also taken which prevent exposing the turbo molecular pump to gas pressures which are above its specification limits. The system is evacuated for at least 5 minutes.

Valves A and C are closed and the flexible stainless bellows is bent manually until the glass tube is heard to crack, releasing the N_2O sample to the manifold and White cell. The sample pressure is allowed to stabilise and measured. In most situations there is more sample than required for an analysis. Small sample aliquots ($\approx$ 1 mL) are removed from the White cell by sequentially fully opening pneumatic valves 1 and 2. The excess sample is either evacuated or more usually, cryogenically collected at valve C (Figure 3.3). This procedure is repeated until the optimum sample measurement pressure is reached. Using this method, it is possible to adjust the sample pressure to 1.000 ± 0.002 torr. The sample is allowed to come to thermal equilibrium with the circulating water and the pressure is measured again. Sample spectra are collected over 30 co-added scans (approximately 31 minutes), at an apodised resolution of 0.012 cm^{-1}. The

acquisition range was between 1980-3310 cm^{-1}, with Hamming apodisation. Detector preamp gain of 1 was used, with a base gain of 1 and positional gain 16 after 2048 fringes. Determination of the optimum spectroscopic conditions are described in detail in Chapter 4. The sample is usually collected cryogenically at valve C after the spectrum has been collected. All valves are opened and the manifold and White cell system is evacuated.

3.3.2 Measuring N_2O working standard and evacuated cell reference spectra

Slow drifts in the DA8 spectrometer occurring on the 30 to 60 minute timescale required that sample measurements were interleaved with measurements of a working standard. The final sample isotopomer δ was calculated by taking the average of the before and after δ of the working standard from the initial sample determination. A typical drift in the DA8 spectrometer was between 3 and 6 ‰ per hour, based on consecutive measurements of N_2O working standard. This drift is believed to be due to changes in the spectrometer optics, particularly in the sampling of the movable mirror position. Interleaving sample measurements with working standard measurements minimises the effect of this drift on the sample measurement.

Two N_2O working standards were used in this work. The first was N_2O sourced from Scott-Marrin Gases (California, USA), generated as a by-product in the industrial production of adipic acid. The second was industrial grade N_2O sourced locally from BOC Gases. Full details of the how these standards were selected and their isotopic characterisation is described in section 3.4. Drift in the isotopic results of a sample was removed by subtracting the mean isotopic signature of the N_2O working standard

measured immediately before and after each sample from the initial sample isotopic signature. A full description of the N_2O working gas standard is given in section 3.4.

The N_2O working standard was expanded to fill the volume between valves D and E in Figure 3.3 (≈ 2 cm^3), thereby removing a small aliquot of N_2O working standard from the reservoir container. This aliquot was expanded into the manifold and White cell and the pressure measured. Valves 1 and 2 (Figure 3.3) were sequentially opened to lower the working standard pressure to 1.000 ± 0.002 torr and the gas was allowed to come to thermal equilibrium over several minutes. The sample pressure was remeasured and the spectrum collected. The N_2O working standard spectra is collected under identical spectroscopic conditions as sample spectra.

An evacuated cell reference spectrum is collected under identical spectral conditions as the N_2O samples and working standard measurements, except for longer acquisition times. Forty five scans, but occasionally as many as 60 scans were usually co added. These evacuated cell reference spectra were used to obtain transmission or absorbance spectra from the sample and working standard single beam measurements. (A single beam spectrum is the infrared intensity as a function of wavenumber as seen at the detector, and it is described by equation 2.6). Two evacuated cell sample spectra were collected in a typical week of measurements. There were no significant differences between evacuated cell sample spectra collected four or five days apart.

3.4 Selection of an N_2O working standard

There is no internationally accepted standard for isotopic measurements of N_2O. The first chapter of this dissertation describes the reference standards V-PDB and V-SMOW

which are accepted internationally for $\delta^{13}C$ and $\delta^{18}O$ measurements for CO_2, CH_4 and H_2O. Previous $\delta^{15}N$ measurements of N_2O have been made relative to atmospheric N_2, and $\delta^{18}O$ of N_2O has been measured relative to both V-SMOW and atmospheric O_2 usually via an intermediate N_2O working standard such as SNOW, (Standard Nitrous Oxide Working gas) used by *Rahn et al.* [1998]. There is no generally accepted standard for measuring the symmetry isotopes of N_2O, $\delta^{14}N^{15}N^{16}O$ and $\delta^{15}N^{14}N^{16}O$ as this area is so new. Toyoda and Yoshida [1999] have made an N_2O standard with accurately known $^{14}N^{15}N^{16}O/^{14}N^{14}N^{16}O$ and $^{15}N^{14}N^{16}O/^{14}N^{14}N^{16}O$ ratio by thermal decomposition of ammonium nitrate, NH_4NO_3. Ammonium nitrate quantitatively decomposes according to the reaction

$$\mathbf{N}H_4NO_3 \xrightarrow[\text{trace } H_2O]{200\ ^\circ C,} \mathbf{N}NO + 2\,H_2O \qquad (3.1)$$

where the terminal nitrogen of N_2O comes exclusively from the ammonium nitrogen, and the central nitrogen exclusively from the nitrate nitrogen [*Friedman and Bigeleisen*, 1950; *Toyoda and Yoshida*, 1999]. *Toyoda and Yoshida* [1999] accurately measured the $^{15}N/^{14}N$ ratio of the individual ammonium and nitrate nitrogens by standard isotope ratio mass spectrometry techniques, and therefore knew the actual $^{15}N/^{14}N$ ratio of the individual N_2O nitrogen atoms. This served as their absolute standard. Preparing an isotopic absolute standard of N_2O was considered beyond the capabilities and equipment available at the University of Wollongong for this study.

Two different internal working standards were used in this work for N_2O isotopic measurements. The first was 99.9 % pure N_2O purchased from Scott-Marrin Gases California, USA and referred to in this work as Scott-Marrin Gases N_2O. This N_2O was reclaimed as a by-product during the industrial manufacture of adipic acid (hexanedioic

acid, $C_6H_{10}O_4$), a feedstock in production of 6,6 nylon. The second was industrial grade N_2O supplied by BOC Gases Australia, manufactured by the industrial scale thermal decomposition of ammonium nitrate as described in equation 3.1, and referred to in this work as BOC Gases N_2O.

Samples of N_2O working standards were exchanged between the Max Planck Institute of Atmospheric Chemistry (Jan Kaiser) and the University of Wollongong and measured with the FTIR technique described in this thesis and the IRMS technique. Samples of the N_2O working standard used by *Rahn et al.* [1998], SNOW, were also included in the intercomparison. Results of this intercomparison as determined from FTIR analysis are given in Table 3.1.

Table 3.1 Relative isotopic signatures of various N_2O working standards determined by the FTIR method

	δ^{456} measured relative to [a]				δ^{546} measured relative to			
	S.M N_2O	BOC N_2O	SNOW	MPI	S.M N_2O	BOC N_2O	SNOW	MPI
Sample								
S.M N_2O [b]	0.0	15.2	13.7	12.2	0.0	-14.6	-19.8	-14.0
BOC N_2O [c]	-15.2	0.0	-1.5	-3.0	14.6	0.0	-5.2	0.6
SNOW [d]	-13.7	1.5	0.0	-1.5	19.8	5.2	0.0	5.8
MPI [e]	-12.2	3.0	1.5	0.0	14.0	-0.6	-5.8	0.0

	$\delta^{15}N$ measured relative to					δ^{456}-δ^{546} measured relative to			
	S.M N_2O	BOC N_2O	SNOW	MPI	Atm N_2 [f]	S.M N_2O	BOC N_2O	SNOW	MPI
Sample									
S.M N_2O	0.0	0.3	-3.1	-0.9	-0.7	0.0	29.8	33.5	26.2
BOC N_2O	-0.3	0.0	-3.4	-1.2	-1.8	-29.8	0.0	3.7	-3.6
SNOW	3.1	3.4	0.0	2.2	1.3	-33.5	-3.7	0.0	-7.3
MPI	0.9	1.2	-2.2	0.0	1.1	-26.2	3.6	7.3	0.0

a. The isotopic signature δ of the sample gases when measured relative to these gases according to the standard δ equation.
b. Scott-Marrin Gases N_2O
c. BOC Gases N_2O
d. Standard Nitrous Oxide Working gas, [*Rahn et al.*, 1998]
e. Working gas used by Kaiser *et al.* at the Max Planck Institute
f. Measured by the Max Planck Institute using IRMS, relative to the isotopic signature of clean background atmospheric N_2

The numbers in the shaded column have been determined by the Max Planck Institute for Atmospheric Chemistry by IRMS. Table 3.1 shows that all four N_2O working standards have approximately the same $\delta^{15}N$ signature, within a few per mille of zero relative to atmospheric N_2. However, the Scott-Marrin Gases N_2O has a difference of approximately 30 ‰ in the position of the ^{15}N, δ^{456}-δ^{546} when measured relative to the other working gas standard. This large difference is attributed to the difference in manufacturing process, as all N_2O gases except the Scott-Marrin N_2O were derived from the thermal decomposition of ammonium nitrate. This is an extremely interesting result. BOC Gases N_2O was chosen as the default working standard for this work as it

is most similar to the N_2O working standards used by other groups. Figure 3.5 shows the difference between measurements by the FTIR (this work) and the IRMS technique (Jan Kaiser, MPI) of several working N_2O standards, measured relative to BOC Gases N_2O.

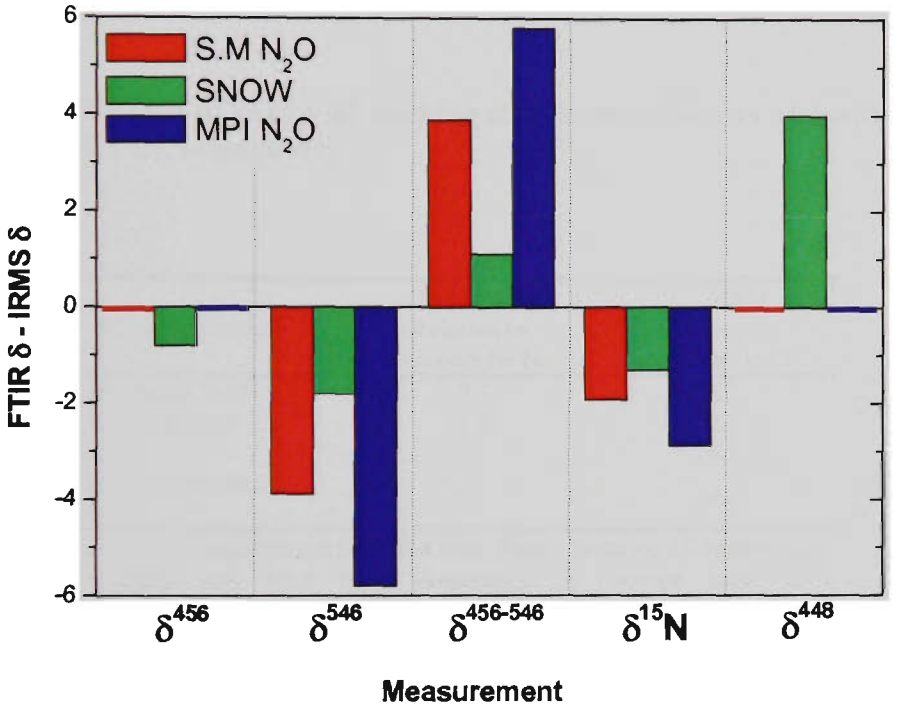

Figure 3.5 Difference between FTIR and IRMS measurement of three N_2O working standards relative to BOC Gases N_2O.
S.M N_2O is Scott Marrin Gases N_2O, SNOW is Standard Nitrous Oxide Working gas, MPI N_2O is the working N_2O standard used by the Max Planck Institute. Measurements are made relative to BOC Gases N_2O.

For most determinations of the working gas standards, the FTIR and IRMS technique agree within 4 ‰, but there is approximately 6 ‰ difference in the measurement of δ^{546} between the two techniques. This is unresolved at the present time.

The Max Planck Institute of Atmospheric Chemistry measured the four N_2O working standards (Scott-Marrin, BOC, SNOW and MPI) relative to atmospheric N_2 and O_2

using isotope ratio mass spectrometry (IRMS) and the results are described in Table 3.2. The Max Planck Institute determination of the BOC Gases N_2O in Table 3.2 was used when quoting $\delta^{15}N$ and $\delta^{18}O$ sample measurements in this work relative to atmospheric N_2 and O_2, respectively. For example, if the $\delta^{15}N$ of an N_2O sample measured relative to BOC Gases N_2O is 10.0 ‰, then the $\delta^{15}N$ of that sample relative to atmospheric N_2 is 8.2 ‰.

Table 3.2 $\delta^{15}N$ and $\delta^{18}O$ of N_2O working standards relative to atmospheric N_2 and O_2, respectively *

Please see print copy for image

* These measurements are from the Max Planck Institute of Atmospheric Chemistry and have been determined by isotope ratio mass spectrometry (IRMS).

3.5 Extracting N_2O from sources

As shown in Chapter 4, a minimum of approximately 0.7 torr of pure N_2O in the 2.4 m White cell is required to measure $\delta^{14}N^{15}N^{16}O$ with the highest precision possible with this FTIR technique. Given the volume of the manifold and White cell system, the optimum amount of N_2O required for isotopic analysis is 5 μmoles. The background concentration of N_2O in clean tropospheric air is currently 314.5 nmol mol^{-1} [*Albritton et al.*, 2001]. Therefore, the N_2O from approximately 400 L of clean air needs to be

quantitatively extracted and separated from the other atmospheric components in order to have enough N_2O to measure by FTIR spectroscopy.

3.5.1 N_2O extraction

An extraction line was constructed to trap and collect N_2O emitted from sources. A constant flow of air, between 2 and 2.5 L min^{-1} was drawn through a Nafion® tube and $MgClO_4$ trap, lowering the dew point of the sample stream to approximately -55°C. The gas stream then passed through an Ascarite® (98 % NaOH on a silica support) trap to remove CO_2, and passed through a second $MgClO_4$ trap to remove the remaining H_2O. A liquid nitrogen cooled stainless steel Russian doll trap [*Brenninkmeijer and Röckmann*, 1996] cryogenically collected the N_2O and any residual CO_2. The pressure in the line was maintained below 150 torr to avoid condensation of liquid oxygen. The remaining non-condensable gases were drawn through a vacuum line and out via a diaphragm pump. The total volume of gas drawn through the extraction line was measured by a standard integrating gas meter (Toyo ML-2500) connected to the outlet of the diaphragm pump.

Once the required volume of air was sampled, the inlet of the Russian doll trap was closed and non condensable gases were pumped out via a rotary oil pump and diffusion pump. The Russian doll trap was sealed and warmed to ambient temperature to volatilise the N_2O and any collected residual CO_2. The contents of the Russian doll trap were cryogenically trapped over into an evacuated glass coil under liquid N_2. Non-condensable gases freed from the original sample were evacuated with the oil pump and diffusion pump. The glass coil was warmed to ambient temperature and the extracted N_2O was cryogenically collected in a 6 mm diameter glass tube and flame sealed. Tests

with air of known N_2O mixing ratio show that the collection efficiency of this system was 100 ± 2%. This extraction line was used in the laboratory for the extraction of N_2O from background air (Chapter 6) and in the field for the extraction of N_2O emitted from a pig-effluent fertilised crop field (Chapter 7).

3.6 References

Albritton, D.L., L.G. Meira Filho, U. Cubasch, X. Dai, Y. Ding, D.J. Griggs, B. Hewitson, J.T. Houghton, I. Isaksen, T. Karl, M. McFarland, V.P. Meleshko, J.F.B. Mitchell, M. Noguer, B.S. Nyenzi, M. Oppenheimer, J.E. Penner, S. Pollonais, T. Stocker, and K.E. Trenberth, Technical Summary of the Working Group 1 Report, pp. 21-83, Intergovernmental Panel on Climate Change Third Assessment Report, 2001.

Brenninkmeijer, C., and T. Röckmann, Russian doll type cryogenic traps: improved design and isotope separation effects, *Analytical Chemistry*, *68*, 3050-3053, 1996.

Friedman, L., and J. Bigeleisen, Oxygen and isotope effects in the decomposition of ammonium nitrate, *Journal of Chemical Physics*, *18* (10), 1325-1331, 1950.

Rahn, T., H. Zhang, M. Wahlen, and G.A. Blake, Stable Isotope fractionation during ultraviolet photolysis of N2O, *Geophysical Research Letters*, *25* (24), 4489-4492, 1998.

Toyoda, S., and N. Yoshida, Determination of Nitrogen Isotopomers of Nitrous Oxide on a Modified Isotope Ratio Mass Spectrometer, *Analytical Chemistry*, *71* (20), 4711-4718, 1999.

White, J.U., Long optical paths of large aperture, *Journal of the Optical Society of America*, *32*, 285-288, 1942.

Chapter 4 Experimental III: Optimal spectroscopic conditions, technique precision and limitations

A theoretical model was developed which allowed estimation of the optimal N_2O amount, instrumental resolution and signal to noise ratio for the highest precision isotopomer determination. This theoretical set of optimal sample and spectroscopic conditions was experimentally validated and modified to meet practical experimental limitations. The theoretical isotopomer precision at these experimental conditions was determined and compared to the achieved isotopomer precision, and causes of variation were investigated. The sensitivity of the isotopomer determination to temperature and pressure variations in the N_2O sample was determined. The impact of spectral lineshape variability on isotopomer precision was investigated. The high resolution Fourier transform infrared technique developed in this work is summarised.

4.1 Estimating the optimal N_2O amount and spectroscopic conditions

MALT was used to develop a theoretical model which allowed estimation of the optimal N_2O amount, instrumental resolution and signal to noise ratio for the highest precision isotopomer determination with high resolution FTIR spectroscopy. There are several practical limitations in measuring high resolution FTIR spectra of N_2O. The amount of N_2O available to be measured is limited to approximately 1 torr to maintain a reasonable sample size. The spectrum acquisition time is limited to approximately 30 minutes as collecting for longer than this time has been found to result in poor results in practice, most likely due to subtle variations in the spectrometer optical components with time. This limits the N_2O amount and spectrum acquisition time within practical

limits. In the absence of spectrometer "drift", the spectral noise should decrease in proportion to the square root of the number of co-added spectra.

A number of synthetic sets of spectra were generated with MALT with each set containing 20 individual identical spectra varying only in random noise. MALT generates calculated, normally-distributed random noise within a peak-to-peak or rms-SNR (root mean square signal to noise ratio) range. The spectrum sets were calculated with variable N_2O amount, variable resolution, variable signal to noise ratio at a constant total pressure buffered by N_2 gas, as described in Table 4.1. Buffering the N_2O sample to a relatively high total pressure with N_2 gas was initially used to ensure that the N_2O line width was dominated by pressure broadening, minimising the influence of the spectrometer line shape function on the measured N_2O lines in real spectra. Each spectrum set was determined with classical least squares using the micro-window method described in Chapter 2. The isotopomer precision was determined as the standard deviation ($\pm$ 1σ) of the isotopomer concentration among the 20 spectra in each set. As the individual spectra in each spectrum set are identical except for random noise, the standard deviation ($\pm$ 1σ) of the isotopomer determination indicates the theoretical precision achievable under those specific spectrum measurement conditions. This defined a three dimensional "precision surface" with precision as the dependent z-variable and spectrum resolution and N_2O amount as independent variables x and y variables, within the practical limits discussed above.

Figure 4.1 shows the theoretical δ^{456} precision as a function of spectral resolution and N_2O amount, within the constraints discussed above, for a constant 30 minute acquisition time. Some N_2O samples were expected to contain less than 1.0 torr.

Therefore Figure 4.2 is a cross section of the precision surface for δ^{456} and δ^{448} for a constant N_2O amount of 0.8 torr, showing the theoretical precision achievable for δ^{456} and δ^{448}. Analysis of Figure 4.1 and Figure 4.2 show that the theoretical δ^{456} precision for an acquisition time of 30 minutes is best when the N_2O amount is approximately between 0.9 and 1.0 torr, and the resolution is higher than approximately 0.02 cm^{-1}. Under these same conditions the theoretical precision for δ^{448} is best when the resolution is higher than approximately 0.016 cm^{-1}.

Table 4.1 Conditions used for estimating the isotopomer precision surface

Variable	Range	Steps [a]	Cumulative spectrum sets [b]
N_2O amount	0.4 – 1.2 torr	5	5
Resolution	0.012 – 0.035 cm^{-1}	7	35
SNR ratio [c]	250 - 2000	4	140
Fixed			
Field of view	1.54×10^{-3} rad (1 mm aperture)		
Optical path length	2.4 m		
Total pressure [d]	30 torr (N_2 buffer)		
Temperature	25°C		
Apodisation	Boxcar[c]		

a. The number of discrete values taken by a particular variable.
b. Each N_2O amount was calculated at each resolution and then at each spectrum SNR.
c. Signal to noise ratio was for a constant 30 minute acquisition time.
d. The spectra were calculated with a fixed total pressure, comprising of a variable N_2O amount augmented to 30 torr with N_2 buffer gas.
e. Boxcar apodisation was used for the model, but Hamming apodisation was used in real measurements to reduce the intensity of secondary lobes from spectral lines

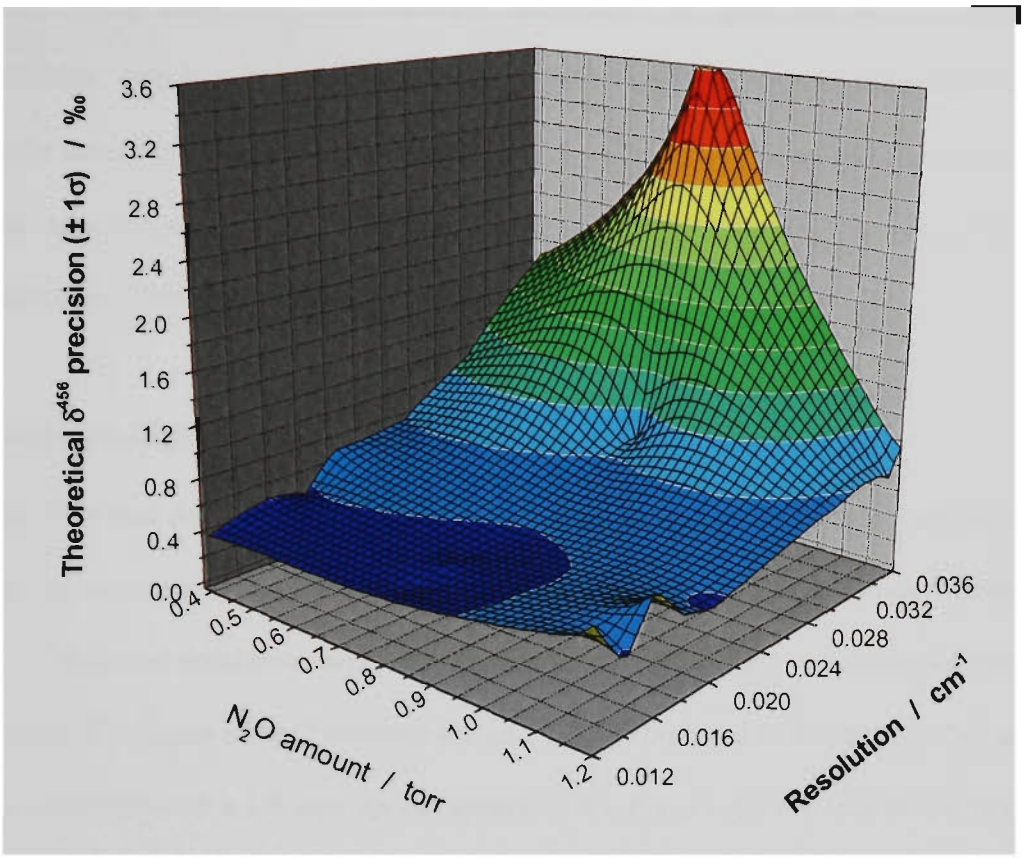

Figure 4.1 **Precision surface for δ^{456} with variable N_2O amount and spectral resolution for a constant 30 minute acquisition time and variable signal to noise ratio.**

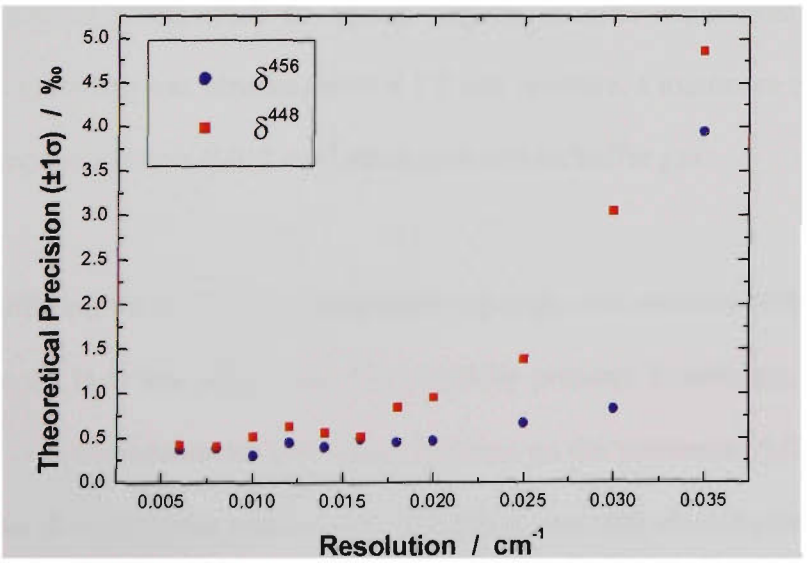

Figure 4.2 **Cross section of precision surface (Figure 4.1) for 0.8 torr N_2O.**

Signal to noise ratio will fundamentally determine the precision of isotopomer determination, which will clearly improve as SNR increases. Acquisition time will ultimately determine the achievable SNR. With the current spectroscopic conditions, a SNR of approximately 1000 at resolution approximately 0.01 cm^{-1} is achieved in approximately 30 minutes acquisition time.

4.2 Validation of the theoretical ideal conditions

Between July and August 1999 a series of experiments was performed to confirm the optimal spectrometer conditions as determined from the modelling study outlined above. The initial conditions were those predicted by the model: resolution of 0.012 cm^{-1}, a partial pressure of N_2O between 0.8 and 1.2 torr buffered to 30 torr with N_2, and spectra measured with a 1.0 mm optical aperture. Each experiment consisted of filling the White cell once with N_2O sample and collecting around 20 consecutive spectra. The spectra were analysed with CLS and the isotopomer standard error of the prediction (SEP) from spectrum to spectrum was calculated, corrected for instrumental drift. The amount of N_2O, the spectral resolution, the total sample pressure and the acquisition time (and therefore SNR) were all varied slightly in each experiment. The best determination precision was obtained with a 1.5 mm aperture, a minimum of 1.0 torr of N_2O, Hamming apodisation, 0.012 cm^{-1} resolution and no buffer gas.

The aim of buffering the N_2O sample to a relatively high total pressure with N_2 gas was to ensure that the N_2O line width was dominated by pressure broadening, minimising the influence of the spectrometer line shape function on the measured N_2O lines. The best isotopomer determination precision was therefore expected when N_2 buffer gas was used. However, the best retrieval precision was obtained with no N_2 buffer gas.

Buffering a sample of N_2O with N_2 leads to a gas mixture whose pressure broadening characteristics are difficult to accurately model with CLS or NLLS, as the pressure broadening coefficient of the N_2O/N_2 mixture is not accurately known. Effectively, there is "mixing" between the line broadening of N_2O and N_2. The uncertainty in the determination of the N_2O/N_2 line broadening effectively adds noise to the isotopomer determination, hence the better precision obtained with no N_2 buffer gas. One incidental advantage of not using a buffer gas is that quantitative cryogenic collection of the N_2O sample after measurement is greatly simplified, due to the much faster N_2O diffusion into the cryogenic trap. This also simplified construction of the sample handling manifold. Alternative buffer gases were not investigated as the limitations discussed above which apply to N_2 will equally limit the effectiveness of other buffer gases.

4.3 The theoretical precision limits

Having selected the optimal resolution and amount of N_2O, MALT was used to estimate the theoretical isotopomer determination precision in a perfectly behaved spectrometer for the standard experimental conditions. Twelve sets of 20 N_2O spectra were calculated with the standard high resolution N_2O spectrum acquisition conditions of 1 torr N_2O, 0.012 cm^{-1} apodised resolution and 1.5 mm aperture – the experimentally determined optimal conditions. The 12 spectra sets were calculated with a rms-SNR which varied between 100 and 10000 and these spectra sets were analysed by both non-linear least squares (NLLS) and linear classical least squares (CLS) methods described in Chapter 2. As the spectra in each set of twenty are identical except for noise, the standard deviation ($\pm$ 1σ) of the isotopomer determination is an indication of the theoretical precision achievable at a given spectrum signal to noise ratio. Figure 4.3

shows the theoretical N_2O isotopomer determination precision as determined by non-linear least squares and classical least squares.

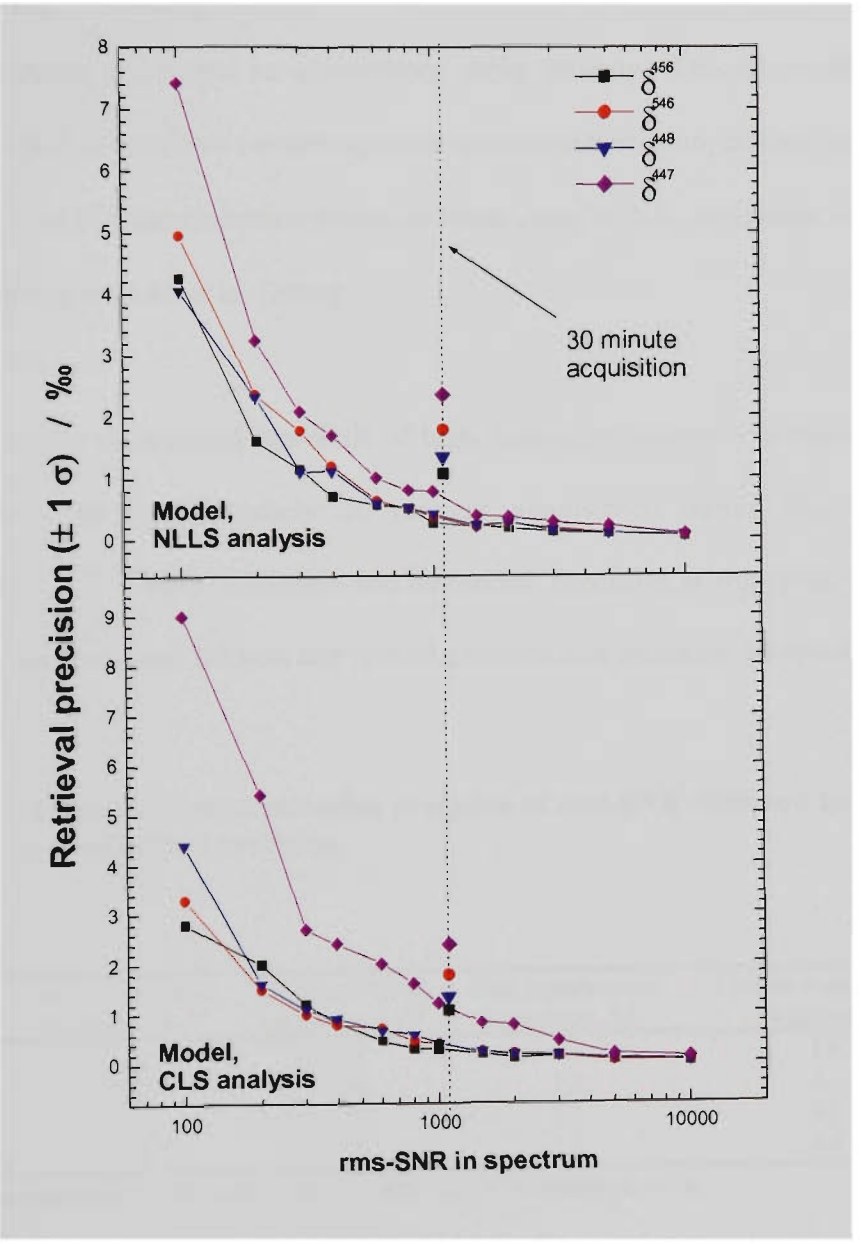

Figure 4.3 **Theoretical determination precision for N_2O isotopomers by non-linear and classical least squares techniques.**
The dotted line represents the typical rms-SNR for a real N_2O spectrum (≈ 1000:1). The symbols on the dotted line represent the best precision achieved during this work.

The theoretical determination precision of δ^{456}, δ^{546}, δ^{448} are close to identical for both NLLS and CLS analysis. There is a significant difference in the theoretical determination precision of δ^{447} between the two analysis techniques, with NLLS giving

consistently better determination precision. As described earlier in this thesis, CLS analysis relies on a number of micro windows typically less than 1 cm^{-1} wide which exclude strongly absorbing (and non-linear) $^{14}N^{14}N^{16}O$ lines, whereas NLLS fits transmission spectra and makes no assumptions about linearity. This allows the fitting of very large spectral windows containing more spectral information, and this is a likely cause of the better δ^{447} determination precision when using NLLS. An earlier version of Figure 4.3 appears in *Esler et al.* [2000].

The experimentally determined rms-SNR of high resolution spectra collected at 0.012 cm^{-1} and 30 scans (approximately 30 minutes acquisition) during this work is approximately 1100. Table 4.2 shows the theoretical precision at rms-SNR 1000 for both analysis methods, and the best and typical experimental precision for spectra.

Table 4.2 Theoretical determination precision at rms-SNR 1000 and best experimental precision.

Isotopomer	NLLS theoretical precision, ‰ [(a)]	CLS theoretical precision, ‰ [(a)]	Best experimental precision, ‰	Typical experimental precision, ‰
δ^{456}	0.26	0.27	1.1	1.8
δ^{546}	0.37	0.39	1.8	2.1
δ^{448}	0.41	0.39	1.3	3.3
δ^{447}	0.78	1.2	2.3	4.4

(a) At root mean square signal to noise ratio 1000:1. Precision is ± 1σ.

The experimental precision is determined by collecting typically 20 consecutive spectra of the same 1.0 torr N_2O sample with 0.012 cm^{-1} resolution and 30 co-added scans. The standard deviation of the 20 isotopic determinations, corrected for instrumental drift, is a measure of the true experimental precision achievable. These consecutive N_2O spectrum runs were usually performed at least once a week during periods of FTIR

measurement. Figure 4.3 and Table 4.2 together show that the best precision performance was between a factor of 3 and 5 worse than expected theoretical (SNR-limited) precision. For a typical experiment, the precision is between a factor of 5 and 8 worse than the theoretical limit. Increasing the scan time beyond 30 minutes does not necessarily significantly improve the signal to noise ratio of the spectra. The SNR for both 45 scans (45 minutes acquisition) and 60 scans (60 minutes acquisition) was approximately 1200. High frequency detector noise decreases proportional to the square root of acquisition time as expected, but drift and other low frequency noise becomes more important as the acquisition time increases.

4.4 Effect of temperature changes on δ determination

The effect of temperature changes on the retrieved N_2O isotopomer values can be easily predicted using MALT. A set of N_2O spectra was calculated with N_2O at 1 torr and rms-SNR of 2000, with temperature varying between 23.0 and 27.0 °C. Isotopomers were determined by both classical and non-linear least squares (CLS and NLLS), and δ values were calculated relative to the N_2O spectrum at 25 °C. Figure 4.4 shows the temperature effect on N_2O partial pressure (or amount) determination (left) and δ (right) as determined by CLS.

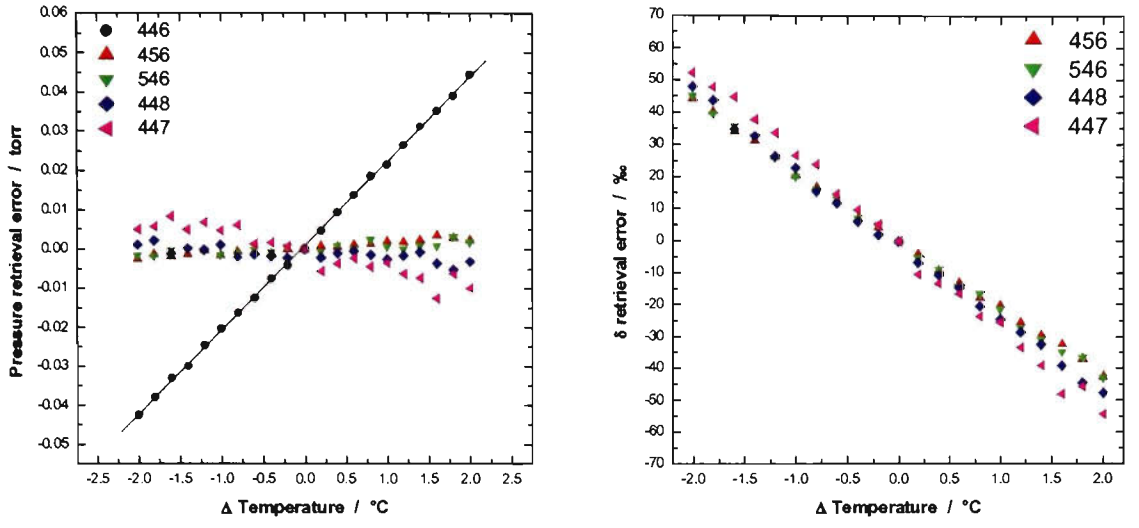

Figure 4.4 The effect of a temperature change on partial pressure determination (left) and δ determination (right) as determined by CLS

When determined by CLS, the δ ratio is strongly temperature dependent to approximately –26 ‰ per °C change in temperature. The right panel of Figure 4.4 shows the error in the partial pressure determination due to a temperature change. The error in the pressure determination of the parent $^{14}N^{14}N^{16}O$ isotopomer (0.02154 ± 0.00008 torr/°C) completely dominates the error in the isotopomer determination. This is a direct consequence of the CLS determination method. As Chapter 2 of this thesis describes, the first micro-window, between 2130.1 and 2160.1 cm^{-1} contributes approximately 70 % to the final $^{14}N^{14}N^{16}O$ determination. This micro window consists of very high *J*-number lines which are very temperature dependent. The spectra used in the above example were also analysed with NLLS and the results shown in Figure 4.5.

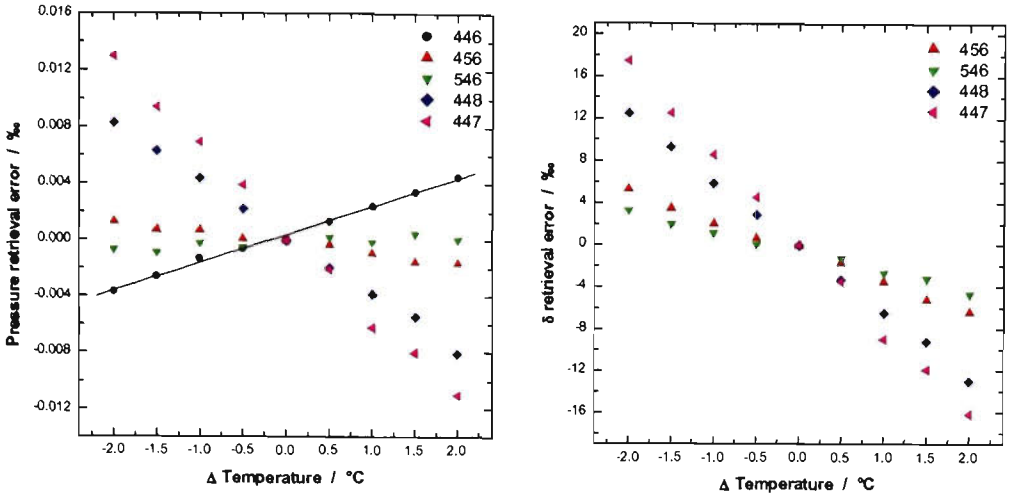

Figure 4.5 The effect of a temperature change on pressure determination (left) and δ determination (right) as determined by NLLS

Using non-linear least squares makes a striking improvement in the temperature sensitivity. The error in the retrieved δ is no longer dominated by the error in determining the parent $^{14}N^{14}N^{16}O$. The temperature effect on $^{14}N^{14}N^{16}O$ has been reduced by an order of magnitude to 0.00200 ± 0.00005 torr/°C, and the resulting error in δ determination ranges from approximately 8.5 ‰ per °C for δ^{447} to approximately 2 ‰ per °C for δ^{546}. The above NLLS determination were generated using the three optimum spectral regions as described in section Chapter 2 of this thesis. The region between 2400 and 2520 cm^{-1} was used for determination of the parent $^{14}N^{14}N^{16}O$. This encompasses all the $\nu_1 + 2\nu_2$ combination band and so is potentially is affected by the temperature sensitivity of the high *J*-number included in this region, in a similar way to micro-window 1 in the CLS analysis, but also includes low *J*-number lines with the opposite temperature dependence. To test the effect of removing high *J*-number lines from the regions fitted by NLLS, the 2440-2480 cm^{-1} region centred on the $\nu_1 + 2\nu_2$ band was used for the $^{14}N^{14}N^{16}O$ determination. Excluding the high *J*-number lines in

the $^{14}N^{14}N^{16}O$ determination lowered the temperature effect by factor of approximately three to 0.00060 ± 0.00006 torr/°C.

Excluding high *J*-number lines from the NLLS determination regions was also trialled for all isotopomers. Regions approximately 40 cm^{-1} wide centred on the respective ν_3 fundamental frequencies were used for NLLS determination. The partial pressure and δ variability was within a few percent of those quoted above for all isotopomers. However, using a narrower spectral region increases the standard error of the partial pressure determination by a factor between approximately 2 and 4. This is the main disadvantage of using narrower spectral ranges, hence the larger spectral ranges were used for NLLS determination

Temperature does have a large effect on the precision of isotopic determination, but it is unlikely to have a major effect in the system constructed for use in this work. The White cell and sample handling manifold are kept at 25.00 ± 0.01 °C by the Julabo F25 water circulator and samples are allowed to come to thermal equilibrium before the spectra are collected. Therefore the temperature variability of this measurement system is not expected to be significant, and is estimated to be a maximum of ± 0.02 °C. Using the 2400-2520 cm^{-1} region for $^{14}N^{14}N^{16}O$ determination and the 2120-2180 cm^{-1} for $^{14}N^{15}N^{16}O$ and $^{15}N^{14}N^{16}O$ determination, the likely temperature dependence of the δ^{456} determination is 2.88 ‰/°C. Therefore the maximum expected uncertainty in the δ^{456} determination from temperature variability is expected to be no greater than 0.06 ‰, about 7% of the difference between the best experimental precision and the theoretical precision (Table 4.2).

4.5 Effect of sample pressure on δ determination

The determination of isotopomer partial pressures and consequently δ measurements are affected by errors in measuring and controlling sample pressure. MALT can be used to estimate the effect of a pressure change on the retrieved N_2O isotopomer values. A set of N_2O spectra were calculated with N_2O at 25.0 °C torr and rms-SNR of 2000, with the total N_2O pressure varying between 0.8 and 1.2 torr. Isotopic determinations were determined by both classical and non-linear least squares (CLS and NLLS) assuming the total N_2O pressure was a constant 1.0 torr. Isotopic determinations were calculated relative to the N_2O spectrum at a true 1.0 torr pressure. The determination error is the error due to the pressure dependence of the N_2O line shapes. During a real experiment, spectra of the N_2O sample and N_2O working standard are collected at the same N_2O partial pressure. Figure 4.6 shows the pressure effect on isotopomer partial pressure determination and δ determination as determined by CLS.

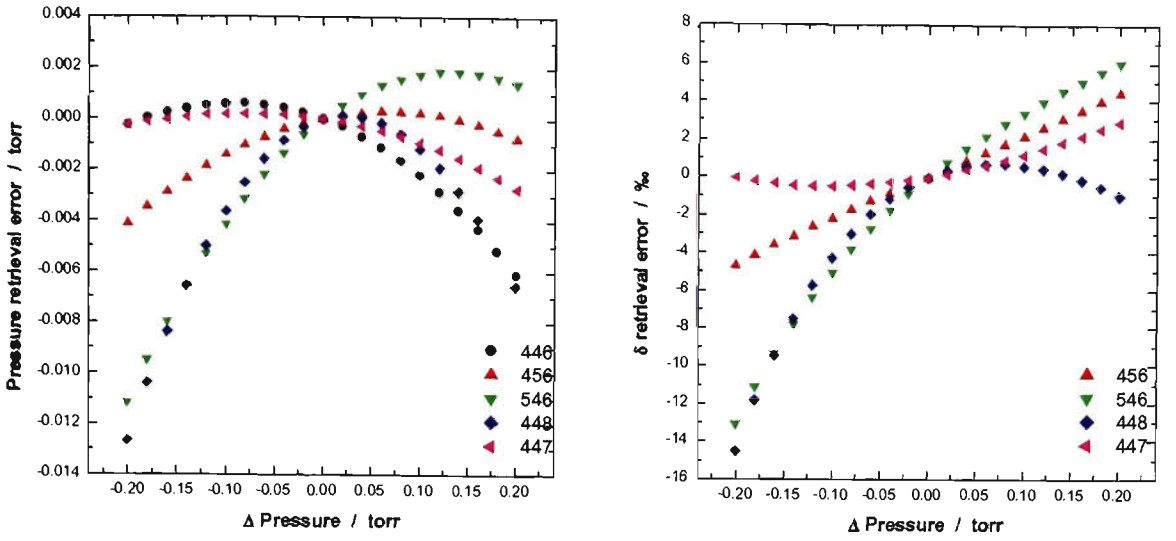

Figure 4.6 The effect of a pressure change on pressure determination (left) and δ determination (right) as determined by CLS

The determination of $^{14}N^{14}N^{16}O$ is not the dominating driver of the determination error under a pressure change, unlike the case of a temperature change. Interestingly the error in partial pressure determination of $^{14}N^{14}N^{16}O$ and $^{14}N^{15}N^{16}O$ are negatively correlated in the CLS analysis, so that the error in δ^{456} determination forms a straight line with slope approximately 22.3 ‰ per torr. The spectra used in the above example were determined with NLLS and the results shown in Figure 4.7.

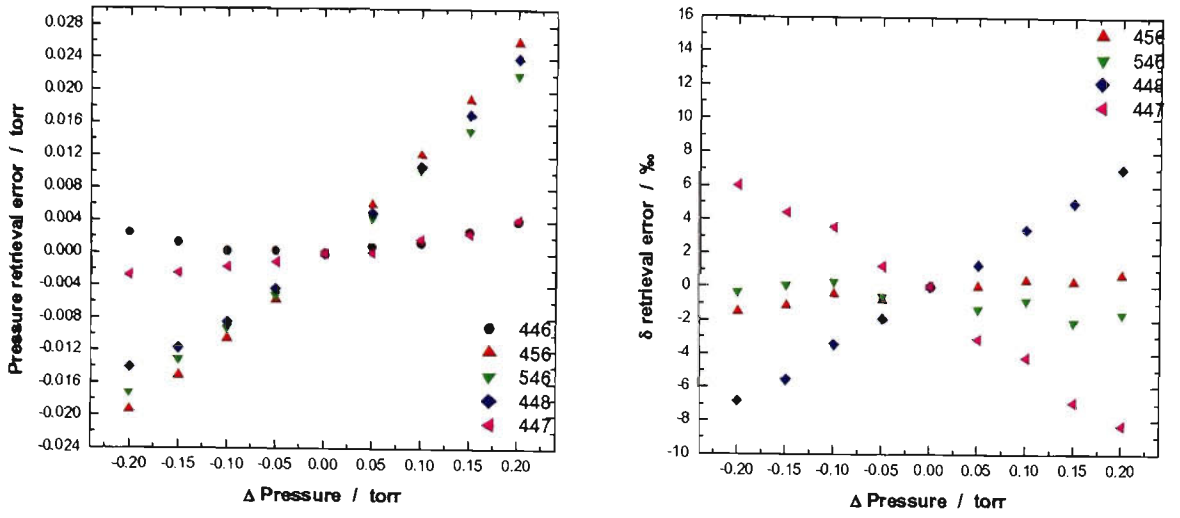

Figure 4.7 **The effect of a pressure change on pressure determination (left) and δ determination (right) as determined by NLLS**

Non-linear least squares determination has mixed effects on the isotopomer determination errors due to pressure variations. The error in δ^{456} determination is approximately 5.5 ‰ per torr, a factor of approximately 4 better than with CLS analysis. Determination of δ^{546} is essentially unaffected by a pressure change. However, the error in determination of δ^{447} has increased with NLLS determination.

Errors in controlling and measuring sample pressure do have a large effect on the precision of isotopic determination, but it are unlikely to have a major effect in the system constructed for use in this work. Samples of N_2O are measured at 1.000 ± 0.005 torr, where maximum error on the δ^{456} determination is expected to be no greater than ± 0.03 ‰. In cases where there is insufficient sample to obtain 1.000 ± 0.005 torr N_2O, all samples and interleaving working standards are measured at the highest available sample pressure. The measured sample pressure is used as the input in the NLLS isotopomer determination.

4.6 Effect of line shape variability on δ determination

Scan to scan reproducibility for the DA8 spectrometer was determined by consecutive measurements of a number of single scan spectra of 1 torr N_2O at 0.012 cm^{-1} resolution. Single scan spectra take approximately 1 minute to acquire and therefore are a good indication of the short term variability in spectrometer performance. Thirty consecutive single scan N_2O spectra were collected. Each single beam spectrum is subtracted from the first single beam spectrum. The transmission of the first spectrum was calculated relative to an evacuated cell spectrum. These 30 single scan difference spectra were overlayed on the same y-scale to give a visual indication of line shape variability, shown in Figure 4.8. Both the series of 30 single scan difference spectra and the transmission of the first spectrum are on the same y-scale but shifted for clarity. Figure 4.8 shows there is large variability in the intensity and line position for a given spectral line over 30 single scan spectra. This figure is representative of many similar tests performed during 1999, 2000 and 2001.

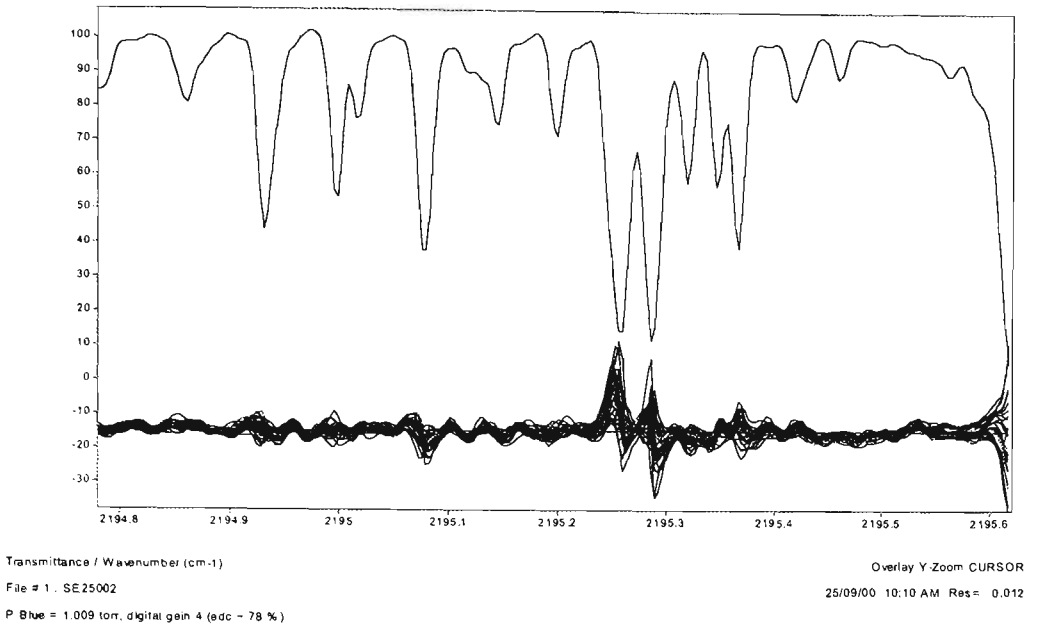

Figure 4.8 Single scan reproducibility for high resolution spectra determined on 25 September 2000.

Typical N_2O spectra are acquired over 30 minutes. The scan to scan variability seen in Figure 4.8 effectively "smears" the line shape in the final 30 co-added scan spectra such that the final line shape is a combination of all the contributing line shapes from the 30 individual scans. This line shape cannot be modelled by CLS. NLLS enables iterative fitting of symmetric and asymmetric line broadening parameters which allow an imperfect, broadened and asymmetric line shape to be fitted, but NLLS cannot remove all the effects of lineshape variability. Figure 4.9 shows the line shapes for 25 consecutive 30 scan spectra of an identical sample of N_2O for one absorbance line in the region of Figure 4.8. Both the line shape and line centre are shifting from spectrum to spectrum. This was later identified as resulting from a fault in the DA8 laser thermal stability.

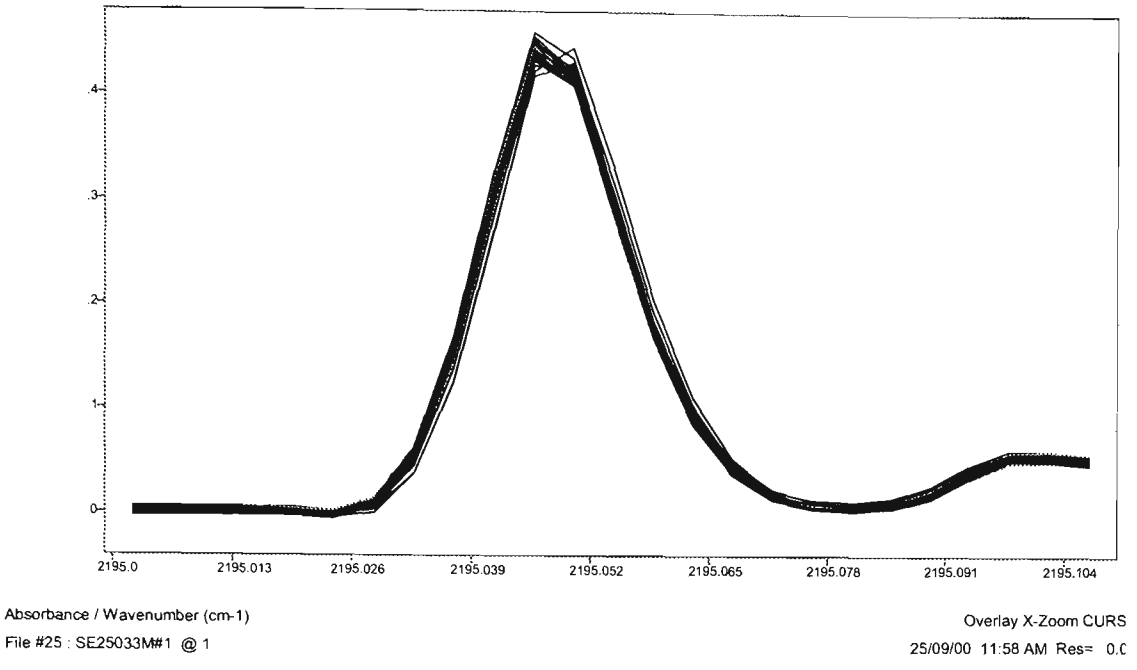

Figure 4.9 Line shape of 25 consecutive 30-scan spectra.

To test the impact of FTIR lineshape on isotopomer determination precision the following test was performed on the Bomem DA8 spectrometer and a Bruker 120 HR spectrometer[1] A 10 cm cell with sapphire windows was filled with 24 torr pure N_2O. This gives the cell the same pressure-pathlength product as the normal isotope experimental conditions. A total of 39 consecutive 30 scan spectra were collected with an aperture of 1.0 mm (1.54 mrad field of view) and 0.012 cm^{-1} resolution. These spectra were quantitatively analysed with the CLS method, with δ measured relative to the first spectrum in the series. Table 4.3 shows the quantitative precision ($\pm$ 1 σ) for δ^{456}, δ^{546}, $\delta^{456\text{-}546}$ and δ^{448} determination for both spectrometers.

[1] Monash University, Melbourne, Australia. Laboratory of Dr Don McNaughton.

Table 4.3 Comparative isotopic determination precisions (± 1 σ) for two FTIR spectrometers

Spectrometer	δ^{456} (‰)	δ^{546} (‰)	$\delta^{456\text{-}546}$ (‰)	δ^{448} (‰)
Bomem DA8	3.90	4.3	5.3	3.9
Bruker 120HR	1.6	2.2	1.9	2.4

The Bruker 120HR spectrometer performed approximately a factor of two or better than the Bomem DA8 spectrometer under similar instrumental conditions. Investigation of the line shape from the 120HR spectrometer shows it is much more stable that the line shape from the DA8 spectrometer.

The design of the DA8 spectrometer is such that the "fixed" interferometer mirror moves slightly to maintain optimum laser fringe alignment during scanning. This causes the interferometer optical axis to move, leading to variability in the spectral line shape. The movable mirror in the DA8 spectrometer does not move at a constant velocity throughout the length of its travel. This creates uncertainty in sampling the interferogram and therefore in the wavenumber axis of the spectrum. These effects in part lead to the lineshape variability discussed above, and consequently affect the precision of the isotopomer determination.

4.7 What limits the isotopomer precision?

The effects of temperature, pressure and lineshape on the isotopomer determination precision were examined in sections 4.4, 4.5 and 4.6. Temperature and pressure both have a large effect on the isotopomer retrieval. However, the experimental system constructed for this work limits the effects of temperature and pressure variability on the N_2O sample. The maximum temperature variability is estimated at ± 0.02 °C and the

maximum pressure variability is ± 0.005 torr. These lead to a maximum error in the δ^{456} determination of ± 0.06 ‰ and 0.03 ‰, respectively. These errors are insignificant compared to the experimentally determined precision for δ^{456} (Table 4.2 and Table 4.6). It seems likely that major limitation on the isotopomer precision is the effect of FTIR lineshape variability.

4.8 A summary of the high resolution FTIR method conditions

This section summarises the high resolution FTIR method developed for isotopomer analysis of N_2O. Unless stated otherwise, all sample measurements and determinations performed in this thesis were carried out using this set of standard measurement conditions. Table 4.4 summarises the standard spectroscopic and sample conditions. Table 4.5 summarises the standard spectral analysis conditions, and Table 4.6 summarises the performance and sensitivities of the analysis method.

Table 4.4 The standard spectroscopic conditions

Spectrometer	Bomem DA8
Beam splitter	Ge on KBr substrate
Detector	InSb
Optical filter	1980-3310 cm^{-1}
Collimator focal length	325 mm
Aperture	1.5 mm
Co added scans	30 (31 minute acquisition)
Resolution	0.012 cm^{-1}
Apodisation	Hamming
Base gain	1
Positional gain	16 (at 2048 fringes)
Sample pressure	1.000 ± 0.005 torr
Sample temperature	25 ± 0.01 °C
Optical path length	2.4 m

Table 4.5 The standard spectral analysis conditions

Method	Non-linear least squares using non-linear MALT3 (NLLS-NLM3)
$^{14}N^{14}N^{16}O$ region	2400-2520 cm^{-1}, $\nu_1 + 2\nu_2$ band
$^{14}N^{15}N^{16}O$ and $^{15}N^{14}N^{16}O$ region	2120-2180 cm^{-1}
$^{14}N^{14}N^{18}O$ and $^{14}N^{14}N^{17}O$ region	2120-2260 cm^{-1}
Iteratively fit	Typically sample pressure, field of view, phase error
χ^2 convergence criterion [a]	Typically within 1×10^{-5}
Iterations [b]	Convergence typically within 10 iterations

a. When consecutive χ^2 determinations are within this limit, the NLLS program exits. This limit is selectable in the NLLS software

b. The number of iterations typically required for convergence if the $\chi 2$ convergence criterion is 1×10^{-5}

Table 4.6 Performance summary for the FTIR method

Isotopomer	Theoretical precision, ‰ [a]	Best experimental precision, ‰	Typical experimental precision, ‰	Temperature sensitivity, ‰ per °C [b]	Pressure sensitivity, ‰ per torr [c]
$\delta^{14}N^{15}N^{16}O$	0.26	1.1	1.8	2.9	5.1
$\delta^{15}N^{14}N^{16}O$	0.37	1.8	2.1	1.9	4.9
$\delta^{14}N^{14}N^{18}O$	0.41	1.3	3.3	6.3	34.5
$\delta^{14}N^{14}N^{17}O$	0.78	2.3	4.4	8.4	36.9

a. As determined in section 4.3 at root mean square signal to noise ratio 1000. Precision is ± 1 σ.

b. The maximum variation in sample temperature is ± 0.02 °C

c. The maximum variation in sample pressure measurement and control is ± 0.005 torr

4.9 References

Esler, M.B., D.W.T. Griffith, F. Turatti, S.R. Wilson, and T. Rahn, N_2O concentration and flux measurements and complete isotope analysis using FTIR spectroscopy, *Chemosphere: Global Change Science*, *2*, 445-454, 2000.

Chapter 5 Results I: Isotopic enrichment factors for $^{14}N^{15}N^{16}O$, $^{15}N^{14}N^{16}O$, $^{14}N^{14}N^{18}O$ and $^{14}N^{14}N^{17}O$ in the laboratory photolysis of N_2O

5.1 Introduction

As outlined in Chapter 1, nitrous oxide is believed to be inert in the troposphere. The major sink for nitrous oxide is photolysis in the stratosphere which accounts for about 90% of N_2O removal via reaction 5.1. The remainder is destroyed via reactions 5.2 and 5.3 with $O(^1D)$.

$$N_2O + h\nu \rightarrow N_2 + O(^1D) \ (\lambda \approx 180\text{-}215 \text{ nm}) \qquad (5.1)$$

$$N_2O + O(^1D) \rightarrow N_2 + O_2 \qquad (5.2)$$

$$N_2O + O(^1D) \rightarrow 2\,NO \qquad (5.3)$$

Yung and Miller [1997] have suggested the heavy isotopomers of N_2O in the stratosphere should be photolysed at slower rates than the parent isotope, $^{14}N^{14}N^{16}O$ (446), leading to an enrichment of the heavy N_2O isotopomers. In particular the two positional isotopomers $^{14}N^{15}N^{16}O$ (456) and $^{15}N^{14}N^{16}O$ (546) should have markedly different stratospheric photolysis rates. According to their theory, differences in the zero point energy (ZPE) of the isotopomers lead to a blue-shift of the UV absorption spectrum for the heavy isotopomers relative to the parent isotope, 446. The blue-shifted UV absorption spectra have lower absorption cross sections in the overlapping region of the solar UV spectrum, so that the heavy isotopomers are photolysed more slowly than

the parent. To a first approximation the photolysis rates are proportional to the size of the ZPE shift, such that photolysis rates are predicted to decrease in the order 446>447>546>448>456. The consequent stratospheric enrichment of the heavy isotopes has been observed for the mean $\delta^{15}N$ and $\delta^{18}O$ from analysis of stratospheric samples [*Kim and Craig*, 1993; *Rahn and Wahlen*, 1997], and laboratory laser-photolysis studies of N_2O [*Rahn et al.*, 1998; *Röckmann et al.*, 2000; *Turatti et al.*, 2000; *Zhang et al.*, 2000]. Confirmation of the stratospheric enrichment of the heavy N_2O isotopomers over the parent $^{14}N^{14}N^{16}O$ has been directly observed by *Griffith et al.* [2000] by a balloon borne high resolution FTIR spectrometer, and by *Yoshida et al.* [2000] and *Röckmann et al.* [2001] by cryogenic sampling of stratospheric air and analysis by isotope ratio mass spectrometry (IRMS) in the laboratory. A more recent N_2O photolysis theory was proposed by *Johnson et al.* [2001] which takes into account the effect of the transition dipole surface and upper state dynamics which are not included in the *Yung and Miller* [1997] ZPE model.

If all N_2O destruction occurs by photolysis in the stratosphere and is irreversible, then it can be described by a Rayleigh distillation model [*Rahn and Wahlen*, 1997]. In this model the resulting isotopic enrichment is related to the fraction of unphotolysed N_2O remaining by:

$$R = R_0 f^{(\alpha-1)} \tag{5.4}$$

where R and R_0 are the remaining and initial heavy-to-light isotopic ratios, f is the unphotolysed fraction of N_2O and α is the ratio of the heavy to light isotopic photolysis rates. If R and R_0 are close to 1, this relationship can be approximated by

$$\delta = \delta_0 + \varepsilon \ln(f) \tag{5.5}$$

where δ and δ_0 are the residual and initial δ values and the slope $\varepsilon = 1000(\alpha\text{-}1)$ is the enrichment factor expressed in parts per mil (‰) [*Fritz and Fontes*, 1980].

This chapter presents measurements of the enrichment factors (ε) for laboratory photolysed N_2O samples. The high resolution FTIR spectroscopy technique developed in this thesis was used to measure the positionally dependent ^{15}N photolysis enrichment factors, ε^{456} and ε^{546}, and also the heavy oxygen isotopic enrichment factors, ε^{448} and ε^{447} in natural abundance at three wavelengths, 193, 211.5 and approximately 207.6 nm. Results are compared to other studies of laboratory N_2O photolysis, to the *Yung and Miller* [1997] and *Johnson et al.* [2001] theories, and to the measured stratospheric N_2O isotopic composition. Advances in the quantitative analysis method allows the photolysis enrichment factors quoted in *Turatti et al.* [2000] to be reported with higher precision.

5.2 Experimental

The same samples of N_2O photolysed at 207.6 nm and 193 nm as described by *Rahn et al.* [1998] in a previous study were analysed in this work. Additional N_2O samples photolysed at 211.5 nm were also included. Briefly, samples of N_2O were introduced to a thermostatted glass cell (approximately 300 mL in volume) and photolysed with laser-generated UV light at 211.5 nm, 207.6 nm or 193 nm with a line width of $\approx$1.5-2.5 nm. After photolysis, the unphotolysed N_2O fraction was determined manometrically and then cryogenically collected. *Rahn et al.* [1998] used Isotope Ratio Mass Spectrometry (IRMS) to determine the bulk $\delta^{15}N$ and $\delta^{18}O$ of these same samples relative to atmospheric N_2 and O_2 respectively.

These samples were analysed by the high resolution FTIR spectroscopy technique as described in Chapters 2, 3 and 4 of this thesis to determine the positional isotopomers and the photolysis enrichment factors by equation 5.6. The standard measurement and analysis conditions as described in Chapter 4 were used. Quantitative analysis of the spectra was performed with both classical least squares (CLS) and non-linear least squares (NLLS) using the procedures described in detail in chapters 2, 3 and 4. The results obtained with CLS analysis have already been published by the author of this thesis [*Turatti et al.*, 2000]. Results from both non linear least squares and classical least squares analysis are compared in this chapter. Spectra of most samples were measured twice, approximately 4 months apart.

Isotopomer values (δ) were calculated relative to the those of the starting N_2O before photolysis, which has $\delta^{15}N = 1.31$ ‰ and $\delta^{18}O = 18.46$ ‰ relative to atmospheric N_2 and O_2, respectively [*Rahn*, 1998]. All FTIR measurements were made relative to the Scott-Marrin N_2O working standard, whose relationship to the starting N_2O before photolysis (Standard Nitrous Oxide Working Gas, SNOW) is well know, as described in section 3.4.

5.3 Results and Discussion

Figure 5.1 shows the retrieved isotopomer δ results relative to those of the starting N_2O before photolysis, Standard Nitrous Oxide Working Gas (SNOW) as a function of the natural logarithm of the unphotolysed N_2O fraction (equation 5.6). The complete data are in Table 5.1. These data have been determined using the non-linear least squares algorithm, NLLS-NLM3 as described in this Chapter 2. In the case of the nitrogen isotopomers, the data fit the Rayleigh distillation model very well (within the scatter).

The determination for the oxygen isotopomers, δ^{448} and δ^{447} are similarly plotted to a linear Rayleigh distillation graph, and these are shown in Figure 5.2. The oxygen isotopomers determinations show more scatter than the δ^{456} and δ^{546} determination, but are still described adequately by the Rayleigh distillation model.

Table 5.1 Isotopomer determinations in per mille relative to SNOW[a] for laboratory photolysed N_2O by non-linear least squares

Sample no. [b]	Measured [c]	Photolysis λ (nm) [d]	f [e]	ln(f)	δ^{456} (‰)	δ^{546} (‰)	δ^{456}-δ^{546} (‰)	$\delta^{15}N$ (‰)	δ^{448} (‰)	δ^{447} (‰)
24	Dec-99	207.6	0.882	-0.1256	8.5	4.2	4.1	6.3	3.8	5.4
24	Aug-99	207.6	0.882	-0.1256	9.1	5.6	3.4	7.3	7.2	10.5
26	Dec-99	207.8	0.807	-0.2144	16.8	6.7	9.9	11.6	4.4	5.0
26	Aug-99	207.8	0.807	-0.2144	15.3	7.2	7.9	11.2	9.6	5.9
27	Dec-99	207.8	0.760	-0.2744	21.5	9.7	11.7	15.5	11.7	9.0
27	Aug-99	207.8	0.760	-0.2744	20.3	8.8	11.4	14.5	14.3	3.2
29	Dec-99	207.4	0.721	-0.3271	23.1	9.2	14.4	16.4	13.3	5.2
29	Aug-99	207.4	0.721	-0.3271	25.1	14.3	10.7	19.7	18.3	18.9
31	Dec-99	207.4	0.824	-0.1936	15.2	8.6	6.5	11.8	8.2	10.4
34	Dec-99	207.4	0.851	-0.1613	12.7	7.8	4.7	10.2	10.2	6.4
34	Aug-99	207.4	0.851	-0.1613	12.2	4.7	7.3	8.4	5.3	4.8
36	Dec-99	211.5	0.871	-0.1381	9.5	7.4	2.0	8.4	10.6	3.7
36	Aug-99	211.5	0.871	-0.1381	12.4	3.7	8.6	8.0	3.6	3.5
37	Dec-99	211.5	0.929	-0.0736	9.2	5.6	3.5	7.3	8.8	9.2
38	Dec-99	211.5	0.732	-0.3120	21.8	8.2	13.4	14.9	16.3	6.2
38	Aug-99	211.5	0.732	-0.3120	20.7	8.2	12.4	14.4	8.5	3.0
39	Dec-99	211.5	0.813	-0.2070	14.0	6.4	7.4	10.2	9.5	-0.1
39	Aug-99	211.5	0.813	-0.2070	14.3	5.7	8.4	10.0	6.9	2.5
41	Dec-99	211.5	0.738	-0.3038	18.9	8.9	9.9	13.9	8.7	3.4
42	Dec-99	211.5	0.648	-0.4339	32.2	15.2	16.8	23.6	23.3	11.6
45	Dec-99	np [f]	1	0.0000	1.6	1.7	-0.2	1.6	-1.7	-2.3
45	Aug-99	np	1	0.0000	1.7	1.0	0.7	1.3	-1.9	4.3
46	Dec-99	np	1	0.0000	1.8	0.7	1.0	1.1	-1.5	-1.5
46	Aug-99	np	1	0.0000	2.5	1.9	0.5	2.1	-2.2	-2.2
49	Aug-99	193	0.850	-0.1625	11.6	8.3	3.2	9.8	8.1	4.4
50	Dec-99	193	0.610	-0.4943	18.3	11.4	6.8	14.8	11.2	6.0
51	Dec-99	193	0.790	-0.2357	12.2	5.8	6.3	8.9	8.3	9.7
52	Dec-99	193	0.750	-0.2877	17.4	7.8	9.5	12.6	11.9	5.4
52	Aug-99	193	0.750	-0.2877	16.5	10.6	5.8	13.5	10.5	8.3
53	Dec-99	193	0.590	-0.5276	23.9	11.4	12.3	17.6	11.4	16.5
53	Aug-99	193	0.590	-0.5276	24.0	14.6	9.3	19.3	17.7	12.4
57	Dec-99	193	0.430	-0.8440	30.3	16.9	13.2	23.6	22.5	13.4
57	Aug-99	193	0.430	-0.8440	30.5	19.7	10.7	25.0	21.4	17.5
58	Dec-99	193	0.440	-0.8210	29.1	16.0	13.0	22.5	13.8	5.7
59	Dec-99	193	0.820	-0.1985	14.6	5.3	9.2	9.9	-8.8	-6.3
61	Dec-99	193	0.830	-0.1863	9.7	6.4	3.2	8.0	1.1	4.5
63	Dec-99	193	0.790	-0.2357	13.0	10.5	2.4	11.7	13.7	10.7
63	Aug-99	193	0.790	-0.2357	13.9	11.1	2.6	12.4	11.7	10.8

a. SNOW: Standard Nitrous Oxide Working gas [*Rahn et al.*, 1998]
b Sample number used by the *Rahn et al.* [1998] photolysis experiment
c. Date when FTIR spectrum was measured
d. N_2O photolysis wavelength (λ) in nanometers
e. Remaining (unphotolysed) N_2O fraction
f. Samples 45 and 46 were not photolysed (np) and included in the calculations for each of the 193 nm, 207 nm and 211 nm photolysis sample sets

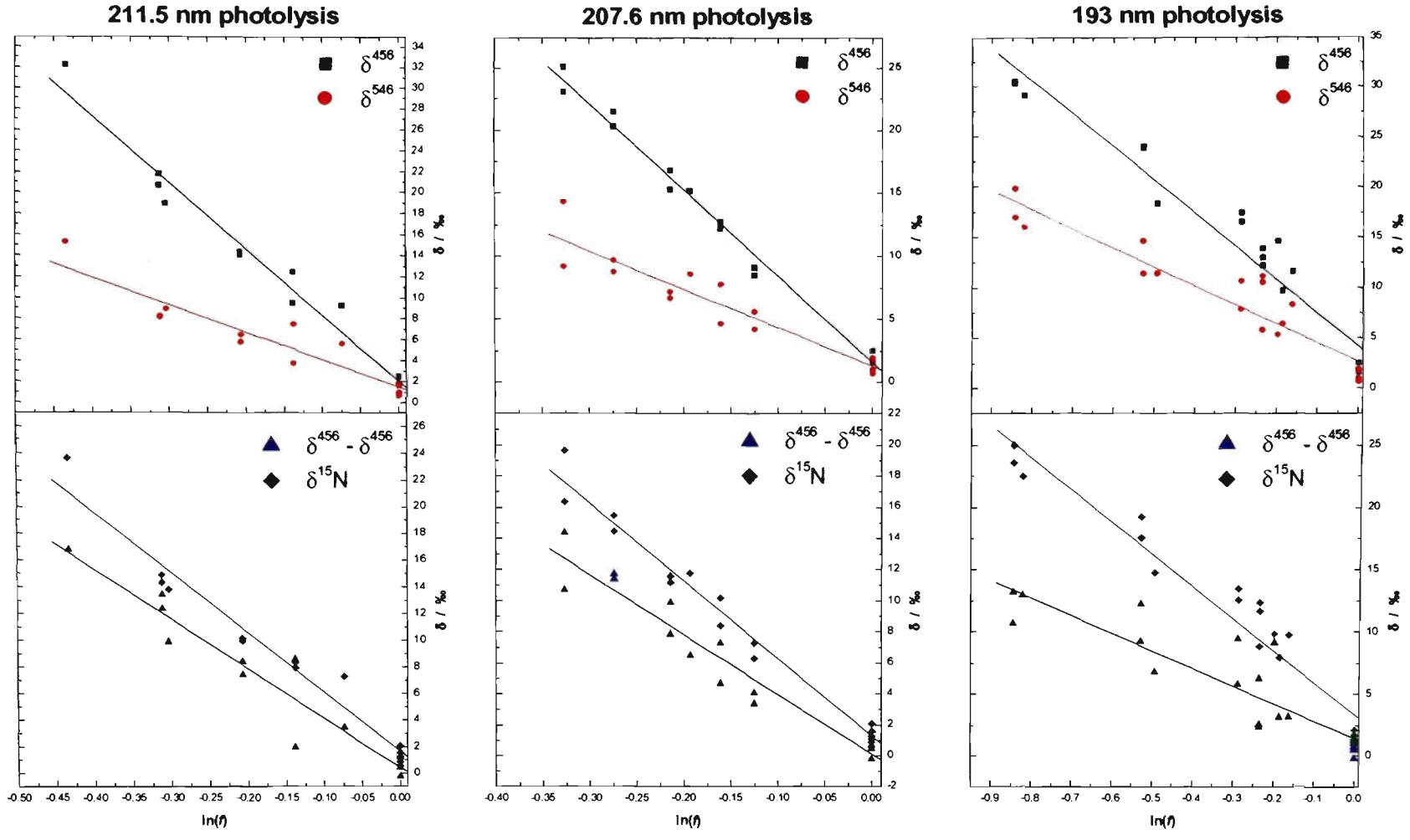

Figure 5.1 Rayleigh distillation plots for N_2O photolysis at 211.5 nm, 207.6 nm and 193 nm for ^{15}N isotopomers

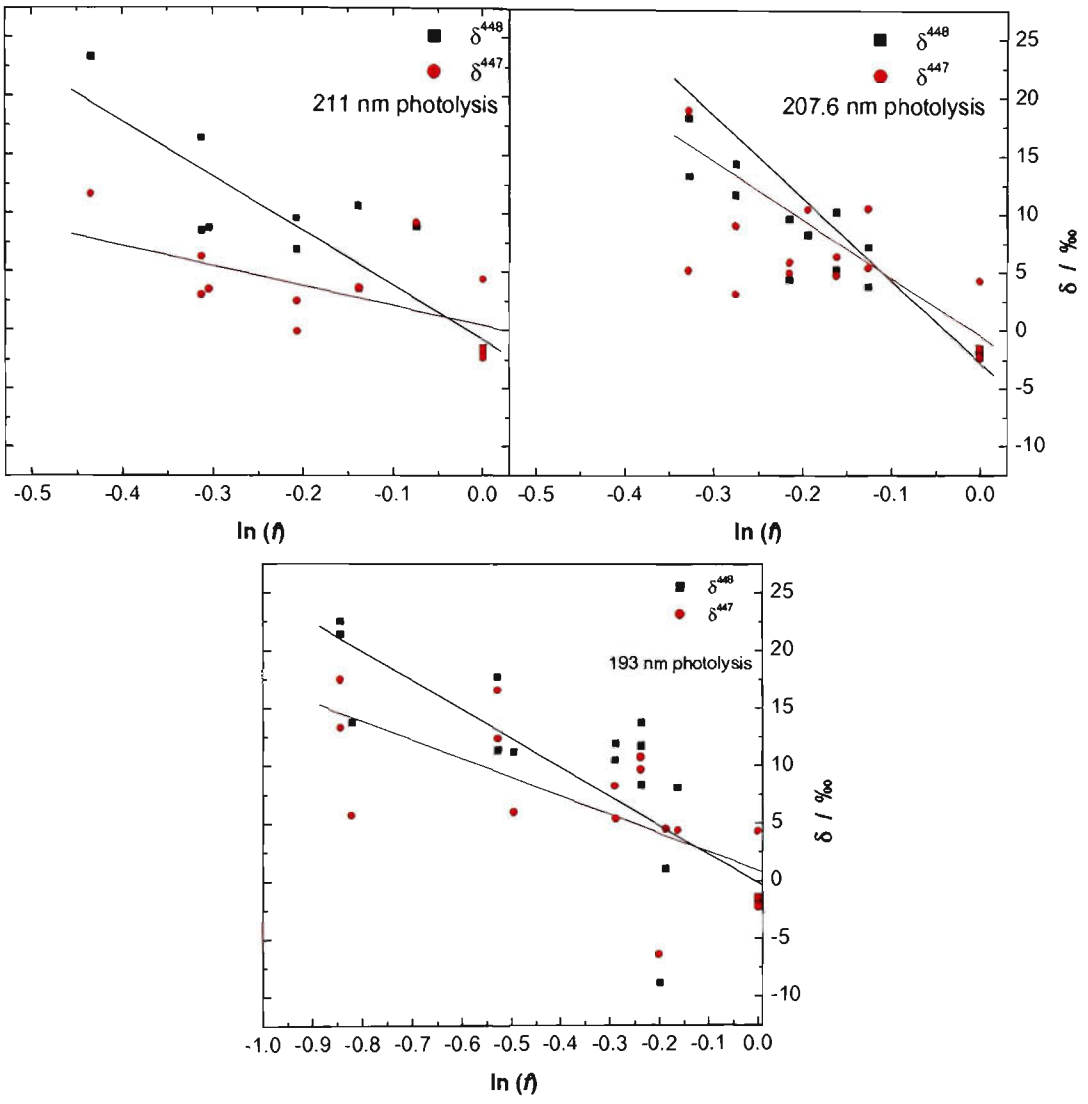

Figure 5.2 Rayleigh distillation plots for N_2O photolysis at 211.5 nm, 207.6 nm and 193 nm for $^{14}N^{14}N^{18}O$ and $^{14}N^{14}N^{17}O$ isotopomers

The slope of the regression line fitted to the Rayleigh distillation model is the enrichment factor (ε) for that particular isotopomer. Table 5.2 summarises the enrichment factors (ε) for the $^{14}N^{15}N^{16}O$, $^{15}N^{14}N^{16}O$ $^{14}N^{14}N^{18}O$ and $^{14}N^{14}N^{17}O$ isotopomers at each photolysis wavelength, determined as the slopes of the regressions of δ against ln(*f*) in Figure 5.1 and Figure 5.2. The errors quoted are the standard deviations of the slopes from the regressions. The ^{15}N enrichment factors are also given

as the mean or bulk $\varepsilon^{15}N = (\varepsilon^{456}+\varepsilon^{456})/2$ for comparison with IRMS measurements of Rahn *et al.* [1998], and the positional ^{15}N isotopic enrichment factor difference, ε^{456}-ε^{546}. Earlier work previously published by *Turatti et al.* [2000] calculated by CLS this difference as ε^{546}- ε^{456}. Enrichment factors calculated by CLS and published by *Turatti et al.* [2000] are included in Table 5.3.

Table 5.2 Photolysis enrichment factors of N_2O determined by non-linear least squares

λ(nm)	ε^{456}	ε^{546}	$\varepsilon^{15}N$	$\varepsilon^{456-546}$	ε^{448}	ε^{447}
193	-32.7 ± 2	-18.6 ± 1.7	-25.6 ± 1.6	-14.1 ± 2	-25.1 ± 4	-15.8 ± 4
207.6	-68.7 ± 2	-30.7 ± 3	-50.0 ± 2	-38.6 ± 3	-52.2 ± 5	-31.5 ± 9
211.5	-63.3 ± 3	-26.1 ± 3	-44.7 ± 3	-37.2 ± 2	-46.6 ± 7	-16.9 ± 7

The enrichment factors (ε) are the slopes of regressions of δ against ln(*f*) as described in equation 5.5. The errors are the standard error of the regression slopes. $\varepsilon^{15}N$ is the average of ε^{546} and ε^{456}, and $\varepsilon^{456-546}$ is the difference ε^{456}-ε^{546}.

Table 5.3 Photolysis enrichment actors of N_2O determined by CLS for this experiment and previously published by *Turatti et al.* [2000]

λ(nm)	ε^{456}	ε^{546}	$\varepsilon^{15}N$	$\varepsilon^{456-546}$	ε^{448}
193	-25.7 ± 2	-13.1 ± 2	-19.4 ± 1.2	-12.6 ± 3	-15.9 ± 3
207.6	-66.5 ± 5	-27.1 ± 6	-46.8 ± 5	-39.3 ± 7	-49 ± 10
211.5	-65.3 ± 4	-31.4 ± 8	-48.3 ± 5	-33.9 ± 9	-46 ± 11

The enrichment factors (ε) are the slopes of regressions of δ against ln(*f*) as described in equation 5.5. The errors are the standard error of the regression slopes. $\varepsilon^{15}N$ is the average of ε^{546} and ε^{456}, and $\varepsilon^{456-546}$ is the difference ε^{456}-ε^{546}.

These new data show interesting trends in comparison to the previously published results [*Turatti et al.*, 2000] determined by classical least squares. Firstly, standard errors for enrichment factors at 193 nm photolysis are generally not significantly better

than those obtained in the previously published work. This is most likely due to the small size of the enrichment at this photolysis wavelength. Aside from data for photolysis at 193 nm, the enrichment factors from the two analysis algorithms agree well within their standard errors. The most important feature of the re-determined enrichment factors is that the standard errors of the slopes have in general become smaller. This is particularly visible in the ε^{546}, $\varepsilon^{456\text{-}546}$ and ε^{448} results. This reduction in scatter also permits the determination of ε^{447}, the photolysis enrichment factor for $^{14}N^{14}N^{17}O$ at the three photolysis wavelengths of 193 nm, 207.6 nm and 211.5 nm. This was not possible in the previously published work which used the classical least squares analysis algorithm, as the enrichment factor was approximately as large as the standard error and therefore not significantly different from zero. The decreased error in N_2O isotopomer determinations and the consequently more accurate enrichment factors illustrates that the NLLS method is more robust than the CLS method.

As initially predicted by the theoretical work of *Yung and Miller* [1997] and developed by *Johnson et al.* [2001], photolysis rates for the positional N_2O isotopomers $^{14}N^{15}N^{16}O$ and $^{15}N^{14}N^{16}O$ are significantly different at all three photolysis wavelengths. The difference in the positional isotopomer enrichment factors ($\varepsilon^{456\text{-}546}$) as shown in Table 5.2 is clearly wavelength dependent, and ranges from -14.1 ± 2 ‰ for 193 nm photolysis to -38.6 ± 3 ‰ for 207.6 nm photolysis. Under the Yung and Miller approximation that photolysis rates are proportional to the ZPE shift of the substituted species from that of the parent $^{14}N^{14}N^{16}O$, the expected $\varepsilon^{456}/\varepsilon^{546}$ ratio should be approximately 1.8 – the ratio of their ZPE shifts. The measured $\varepsilon^{456}/\varepsilon^{546}$ ratios are 2.43 ± 0.3, 2.24 ± 0.2 and 1.76 ± 0.2 for the photolysis wavelengths 211.5 nm, 207.6 nm and 193 nm respectively, supporting the Yung and Miller mechanism. However, all

measured enrichment factors are nearly twice as large as those predicted by the *Yung and Miller* [1997].

The photolysis enrichment factors of the N_2O oxygen isotopomers, $^{14}N^{14}N^{18}O$ and $^{14}N^{14}N^{17}O$ are also wavelength dependent. The ε^{447} enrichment factor is most negative for photolysis at 207.6 nm, but ε^{448} enrichment factors at 207.6 nm and 211.5 nm are not significantly different.. The difference $\varepsilon^{448-447}$ is also wavelength dependent, and ranges from 9.3 ± 6 ‰ for photolysis at 193 nm to 29.7 ± 10 ‰ for photolysis at 211.5 nm. Similar to the nitrogen isotopomers, the $\varepsilon^{448}/\varepsilon^{447}$ ratio is expected to be 1.8, the ratio of the ZPE shifts of the individual isotopomers. The measured $\varepsilon^{448}/\varepsilon^{447}$ ratio in this work is 1.59 ± 0.5, 1.66 ± 0.9 and 2.8 ± 1 for photolysis at 193 nm, 207.6 nm and 211.5 nm, respectively. This is in agreement with the Yung and Miller theory, but as is the case with the nitrogen isotopomers, the measured enrichment factors are approximately twice as large as this theory predicts. The ratio of the expected enrichment factors $\varepsilon^{456}/\varepsilon^{546}$ and $\varepsilon^{448}/\varepsilon^{447}$ as determined by the Johnson *et al.* theory is not constant like the Yung and Miller theory, but depends on both temperature and the photolysis wavelength. There is significant variation between the two theories in their mathematical modelling approaches.

Two recent complementary studies [*Röckmann et al.*, 2000; *Zhang et al.*, 2000] have also determined the positionally dependent enrichment factors for laboratory photolysed N_2O. *Röckmann et al.* [2000] employed a modified isotope ratio mass-spectrometry technique [*Brenninkmeijer and Röckmann*, 1999, and references therein; *Toyoda and Yoshida*, 1999] for measuring positionally dependent enrichment factors during N_2O photolysis at 193 nm. *Zhang et al.* [2000] measured enrichment factors for laboratory

photolysis of equimolar mixtures of pure isotopomers of N_2O at a single wavelength (213 nm) using low resolution (0.5 cm^{-1}) FTIR spectroscopy to measure the Q-branch of the $\nu_2+\nu_3$ combination band. The original work by *Rahn et al.* [1998] measured the average ^{15}N enrichment factor, $\varepsilon^{15}N$, by conventional IRMS methods. Figure 5.3 shows the enrichment factors ε^{456} and ε^{546} as predicted by the *Yung and Miller* [1997] and *Johnson et al.* [2001] theories. Figure 5.4 and Figure 5.5 summarise the enrichment factors $\varepsilon^{15}N$, $\varepsilon^{456\text{-}546}$, ε^{448} and ε^{447} and their errors for N_2O photolysis from all laboratory studies reported to date, together with the predictions of the *Yung and Miller* ZPE theory and the recent theory by *Johnson et al.* [2001]. Figure 5.6 compares the enrichment factor ratios $\varepsilon^{456}/\varepsilon^{546}$ and $\varepsilon^{448}/\varepsilon^{447}$ obtained by this work to the theories of *Yung and Miller* [1997] and *Johnson et al.* [2001].

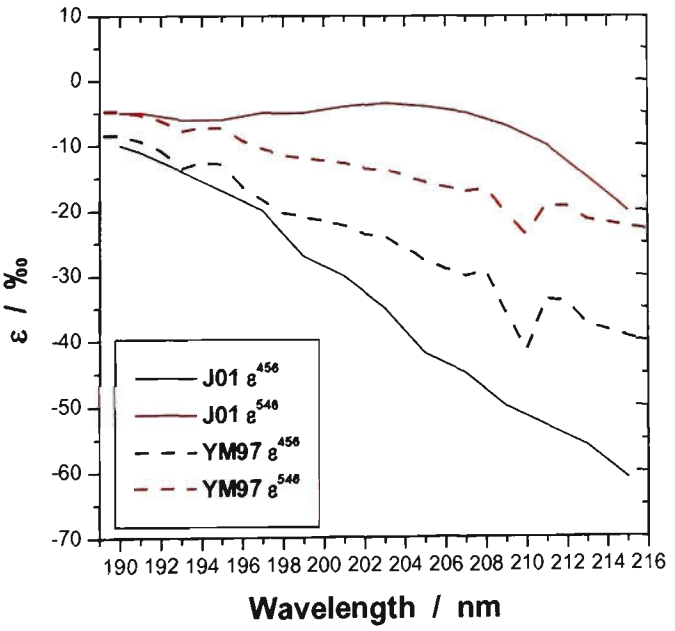

Figure 5.3 Comparison of ε^{456} and ε^{546} enrichment factors predicted by two N_2O photolysis theories

J01: *Johnson et al.*, [2001]
YM97: *Yung and Miller* [1997]

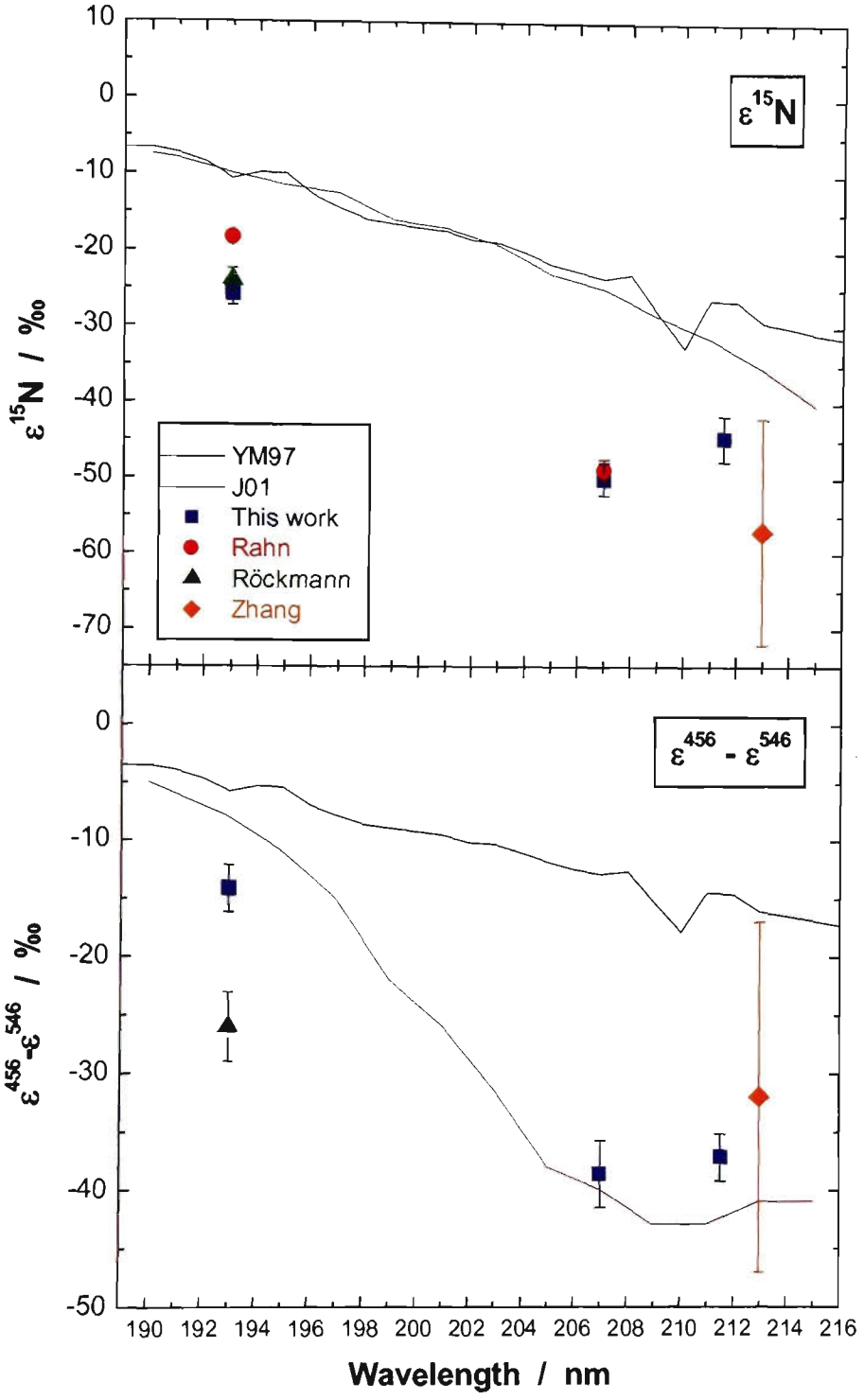

Figure 5.4 **Enrichment factors $\varepsilon^{15}N$ and $\varepsilon^{456\text{-}546}$ for the laboratory photolysis of N_2O.**

Error bars (±1σ) are determined from the scatter in the respective measurements.

YM97:	[*Yung and Miller*, 1997]
J01:	[*Johnson et al.*, 2001]
Rahn:	[*Rahn et al.*, 1998]
Röckmann:	[*Röckmann et al.*, 2000]
Zhang:	[*Zhang et al.*, 2000]

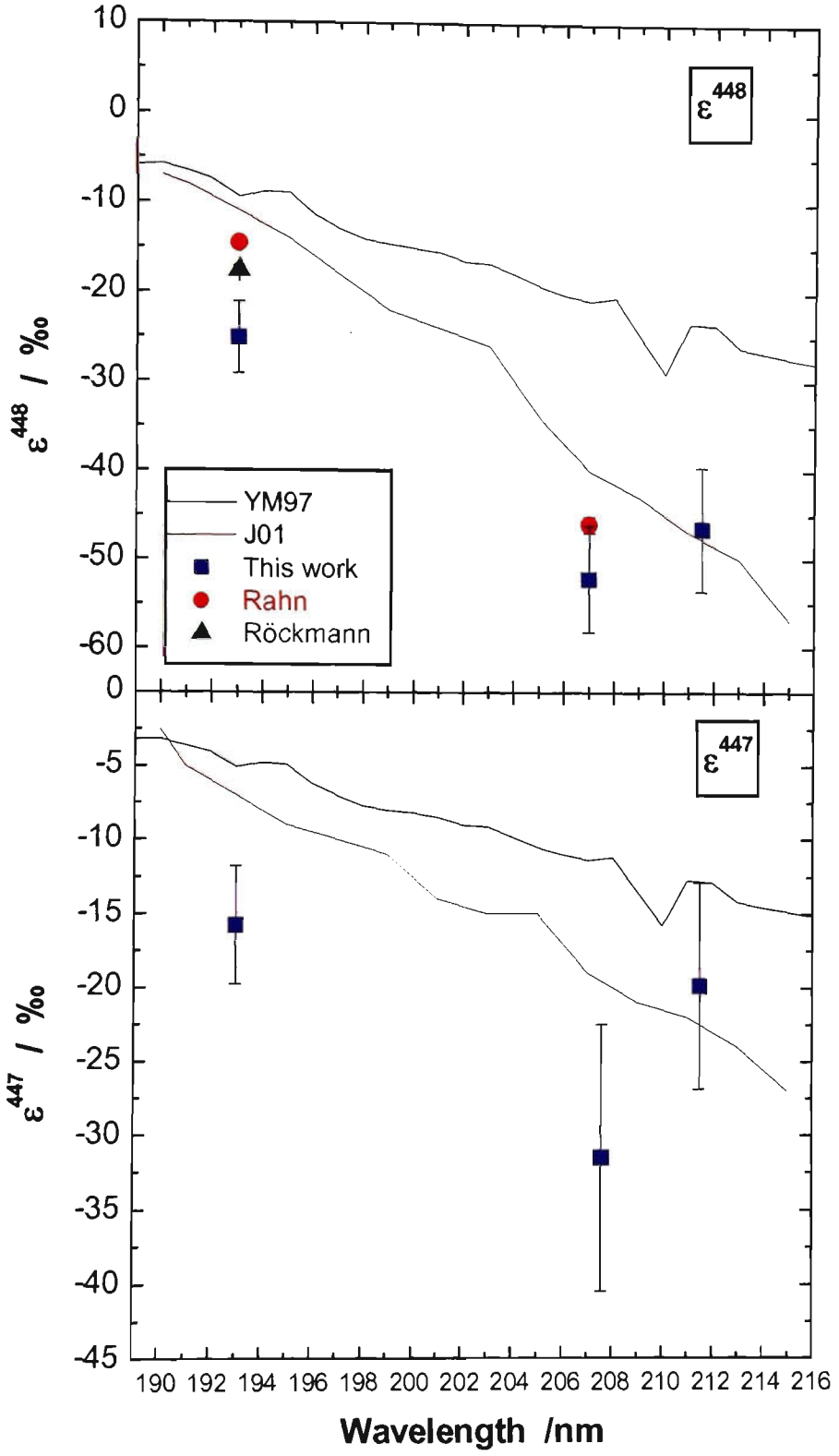

Figure 5.5 **Enrichment factors ε^{448} and ε^{447} for the laboratory photolysis of N_2O.**
Error bars (±1σ) are determined from the scatter in the respective measurements.
YM97: [*Yung and Miller*, 1997]
J01: [*Johnson et al.*, 2001]
Rahn: [*Rahn et al.*, 1998]
Röckmann: [*Röckmann et al.*, 2000]
Zhang: [*Zhang et al.*, 2000]

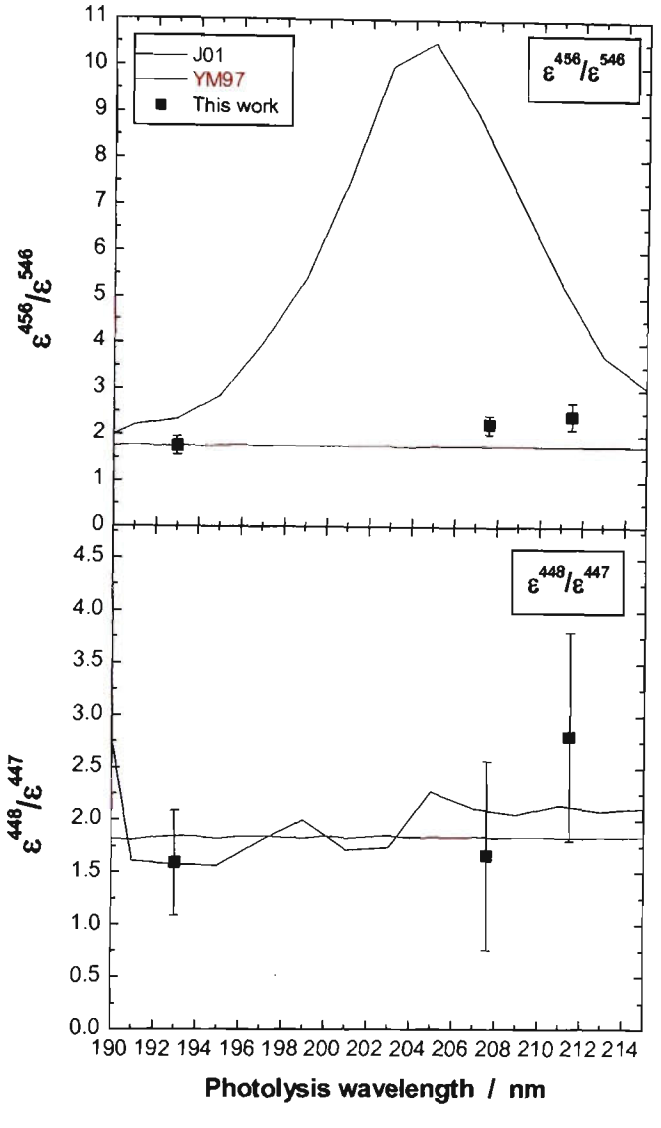

Figure 5.6 **Enrichment factor ratios $\varepsilon^{456}/\varepsilon^{546}$ and $\varepsilon^{448}/\varepsilon^{447}$ for this work and two theories**
J01: [*Johnson et al.*, 2001]
YM97: [*Yung and Miller*, 1997]

In most cases there is good agreement within the error estimates for the experimentally derived $\varepsilon^{15}N$ and $\varepsilon^{456\text{-}546}$ enrichment factors. The error estimates in Figure 5.4 and Figure 5.5 are dominated by random errors. Minor systematic differences may be due to the different calibration methods used in each study. In this work, calibration is based on N_2O line parameters provided by *Toth* [*Toth*, 1991; *Toth*, 1993; *Toth*, 1999; *Toth*, 2000] and the calculation of synthetic spectra, whereas *Zhang et al.* [2000] used

laboratory measurements of the pure isotopomer spectra. In the work of *Röckmann et al.* [2000] calibration is dependent on reactions in the ion source, in particular scrambling of the end and central N atoms in N_2O. Since each study reports enrichments relative to the starting N_2O isotopic composition, most systematic errors should cancel, but non-linearities could lead to small systematic discrepancies. With the exception of the measurements at 193 nm, any such systematic differences appear to be smaller than random errors. At 193 nm, the magnitudes of the enrichment factors of *Röckmann et al.* [2000] are significantly larger than those from the other studies, and the cause of this particular discrepancy is unresolved at present. *Röckmann et al.* [2000] suggested a saturation effect in the photolysis experiments of *Rahn et al.*, [1998] but the exact cause is as yet unidentified. Further measurements and exchange of calibration standards currently underway should resolve this difference.

Experimentally derived enrichment factors ε^{448}, ε^{447} and ε^{456}-ε^{546} are in good agreement to the theory proposed by *Johnson et al.* [2001]. There is still poor agreement in $\varepsilon^{15}N$, and consequently in the $\varepsilon^{456}/\varepsilon^{546}$ ratio between the experimentally derived and *Johnson et al.* [2001] enrichment factors. The uncertainty of the enrichment factors as determined by this theory is approximately 10 ‰, and is due to uncertainties in potential energy and dipole moment surfaces and uncertainties in the ε calculation itself. The agreement between experimentally determined $\varepsilon^{15}N$ and the *Johnson et al.* [2001] theory is not as good as for other enrichment factors. Whilst the absolute magnitude of this enrichment of the N_2O isotopomers is still somewhat in question, it seems that the principle behind the *Johnson et al.* [2001] and *Yung and Miller* [1997] model of isotopic enrichment is valid.

5.4 Conclusions

This work presents the first high resolution FTIR measurements of the positionally dependent enrichment factors for the UV photolysis of N_2O in natural isotopomeric abundance. The high resolution FTIR technique complements IRMS techniques for N_2O isotopic analysis. The positional dependence of the photolysis of N_2O is confirmed, with $^{14}N^{15}N^{16}O$ being photolysed approximately twice as fast as $^{15}N^{14}N^{16}O$. Further, there is a clear wavelength dependence in the enrichment factors, with the difference in the enrichment factors ε^{456}-ε^{546} becoming larger with increasing photolysis wavelength. Where they can be compared, the FTIR measurements are generally in good agreement with other experimental studies. The measured enrichment factors relative to each other and their wavelength dependence are in qualitative agreement with the *Yung and Miller* [1997] theory, but are consistently nearly double those predicted by the theory. Enrichment factors ε^{448}, ε^{447} and ε^{456}-ε^{546} are in very agreement to the theory proposed by *Johnson et al.* [2001]. The isotopic enrichment factors are neatly described by a Rayleigh distillation model, consistent with enrichment by an irreversible sink process.

5.5 References

Brenninkmeijer, C.A.M., and T. Röckmann, Mass spectrometry of the intramolecular nitrogen isotope distribution of environmental nitrous oxide using fragment-ion analysis, *Rapid Communications in Mass Spectrometry, 13* (20), 2028-2033, 1999.

Fritz, P., and J.C. Fontes, Handbook of Environmental Isotope Geochemistry Volume 1, pp. 545, Elsevier, New York, 1980.

Griffith, D.W.T., G.C. Toon, B. Sen, J.F. Blavier, and R.A. Toth, Vertical profiles of nitrous oxide isotopomer fractionation measured in the stratosphere, *Geophysical Research Letters, 27* (16), 2485-2488, 2000.

Johnson, M.S., G. Due-Billing, A. Gruodis, and M.H.M. Janssen, Photolysis of nitrous oxide isotopomers studied by time-dependent Hermite propagation, *Journal of Physical Chemistry, 105* (38), 8672-8680, 2001.

Kim, K.R., and H. Craig, Nitrogen-15 and Oxygen-18 Characteristics of Nitrous Oxide - a Global Perspective, *Science, 262* (5141), 1855-1857, 1993.

Rahn, T., Enrichment of ^{15}N and ^{18}O in stratospheric nitrous oxide: observations, experimental results and implications, PhD thesis, University of California, San Diego, 1998.

Rahn, T., and M. Wahlen, Stable isotope enrichment in stratospheric nitrous oxide, *Science*, *278*, 1776-1778, 1997.

Rahn, T., H. Zhang, M. Wahlen, and G.A. Blake, Stable Isotope fractionation during ultraviolet photolysis of N_2O, *Geophysical Research Letters*, *25* (24), 4489-4492, 1998.

Röckmann, T., C.A.M. Brenninkmeijer, M. Wollenhaupt, J.N. Crowley, and P.J. Crutzen, Measurement of the isotopic fractionation of $^{15}N^{14}N^{16}O$, $^{14}N^{15}N^{16}O$ and $^{14}N^{14}N^{18}O$ in the UV photolysis of nitrous oxide, *Geophysical Research Letters*, *27* (9), 1399-1402, 2000.

Röckmann, T., J. Kaiser, R. Crowley, R. Borchers, W.A. Brand, and P.J. Crutzen, The isotopic enrichment of nitrous oxide ($^{15}N^{14}NO$, $^{14}N^{15}NO$, $^{14}N^{14}N^{18}O$) in the stratosphere and in the laboratory, *Journal of Geophysical Research-Atmospheres*, 10403-10410, 2001.

Toth, R.A., Line-frequency measurements and analysis of N_2O between 900 and 4700 cm^{-1}, *Applied Optics*, *30* (36), 5289-5315, 1991.

Toth, R.A., Line strengths (900-3600 cm^{-1}), self-broadened linewidths, and frequency shifts (1800-2360 cm^{-1}) of N_2O, *Applied Optics*, *32* (36), 7326-7365, 1993.

Toth, R.A., Line positions and strengths of N_2O between 3515 and 7800 cm^{-1}, *Journal of Molecular Spectroscopy*, *197* (2), 158-187, 1999.

Toth, R.A., N_2 and air broadened-linewidths and frequency-shifts of N_2O, *Journal of Quantitative Spectroscopy and Radiative Transfer*, *66*, 285-304, 2000.

Toyoda, S., and N. Yoshida, Determination of Nitrogen Isotopomers of Nitrous Oxide on a Modified Isotope Ratio Mass Spectrometer, *Analytical Chemistry*, *71* (20), 4711-4718, 1999.

Turatti, F., D.W.T. Griffith, S.R. Wilson, M.B. Esler, T. Rahn, H. Zhang, and G.A. Blake, Positionally dependent ^{15}N fractionation factors in the photolysis of N_2O determined by high resolution FTIR spectroscopy, *Geophysical Research Letters*, *27* (16), 2489-2492, 2000.

Yoshida, N., and S. Toyoda, Constraining the atmospheric N_2O budget from intramolecular site preference in N_2O isotopomers, *Nature*, *405* (18 May), 330-334, 2000.

Yung, Y.L., and C.E. Miller, Isotopic fractionation of stratospheric nitrous oxide, *Science*, *278*, 1778-1780, 1997.

Zhang, H., P.O. Wennberg, V.H. Wu, and G.A. Blake, Fractionation of $^{14}N^{15}N^{16}O$ and $^{15}N^{14}N^{16}O$ during photolysis at 213 nm, *Geophysical Research Letters*, *27* (16), 2481-2484, 2000.

Chapter 6 Results II: Isotopomeric characterisation of tropospheric N_2O

6.1 Introduction

Isotopic analysis can be used to narrow uncertainties in global budgets of important gases. Analysis of $^{13}CO_2$ has lead to a better understanding of the global CO_2 budget [for example *Bakwin et al.*, 1998; *Bergamaschi et al.*, 1998]. The global CO_2 emissions are estimated to 6.3 ± 6 % Pg C yr^{-1} (Pg = 10^{15} g), whereas the best estimate for global N_2O emissions are 15.3 ± 52 % Tg N-N_2O [*Prather et al.*, 1995]. The bulk ^{15}N isotopic ratio of N_2O has already been used by others in the past to illustrate the geochemical cycle of N_2O [*Kim and Craig*, 1993; *Yoshida and Matsuo*, 1983] and to better estimate the global N_2O budget [*Bange et al.*, 1996; *Kim and Craig*, 1993; *Naqvi et al.*, 1998; *Perez et al.*, 2001; *Rahn and Wahlen*, 2000]. The first use of the positional isotopomers and the difference $\delta^{14}N^{15}N^{16}O$-$\delta^{15}N^{14}N^{16}O$ to constrain the N_2O budget was by *Yoshida et al.* [2000]. The intramolecular ^{15}N difference can be used as a fifth independent constraint on the N_2O budget, along with the N_2O mixing ratio, mean $\delta^{15}N$, $\delta^{18}O$ and $\delta^{17}O$. The intramolecular ^{15}N difference provides more sensitive and fundamental information than the mean $\delta^{15}N$, as it directly relates to the processes forming the N-N bond. It is hoped that this new constraint will aid in narrowing the uncertainty in the estimates of N_2O source and sink sizes.

This chapter deals with measuring the isotopomeric signature $\delta\ ^{14}N^{15}N^{16}O$ (δ^{456}) and $\delta\ ^{15}N^{14}N^{16}O$ (δ^{546}) from samples of tropospheric N_2O collected over the period of a year from the Wollongong campus of the University of Wollongong, Australia. Nitrous oxide extraction methods, spectroscopic techniques and spectral analysis techniques will be briefly reintroduced. Results will be analysed in terms of potential source processes and a simple box model for N_2O will be described using the collected isotopomeric characterisations

6.2 Experimental

Seventeen samples of nitrous oxide were extracted from whole tropospheric air collected from the Wollongong campus of the University of Wollongong, Australia, over the period of approximately one year. Wollongong (150.9° E, 34.45° S) is situated on a narrow coastal plain between the Pacific Ocean and the Illawarra Escarpment which rises to 450 meters. The University of Wollongong campus is in an urban region and adjacent to the major north-south highway through Wollongong. The campus is approximately 10 km north of Australia's largest integrated steelworks at Port Kembla. Samples of whole air and N_2O were collected from outside a window on the second floor of the Chemistry Department building, approximately 6 m above ground level and approximately 36 m above sea level. The Chemistry Department building is in the centre of the University of Wollongong campus and is surrounded on three sides by buildings of similar or greater height, and on the fourth (southern) side by a number of trees.

Samples of N_2O were extracted from whole air by the procedure described in detail in section 3.5 of this thesis. This extraction procedure is similar to those described by *Huff*

et al. [1997] and *Brenninkmeijer et al.* [1996]. The isotopic composition of the extracted N_2O was determined using the standard FTIR method and analysis procedure detailed in depth in chapters 2, 3 and 4 of this thesis.

An evacuate 2 L glass bulb was used to sample whole air during extraction of the N_2O. The flow rate into the bulb was selected such that the bulbs would be completely filled to atmospheric pressure with whole air in the time taken for the extraction of N_2O for isotopic analysis. For a typical 3 hour collection, the flow into a 2 L bulb was controlled between 10 and 12 mL min^{-1}. The N_2O, CO_2, CO and CH_4 concentrations in the 2 L bulb were determined by low resolution (1 cm^{-1}) FTIR spectroscopy [*Esler et al.*, 2000]. This sample represents the time-averaged composition of the air sampled for N_2O extraction.

6.3 Results and interpretations

6.3.1 Local and large scale weather conditions

Local weather conditions are recorded daily at 0900 and 1500 for the Bureau of Meteorology from the University of Wollongong site. Rainfall, temperature, humidity, atmospheric pressure, wind direction and wind speed are available. These have been collected for each of the atmospheric N_2O sample days and included in Table 6.1. Continental scale surface pressure and gradient wind analysis charts were collected for the days and times of N_2O sample collection. These charts are available from the Bureau of Meteorology web site (http://www.bom.gov.au) free of charge. Weather patterns such as cold fronts pass over Wollongong almost exclusively from the south west and west. Wind directions are variable with a bias against westerlies.

Table 6.1 Local scale weather conditions for each N_2O sample collection

Sample	Date	Rainfall (a) (mm)			Pressure (b) (mb)		Humidity (c) (%)		Temperature (d) (°C)			Wind (e) (m/s)						
		0900	1500	24h to 0900	0900	1500	0900	1500	Max	Min	Avg	0900	Bear. (°)	1500	Bear. (°)	Max speed	Bear. (°)	Time of Max
1	3/04/00	0	0	0	1018	1014	73	52	30.5	17.4	24.0	0.51	292.5	4.12	315	11.84	67.5	4.50
2	17/04/00	0	0	0	1014	1014	58	55	23.8	15.8	19.8	2.06	270	2.57	135	7.72	225	1.55
3	8/06/00	0	0	0	1026	1025	83	50	18.2	4.9	11.6	0		0.51	67.5	11.84	270	23.00
4	9/06/00	18.6	0.2	18.6	1023	1022	55	46	18.2	3.4	10.8	1.03	180	3.09	270	11.32	270	18.40
5	12/06/00	6	0.1	6.4	1034	1033	80	87	14.6	10	12.3	2.06	225	2.57	225	7.2	225	11.10
6	27/06/00	0	0	0	1018	1012	78	54	18.7	7.8	13.3	0		0.51	315	10.81	315	18.30
7	17/07/00	3.9	1.2	3.9	1018	1023	71	81	17.2	10.7	14.0	3.09	225	5.15	202.5	12.87	202.5	12.45
8	7/11/00	0	0	0	1021	1021	74	55	19.1	12.2	15.7	2.06	202.5	5.15	135	10.29	67.5	22.40
9	8/11/00	0	0	0	1022	1019	65	51	21.1	13.2	17.2	0.51	90	5.15	45	10.29	45	14.00
10	8/11/00	4.2	0.4	5.6	1022	1019	65	51	21.1	13.2	17.2	0.51	90	5.15	45	10.29	45	14.00
11	9/11/00	0	0	0	1019	1018	59	60	21.5	13.4	17.5	5.15	22.5	7.2	22.5	12.87	22.5	14.45
12	31/01/01	0	0	0	1019	1019	92	74	21.2	17.6	19.4	1.54	180	4.12	157.5	10.81	157.5	4.05
13	1/02/01	13.6	0.4	26	1020	1021	92	79	23.7	17.8	20.8	0		5.15	112.5	9.78	112.5	11.30
14	9/02/01	0	0	0	1015	1012	71	82	26.6	19	22.8	1.03	90	3.6	337.5	9.26	337.5	16.25
15	12/02/01	16	8.4	16.4	1012	1011	66	67	29.1	20.5	24.8	4.12	67.5	2.06	45	9.26	67.5	8.50
16	15/02/01	5.8	0.2	5.8	1019	1019	86	62	20.5	18.5	19.5	3.6	180	5.15	135	10.29	135	14.50
17	21/02/01	0	0	0	1016	1014	82	76	26.6	19.2	22.9	0		3.09	45	6.18	45	17.20

(a), (b), (c) Rainfall, pressure and humidity are recorded for the hours 0900 and 1500. Rainfall (a) is also quoted for the preceding 24 hours to 0900

(d) Maximum, minimum and average temperature are recorded

(e) Wind speed (m/s) and bearing in degrees (North = 0°) are recoded for hours 0900 and 1500. The maximum wind speed is recorded together with its bearing and time

6.3.2 *The N_2O, CO_2, CH_4 and CO mixing ratios*

Table 6.2 shows the mixing ratios of N_2O, CO_2, CH_4 and CO for the time-averaged integrated air samples collected concurrently with the N_2O for isotopic determination. Small calibration scale differences could be present in the different methods used to determine mixing ratios between the University of Wollongong and GASLAB (Table 6.4). Samples 7 and 12 do not have time-averaged integrated samples. Sample numbers 1 and 2 have extremely low concentrations of both N_2O and CO_2, most likely due to insufficient evacuation of the sample flask prior to use or contamination of the low resolution spectrometer measurement cell by nitrogen. The results are not reliable and therefore not quoted. Sample 14 results were removed due to an error in the N_2O sample extraction procedure resulting in a very low N_2O collection efficiency of approximately 60 %.

Table 6.2 Mixing ratios of N_2O, CO_2, CH_4 and CO for collected tropospheric air samples

Sample No.	Date	N_2O (ppb)	CO_2(ppm)	CO (ppb)	CH_4 (ppb)
1	3/04/00				
2	17/04/00				
3	8/06/00	313.25	390.88	416.85	1942
4	9/06/00	313.63	386.24	91.39	1775.4
5	12/06/00	318.72	387.3	98.724	1698.1
6	27/06/00	320	707.21	267.03	1983
7	17/07/00				
8	7/11/00	377.12	3170.7	813.7	1865.3
9	8/11/00	325.56	516.12	233.54	1925.4
10	8/11/00	321.95	492.68	170.42	1861.2
11	9/11/00	321.44	478.19	264.44	2043.7
12	31/01/01				
13	1/02/01	312.72	577.85	173	2027.7
14	9/02/01	312.13			
15	12/02/01	313.38			
16	15/02/01	313.59	539.25	508.15	2049.6
17	21/02/01	317.29	418.5	378.6	1919

Sample 8 shows an extremely elevated mixing ratios of N_2O, approximately 377 ppb. This sample also contained approximately 3200ppm CO_2, and approximately 810 ppb CO. At the time of the collection of sample 8, the chemistry department building was undergoing extensive renovation and a large number of trucks were routinely parked directly underneath the sample intake, so it is most likely that this sample is contaminated from local vehicle emissions. There is nothing out of the ordinary about the prevailing weather conditions at the time sample 8 was collected. Experimental error cannot be excluded as a cause for the highly elevated mixing ratios. Removing the influence of sample 8 gives an average N_2O concentration of 317 ± 4 ppb N_2O. This is slightly above the accepted value for clean background air of 314 ppb N_2O [*Albritton et al.*, 2001]. One possibility for the elevated N_2O could be emissions from nearby sources such as sewage treatment plants south of the University of Wollongong campus. The majority of samples have elevated CO mixing ratios, generally much greater than 100 ppb. This is consistent given the urban location of the University of Wollongong campus and its proximity to major road ways.

6.3.3 The mean $\delta^{15}N$ relative to atmospheric N_2

Table 6.3 shows the measured isotopomer determinations for the tropospheric N_2O samples. Samples 1, 3, 6 and 12 were contaminated with hydrocarbons absorbing strongly with broad absorption features in the 2850 to 3070 region. This makes the isotopomer results in these samples unreliable due to inaccuracies in measuring the total pressure of N_2O in the high resolution FTIR sample (Chapter 4). Excluding these samples the average bulk $\delta^{15}N$ relative to atmospheric N_2 is 7.7 ± 2.8 ‰. The $\delta^{15}N$ of N_2O from clean background air has been measured to be 7.0 ± 0.6 ‰ relative to

atmospheric N_2 [*Kim and Craig*, 1993; *Yoshida and Toyoda*, 2000]. There are insufficient data to see any annual variation in $\delta^{15}N$ as a seasonally complete sample set is not available. Samples 2, 7 and 9 are depleted in $\delta^{15}N$ relative to clean atmospheric N_2O and potentially reflect biogenic sources such as grassed sporting fields, sewage treatment plants and biological treatment of landfill run-off. Sample 8 is also depleted in $\delta^{15}N$ but could be contaminated from local vehicle emissions. Biogenic sources are known to be depleted in $\delta^{15}N$ as in most conditions microbial activity favours the lighter isotopomers [*Delwiche*, 1981; *Moore*, 1974; *Urey*, 1946].

Table 6.3 Isotopomer results[(a)] for tropospheric N_2O samples collected from Wollongong, Australia

Sample No.	Date	N_2O (ppb)	δ^{456}	δ^{546}	δ^{456}-δ^{546}	$\delta^{15}N$ [(b)]	$\delta^{18}O$ [(c)]	δ^{447}
1 [(d)]	3/04/00		14.1	-5.4	19.5	2.5	15.2	7.4
2	17/04/00		17.2	-2.3	19.4	5.7	48.0	58.8
3 [(d)]	8/06/00	313.25	15.6	-7.4	23.0	2.3	28.6	56.1
4	9/06/00	313.63	29.0	-0.49	29.5	12.5	16.8	-1.2
5	12/06/00	318.72	16.4	4.0	12.4	8.4	19.8	13.0
6 [(d)]	27/06/00	320	28.7	8.1	20.6	16.6	21.4	-2.4
7	17/07/00		18.15	-3.2	21.3	5.6	30.3	-12.7
8	7/11/00	377.12	15.7	-3.7	19.4	4.2	27.1	1.2
9	8/11/00	325.56	13.6	-3.5	17.1	3.2	14.5	-2.6
10	8/11/00	321.95	17.4	0.40	17.0	7.1	19.2	10.8
11	9/11/00	321.44	17.3	2.5	14.7	8.1	28.7	10.4
12 [(d)]	31/01/01		26.3	11.2	15.0	16.9	28.7	22.0
13	1/02/01	312.72	23.3	4.8	18.5	12.2	9.0	13.3
14	9/02/01	312.13						
15	12/02/01	313.38	21.3	1.1	20.1	9.4	17.2	3.4
16	15/02/01	313.59	24.2	-4.6	28.8	8.0	13.4	11.0
17	21/02/01	317.29	18.2	2.3	15.9	8.4	18.4	-5.9
Avg [(e)]		317.0	19.3	-0.2	19.5	7.7	21.9	8.3
Std dev ($\pm 1\sigma$) [(e)]		4.5	4.3	3.2	5.1	2.8	10.4	17.9

(a) Isotopomer determinations are quoted relative to BOC Gases N_2O working standard (in ‰) unless otherwise specified.

(b) Relative to atmospheric N_2, ‰

(c) Relative to atmospheric O_2, ‰

(d) Contaminated with hydrocarbons in the 2850–3070 cm^{-1} region and are likely to be unreliable.

(e) δ average and standard deviation exclude the samples described in (d). N_2O concentration average excludes sample 8 only.

Samples 4, 5, 11, 13, 15, 16 and 17 are enriched in $\delta^{15}N$ compared to tropospheric background N_2O and potentially reflect the influence of non biogenic source processes. The University of Wollongong campus is adjacent to a major freeway, and N_2O from internal combustion engines might be present in these samples. Interestingly, samples 4 and 13 samples correlate with the highest rainfall in the 24 hours to 0900 of the sampling day. Due to the complex wind patterns between buildings of the University of Wollongong campus, it is not generally possible to isolate the specific local source locations. Figure 6.1 shows $\delta^{15}N$ of the collected N_2O (relative to atmospheric N_2) as a function of N_2O mixing ratio.

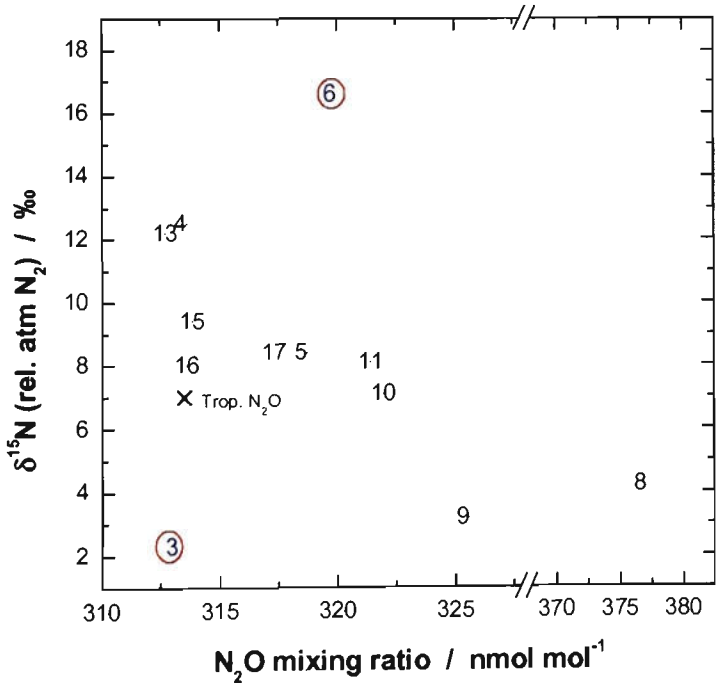

Figure 6.1 **$\delta^{15}N$ as a function of N_2O mixing ratio for the collected tropospheric N_2O samples**

Labels are the N_2O sample number. Sample 3 and 6 are contaminated with hydrocarbons and very likely to be incorrect. The green cross marks clean tropospheric N_2O $\delta^{15}N$ relative to atmospheric N_2.

Removing the contaminated samples 3 and 6 from Figure 6.1 (circled in red), a reasonable inverse correlation is evident between $\delta^{15}N$ and N_2O mixing ratio. This relationship can be used to estimate the $\delta^{15}N$ signature of the "average" N_2O source. A large reservoir of N_2O such as exists in the well mixed troposphere, can be assumed to have N_2O concentration c and isotopic signature δ. The injection of a source of N_2O into this reservoir with isotopic signature δ_{source} and with a pure N_2O concentration of c_{source} can be schematically described by the following figure:

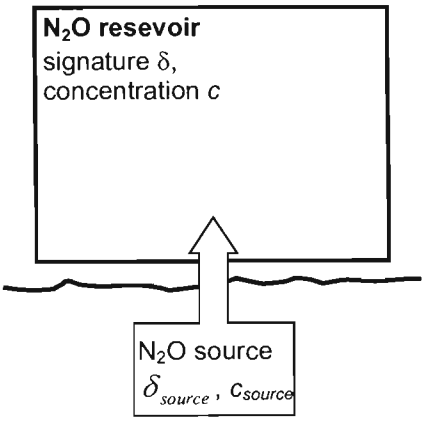

Figure 6.2 Perturbation of an N_2O reservoir of constant concentration and δ by an N_2O source (schematic)

The measured isotopic signature from an N_2O sample taken from the reservoir after the injection of some source N_2O is therefore given by the concentration weighted average

$$\delta' = \frac{\delta \cdot c}{c + c_{source}} + \frac{\delta_{source} \cdot c_{source}}{c + c_{source}} \qquad (7.1)$$

where c and c_{source} are the N_2O concentrations of the reservoir and source respectively, δ and δ_{source} are the isotopic signatures of the reservoir and pure source respectively, and

δ' is the measured isotopic signature. The term $\delta.c$ is assumed to be constant. If the source emissions are allowed to increase until c_{source} is much larger than c, then the measured isotopic signature (δ') can be expressed as

$$\delta' = \frac{m}{c + c_{source}} + \delta_{source} \tag{7.2}$$

where m is the constant term $\delta.c$. A plot of the measured δ' as a function of the inverse measured concentration, $1/(c + c_{source})$, will result in a y intercept that is the predicted pure source N_2O isotopic signature.

This is the derivation of the Keeling equation [*Keeling*, 1958]. In the majority of cases where the Keeling plot has been applied the concentration of the gas of interest has been measured close to a known strong source, for example by *Esler et al.* [2000]. Using towers close to a known strong source allows a wide range of concentrations to be measured, making the extrapolation to the y-intercept statistically robust. Use of the Keeling plot in this work is limited by a narrow range of N_2O mixing ratios. In this work, the y-intercept of the Keeling plot represents the isotopic signature of the "average" N_2O source process. Figure 6.3 shows the Keeling plot for $\delta^{15}N$ for the collected tropospheric samples, excluding the hydrocarbon contaminated samples and sample 8, which was potentially heavily contaminated from local vehicle emissions (Section 6.3.2).

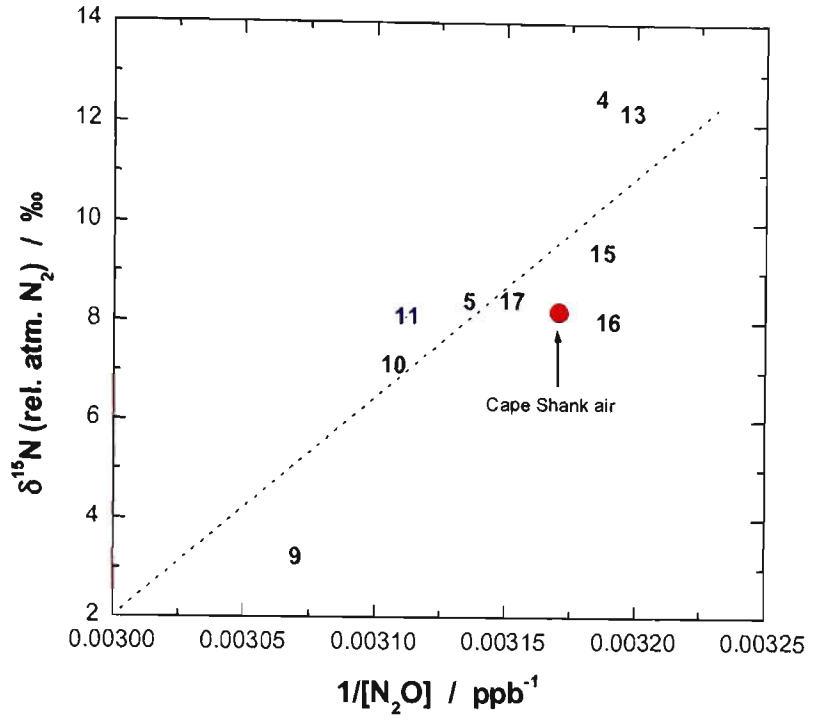

Figure 6.3 **Keeling plot for $\delta^{15}N$ for collected tropospheric N_2O samples**
Labels are the N_2O sample number. Analysis of Cape Shank air is described in Table 6.4.

The y-intercept of the Keeling plot for $\delta^{15}N$ of Figure 6.3 is -153 ± 39 ‰ ($r^2 = 0.71$). If sample 9 is excluded the intercept is –108 ± 49 ‰. The very large error is due to extrapolating the y-intercept using a very narrow N_2O concentration range, and to an extent the error is also due to the noise in these data. If the assumptions in the Keeling plot hold, then the $\delta^{15}N$ signature of the pure N_2O pseudo-source is extremely isotopically light with respect to atmospheric N_2. The typical conditions that lead to isotopically light N_2O sources are emissions from biogenic sources, especially from soils. Nitrous oxide emissions from soils have been measured by other studies to range between –50 ‰ [*Perez et al.*, 2000] and 20 ‰ (this work, chapter 6). Therefore the Keeling plot y-intercept is not, at face value, a realistic $\delta^{15}N$ estimate.

Samples 4 and 13 are unusual. If the lowest N_2O mixing ratio is taken to be representative of clean background air, then the measured $\delta^{15}N$ for these samples should be closer to 7 ‰ than they are. There is no obvious contamination in the spectra of these two samples. One possible explanation is that the University of Wollongong site is never exposed to clean background air, further supported by the generally high CO, CO_2 and CH_4 mixing ratios in the integrated air samples (Table 6.2). *Yoshida and Toyoda* [2000] performed a similar N_2O sampling experiment, and they show an unusual point with $\delta^{15}N$ of 21 ‰. They make no explanation for the possible source of this sample.

A source of clean background tropospheric air, collected by CSIRO Atmospheric Research from Cape Shank, Victoria was analysed with the procedures described in this thesis for N_2O isotopomers. Results are described in Table 6.4.

Table 6.4 Analysis of clean background air from Cape Shank, Victoria

Cylinder number	CA 04535
CO_2 [(a)]	367.27 ppm
N_2O [(a)]	315.4 ppb
CH_4 [(a)]	1693.9 ppb
CO [(a)]	47.7 ppb
δ^{456} [(b)]	21.2 ‰
δ^{546} [(b)]	-1.2 ‰
δ^{456}-δ^{546} [(b)]	22.4 ‰
$\delta^{15}N$ [(c)]	8.2 ‰
δ^{448} [(d)]	19.4 ‰
δ^{447} [(b)]	-16.5 ‰

(a) Measured by GASLAB, CSIRO Atmospheric Research
(b) Relative to BOC Gases N_2O
(c) Relative to atmospheric N_2
(d) Relative to atmospheric O_2

The N_2O isotopomer results for Cape Shank air collected under known background conditions are very close to the $\delta^{15}N$ and $\delta^{18}O$ measured from background air by both *Kim and Craig* [1993] and *Yoshida and Toyoda* [2000]. Both these works measured $\delta^{15}N$ of tropospheric N_2O of 7.0 ‰ and $\delta^{18}O$ of 20.7 ‰ relative to atmospheric N_2 and O_2, respectively. It therefore seems likely that the University of Wollongong site is never exposed to clean background air.

The estimated $\delta^{15}N$ of the "average" N_2O source, according to the Keeling plot in Figure 6.3 is between -153 and –108 ‰ relative to atmospheric N_2. Sources of N_2O this depleted are very unlikely to exist. *Naylor* [2001] also collected tropospheric N_2O from the University of Wollongong site and determined its isotopomeric composition with the FTIR technique described in Chapters 2, 3 and 4. His $\delta^{15}N$ results show a high anticorrelation with N_2O mixing ratio similar to these results. Similarly, his estimate of the pure $\delta^{15}N_{source}$ is equally large. Therefore the assumptions of the Keeling model described above do not correctly describe the situation around the University of Wollongong site. One possible explanation for these results is the presence of an unknown local process involving N_2O, such as a localised N_2O soil sink.

6.3.4 Individual ^{15}N isotopomers and the intramolecular ^{15}N difference, δ^{456}-δ^{546}

Figure 6.4 shows δ^{456}, δ^{546} and δ^{456}-δ^{546} for the tropospheric N_2O samples as a function of N_2O mixing ratio.

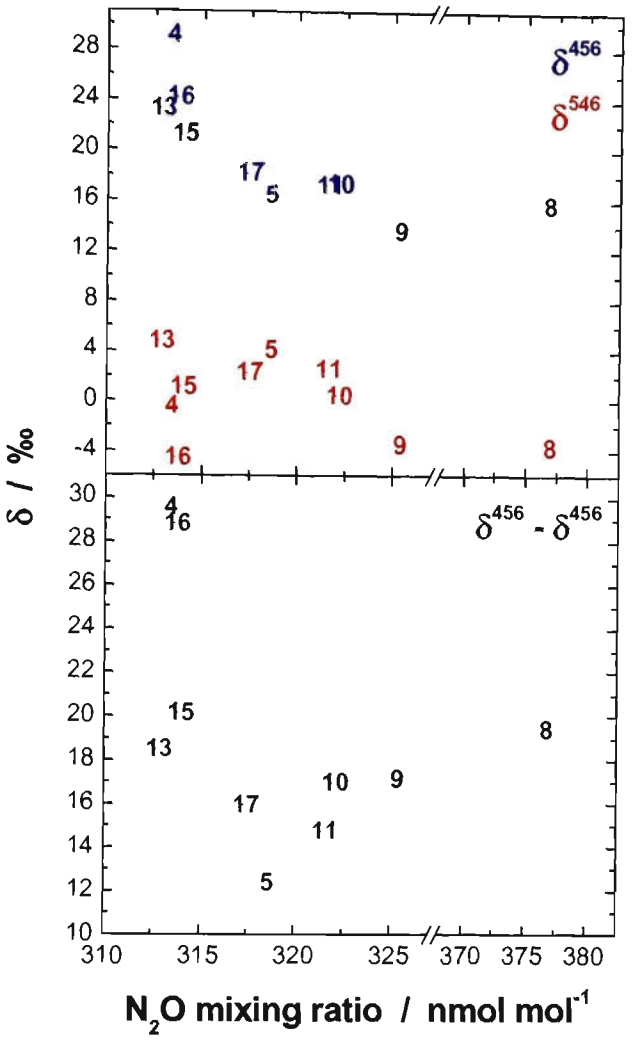

Figure 6.4 **δ^{456}, δ^{546} and δ^{456}-δ^{546} as a function of N_2O mixing ratio**
Number labels are the N_2O sample numbers. Contaminated samples 1, 3, 6 and 12 are not displayed. δ measured relative to BOC Gases N_2O working standard.

The δ^{456} ranges approximately from 29 to 14 ‰ and δ^{546} from approximately 4.8 to -4.6 ‰. According to *Yohsida and Toyoda* [2000], δ^{456} is expected to vary more than δ^{546} during nitrification and denitrification processes in soils. Chapter 7 of this thesis, and samples from recent studies [*Menegazzo*, 2000; *Perez et al.*, 2001] measured at the University of Wollongong using the FTIR technique described in this thesis, confirm that δ^{456} varies more than δ^{546} for soil N_2O samples.

Samples 4 and 16 have δ^{456}-δ^{546} of 29.5 ‰ and 28.8 ‰, respectively, and are significantly different from the other samples. The $\delta^{15}N$ relative to atmospheric N_2 for sample 4 and 16 is 12.5 ‰ and 8 ‰, respectively. The δ^{456} for sample 4 and 16 is the highest and second highest for any of the N_2O samples collected. Both these samples were collected in the first few hours after a cold front passed over Wollongong. There is increased downward atmospheric transport after a cold front has passed [*Wayne*, 2000]. Samples 4 and 16 could therefore reflect the N_2O high δ^{456}-δ^{546} which has been measured in the stratosphere [*Griffith et al.*, 2000; *Yoshida and Toyoda*, 2000]. No other samples of N_2O were collected under similar atmospheric conditions. Another possible explanation for samples 4 and 16 could be from the direction the cold front was travelling. The cold front was passing from the south-west to the north-east and would have contained parcels of air from the forests surrounding the Wollongong region. According to *Yoshida and Toyoda* [2000], and N_2O emitted from soils is expected to have high δ^{456}-δ^{546} and low δ^{546}. This is evident in sample 16 which has the lowest δ^{546} (-4.6 ‰) of all the samples collected, but not so clear in the case of sample 4, which has a δ^{546} of –0.5 ‰ which is roughly the median of all δ^{546} determinations.

The *Yoshida and Toyoda* [2000] study is the only other current work to have analysed samples of tropospheric N_2O for δ^{456}-δ^{546}, using a modified isotope ratio mass spectrometer (IRMS). Their determination of the individual isotopomers δ^{456} and δ^{546} was made relative to an internal N_2O standard from the thermal decomposition of ammonium nitrate (NH_4NO_3), as described in chapter 3.4. The relationship between *Yoshida and Toyoda's* [2000] N_2O standard and the BOC Gases N_2O standard used in

this thesis is not known, therefore directly comparing δ^{456} and δ^{546} between this work and *Yohsida and Toyoda's* [2000] is not strictly correct.

However, there are certain assumptions that can be made in order to compare the *Yoshida and Toyoda* [2000] results to this work. As described in chapter 3.4, BOC Gases N_2O, SNOW (Standard Nitrous Oxide Working gas), MPI (Max Planck Institute) N_2O all have $\delta^{15}N$ within ± 3 ‰ of each other, and all have been made from the industrial scale thermal decomposition of ammonium nitrate. The *Yohsida and Toyoda* [2000] N_2O standard is also made from the thermal decomposition of ammonium nitrate. There is no mention by *Yoshida and Toyoda* that NH_4NO_3 enriched or depleted in ^{15}N was used. Therefore to a first approximation, it can be assumed that the *Yohsida and Toyoda* [2000] absolute N_2O standard and the BOC Gases N_2O working gas used in this work have similar $\delta^{15}N$. If these reasonable assumptions are made a comparison can be made between results from this chapter and those of *Yoshida and Toyoda* [2000]. Figure 6.5 shows δ^{456}-δ^{546} as a function of $\delta^{15}N$ and δ^{546} for this work and that of *Yoshida and Toyoda* [2000].

There is a reasonable match between the *Yoshida and Toyoda* [2000] results and those of this work. If the *Yoshida and Toyoda* [2000] spurious point is excluded, there is more scatter in $\delta^{15}N$ in results of this work than those of *Yoshida and Toyoda* [2000] which likely reflects either the better precision achievable with the IRMS technique, or the diversity of N_2O sources in the Wollongong region. In both studies there is greater variation in the δ^{456}-δ^{546} than in the mean $\delta^{15}N$, showing that the positional isotopomer difference is a more sensitive discriminator of source processes than the mean $\delta^{15}N$ on its own. According to *Yoshida and Toyoda* [2000], N_2O from fossil fuel combustion is

expected to have a small δ^{456}-δ^{546} and enriched δ^{546}. Figure 6.5 (right panel) is a copy of the graph published by *Yoshida and Toyoda* [2000] and is included for a direct comparison.

6.3.5 The oxygen isotopomers, $^{14}N^{14}N^{18}O$ and $^{14}N^{14}N^{17}O$

The δ^{448} for the tropospheric N_2O samples varies from 9.0 to 48.0 ‰ relative to atmospheric O_2, and δ^{447} varies from −12.7 to 58.8 ‰ relative to BOC Gases N_2O working standard. The δ^{448} of N_2O from clean background air is 20.7 ‰ relative to atmospheric O_2 [*Kim and Craig*, 1993; *Yoshida and Toyoda*, 2000]. There is no correlation between the oxygen isotopomers and N_2O mixing ratio. The oxygen isotopomers results are very scattered and there is no discernable correlation between δ^{448} and δ^{447}. Oxygen isotopomers of N_2O measured from a pig-effluent fertilized field site (Chapter 7) show a relationship between δ^{448} and δ^{447} with a slope equal to 1. No similar pattern is seen in these results. Results for δ^{448} and δ^{447} are difficult to interpret, due in part to the lower precision to which they can be measured with this technique. Generally δ^{447} is expected to decrease as δ^{448} decreases, however these data are too scattered to see any discernable pattern.

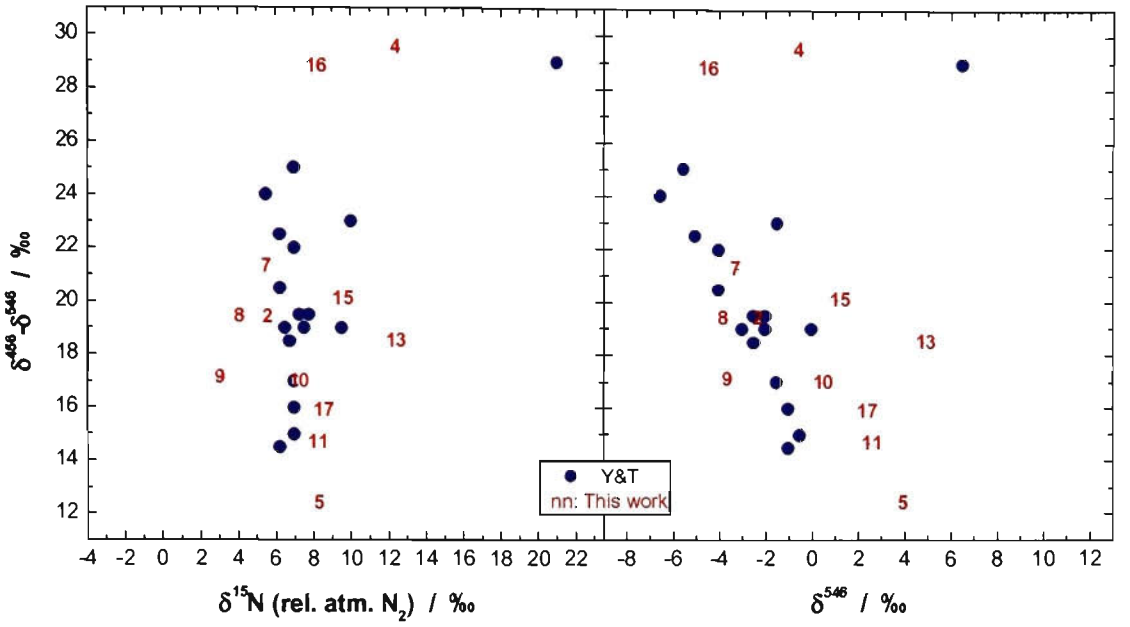

Figure 6.5 δ^{456}-δ^{546} **as a function of** $\delta^{15}N$ **(left) and** δ^{546} **(right) for this work and *Yoshida and Toyoda* [2000]**
Number labels are the N_2O sample numbers

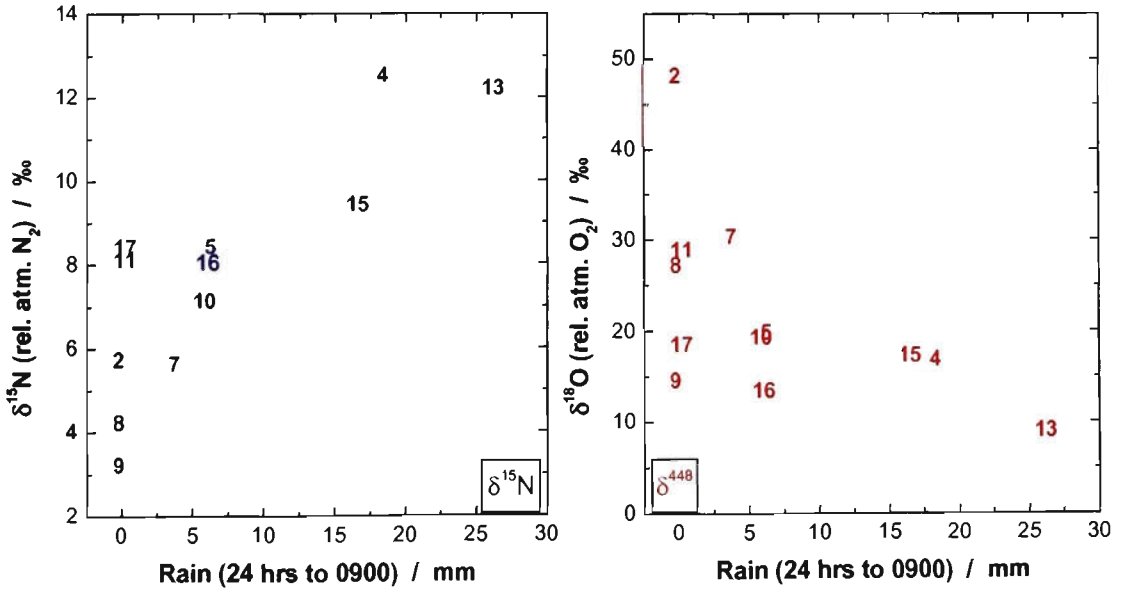

Figure 6.6 $\delta^{15}N$ **(right) and** δ^{448} **(left) as a function of rain fall, 24 hours to 0900.**
Number labels are the N_2O sample numbers

6.3.6 Isotopomer correlation with local scale weather conditions

There is no correlation between wind bearing and isotopic signature. The wind bearing and speed data collected at 0900 and 1500 are single readings and do not contain any information about wind history. The wind field in the vicinity of the sampling point is extremely complex due to the presence of other buildings, trees and obstructions. For local scale wind velocity and speed measurements to be meaningful, the sample intake, wind vane and anemometer all need to be approximately ten meters above any obstruction within 100 m of the sampling point [*Denmead and Raupach*, 1993]. This is not possible at a site as complex as the University of Wollongong campus. There is no relationship between isotopomer measurements and wind speed

During periods of high atmospheric pressure, the $\delta^{15}N$ of tropospheric N_2O might be enriched higher than normal due to the downward mixing of isotopically enriched N_2O from the stratosphere mixing with tropospheric air, but no relationship between $\delta^{15}N$ and atmospheric pressure was observed.

Figure 6.6 shows $\delta^{15}N$ and δ^{448}, relative to atmospheric N_2 and O_2 respectively, as a function of rainfall in the 24 hours to 0900 on the day the samples were collected. There is expected variation in δ^{448} and $\delta^{15}N$ when there has been no rainfall. As rainfall increases $\delta^{15}N$ apparently increases and δ^{448} apparently decreases, but this is difficult to be certain of given the scatter in Figure 6.6b. There is no correlation between δ^{448} and N_2O mixing ratio, which is an independent measurement to rainfall. These results could suggest that a process initiated by rainfall is a contributor to the measured $\delta^{15}N$ and δ^{448} isotopic signature. One possibility is that rainfall acts as a "trigger" for nitrification in dry soils by increasing the moisture in the soil.

6.4 Summary and conclusions

Seventeen samples of nitrous oxide were extracted from whole tropospheric air collected from the grounds of the University of Wollongong, Australia over the period of approximately one year and the isotopomeric signatures were determined by high resolution FTIR spectroscopy. The average bulk $\delta^{15}N$ relative to atmospheric N_2 was measured at 7.7 ± 2.8 ‰, comparable to the measured $\delta^{15}N$ of background tropospheric N_2O of 7.0 ± 0.6 ‰ [*Kim and Craig*, 1993; *Yoshida and Toyoda*, 2000]. Insufficient data were available to see a seasonal variation in $\delta^{15}N$.

There is an inverse correlation between N_2O mixing ratio and $\delta^{15}N$. The intramolecular difference δ^{456}-δ^{546} ranges approximately from 29.5 ‰ to 12.4 ‰. The only other study to our knowledge to have measured tropospheric N_2O positional isotopomers is that of *Yoshida and Toyoda* [2000]. If certain reasonable assumptions are made about the working standard used by *Yoshida and Toyoda* [2000], comparisons between their results and this work can be made. Results of this work in $\delta^{15}N$, δ^{546} and δ^{456}-δ^{546} are broadly comparable to those of *Yoshida and Toyoda* [2000] who similarly sampled tropospheric N_2O from an urban location.

The estimated $\delta^{15}N$ signature of the "average" N_2O source process based on the Keeling plot is between -153 and –108 ‰ relative to atmospheric N_2, which clearly does not describe the real case. Therefore the assumptions inherent in the Keeling model seem to break down when applied to data obtained in this work from the University of Wollongong campus site. Isotopic analysis of N_2O from a cylinder of Cape Shank air, collected under clean background conditions, suggests that the University of Wollongong is not exposed to clean background air conditions.

There is evidence of $\delta^{15}N$ increasing with increasing rainfall, and a corresponding decrease in δ^{448} as rainfall increases. This suggests that rainfall is acts to initiate a process, dependent on moisture, which generates N_2O with different isotopomer characteristics than is seen in dry conditions. One possibility is the initiation of nitrification in dry soils.

6.5 References

Albritton, D.L., L.G. Meira Filho, U. Cubasch, X. Dai, Y. Ding, D.J. Griggs, B. Hewitson, J.T. Houghton, I. Isaksen, T. Karl, M. McFarland, V.P. Meleshko, J.F.B. Mitchell, M. Noguer, B.S. Nyenzi, M. Oppenheimer, J.E. Penner, S. Pollonais, T. Stocker, and K.E. Trenberth, Technical Summary of the Working Group 1 Report, pp. 21-83, Intergovernmental Panel on Climate Change Third Assessment Report, 2001.

Bakwin, P.S., P.P. Tans, J.W.C. White, and R.J. Andres, Determination of the isotopic ($^{13}C/^{12}C$) discrimination by terrestrial biology from a global network of observations, *Global Biogeochemical Cycles*, *12* (3), 555-562, 1998.

Bange, H.W., S. Rapsomanikis, and M.O. Andreae, Nitrous Oxide Emissions From the Arabian Sea, *Geophysical Research Letters*, *23* (22), 3175-3178, 1996.

Bergamaschi, P., C.A.M. Brenninkmeijer, M. Hahn, T. Röckmann, D.H. Scharffe, P.J. Crutzen, N.F. Elansky, I.B. Belikov, N.B.A. Trivett, and D.E.J. Worthy, Isotope analysis based source identification for atmospheric CH_4 and CO sampled across Russia using the trans-Siberian railroad, *Journal of Geophysical Research*, *103* (D7), 8227-8236, 1998.

Brenninkmeijer, C., and T. Röckmann, Russian doll type cryogenic traps: improved design and isotope separation effects, *Analytical Chemistry*, *68*, 3050-3053, 1996.

Delwiche, C.C., Denitrification, Nitrification and Atmospheric Nitrous Oxide, John Wiley and Sons, 1981.

Denmead, O.T., and M.R. Raupach, Methods for measuring atmospheric gas transport in agricultural and forest systems, in *Agricultural ecosystems effects on trace gases and global climate change*, edited by J.M. Duxburg, L.A. Harper, A.R. Mosier, and D.E. Rolston, pp. 19-43, American Society of Agronomy, Crop Science Society of America, Soil Science Society of America, 1993.

Esler, M.B., D.W.T. Griffith, F. Turatti, S.R. Wilson, and T. Rahn, N_2O concentration and flux measurements and complete isotope analysis using FTIR spectroscopy, *Chemosphere: Global Change Science*, *2*, 445-454, 2000.

Griffith, D.W.T., G.C. Toon, B. Sen, J.F. Blavier, and R.A. Toth, Vertical profiles of nitrous oxide isotopomer fractionation measured in the stratosphere, *Geophysical Research Letters*, *27* (16), 2485-2488, 2000.

Huff, A.K., S.S. Cliff, and M.H. Thiemens, Portable Cryogenic Collection of Atmospheric Nitrous Oxide and Carbon Monoxide For High-Precision Isotopic Analysis, *Analytical Chemistry*, *69* (20), 4267-4270, 1997.

Keeling, C.D., The concentration and isotopic abundances of atmospheric carbon dioxide in rural areas, *Geochimica et Cosmochimica Acta*, *13*, 322-334, 1958.

Kim, K.R., and H. Craig, Nitrogen-15 and Oxygen-18 Characteristics of Nitrous Oxide - a Global Perspective, *Science*, *262* (5141), 1855-1857, 1993.

Menegazzo, J., Isotopic signature of nitrous oxide emitted from agricultural soils, Honours thesis, University of Wollongong, Wollongong, 2000.

Moore, H., Isotopic measurement of atmospheric nitrogen compounds, *Tellus*, *XXVI*, 169-174, 1974.

Naqvi, S.W.A., T. Yoshinari, D.A. Jayakumar, M.A. Altabet, P.V. Narvekar, A.H. Devol, J.A. Brandes, and L.A. Codispoti, Budgetary and biogeochemical implications of N_2O isotope signatures in the Arabian Sea, *Nature*, *394*, 462-464, 1998.

Naylor, T., Nitrous Oxide Isotopomers from Two Urban Sources Measured using High Resolution FTIR Spectroscopy, Honours thesis, University of Wollongong, Wollongong, 2001.

Perez, T., S.E. Trumbore, S.C. Tyler, E.A. Davidson, M. Keller, and P.B. de Camargo, Isotopic variability of N_2O emissions from tropical forest soils, *Global Biogeochemical Cycles*, *14* (2), 525-535, 2000.

Perez, T., S.E. Trumbore, S.C. Tyler, P.A. Matson, I. Ortiz-Monasterio, T. Rahn, and D.W.T. Griffith, Identifying the agricultural imprint on the global N_2O budget using stable isotopes, *Journal of Geophysical Research-Atmospheres*, *106* (D9), 9869-9878, 2001.

Prather, M., R. Derwent, D. Ehhalt, P. Fraser, E. Sanhueza, and X. Zhou, Other trace gases and atmospheric chemistry, in *Climate Change 1994: Radiative Forcing of Climate Change and An Evaluation of the IPCC IS92 Emission Scenarios (IPCC 94)*, edited by J.T. Houghton, L.G.M. Filho, J. Bruce, H. Lee, B.A. Callender, E. Haites, N. Harris, and K. Maskell, pp. 73-126, Cambridge University Press, Cambridge, 1995.

Rahn, T., and M. Wahlen, A reassessment of the global isotopic budget of atmospheric nitrous oxide, *Global Biogeochemical Cycles*, *14* (2), 537-543, 2000.

Urey, H.C., The thermodynamic properties of isotopic substances, *Journal of the Chemical Society*, 562-581, 1946.

Wayne, R.P., *Chemistry of Atmospheres*, Oxford University Press, 2000.

Yoshida, N., and S. Matsuo, Nitrogen isotope ratio of atmospheric N_2O as a key to the global cycle of N2O, *Geochemical Journal*, *17*, 231-239, 1983.

Yoshida, N., and S. Toyoda, Constraining the atmospheric N_2O budget from intramolecular site preference in N2O isotopomers, *Nature*, *405* (18 May), 330-334, 2000.

Chapter 7 Results III: Isotopic characterisation of N_2O from pig effluent fertilised crop soils

7.1 The role of soils in global N_2O emissions

As outlined in Chapter 1, emissions from both natural and cultivated soils are accepted to be the largest source of N_2O. According to the best available estimates, the identified global sources of N_2O are in the range of 10–17 Tg N-N_2O yr^{-1} [*Bouwman et al.*, 1995]. The contribution of this from anthropogenic and natural soil emissions is 5.1–15 Tg N-N_2O yr^{-1}, therefore between 50 and 88 % of the total N_2O emissions into the atmosphere are attributed to soil emissions. Approximately 1.8–5.3 Tg N-N_2O yr^{-1} is attributed to cultivated soils [*Bouwman et al.*, 1995] and is expected to increase as more land is put to agriculture and the amount of nitrogen based fertilizers increase.

The aim of this experiment was to characterise the intramolecular isotopic composition of N_2O fluxes from a crop field irrigated by treated pig effluent, and to characterise the isotopic signature during soil processing of the effluent. This experiment was conducted as part of a much larger Commonwealth Scientific and Industrial Research Organization (CSIRO) Land and Water division experiment studying nitrogen cycling in this particular soil, crop and irrigation system.

7.2 Experimental

7.2.1 Site and experiment description

The experiment took place on a 113 hectare circular plot of land in Corowa (146.38° E, 35.98° S) in south-western NSW, Australia. Figure 7.1 shows the location of Corowa in relation to the south-eastern Australian states. The plot is sown with cereals during the winter (May-Nov) and maize during the summer (Dec-April) with both crops harvested for silage. Both the summer and winter crops are irrigated with treated effluent from a nearby piggery via a rotating boom, 600 m long, pivoting from the centre of the field and extending to the perimeter of the field. The boom rotates at 5 degrees per hour, spray-irrigating the whole field over the course of three days with approximately 18 mm (i.e. 18 L m^{-2}) of treated effluent. Approximately 25% of the site was low lying and often waterlogged; the remainder of the crop field had quite good drainage [*Val Snow, CSIRO* personal communication]. The maize had a height of between 1.5–2 m in the well drained part of the field, and approximately 1 m in the waterlogged section. The isotopic experiment was carried out between 5 and 10 February 2000.

Three sites with varying surface soil drainage characteristics were selected for isotopic characterisation of N_2O fluxes. The three sites were located approximately 50 m from the centre of the field at bearings of 100°, 220° and 320° from North. Site 1 was extremely well drained, site 2 had average soil drainage, and site 3 was permanently waterlogged. N_2O samples were collected at different times after watering with the treated pig effluent fertilizer. Figure 7.2 shows a schematic diagram of the Corowa experiment site with the three experimental sites marked.

7.2.2 Extraction of N_2O from soil gas emissions

Isotopic analysis of N_2O by FTIR requires approximately 5-10 μmol N_2O (Chapter 4). A chamber on loan from CSIRO Atmospheric Research (courtesy of Dr Roger Francey) was used to concentrate the soil gas emissions from each of the three sites. An extraction line (section 3.5) was used to separate the N_2O from non condensable gases and CO_2.

The use of chambers in soil gas-flux measurements is well established [for example *Galle et al.*, 1994; *Myer et al.*, 2001]. The chamber used consisted of a rectangular base, approximately 0.7 m by 0.5 m, which was inserted approximately 5 cm into the soil. A cover, approximately 0.3 m high was sealed onto the base via a silicone tubing seal. Once assembled the chamber had a surface area of 0.35 m^2 and a total volume of 105 L. A small vent ensured the chamber volume was always at ambient pressure. The chamber size used in this experiment was limited by the distance between individual maize plants, and the unavailability of a larger chamber. The N_2O flux measured using this chamber system is not necessarily representative of the natural N_2O flux from the soil, as small variations in atmospheric pressure inside the chamber and the relatively large volumes of gas sampled could cause N_2O to be forced from open pore spaces within the soil.

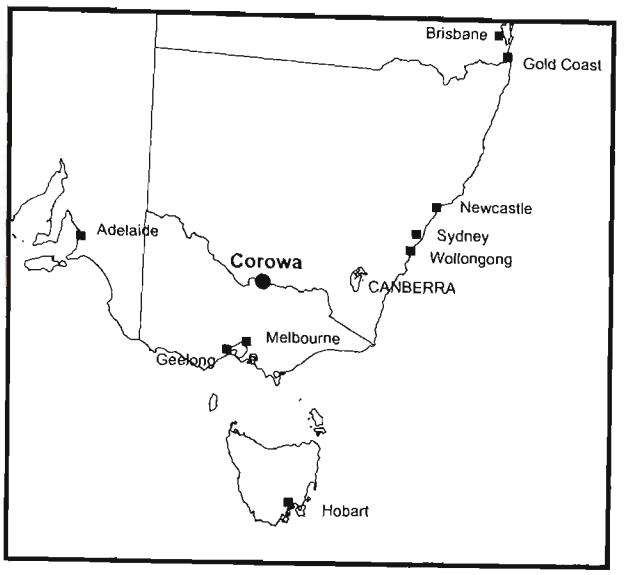

Figure 7.1 Location of Corowa, NSW.

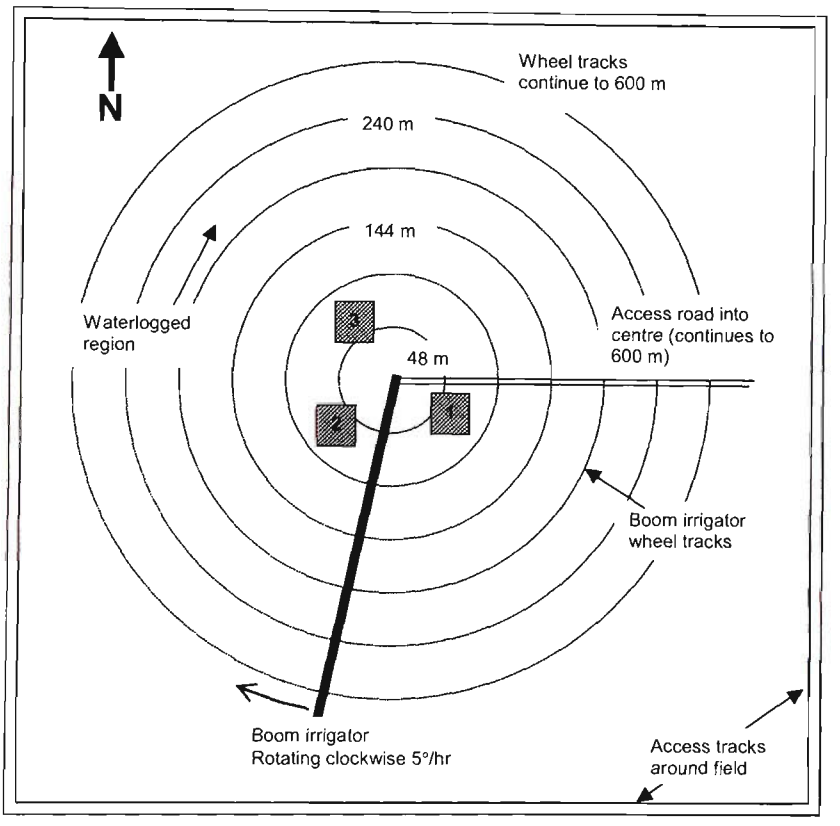

Figure 7.2 Schematic diagram of the Corowa experiment site.
Wheel tracks extend to approximately 600 m. The boom is 600 m long, only a section of the experiment site is shown.

Gas samples were collected from each of the three sites with the chamber prior to main sampling experiment to estimate N_2O fluxes. The chamber was placed on the base and the lid closed. A 2 L gas sample was collected from the chamber after 20-30 minutes. This sample was analysed for N_2O by low resolution (1 cm^{-1}) FTIR spectroscopy [*Esler et al.*, 2000a; *Esler et al.*, 2000b] for an estimate of the N_2O flux from each site. This was used to estimate how much air from the chamber was required to collect sufficient N_2O for high resolution FTIR isotopic analysis. Based on these measurements, between 150 and 500 L of chamber air was collected.

An extraction line was used to trap and collect N_2O emitted from the soil site covered by the chamber. The extraction line was connected to the chamber via ¼" polypropylene tubing, and mounted in a 4WD vehicle which was parked within 5 m of the soil site. A constant flow of air from the chamber, between 2 and 2.5 L min^{-1} was drawn through the extraction line. Detailed information on the extraction line operation is given in chapter 3.5. The extracted N_2O was cryogenically trapped in a 6 mm diameter glass tube, flame sealed and taken to the University of Wollongong for high resolution FTIR isotopic analysis. Figure 7.3 and Figure 7.4 are photographs showing the Corowa field site and the boom irrigator, respectively. Figure 7.5 is a photograph of the waterlogged region of the crop field, and Figure 7.6 shows the N_2O extraction line mounted inside the 4WD vehicle.

Figure 7.3 The Corowa field site, looking east towards the access road

Figure 7.4 The boom irrigator

Figure 7.5 The waterlogged region of the crop field site

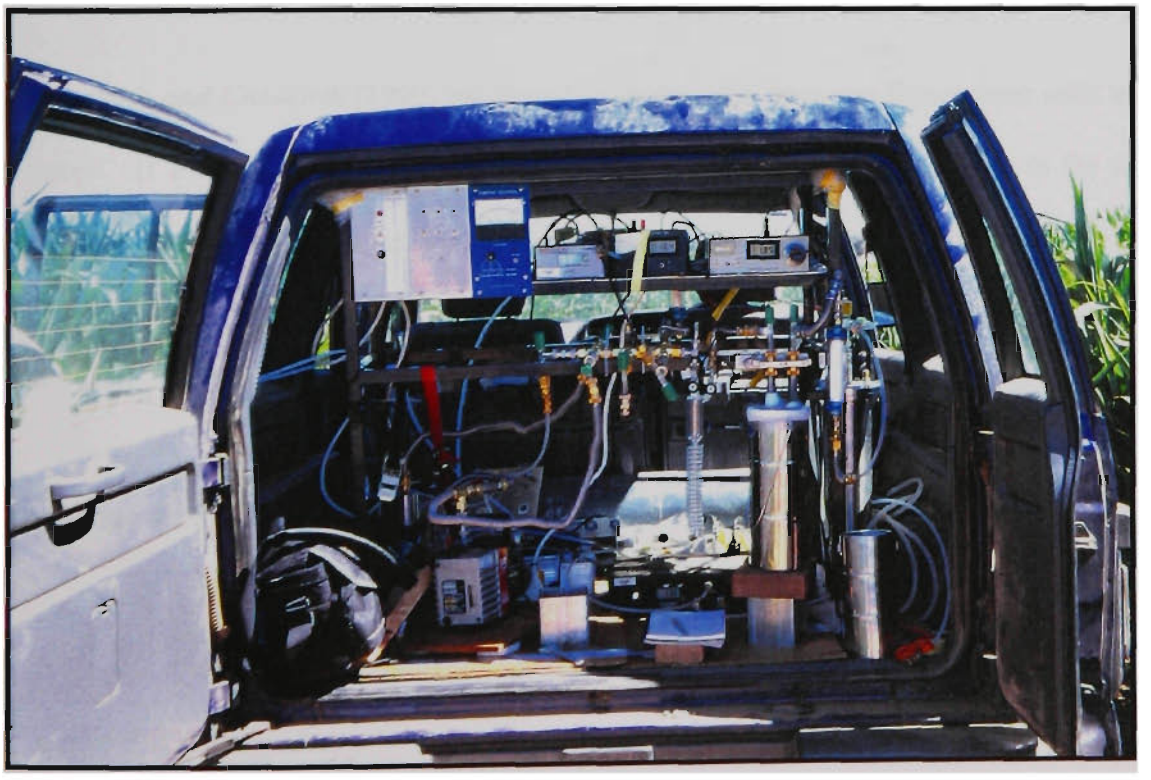

Figure 7.6 The N_2O extraction line mounted inside the 4WD vehicle
Extraction line on loan from Dr Roger Francey, CSIRO Atmospheric Research

7.2.3 Measuring the N_2O flux and isotopic composition

A ¼" polypropylene line was connected via a T-junction to main N_2O extraction line, through a digital flow meter and into a pre-evacuated 2 L glass bulb. The pre-evacuated glass bulb was opened when cryogenic collection of N_2O with the main extraction line commenced and sample flow into the bulb was controlled manually via a digital flow meter and needle valve. The flow rate was selected such that the bulbs would be filled to near atmospheric pressure with air from the chamber over the time taken for the extraction of N_2O for isotopic analysis. For a typical 3 hour collection, the flow into a 2 L bulb was controlled between 10 and 12 mL min^{-1}. This bulb sample is therefore a time-averaged integrated air sample from the chamber for the N_2O extraction. The N_2O concentration of these bulbs was determined by low resolution (1 cm^{-1}) FTIR spectroscopy [*Esler et al.*, 2000a], and it consists of a soil-flux contribution and a contribution from the background air via the pressure vent into the chamber.

Monteith and Unsworth [1990] mathematically describe trace gas fluxes from soils and crops. If c' is defined as the N_2O concentration in the chamber due solely to the soil flux, c_0 as the background N_2O concentration, and c_{bulb} as the actual chamber N_2O concentration measured from the 2 L bulb as integrated sample described above, then

$$c' = c_{bulb} - c_0 \qquad (\text{mol m}^{-3}) \qquad (7.1)$$

and therefore by mass balance

$$\frac{dc'}{dt} = F - \gamma c' \qquad (7.2)$$

where F is the rate of change in the N_2O concentration, given by

$$F = \frac{Area_{chamber}}{Volume_{chamber}} \times Flux_{N_2O} \qquad (\text{mol m}^{-3}\ \text{s}^{-1}) \quad (7.3)$$

where $Flux_{N_2O}$ is the true soil N_2O flux and

$$\gamma = \frac{Flow_{\text{ into (and out of) chamber}}}{Volume_{chamber}} \qquad (\text{s}^{-1}) \quad (7.4)$$

γ has the units of s^{-1} and represents the number of "chamber volumes" exchanged per second. Integrating over time t gives

$$c' = \frac{F}{\gamma}\left(1 - e^{-\gamma t}\right) \qquad (\text{mol m}^{-3}) \quad (7.5)$$

where t is time. The integrated flux-derived concentration $c_{flux\ derived}$ (equal to $\int_0^t c'dt'$) is therefore

$$c_{flux\ derived} = \frac{Ft}{\gamma} + \frac{Fe^{-\gamma t}}{\gamma^2} - \frac{F}{\gamma^2} \qquad (\text{mol m}^{-3}\ \text{s}) \quad (7.6)$$

The true soil flux, in mol N_2O m^{-2} s^{-1} is then

$$Flux\ N_2O = \frac{Volume_{chamber}}{Area_{chamber}} \times \gamma c' t \left(t + \frac{e^{-\gamma t}}{\gamma} - \frac{1}{\gamma} \right)^{-1} \quad (7.7)$$

The true N_2O flux for each sampled site can be determined from measuring the N_2O concentration in the time averaged integrated bulb samples.

The isotopic composition of the extracted N_2O was determined using the standard FTIR method and analysis procedure described in Chapter 2, 3 and 4 of this thesis. The isotopic signature measured from the extracted N_2O inside the chamber consists of two components: the average soil N_2O isotopic signature and the contribution from the

background air flowing into the chamber. The measured N_2O isotopic signature is in effect the weighted average of the these two components, and therefore the true soil N_2O isotopic signature is calculated from

$$\delta_{soil} = \frac{\delta_{measured} c_{measured} - \delta_{background} c_{background}}{c_{measured} - c_{background}} \tag{7.8}$$

where δ is the isotopic signature and c is the N_2O concentration in either the integrated air sample (measured) or the background. The isotopic signatures in this work have been determined using this equation. The background N_2O concentration and isotopic composition were measured once from the top of a 9 m mast (north tower) under still background atmospheric conditions. The background N_2O concentration and isotopic composition were assumed to be constant during the experiment period, which may not be a strictly valid assumption given the experiment location – a heavily fertilised agricultural field.

7.3 Results

7.3.1 Fluxes of N_2O and CO_2

Fluxes of N_2O and CO_2 were calculated for each time-averaged integrated bulb sample collected using equation 7.7. Calculated fluxes for the three measurement sites are given in Table 7.1. Fluxes of CO_2 are included for comparison with N_2O fluxes. The estimated uncertainty in the flux calculation is approximately ± 20 %.

Table 7.1 Fluxes of N_2O and CO_2 for the Corowa field experiment sites

Site [a]	Time post irrigation (hrs) [b]	$[N_2O]$ (ppb) [c]	$[CO_2]$ (ppm) [c]	Flux N_2O (ng-N m^{-2} s^{-1}) [d]	Flux CO_2 (μg m^{-2} s^{-1}) [d]
1	8.5	681	705	220	143
1	36.5	1117	608	144	73
1	58.5	919	853	110	144
2	11	876	721	145	151
2	33.5	761	630	87	85
2	56	657	814	56	120
3	67.5	12830	2258	3450	826
N Background [e]		315	360		

a. The site description as described in the text.
b. Elapsed time in hours after the boom irrigator last watered the sample site.
c. Time averaged integrated mixing ratio, *including* the background mixing ratio.
d. The flux as calculated from equation 7.7.
e. North background: collected 9 m above the field site from the North tower and taken as background atmospheric conditions.

7.3.2 N_2O isotopic composition

Table 7.2 shows the isotopic values for the three experiment sites. Site 3 was measured once for N_2O isotopes as it was permanently waterlogged under all conditions, and can be expected to not vary significantly. The background N_2O concentration and isotopic composition was measured once from the top of a 9 m mast (north tower) under still background atmospheric conditions. The background N_2O concentration and isotopic composition were assumed to be constant during the experiment period. A large fraction of the sampled chamber air came from outside the chamber and this was assumed to have the same N_2O concentration and isotopic composition as the background air. Ideally, a second extraction line would be used to sample the N_2O from outside the chamber for isotopic characterisation. This was not possible in this experiment due to the size and complexity of the extraction line. The extraction line has been substantially simplified since this experiment (Chapter 8) allowing for much simpler extraction of N_2O from whole air in future experiments. Results show that with

the current experimental design, the background isotopic correction (equation 7.8) leads to a $\delta^{15}N$ correction of between 3 and 9 ‰ for all experimental sites. The δ^{456}-δ^{546} correction is between 0.7 and 3.5 ‰ for sites 2 and 3, and between 6 and 27 ‰ for site 1 measurements.

Table 7.2 N_2O isotopic signatures for Corowa field experiment sites [a]

Site [b]	Air collected (L)[c]	Time post irrigation [d]	Flux N_2O[e]	δ^{456}	δ^{546}	δ^{456}–δ^{546}	$\delta^{15}N$[f]	δ^{448} [g]	δ^{447}
1	161	8.5	220	-55.3	26.9	-82.2	-16.0	-19.2	-34.7
1	260	36.5	144	-8.9	-15.4	6.5	-13.9	-5.6	-26.2
1	471	58.5	110	-40.9	17.3	-58.2	-13.6	28.5	12.4
2	153	11	145	3.1	-19.6	22.7	-10.0	7.2	-15.6
2	335	33.5	87	5.9	-6.4	12.3	-2.1	-20.4	-25.8
2	500	56	56	12.9	-6.2	19.2	1.6	17.7	14.5
3[h]	123	67.5	3450	8.3	37.1	-28.8	20.9	16.5	-1.5
N backgd [i]				19.7	-1.0	20.7	7.6	27	4.7

a. Quoted relative to the BOC gases internal working standard in ‰ unless otherwise stated.
b. The Corowa site description as defined in the text.
c. The volume of air collected for N2O extraction from the chamber.
d. Elapsed time in hours after the boom irrigator last watered the sample site.
e. Units of ng-$Nm^{-2}s^{-1}$.
f. Quoted relative to atmospheric N_2 in ‰.
g. Quoted relative to atmospheric O_2 in ‰.
h. Site 3 was completely waterlogged regardless of the length of time post irrigation.
i. North background: collected 9 m above the field site from the North tower and taken as background atmospheric conditions.

7.4 Result interpretation and discussion

7.4.1 N_2O Fluxes

The N_2O fluxes are up to two orders of magnitude larger than N_2O fluxes measured from forest soils [*Perez et al.*, 2000; *Perez et al.*, 2001], but comparable to fluxes measured by *Whalen et al.* [2000] from a field also fertilized with liquid pig effluent. It

is not surprising that N_2O flux from unfertilised natural forest soils [*Brumme et al.*, 1999] should be on average an order magnitude lower than N_2O flux from this experiment, as fertilization with nitrogen rich fertilizer is known to produce substantial N_2O emissions from soils [*Bouwman et al.*, 1993; *Bouwman et al.*, 1995]. Site 3 was continuously saturated with effluent and is an extremely active N_2O emitter. This site was permanently waterlogged with the irrigating pig effluent compared to sites one and two, and can be thought of as being in an N_2O production regime which is not limited by fertilizer amount in the soil. The N_2O flux from site 3 is between 15 and 60 times larger than that from the other two sites. The N_2O flux from site 3 is comparable to the 2560 ng $N\text{-}N_2O$ m^{-2} s^{-1} measured by *Whalen et al.* [2000] shortly after fertilization of soil with liquid pig effluent, but lower than the 3600 ng $N\text{-}N_2O$ m^{-2} s^{-1} measured by *Chadwick et al.* [2000] after applying animal manure to grassland. The peak N_2O flux observed by *Scott et al.* after fertilizing grassland with sewage sludge was 1620 $N\text{-}N_2O$ m^{-2} s^{-1} [*Scott et al.*, 2000]. Therefore the N_2O fluxes measured from the three measurement sites are consistent with other flux measurements made under similar conditions.

The small size of the maize on site 3 (1 m tall), and its withered condition compared to the maize on sites 1 and 2 (approximately 2 m tall) points to poor extraction of nitrogen from the fertilizer by the maize on site 3. Consequently, more nitrogen is available in the soil to be processed into N_2O gas. This in part explains the very large N_2O flux measured from site 3. Maize from sites 1 and 2 was tall and not withered, and can be assumed to efficiently using most of the nitrogen in the fertilizer. Therefore less nitrogen is available to be processed into N_2O, explaining the lower N_2O fluxes compared to site 3. Permanent water saturation of the soil in site 3 can also hinder

maize growth, potentially due to low oxygen availability in the soil, root rot and the inability of the roots to respire CO_2.

The condition of site 3 is a special case that warrants further examination. The amount of oxygen available in a soil system is regulated by water, and the balance between aerobic and anaerobic conditions is extremely important in determining the relative rates of nitrification and denitrification [*Linn and Doran*, 1984]. One measure of the water available in a soil system is the water filled pore space (WFPS), [*Paul and Clark*, 1996] defined as

$$WFPS_{(\%)} = \frac{\Theta_m \cdot D_b}{1-(D_b/2.65)} \times 100 \tag{7.9}$$

where

Θ_m is the gravimetric soil water content (mass of water/mass of soil), unitless, and

D_b is the soil dry bulk density (mass of dried soil/original soil sample volume), units g cm^{-3}.

The denominator of the above expression is defined as the total soil porosity, where the term 2.65 has units of g cm^{-3} and is taken to be the soil particle density [*Paul and Clark*, 1996]. WFPS effectively measures relative soil-water saturation, and is 0 % for completely dry soil and 100 % for completely saturated soil. There is a relationship between soil WFPS and the relative activity of nitrification and denitrification, best expressed by Figure 7.7.

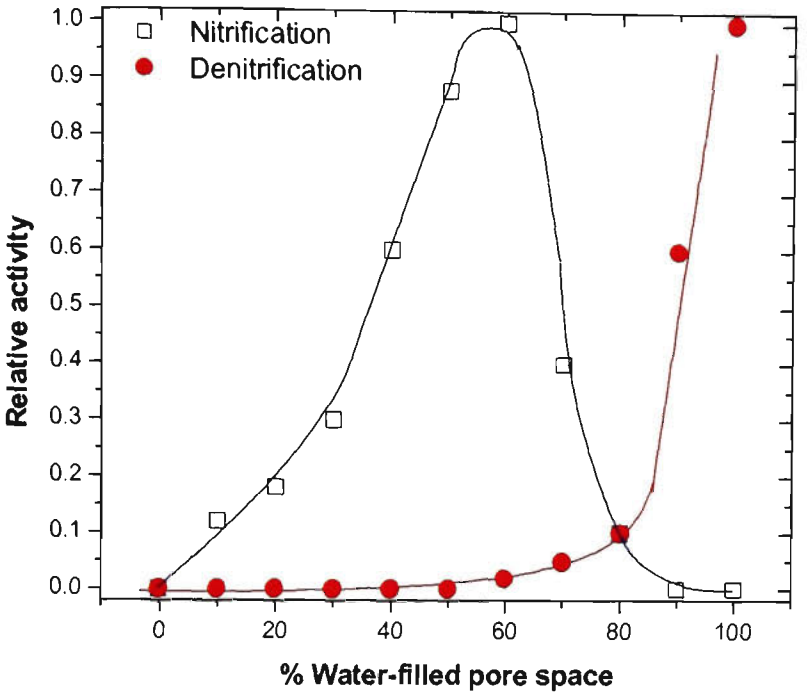

Figure 7.7 **Relative rates of nitrification and denitrification as a function of water filled pore space.**
[adapted from *Linn and Doran*, 1984]

At WFPS greater than 80 %, such as exists in saturated soils, nitrification decreases to zero and denitrification is the dominant soil process in these anaerobic conditions. At WFPS smaller than approximately 80 %, enough oxygen is available in the soil system for nitrification to occur. Between 60 % and 90 % WFPS, a combination of nitrification and denitrification occurs. This behaviour has been shown in numerous recent studies [*Abbasi and Adams*, 2000; *Beline et al.*, 2001; *Dalsgaard et al.*, 1995; *Harper et al.*, 2000; *Hwang and Hanaki*, 2001; *Itokawa et al.*, 2001; *Maag and Vinther*, 1996; *Maag and Vinther*, 1999; *Smith et al.*, 1998]. Site 3 was completely waterlogged under all conditions, as is seen in Figure 7.5. Although WFPS was not measured directly for this site, it can be safely assumed that its WFPS is greater than 90 %, based solely on an observation of the soil conditions in and around site 3. Therefore site 3 potentially

represents a source of N_2O from predominantly, if not exclusively, denitrification. The exact NH_4^+/NO_3^- composition of the pig effluent is not known at this time, but it is suspected that it is predominantly NH_4^+ [*Val Snow, CSIRO* personal communication].

Figure 7.8 shows N_2O flux as a function of time post-irrigation with pig effluent. The nitrous oxide flux decreases steadily after fertilizer application, but as fertilizer is applied every three days the fluxes do not decrease back to background levels. A similar flux pattern was seen by *Whalen et al.* [2000] and *Abasi and Adams* [*Abbasi and Adams*, 2000]. Site 3 has an extremely high N_2O flux which is independent of the time post irrigation – consistent with a site which is constantly fertilizer rich and denitrifying.

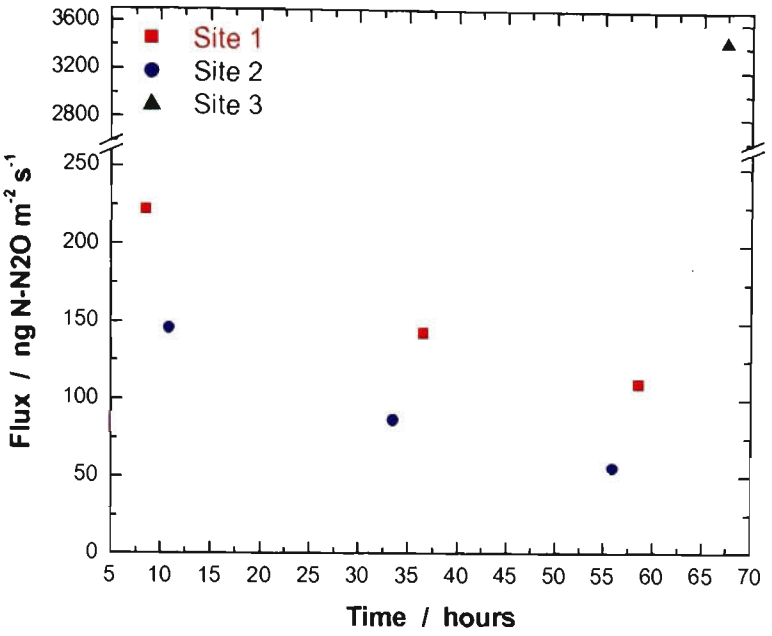

Figure 7.8 Flux N_2O as a function of time post-irrigation

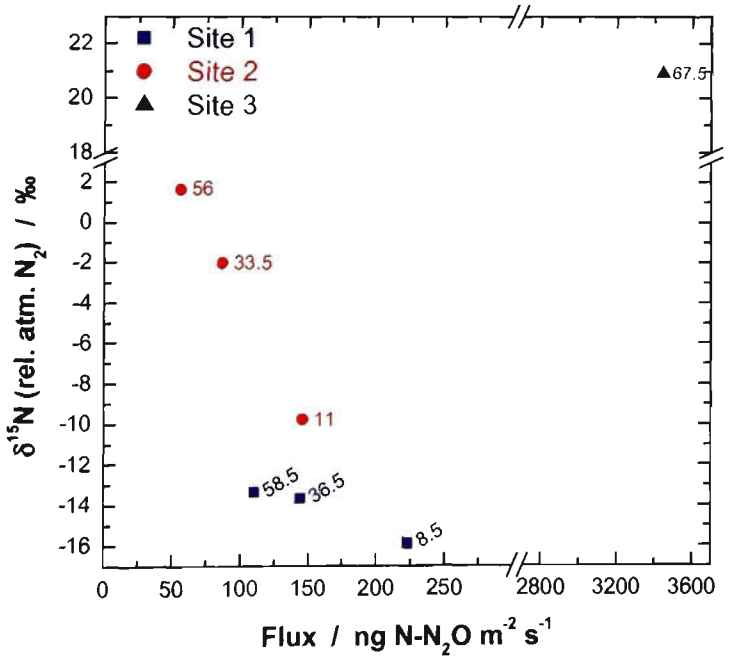

Figure 7.9 $\delta^{15}N$ of N_2O soil emissions as a function of N_2O flux for Corowa field sites

The symbol labels are the number of hours post irrigation with pig effluent. Site 3 was completely waterlogged.

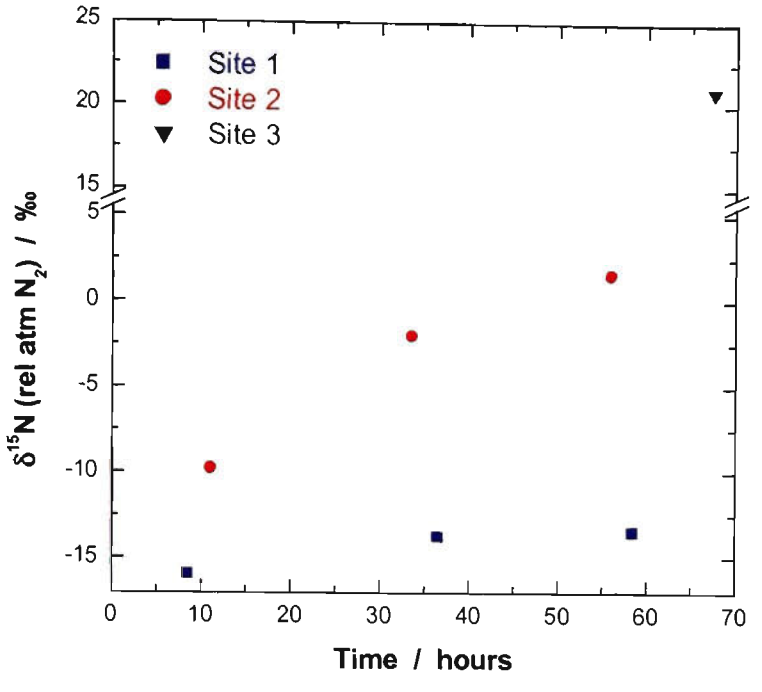

Figure 7.10 $\delta^{15}N$ of N_2O soil emissions as a function of time post-irrigation for Corowa field sites

7.4.2 $\delta^{15}N$ of N_2O from experiment sites

Figure 7.9 shows the $\delta^{15}N$ of the emitted N_2O from the field sites, measured relative to atmospheric N_2, as a function of N_2O flux. Figure 7.10 shows the $\delta^{15}N$ of the emitted N_2O as a function of time post irrigation. The $\delta^{15}N$ of clean background tropospheric N_2O relative to atmospheric N_2 is approximately 7 ‰ [*Kim and Craig*, 1993]. The labels represent the number of hours post irrigation, as per Table 7.1.

The $\delta^{15}N$ of N_2O from site 2 increases with time at the rate of 0.26 ± 0.06 ‰ $hour^{-1}$, if a linear relationship is assumed (r^2=0.96). The $\delta^{15}N$ of site 1 also increases with time but it is difficult to tell whether this is a linear relationship. Changes in $\delta^{15}N$ of N_2O from site 2 are much higher than that for site 1 N_2O, implying that site 2 is a much faster

processor of source N. Sites 1 and 2 show clear correlation between N_2O flux and measured $\delta^{15}N$ (r^2 = 0.97 and 0.99, respectively), with the highest flux obtained under the most water saturated soil conditions (Figure 7.9). Nitrous oxide is produced during both nitrification (oxidation of NH_4^+ to NO_3^-) and denitrification (reduction of NO_3^- to N_2). Nitrification produces N_2O as depleted as –66 ‰ in $\delta^{15}N$ [*Yoshida*, 1988]. However N_2O in denitrification is both an intermediate product which is consumed, and a by-product which is emitted. Both processes act to fractionate N_2O in $\delta^{15}N$, with the overall $\delta^{15}N$ enrichment of N_2O in denitrification being –13 to –28 ‰ [*Barford et al.*, 1999]. If the nitrogen substrate has an average $\delta^{15}N$ of zero, then denitrification will produce N_2O which is less depleted in $\delta^{15}N$ than nitrification.

The N_2O emitted from the site 3, the saturated site, exists in a completely different emission and isotopic signature regime from sites 1 and 2. The $\delta^{15}N$ of site 3 is 20.9 ‰ relative to atmospheric N_2. As discussed in section 7.4.1, the process generating N_2O is expected to be exclusively denitrification under such anaerobic conditions. Various studies have measured $\delta^{15}N$ of N_2O from exclusively denitrifying conditions. For example, *Whalen and Yoshinari* [1985] measured N_2O from Green Lake with $\delta^{15}N$ of approximately 10 ‰ with respect to atmospheric N_2. *Boontanon et al.* [2000] report N_2O from waterlogged swamps in Thailand with $\delta^{15}N$ as high as 15.6 ‰ with respect to atmospheric N_2. *Yoshinari et al.* [1997] measured $\delta^{15}N$ up to 15 ‰ for waters in the eastern tropical North Pacific. *Mandernack et al.* [2000], measuring $\delta^{15}N$ of N_2O from covered landfills of 19.4 ‰ with relative to atmospheric N_2, which is the closest match in the literature to the site 3 $\delta^{15}N$ results. The $\delta^{15}N$ from site 3 measurement obtained in

this work, approximately -21 ‰ relative to atmospheric N_2, is comparable to results obtained from other studies.

The $\delta^{15}N$ N_2O of site 1 and 2 from this work is generally heavier than that from a similar experiment by *Perez et al.* [2001]. In the *Perez et al.* [2001] experiment, urea fertilizer was placed on an agricultural field once and N_2O isotopomers measured as a function of time for 14 days after the initial fertilizer application. Results for $\delta^{15}N$ of N_2O obtained by *Perez et al.*, for the first 96 hours post fertilisation range from –46 to -35 ‰ and are generally much more depleted than those obtained by this work. Pig effluent fertilizer is applied every 3 days to the Corowa site and a pool of NH_4^+ therefore exists in the soil. As time progresses, nitrification and denitrification preferentially generate N_2O and N_2 isotopically light in $\delta^{15}N$ relative to the substrate $\delta^{15}N$, leaving isotopically heavy nitrogen behind in the nutrient "pool". During denitrification, the $\delta^{15}N$ of the residual nitrate in the pool is known to increase proportionally to the natural logarithm of the residual nitrate fraction, in a classical Rayleigh distillation fashion [*Kendall*, 1988]. Thus the overall $\delta^{15}N$ of the N_2O should increase with time, as the N pool from which N_2O is sourced becomes isotopically heavier. Plants negligibly fractionate NH_4^+ and NO_3^- during uptake [*Kendall*, 1988] and therefore the $\delta^{15}N$ of the pool nitrogen should be unaffected by the nutrient uptake by the maize plants used in this experiment. In sites 1 and 2, where drainage was relatively good, the relative change in $\delta^{15}N$ of N_2O reflects the swing from denitrification to nitrification as the soil drains, but the absolute $\delta^{15}N$ is governed by the ^{15}N of the source N pool. The differences in $\delta^{15}N$ N_2O between this experiment and that of *Perez et al.* [2001] are therefore explained by the diffcrent fertilisation regimes.

In the case of Corowa site 3, the pool of source N can be thought of as being relatively old – that is, relatively enriched in ^{15}N due to preferential emission of isotopically light N_2O due to high denitrification and little nitrogen removal by the maize crops. This explains the high $\delta^{15}N$ N_2O enrichment of site 3 compared to sites 1 and 2. The high $\delta^{15}N$ of N_2O from site 3 reflects the $\delta^{15}N$ of the source nitrogen. Both nitrification and denitrification emit N_2O which is depleted in $\delta^{15}N$ relative to the substrate N, but the absolute $\delta^{15}N$ value is governed by the ^{15}N of the source N pool. It is unlikely that $\delta^{15}N$ alone can distinguish between nitrification and denitrification. However, the isotopic difference δ^{456}–δ^{546} should not be affected by the $\delta^{15}N$ of the source N and might prove to be a more sensitive discriminator between nitrification and denitrification. The formation of the N-N bond in N_2O, and any associated positional fractionation in ^{15}N is solely dependent on nitrification and denitrification mechanistic processes and not governed by the $\delta^{15}N$ of the source N.

The slope in the $\delta^{15}N$–flux graph (Figure 7.9) gives further clues about soil and plant processes. A large slope such as seen in site 2 shows that $\delta^{15}N$ of the emitted N_2O increases rapidly with decreasing N_2O flux. As discussed above, the relative change in $\delta^{15}N$ of the emitted N_2O reflects the change from denitrification to nitrification in the soil, but the absolute $\delta^{15}N$ is governed by the ^{15}N of the source N pool. Therefore, a large change in $\delta^{15}N$ of the N_2O reflects a high rate of nitrogen processing by the maize, and a high level of plant activity. The slope of the site 1 results from Figure 7.9 is –0.02 ‰·(ng N-N_2O m^{-2} s^{-1})$^{-1}$, compared to site 2 of –0.13 ‰·(ng N-N_2O m^{-2} s^{-1})$^{-1}$. Maize on site 2 is therefore is a much faster processor of substrate N than site 1. The faster the maize processes substrate N, the quicker the rate of change in the $\delta^{15}N$ of the emitted N_2O.

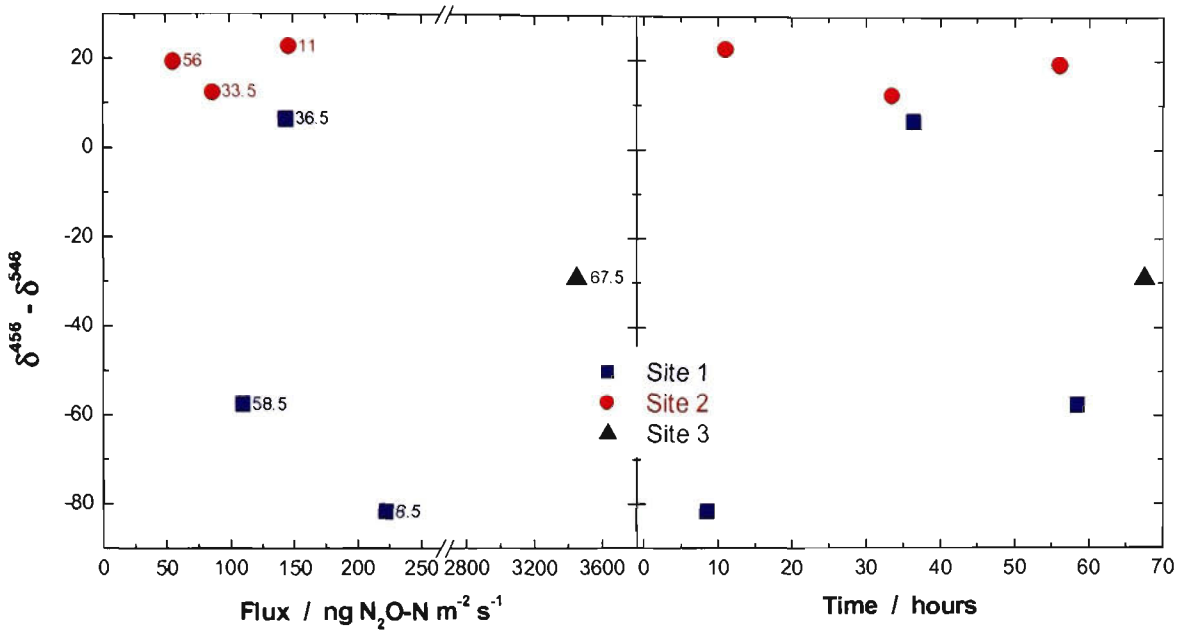

Figure 7.11 **Intramolecular ^{15}N difference (δ^{456}-δ^{546}) of N_2O soil emissions as a function of N_2O flux for Corowa field sites**
The symbol labels are the number of hours post irrigation with pig effluent. Site 3 was completely waterlogged.

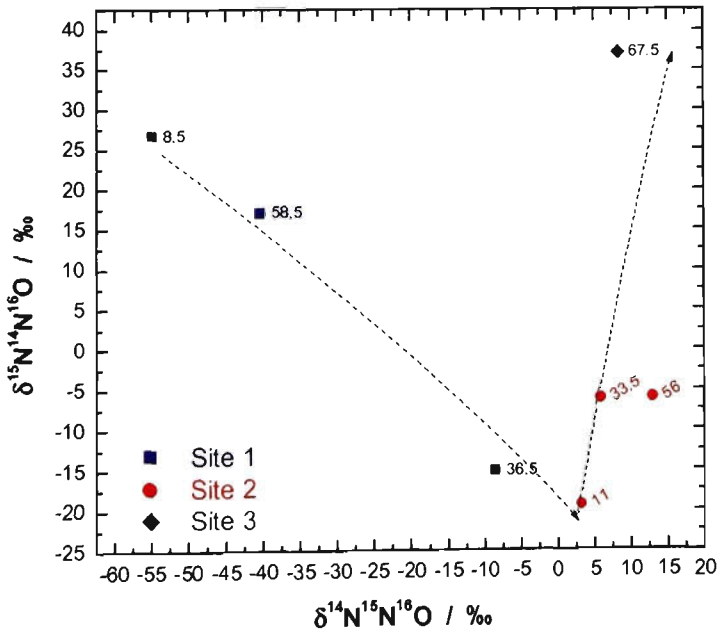

Figure 7.12 **δ^{546} as a function of δ^{456} for the Corowa field sites.**
The symbol labels are the number of hours post irrigation with pig effluent. Site 3 was completely waterlogged.

7.4.3 The intramolecular ^{15}N difference: δ^{456}-δ^{546} and the individual δ^{456} and δ^{546}

Figure 7.11 shows the intramolecular ^{15}N difference δ^{456}-δ^{546} of N_2O soil emissions from the Corowa experiment sites as a function of N_2O flux and time post irrigation. Figure 7.12 shows the relationship between δ^{456} and δ^{546} for the three Corowa field sites. At the time of writing only two other studies have been performed which measured δ^{456}-δ^{546} of N_2O from fertilized soils, *Perez et al.* [2001] and *Mengazzo* [2000]. Both were measured at the University of Wollongong using the FTIR technique developed in this thesis. *Perez et al.* [2001] found that δ^{456}–δ^{546} for N_2O from urea fertilised soil increased from 4.9 to 14.2 ‰ over the course of 4 days after fertilisation. *Mengazzo* [2000] found a δ^{456}–δ^{546} range of 14-28 ‰ for soil fertilised with waste water from a starch plant. In this work δ^{456}-δ^{546} ranges from –81.6 ‰ to +22.7 ‰. *Yoshida and Toyoda* [2000] recently published a δ^{456}-δ^{546} range for soil and oceanic sources of between –0.5 ‰ to 15 ‰ measured relative to an approximately equivalent working standard to this work (refer to chapter 6 for a fuller discussion of the *Yoshida and Toyoda* [2000] working standard in relation to the BOC Gases N_2O working standard used in this work). While the Corowa results are generally outside this range, so few data exist that it is difficult to interpret these results in relation to the work of others.

Across all sites and conditions, the variation in δ^{456} is 68.2 ‰ while the variation in δ^{546} is 52.9 ‰. These results are broadly consistent with those of *Menegazzo* [2000], and are also broadly consistent with the *Yoshida and Toyoda* [2000] statement that the central ^{15}N is expected to vary more than the terminal ^{15}N in microbiological processes producing N_2O.

Figure 7.13 shows δ^{456}-δ^{546} as a function of $\delta^{15}N$ for N_2O from the Corowa experiment sites, and for the two other existing studies that have measured δ^{456}-δ^{546} from soils, *Perez et al.* [2001] and *Menegazzo* [2000]. This work and the *Menegazzo* [2000] experiment are similar in that a field is regularly fertilized, whereas the *Perez et al.* [2001] experiment involved placing fertiliser on a previously unfertilised soil. As discussed above, the $\delta^{15}N$ of the emitted N_2O is an indicator of bulk processing. Therefore, when fertiliser is placed on a previously unfertilised soil, the $\delta^{15}N$ of the emitted N_2O is expected to be very depleted, as is seen in the results of *Perez et al.* [2001].

The δ^{456}-δ^{546} results fall into two broad groups, or regimes. One regime, consisting of the *Perez et al.* [2001], *Menegazzo* [2000], one result from site 1 and all of site 2, has δ^{456}-δ^{546} between approximately +2.3 and +27.9 ‰, relative to BOC Gases N_2O. A second regime, consisting of two site 1 samples and site 3, has δ^{456}-δ^{546} between –28.8 and –81.6 ‰. The δ^{456}–δ^{546} of the emitted N_2O arises directly from the formation of the N-N bond in the nitrification and denitrification mechanisms and is therefore is independent of the $\delta^{15}N$ of the source nitrogen. Figure 7.13 suggests that the N_2O emitted results from a mix of two clearly differentiable δ^{456}-δ^{546} regimes which are independent of $\delta^{15}N$. One regime favours δ^{456} and one favours δ^{546}. This could be as significant results as it suggests that there is a combination of at least two soil processes generating N_2O – for example a mixture of nitrification and denitrification. Therefore δ^{456}-δ^{546} can be a more sensitive discriminator for soil processes than the mean $\delta^{15}N$ on its own.

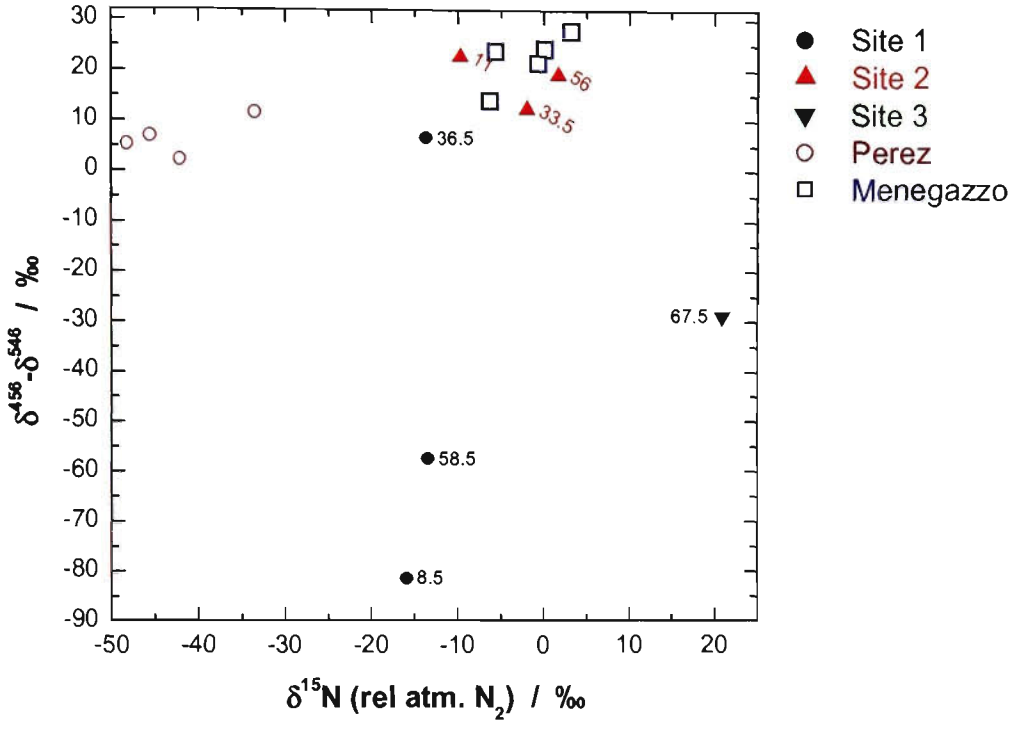

Figure 7.13 δ^{456}-δ^{546} **as a function of** $\delta^{15}N$ **for this work,** ***Perez et al.*** **[2001] and** ***Menegazzo*** **[2000].**
The symbol labels are the number of hours post irrigation with pig effluent.

7.4.4 The oxygen isotopomers

Figure 7.14 and Figure 7.15 show the measured δ^{448} (relative atmospheric O_2) and δ^{447}, respectively, as a function of N_2O flux and time post irrigation for the Corowa field sites. Site 1 shows an inverse correlation between δ^{448} and δ^{447} for emitted N_2O and the N_2O flux. As flux increases δ^{448} and δ^{447} decrease, consistent with increasing biological discrimination against the heavier isotopes. Site 2 results do not show this trend. If all results are viewed as one it can be argued that δ^{448} and δ^{447} decrease as flux increases. The N_2O flux and isotopic signature from site 3 is assumed not to change significantly with time as the N_2O producing reagents, water and nitrogen from pig effluent are in such excess that they are assumed not change with time.

Generally δ^{448} increases with time after irrigation, implying that the oxygen in the soil system becomes isotopically heavier with time. The oxygen of N_2O produced from nitrification and denitrification in a soil-fertiliser system is primarily from water, which is subject to evaporation with an associated isotopic fractionation [*Bigeleisen*, 1949; *Urey*, 1946]. Water is not is negligibly fractionated in uptake by the maize [*Kendall*, 1988]. The oxygen and nitrogen isotopes in this soil system are from different "pools" as they are subject to different processes. Therefore, while the lighter oxygen isotopes are preferentially used in N_2O formation, the process which dominates the $\delta^{18}O$ of N_2O is likely to be evaporation. The oxygen "pool" is replenished every three days as the crop field is fertilized.

The measured range of $\delta^{14}N^{14}N^{18}O$ of approximately –20 ‰ to approximately 29 ‰ relative to atmospheric O_2 is larger than the range measured by *Perez et al.* [2001] of –3 % to +9 ‰ from urea fertilized soils, but spans that measured by *Perez et al.* [2000] from tropical soil N_2O emissions of between -4 ‰ to +18 ‰. To our knowledge these results are the first δ^{447} measurement of N_2O from fertilised soils. Site 1 δ^{447} follows a similar pattern to δ^{448} - an inverse correlation with flux, and a positive correlation with time after irrigation. The δ^{448} and δ^{447} data look similar except for the actual per mille values. This adds credibility to these results as the oxygen isotopomers of N_2O are expected to behave similarly in this experimental system.

Figure 7.16 summarises δ^{448} (relative to atmospheric O_2) as a function of $\delta^{15}N$ (relative to atmospheric N_2) for this work and two comparable studies [*Menegazzo*, 2000; *Perez et al.*, 2001]. This figure illustrates the large measured variability in isotopomers of N_2O emissions from soils.

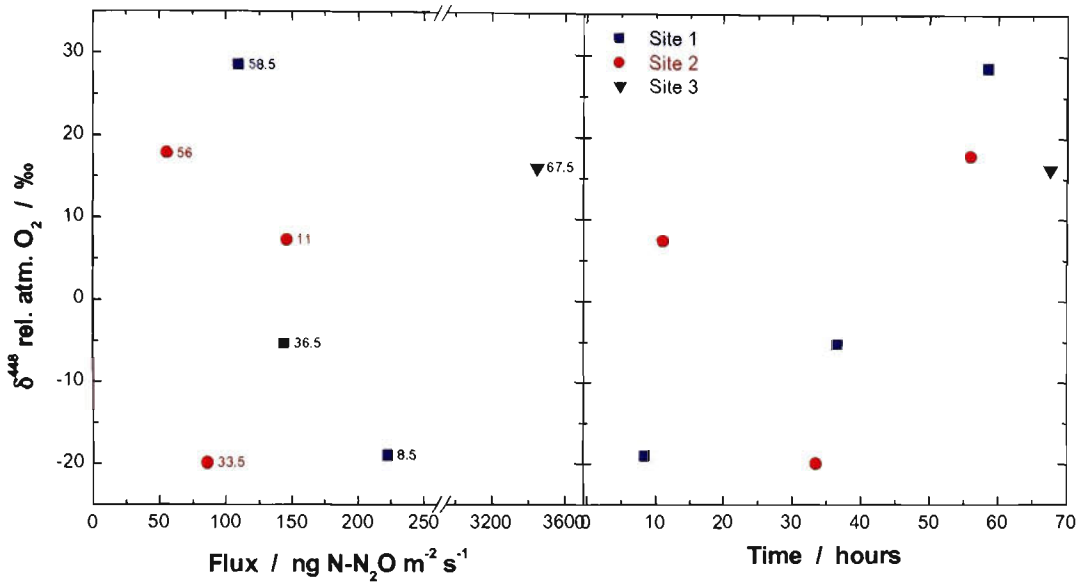

Figure 7.14 **δ^{448} relative to atmospheric O_2 for N_2O soil emissions as a function of N_2O flux (left) and time post-irrigation (right) for Corowa field sites**
The symbol labels are the number of hours post irrigation with pig effluent.

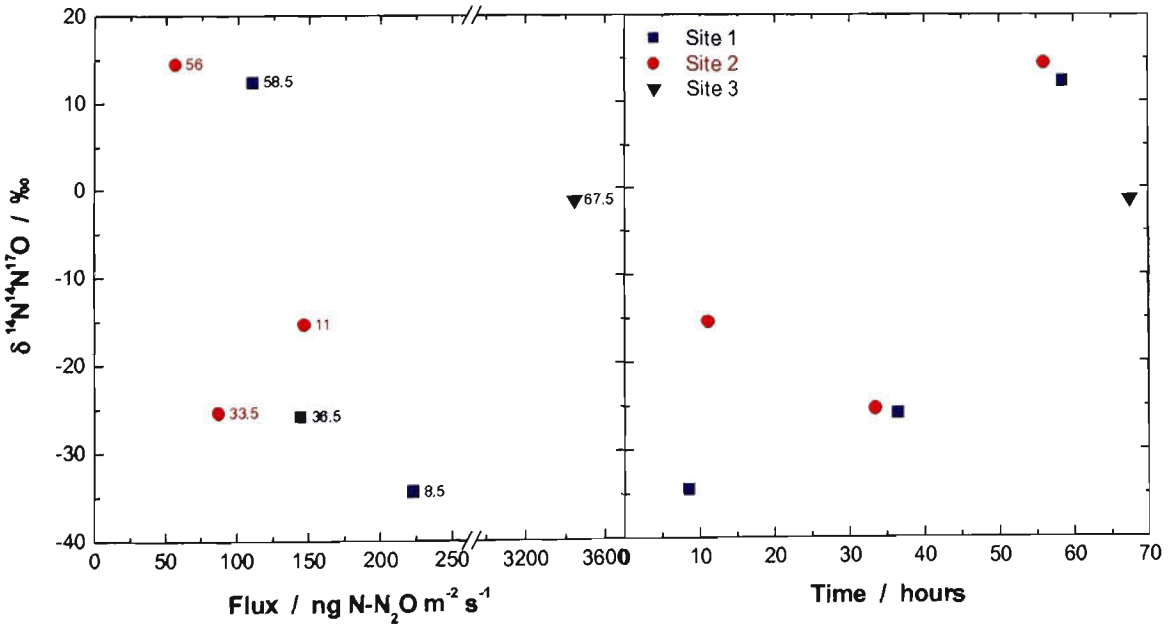

Figure 7.15 **δ^{447} for N_2O soil emissions as a function of N_2O flux (left) and time post-irrigation (right) for Corowa field sites**
The symbol labels are the number of hours post irrigation with pig effluent.

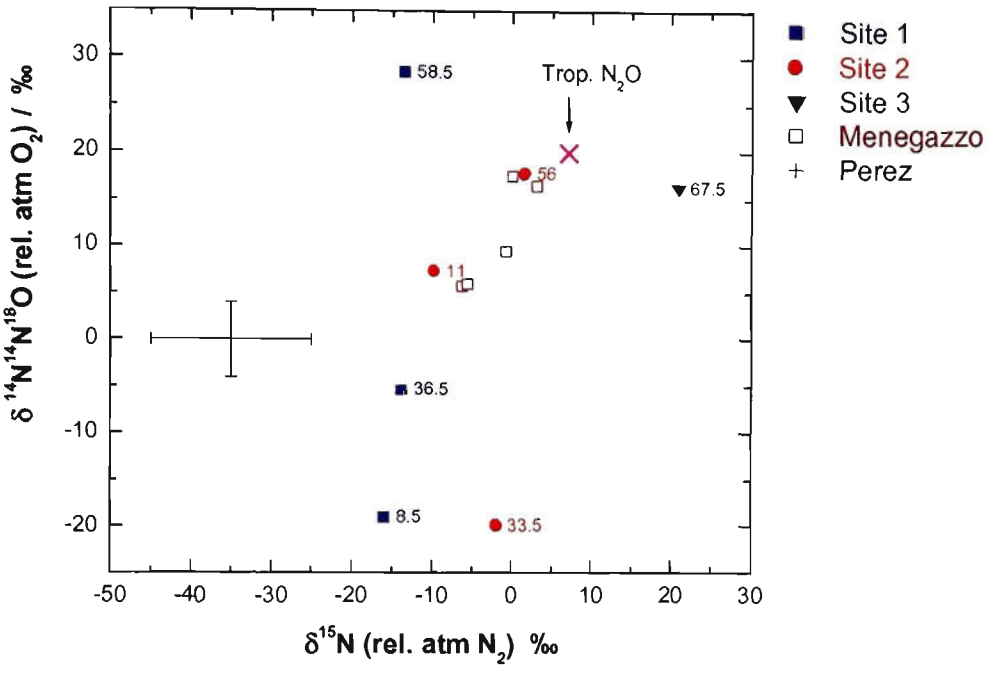

Figure 7.16 δ^{448} **(rel. atm. O_2) as a function of $\delta^{15}N$ (rel. atm. N_2) for this work, *Perez et al.* [2001] and *Menegazzo* [2000].**
Numerical symbol labels are the number of hours post irrigation. The *Perez et al.* cross is the emission weighted average (± 1σ) for that study. The X marks the signature of clean tropospheric N_2O.

Figure 7.17 shows δ^{447} as a function of δ^{448} for N_2O from the Corowa field sites. The slope of the regression line is 1.0 ± 0.1, with the average error in δ^{448} and δ^{447} approximately 3 ‰ and 4 ‰, respectively. This is an unexpected result. The oxygen isotopomers are expected to be related by $\delta^{447} = 0.515 \times \delta^{448}$, as the great majority of known chemical and physical processes fractionate isotopomers strictly according to the masses of the isotopes [*Kaye*, 1987; *Thiemens*, 1992] – mass-dependent fractionation.

Mass-independent fractionation, where $\delta^{447} \neq 0.515 \times \delta^{448}$, has been measured for stratospheric N_2O [*Cliff et al.*, 1999; *Cliff and Thiemens*, 1997; *Griffith et al.*, 2000; *Rahn and Wahlen*, 1997; *Röckmann et al.*, 2001b; *Thiemens*, 1992]. *Thiemens* [1992]

introduced the concept of $\Delta^{17}O$ to quantify the amount of mass independent fractionation in N_2O, where $\Delta^{17}O$ is defined as the excess ^{17}O in a sample of N_2O such that $\Delta^{17}O=\delta^{447}-0.515\times\delta^{448}$. The excess $^{14}N^{14}N^{17}O$ of stratospheric N_2O has been measured at $\Delta^{17}O=1.0 \pm 0.2$ ‰ [*Röckmann et al.*, 2001a]. An indirect chemical pathway for the transfer of heavy oxygen from O_3 to N_2O via NO has been proposed to explain the excess ^{17}O in stratospheric N_2O [*Röckmann et al.*, 2001b].

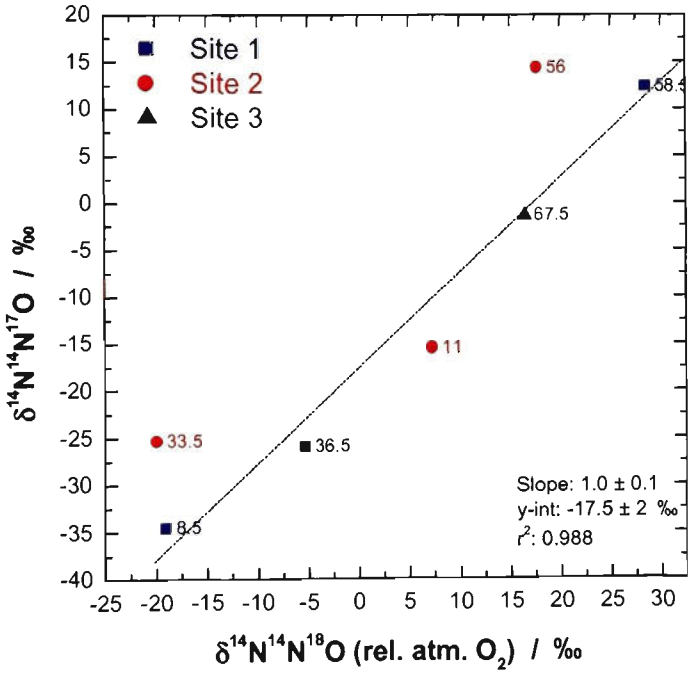

Figure 7.17 δ^{447} **as a function of** δ^{448} **for Corowa field sites**
The symbol labels are the number of hours post irrigation with pig effluent.

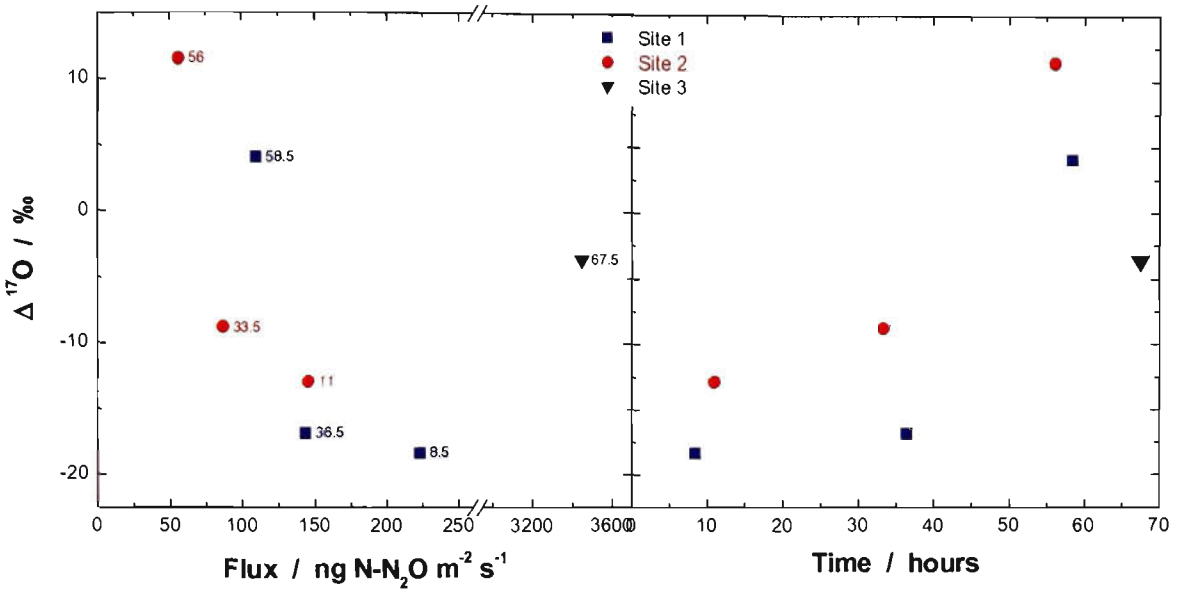

Figure 7.18 $\Delta^{17}O$ for N_2O soil emissions as a function of N_2O flux (left) and time post-irrigation (right) for Corowa field sites
The symbol labels are the number of hours post irrigation with pig effluent.

Figure 7.18 shows $\Delta^{17}O$ as a function of N_2O flux and time after irrigation, where $\Delta^{17}O$ was calculated using the δ^{448} values relative to the same working standard as δ^{447} (BOC Gases N_2O). The $\Delta^{17}O$ decreases with increasing N_2O flux and increases with time post integration for the Corowa experiment. The *Menegazzo* [2000] results do not show a pattern between δ^{448} and δ^{447}. No known mechanism exists to explain the apparent mass-independent fractionation in N_2O measured in this work. These results could be an artefact of the analysis method, but $^{14}N^{14}N^{18}O$ and $^{14}N^{14}N^{17}O$ have different infrared spectra and are determined separately. Some other as yet unknown process could be responsible for the apparent mass-independent fractionation of the oxygen isotopomers.

7.5 Conclusions

Whole air and nitrous oxide were collected beneath a chamber from three experimental sites on a Corowa crop field after irrigation with pig effluent. High resolution FTIR analysis was used to determine the isotopomeric composition of the N_2O. The N_2O flux from each measurement site was determined. The three experimental sites are extremely active emitters of N_2O, with fluxes varying between 56 ng N-N_2O m^{-2} s^{-1} and 3450 ng N-N_2O m^{-2} s^{-1} for the study period. The N_2O fluxes are up to two orders of magnitude larger than those measured from forest soils [*Perez et al.*, 2000; *Perez et al.*, 2001] but comparable to those measured from other pig effluent fertilised fields [*Whalen et al.*, 2000]. Nitrous oxide fluxes decrease between 8.5 and 58.5 hours after fertilizer application. The nitrous oxide fluxes measured in this experiment are not necessarily representative of the natural N_2O flux from the soil.

The $\delta^{15}N$ of the emitted N_2O ranges from –16 ‰ to +20.9 ‰ relative to atmospheric N_2. The highest $\delta^{15}N$ was for site 3. Sites 1 and 2 show a clear inverse correlation between N_2O flux and $\delta^{15}N$ of N_2O. The slope of the $\delta^{15}N$ – N_2O flux graph can be though of as and indicator of plant activity, and on this basis site 2 is a much more active processor of nitrogen than site 1. The $\delta^{15}N$ signature of the source nitrogen becomes heavier with time as light nitrogen isotopes are preferentially converted into N_2O by nitrification and denitrification. Plants negligibly fractionate the nitrogen in soil during uptake. The $\delta^{15}N$ of emitted N_2O is therefore suggested as primarily reflecting the $\delta^{15}N$ of the nitrogen source "pool".

The intramolecular difference δ^{456}-δ^{546} was measured for each N_2O sample collected and ranges from –82.2 to 12.3 ‰, which is a much larger range than has been measured

in two other experiments using the FTIR technique [*Menegazzo*, 2000; *Perez et al.*, 2001]. The *Menegazzo* [2000] results are comparable to results obtained from site 2. The isotopic difference δ^{456}–δ^{546} should not be affected by the $\delta^{15}N$ of the source N as any δ^{456}-δ^{546} signal arises directly during the formation of the N-N bond in nitrification and denitrification. Comparison of δ^{456}-δ^{546} results from this work and two similar studies [*Menegazzo*, 2000; *Perez et al.*, 2001] shows two distinct N_2O production regimes, possibly a nitrification and denitrification, with clearly differentiable δ^{456}-δ^{546} signatures. The δ^{456}-δ^{546} is therefore suggested as a much better indicator of nitrification and denitrification than the mean $\delta^{15}N$, which primarily reflects the isotopic signature of the source nitrogen.

The oxygen isotopomers δ^{448} and δ^{447} were measured for this experiment. The range of δ^{448} is –20 to 20 ‰ relative to atmospheric O_2. This range is larger than that measured by *Perez et al.* [2001] of –3 % to +9 ‰ from urea fertilized soils, and by *Perez et al.* [2000] from tropical soils of between -4 ‰ to +18 ‰. The range of δ^{447} for the Corowa N_2O is from –34.7 to 12.4 ‰ relative to the BOC Gases N_2O working standard. When sites 1 and 2 are viewed together, δ^{448} and δ^{447} decrease as flux increases, and increase as time after fertilisation increases. There is an apparent mass-independent fractionation between in the N_2O oxygen isotopomers, which is not explained by any known mechanism.

Interpretation of the results in terms of underlying mechanisms is extremely difficult. To further understand the mechanisms producing N_2O in fertilised soil, the following parameters must also be measured at the same sites which are being studied, as was carried out by *Perez et al.* [2001]: concentrations of NO_3^- and NH_4^+ and their isotopic

signatures as a function of soil depth, gravimetric water amount and WFPS as a function of soil depth, temperature as a function of soil depth, the NO/N_2O ratio, the $\delta^{18}O$ of H_2O, the amount of N_2O that is reduced to N_2 as an indicator of nitrification, and nitrifying and denitrifying bacteria types and concentration as a function of soil depth.

7.6 References

Abbasi, M.K., and W.A. Adams, Gaseous N emission during simultaneous nitrification-denitrification associated with mineral N fertilization to a grassland soil under field conditions, *Soil Biol. Biochem.*, *32*, 1251-1259, 2000.

Barford, C., J.P. Montoya, M.A. Alabet, and R. Mitchell, Steady State Nitrogen Isotope Effects of N_2 and N_2O Production in *Paracoccus denitrificans*, *Applied and Environmental Microbiology*, *65* (3), 989-994, 1999.

Beline, F., J. Martinez, C. Marol, and G. Guiraud, Application of the ^{15}N technique to determine the contributions of nitrification and denitrification to the flux of nitrous oxide from a aerated pig slurry, *Water Research*, *35* (11), 2774-2778, 2001.

Bigeleisen, J., The Relative Reaction Velocities of Isotopic Molecules, *Journal of Chemical Physics*, *17* (8), 675-678, 1949.

Boontanon, N., S. Ueda, P. Kanatharana, and E. Wada, Intramolecular stable isotope ratios of N_2O in the tropical swamp forest in Thailand, *Naturwissenschaften*, *87* (4), 188-192, 2000.

Bouwman, A.F., I. Fung, Matthews, and J. J, Global analysis of the potential for N_2O production in natural soils, *Global Biogeochemical Cycles*, *7* (3), 557-597, 1993.

Bouwman, A.F., K.W.v.d. Hoek, and J.G.J. Olivier, Uncertainties in the global source distribution of nitrous oxide, *Journal of Geophysical Research-Atmospheres*, *100* (D2), 2785-2800, 1995.

Brumme, R., W. Borken, and S. Finke, Hierarchical control on nitrous oxide emissions in forest ecosystems, *Global Biogeochemical Cycles*, *13* (4), 1137-1148, 1999.

Chadwick, D.R., B.F. Pain, and S.K.E. Brookman, Nitrous oxide and methane emissions following application of animal manures to grassland, *Journal of Environmental Quality*, *29*, 277-287, 2000.

Cliff, S.S., C.A.M. Brenninkmeijer, and M.H. Thiemens, First measurement of the $^{18}O/^{16}O$ and $^{17}O/^{16}O$ ratios in stratospheric nitrous oxide: A mass-independent anomaly, *Journal of Geophysical Research-Atmospheres*, *104* (D13), 16171-16175, 1999.

Cliff, S.S., and M.H. Thiemens, The $^{18}O/^{16}O$ and $^{17}O/^{16}O$ ratios in atmospheric nitrous oxide: a mass-independent anomaly, *Science*, *278*, 1774-1776, 1997.

Dalsgaard, T., J. de Zwart, L.A. Robertson, J.G. Kuenen, and N.P. Revsbech, Nitrification, denitrification and growth in artificial Thiosphaera pantotropha biofilms as measured with a combined microsensor for oxygen and nitrous oxide, *FEMS Microbiology Ecology*, *17*, 137-148, 1995.

Esler, M.B., D.W.T. Griffith, F. Turatti, S.R. Wilson, and T. Rahn, N_2O concentration and flux measurements and complete isotope analysis using FTIR spectroscopy, *Chemosphere: Global Change Science*, *2*, 445-454, 2000a.

Esler, M.B., D.W.T. Griffith, S.R. Wilson, and L.P. Steele, Precision trace gas analysis by FT-IR spectroscopy. 1. Simultaneous analysis of CO_2, CH_4, N_2O, and CO in air, *Analytical Chemistry*, *72* (1), 206-215, 2000b.

Galle, B., L. Klemedtsson, and D.W.T. Griffith, Application of a Fourier transform IR system for measurements of N_2O fluxes using micrometeorological methods, an ultralarge chamber system, and conventional field chambers, *Journal of Geophysical Research*, *99* (D8), 16,575-16,583, 1994.

Griffith, D.W.T., G.C. Toon, B. Sen, J.F. Blavier, and R.A. Toth, Vertical profiles of nitrous oxide isotopomer fractionation measured in the stratosphere, *Geophysical Research Letters*, *27* (16), 2485-2488, 2000.

Harper, L.A., R.R. Sharpe, and T.B. Parkin, Gaseous nitrogen emissions from anaerobic swine lagoons: Ammonia, nitrous oxide, and dinitrogen gas, *Journal of Environmental Quality*, *29* (4), 1356-1365, 2000.

Hwang, S., and K. Hanaki, Effects of oxygen concentration and moisture content of refuse on nitrification, denitrification and nitrous oxide production, *Bioresource Technology*, *2000* (71), 159-165, 2001.

Itokawa, H., K. Hanaki, and T. Matsuo, Nitrous oxide production in high-loading biological nitrogen removal process under low COD/N ratio condition, *Water Research*, *35* (3), 657-664, 2001.

Kaye, J.A., Mechanisms and observations for isotopic fractionation of molecular species in planetary atmospheres, *Reviews of Geophysics*, *28* (8), 1609-1658, 1987.

Kendall, C., Tracing nitrogen sources and cycling in catchments, 1988.

Kim, K.R., and H. Craig, Nitrogen-15 and Oxygen-18 Characteristics of Nitrous Oxide - a Global Perspective, *Science*, *262* (5141), 1855-1857, 1993.

Linn, D.M., and J.W. Doran, Effect of water-filled pores on carbon dioxide and nitrous oxide production in tilled and non tilled soils, *Soil Science Society of America Journal*, *48*, 1267-1272, 1984.

Maag, M., and F.P. Vinther, Nitrous oxide emission by nitrification and denitrification in different soil moisture contents and temperatures, *Applied Soil Ecology*, *4*, 5-14, 1996.

Maag, M., and F.P. Vinther, Effect of temperature and water on gaseous emissions from soils treated with animal slurry, *Journal of the Soil Science Society of America*, *63*, 858-865, 1999.

Mandernack, K.W., T. Rahn, C. Kinney, and M. Wahlen, The biogeochemical controls of the delta N-15 and delta O-18 of N_2O produced in landfill cover soils, *Journal of Geophysical Research-Atmospheres*, *105* (D14), 17709-17720, 2000.

Menegazzo, J., Isotopic signature of nitrous oxide emitted from agricultural soils, Honours thesis, University of Wollongong, Wollongong, 2000.

Monteith, J.L., and M. Unsworth, *Principles of Environmental Physics,* 291 pp., Edward Arnold, London, 1990

Myer, C.P., I.E. Galbally, Y.P. Wang, L.A. Weeks, I.M. Jamie, and D.W.T. Griffith, Two Automatic Chamber Techniques for Measuring Soil-Atmosphere Exchanges of Trace Gases and Results of their use in the OASIS Field experiment, CSIRO Atmospheric Research, Melbourne, 2001.

Paul, E.A., and F.E. Clark, *Soil Microbiology and Biochemistry*, 340 pp., Academic Press, New York, 1996.

Perez, T., S.E. Trumbore, S.C. Tyler, E.A. Davidson, M. Keller, and P.B. de Camargo, Isotopic variability of N_2O emissions from tropical forest soils, *Global Biogeochemical Cycles*, *14* (2), 525-535, 2000.

Perez, T., S.E. Trumbore, S.C. Tyler, P.A. Matson, I. Ortiz-Monasterio, T. Rahn, and D.W.T. Griffith, Identifying the agricultural imprint on the global N_2O budget using stable isotopes, *Journal of Geophysical Research-Atmospheres*, *106* (D9), 9869-9878, 2001.

Rahn, T., and M. Wahlen, Stable isotope enrichment in stratospheric nitrous oxide, *Science*, *278*, 1776-1778, 1997.

Röckmann, T., J. Kaiser, R. Crowley, R. Borchers, W.A. Brand, and P.J. Crutzen, The isotopic enrichment of nitrous oxide ($^{15}N^{14}NO$, $^{14}N^{15}NO$, $^{14}N^{14}N^{18}O$) in the stratosphere and in the laboratory, *Journal of Geophysical Research-Atmospheres*, 10403-10410, 2001a.

Röckmann, T., J. Kaiser, R. Crowley, C.A.M. Brenninkmeijer, and P.J. Crutzen, The Origin of the Anomalous or "Mass-Independent" Oxygen Isotope Fractionation in Atmospheric N_2O, in *1st International Symposium on Isotopomers*, edited by N. Yoshida, pp. 35-36, Yokohama, Japan, 2001b.

Scott, A., B.C. Ball, I.J. Crichton, and M.N. Aitken, Nitrous oxide and carbon dioxide emissions from grassland amended with sewage sludge, *Soil Use and Management*, *16*, 36-41, 2000.

Smith, K.A., P.E. Thomson, H. Clayton, I.P. McTaggart, and F. Conen, Effects of temperature, water content and nitrogen fertilisation on emissions of nitrous oxide by soils, *Atmospheric Environment*, *32* (19), 3301-3309, 1998.

Thiemens, M.H., Mass-independent isotopic fractionations and their applications, in *Isotope effects in gas phase chemistry*, edited by J.A. Kaye, pp. 138-154, Amer. Chem. Soc., Boston, 1992.

Urey, H.C., The thermodynamic properties of isotopic substances, *Journal of the Chemical Society*, 562-581, 1946.

Wahlen, M., and T. Yoshinari, Oxygen isotope ratios in N_2O from different environments, *Nature*, *313*, 780-782, 1985.

Whalen, S.C., R.L. Phillips, and E.N. Fischer, Nitrous oxide emission from an agricultural field fertilized with liquid lagoonal swine effluent, *Global Biogeochemical Cycles*, *14* (2), 545-558, 2000.

Yoshida, N., ^{15}N depleted N_2O as a product of nitrification, *Nature*, *335*, 528-529, 1988.

Yoshida, N., and S. Toyoda, Constraining the atmospheric N_2O budget from intramolecular site preference in N2O isotopomers, *Nature*, *405* (18 May), 330-334, 2000.

Yoshinari, T., M.A. Altabet, S.W.A. Naqvi, L. Codispoti, A. Jayakumar, M. Kuhland, and A. Devol, Nitrogen and oxygen isotopic composition of N2O suboxic waters of the eastern North Pacific and the Arabian Sea - measurement by continuous-flow isotope-ratio monitoring, *Marine Chemistry*, *56* (253-264), 1997.

Chapter 8 Conclusions

A novel high resolution Fourier transform infrared spectroscopy technique has been developed for the isotopic characterisation of atmospheric nitrous oxide. This technique is analytically robust, insensitive to minor amounts of contaminant gases, non-destructive and complementary to the more established isotope ratio mass spectrometry (IRMS) technique. Sample handling and measurement equipment constructed for the FTIR technique has the following major features:

- A high pathlength to volume ratio White cell (2.4 m, 120 mL);
- the total volume of the White cell and sample manifold of 143.5 ± 1 mL;
- temperature is controlled to 25 ± 0.01 °C;
- sample pressure is controlled to 1.000 ± 0.005 torr; and
- sample manifold allows quantitative recovery of N_2O samples after FTIR analysis.

The FTIR technique requires a minimum of 5×10^{-6} mol N_2O, which corresponds to approximately 400 L of clean tropospheric air at the current N_2O background concentration of 314 nmol mol^{-1}. A procedure for the quantitative extraction of N_2O from whole air samples was developed allowing the quantitative extraction of N_2O from background air. The N_2O measurements were made relative to an internal working standard of BOC Gases industrial N_2O which has similar isotopic composition to N_2O working standards in use for IRMS measurements.

Two analytical methods were developed for the determination of N_2O isotopomers from high resolution FTIR spectra: Multi-micro-window classical least squares, and non-linear least squares. Tests of the two methods showed non-linear least squares determined N_2O isotopomers to a factor of approximately 2 better precision than multi-micro-window classical least squares, primarily due to the ability to accurately fit large regions of the N_2O spectrum containing saturated $^{14}N^{14}N^{16}O$ lines.

The best experimental precision achieved for the FTIR technique is between ± 1.1 ‰ for δ^{456} and ± 2.3 ‰ for δ^{447}, which are a factor of 3 to 5 worse than the theoretical precision. Temperature and pressure variations of the N_2O sample are accurately controlled and have a negligible impact on precision. The spectral lineshape was not constant from scan-to-scan. The discrepancy between experimental and theoretical precision is attributed to the scan-to-scan lineshape variation of the DA8 spectrometer.

The high resolution FTIR technique has several strengths:

- The technique is non-destructive and N_2O samples can be quantitatively recovered after analysis permitting repeat analyses;
- All N_2O isotopomers are measured simultaneously and directly. Unlike IRMS, the $^{18}O/^{17}O$ ratio does not need to be assumed and both $^{14}N^{15}N^{16}O$ and $^{15}N^{14}N^{16}O$ are measured simultaneously;
- The technique can tolerate a small amount of contaminating gas such as N_2 or CO_2;
- There is no risk of "scrambling" or altering the N_2O isotopomers as there is in IRMS;

- The technique can be easily adopted to measuring isotopomers of other gases without requiring expensive instrumental modifications; and
- It is a fundamentally different method than IRMS analysis and therefore acts as an independent and complementary technique.

The high resolution FTIR technique has some limitations:

- The technique requires large sample amounts – approximately 5×10^{-6} mol N_2O is required. This equates to approximately 400 L of air if clean background air at the current tropospheric N_2O mixing ratio of 314 nmol mol^{-1}. IRMS, in comparison, requires in the order of nanomolar amounts of N_2O and approximately 100-150 mL of whole air. Sample extraction and purification might be much more difficult for other gases.
- The technique is not as precise as IRMS. Typical $\delta^{15}N$ precisions achieved in this work are approximately ± 2 ‰. Theoretical studies indicate that ± 0.5 ‰ should be achievable. The IRMS precision is approximately 0.4 ‰ for a 1 nmol N_2O sample, and approximately 0.02 ‰ for a 1 μmol N_2O sample.

The FTIR technique was used to determine the fractionation factors for $^{14}N^{15}N^{16}O$, $^{15}N^{14}N^{16}O$, $^{14}N^{14}N^{18}O$ and $^{14}N^{14}N^{17}O$ in the laboratory photolysis of N_2O at several wavelengths. The non-linear least squares technique gives fractionation factors comparable to the classical least squares technique, but with significantly smaller standard errors. The fractionation factors are largely consistent with those obtained by IRMS measurements and compare well with theories of N_2O photolysis. This experiment provided a measurement fractionation factor data set more comprehensive than other similar measurements.

The FTIR technique was used to characterise the isotopic composition of tropospheric N_2O from an urban site over the course of approximately one year. The average $\delta^{15}N$ of the collected N_2O samples is 7.7 ± 2.8 ‰ (± 1 σ) relative to atmospheric N_2, which is slightly higher than the $\delta^{15}N$ of N_2O from clean background air (7.0 ± 0.6 ‰ relative to atmospheric N_2). The intramolecular δ^{456}–δ^{546} varies from 12.4 to 29.5 ‰. The results obtained from this experiment are comparable to those obtained in similar study of N_2O from an urban location by IRMS by *Yoshida and Toyoda* [2000].

The FTIR technique was used to characterise the isotopic composition of N_2O emissions from a pig effluent fertilised crop field. The $\delta^{15}N$ of the emitted N_2O ranges from –16 to +20.9 ‰ relative to atmospheric N_2, the highest $\delta^{15}N$ measured from an experimental plot continuously saturated with effluent. The N_2O intramolecular δ^{456}-δ^{546} ranges from -82.2 to +12.3 ‰ which is a much larger range than has been measured by two comparable studies. Measurement of δ^{456}-δ^{546} and $\delta^{15}N$ of N_2O leads to insights into nitrification and denitrification, as δ^{456}-δ^{546} reflects processes which form the N-N bond. In contrast, the $\delta^{15}N$ of emitted N_2O is primarily due to changes in the $\delta^{15}N$ of the source or substrate nitrogen.

8.1 Further work already in progress

The line shapes variations observed with the DA8 spectrometer have lead to a major spectrometer upgrade which effectively replaced all interferometer components. The fixed interferometer mirror is now truly fixed and the movable mirror tilts to maintain optimum laser fringe alignment. This maintains a constant optical axis through the interferometer during a scan, thereby reducing spectral line shape variability. Early

tests have confirmed that line shape stability is much better than achieved with the previous DA8 configuration. A 2-3 fold increase in infrared energy throughput through the interferometer and White cell assembly was measured, due to a new beam splitter and new interferometer mirrors. A novel data acquisition system is nearing commission which uses an audio analogue-to-digital converter to sample the interferogram at 50 kHz. This data system follows the description of *Brault* [1996] and should reduce errors due to variable velocity of the movable mirror. These two major upgrades should bring the isotopomer precision performance significantly closer to the theoretical limits than what is currently achieved.

The N_2O extraction system developed in this work is large and cumbersome, requiring mains power (240 V, 50 Hz) and access to oxygen, liquefied petroleum (LP) and nitrogen gas bottles. This extraction system is inconvenient in a field experiment as it requires mounting inside a vehicle for easy transport between sample sites. This system has been condensed to a much more portable system by students in this group. Final N_2O sample processing is performed in the laboratory, removing the need the need for mains power and gas bottles. A 12 V car battery powers a small diaphragm pump which draws the sample air through the extraction line. This extraction line is approximately 600 mm × 700 mm and weighs approximately 7 kg (excluding the 12V battery). It is easily transportable by one person and can be positioned close to spot N_2O sources. This extraction line has become the normal method for extracting N_2O from sources.

Work by an Honours student (Travis Naylor) in this research group has involved sampling N_2O from sewage treatment tanks and landfill run-off settling tanks. A

method has been developed that allows gas in a water solution such as the ones described to be extracted by "sparging" a sample of water with air. The gas extracted from landfill run-off and sewage treatment ponds is extremely concentrated in N_2O, with concentrations of greater than 2000 ppm common. Under these conditions a 2 L whole-air sample contains sufficient N_2O for isotopic analysis. Clear shifts are seen in δ^{456}-δ^{546} correlating to shifts in N_2O production processes.

8.2 Further work

More work is required in understanding the effects of nitrification and denitrification on N_2O isotopic composition. These processes are very complex and their full explanation and assessment was beyond the scope of this thesis. The next study of N_2O isotopic composition from fertilised soils needs to be conducted over several weeks, with full information on soil composition and fertiliser composition. For example, the soil concentrations of NO_3^- and NH_4^+ and their isotopic signatures, as a function of soil depth is required. Also required is the gravimetric water amount and water filled pore space (WFPS) as a function of soil depth. Soil temperature profiles are required, as are the NO/N_2O ratio emitted from the soil and the $\delta^{18}O$ of soil H_2O.

Characterisation of N_2O isotopomers from air trapped in Antarctic firn ice could be performed. The firn is the region of packed snow on the Antarctic mainland which represents the short term history of atmospheric air, typically extending 50-100 years before the present. The depth limit of the firn is the top of the ice formed by compression of the firn. Because it is loosely packed, it contains large quantities of trapped air from which sufficient N_2O can be extracted for FTIR analysis. CSIRO

Atmospheric Research have collected several large samples of Antarctic firn air, from which N_2O will be isotopically characterised by FTIR in the near future.

The FTIR technique can be easily adopted to other species. For example, δ CH_3D and δ $^{13}CH_4$ have been measured simultaneously using the experimental hardware built for this work to a precision of approximately 2 ‰. More work needs to be performed in designing procedures for extracting the required amount of CH_4 from air. Carbon dioxide isotopomers $^{13}CO_2$, $CO^{18}O$ and $CO^{17}O$ have been also measured with this technique. A further application is the analysis of the symmetry isotopomers of ozone. For example $^{18}O^{16}O^{16}O$ and $^{16}O^{18}O^{16}O$ are non-equivalent and therefore have independent infrared spectra, which can be determined using this technique.

8.3 Overall conclusion

A high resolution FTIR technique has been developed which allows the characterisation of all the significant isotopes of atmospheric N_2O. The technique is non-destructive, analytically robust, insensitive to minor amounts of contaminant gases and complementary to IRMS. The FTIR technique has been used for:

- the determination of fractionation factors in the laboratory photolysis of N_2O,
- the isotopic characterisation of N_2O from an urban location over the period of one year, and
- the isotopic characterisation of N_2O emitted from a pig effluent fertilised crop field.

The method developed in this work can be used for determination of other isotopomers of key atmospheric gases such as CH_3D and $^{13}CH_4$, $^{13}CO_2$, $CO^{18}O$ and $CO^{17}O$, and the ozone symmetry isotopomers.

8.4 References

Brault, J.W., New approach to high-precision Fourier transform spectrometer design, *Applied Optics*, *35* (16), 2891-2896, 1996.

Yoshida, N., and S. Toyoda, Constraining the atmospheric N_2O budget from intramolecular site preference in N_2O isotopomers, *Nature*, *405* (18 May), 330-334, 2000.

Appendix A Procedures and publications

A.1 Procedure for dismantling the vacuum line and White cell

This is a difficult and time consuming procedure and should only be attempted when a minimum of three days are available. Approximately three days after reassembly are required to fully evacuate the White cell and sample line due to water vapour adhesion and out-gassing from the seals

1. Turn off the Julabo circulator, pressure gauge and small internal fan.
2. Power down the turbo molecular pump and diaphragm pump.
3. Disconnect the turbo molecular pump assembly from the vacuum line.
4. Remove one of the water hoses from the cell manifold plate and drain into a bucket. Pass some compressed air through the radiator plate to ensure that all water has been removed.
5. Disconnect the pressure gauge cables from the Perspex housing. Disconnect the internal fan cables from the white clip.
6. Gently raise the top half of the Perspex covering and place it on the spectrometer sample compartment lid. Remove the cables from the pressure gauge socket.
7. Close both pneumatic valves and disconnect the black nylon compressed air tubing from the compressed air solenoid valves.
8. Remove the flexible stainless steel bellows.
9. Disconnect the vacuum line from the side plate of the spectrometer sample compartment. You might need two spanners for this. The side plate must not

have anything left attached to it. The vacuum line is now free and can be placed in a secure place.

10. Remove the bottom half of the Perspex housing.
11. Carefully remove the four screws securing the side plate to the spectrometer sample compartment housing. The easiest way is to sit on a small stool next to the spectrometer and use your knee for support. The White cell assembly is now free.
12. Place the assembly on a bench with the side plat flat on the bench and the radiator plate off the edge. This makes the cell point up out of the plane of the bench for easy access.
13. Remove the copper coil which surrounds the White cell.
14. Gently and carefully undo the 8 Allen screws which secure the cell to the mounting ring. Note how this is assembled before you undo everything.
15. The White cell is now free and can be cleaned.

A.2 Procedure for washing the White cell

Ideally, before the cell is washed, the wedged CaF_2 window should be removed.

1. Secure the White cell to the bench using plenty of sticky tape, such that the cell is perpendicular to the bench surface with the CaF_2 window on top.
2. Heat the CaF_2 window with a heat gun gently and evenly such that the Apiezon "Black Wax" seal softens.
3. With some tissues for heat protection, pry the window off the cell walls when the black wax is soft enough.

4. Once the window is cooled, place in a small beaker of petroleum ether (or other non-polar solvent such as heptane) for a few hours to dissolve the black wax. You will need at least one change of solvent.
5. The White cell can now be gently washed in soapy water, followed by distilled water, rinsed in ethanol and dried under a nitrogen atmosphere.

A.3 Procedure for attaching CaF_2 window to the White cell

New black wax needs to be laid on the surface of the cell walls in order to reseal the window to the cell. Do the next section in a well ventilated area, and only after you can confidently perform the procedure on a scrap piece of glass tube

1. Light the Pyren butane soldering iron as per the instructions enclosed in the box and leave to heat up. The temperature should be on 3 to 4.
2. Take a stick of black wax. Use the tip of the soldering iron to soften the black wax to the point it just flows. Run a small bead of wax around the white cell where the window will seal. At the end of this step, you should have an even black wax layer on the perimeter of the cell no more than 3 mm high. If you have more than this, or the layer is uneven, wait for the black wax to cool and scrape away with a knife, and restart.
3. Take the heat gun and heat the layer of black wax evenly and gently to the point it softens.
4. Quickly take the window and with your hand place it on the glass cell and gently push to create the seal
5. Again, use the heat gun on the cell/window assembly as so to again soften the black wax. Press evenly across the window when the black wax is soft to ensure a good seal. Inspect the seal for any obvious bubbles or channels.

6. Do not, under any circumstances, allow any Black Wax to come in contact with the cell mirrors.

A.4 Reassembly procedure

The most important step when re assembling the white cell is that all components making up the o-ring seal to the white cell need to be scrupulously clean. This is most important, other wise the cell will leak under vacuum.

1. Remove all vacuum grease with a new Kimwipe tissue.
2. Replace with fresh high vacuum grease, evenly coating all sealing surfaces with your fingers. Make sure fingers and all surfaces are scrupulously clean.
3. Reassemble the White cell and the vacuum line following the dismantling procedure in reverse.
4. Start evacuating the White cell and vacuum line. Check for initial leaks every hour for the first few hours. Allow to evacuate for approximately 3 days before sample measurement.

A.5 Publications

Attached overleaf are photocopies of publications by the author of this thesis, Federico Turatti

GEOPHYSICAL RESEARCH LETTERS, VOL. 27, NO. 16, PAGES 2489-2492, AUGUST 15, 2000

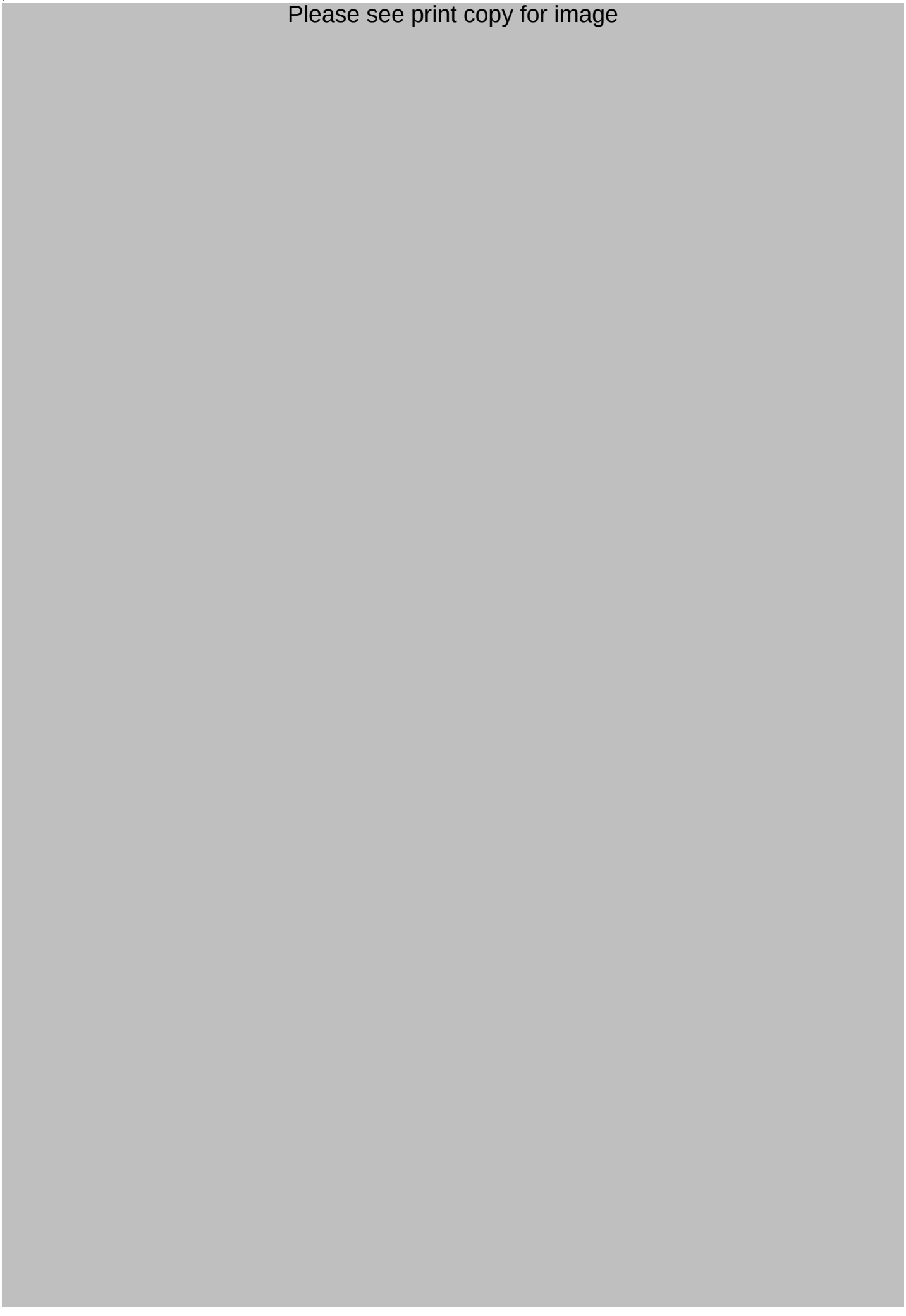

Please see print copy for image

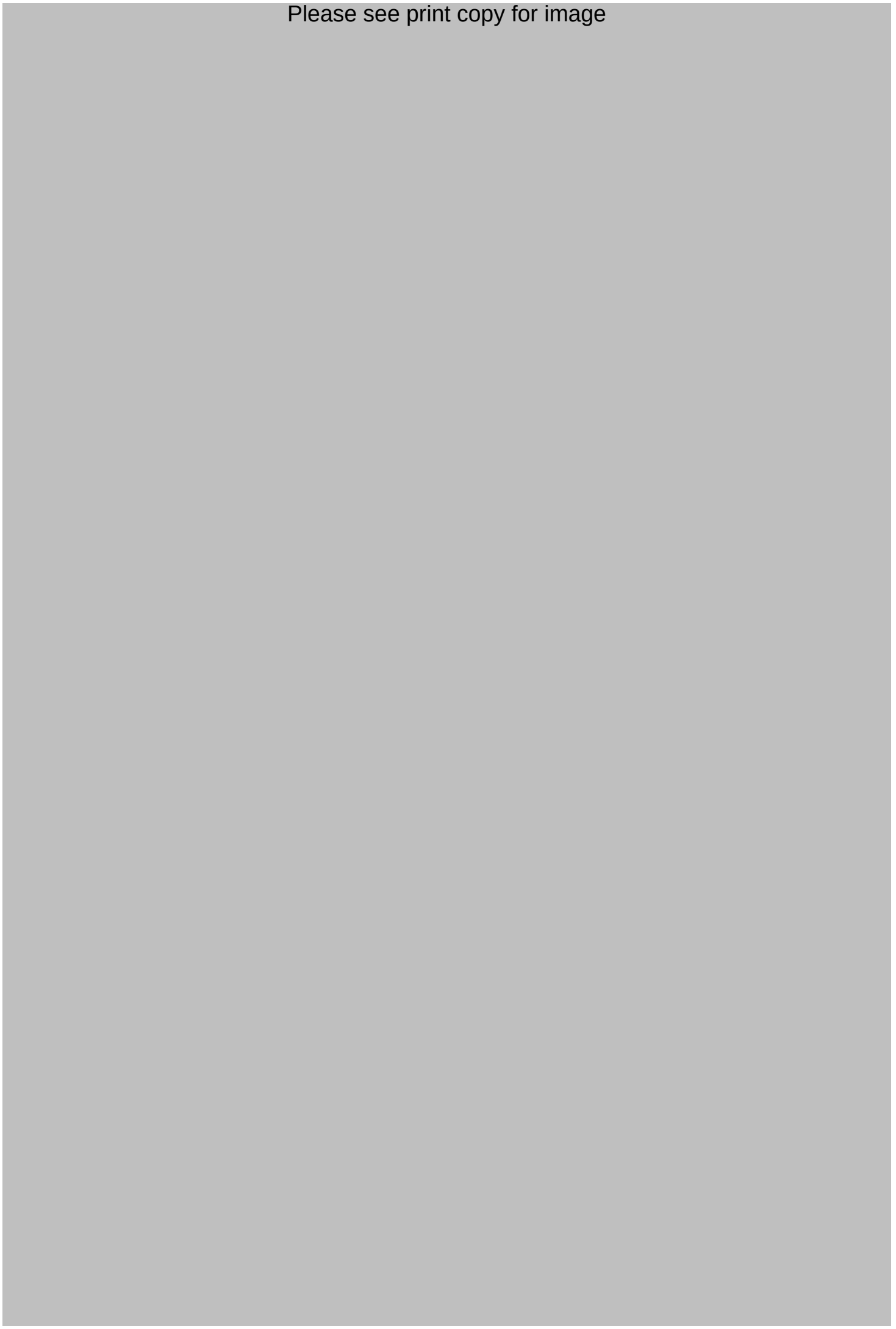
Please see print copy for image

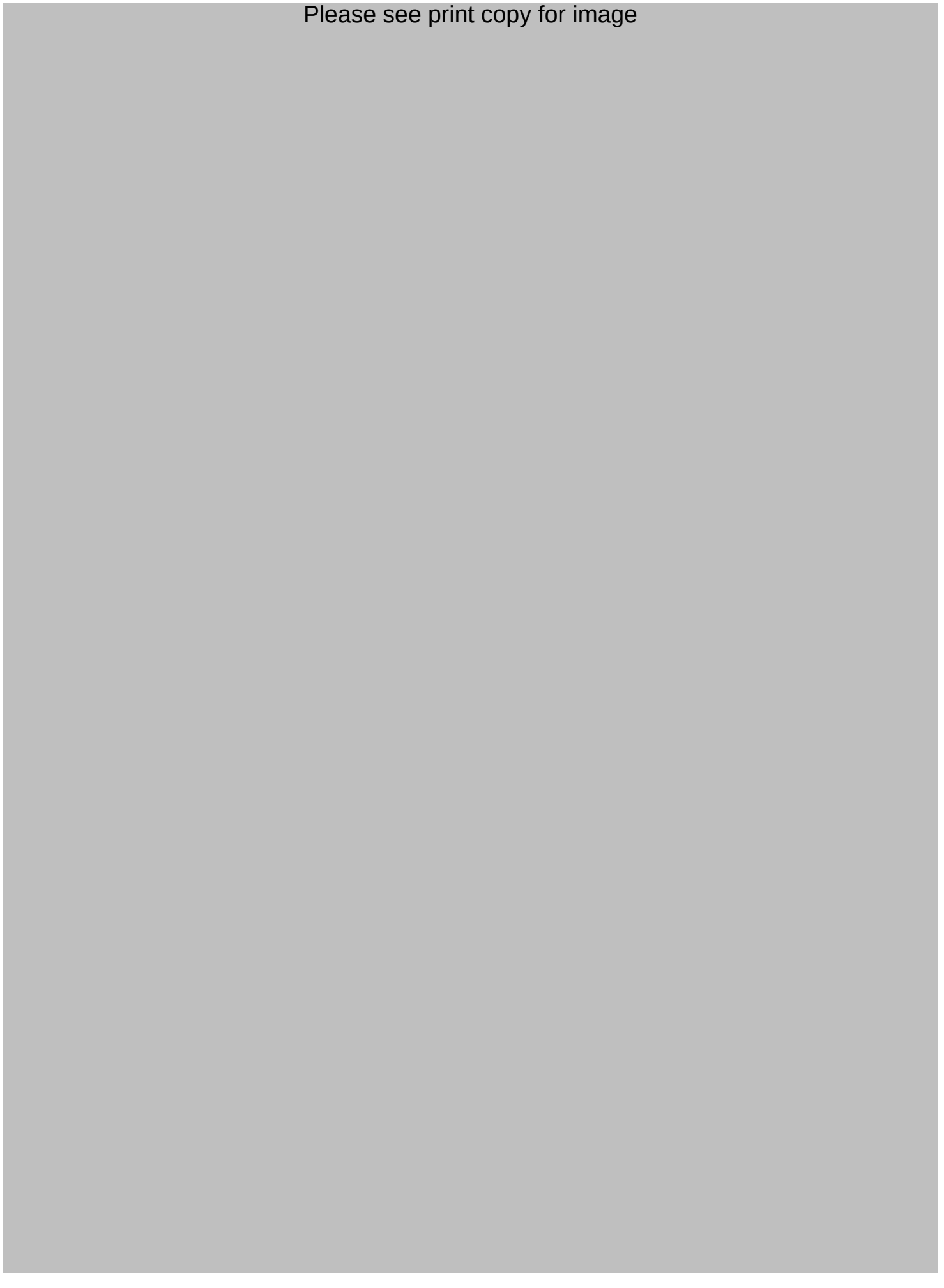
Please see print copy for image

PERGAMON

Chemosphere – Global Change Science 2 (2000) 445–454

CHEMOSPHERE – GLOBAL CHANGE SCIENCE

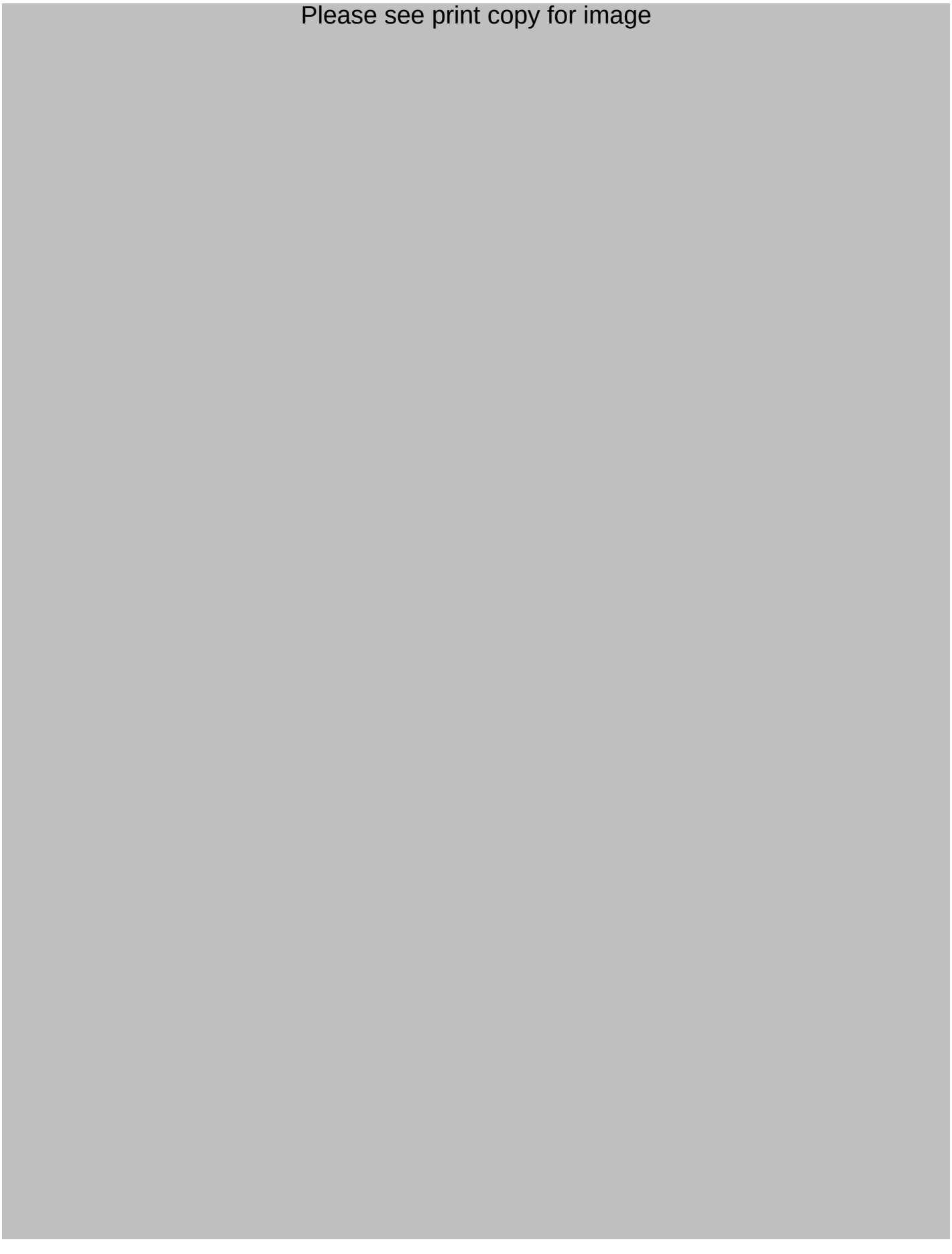

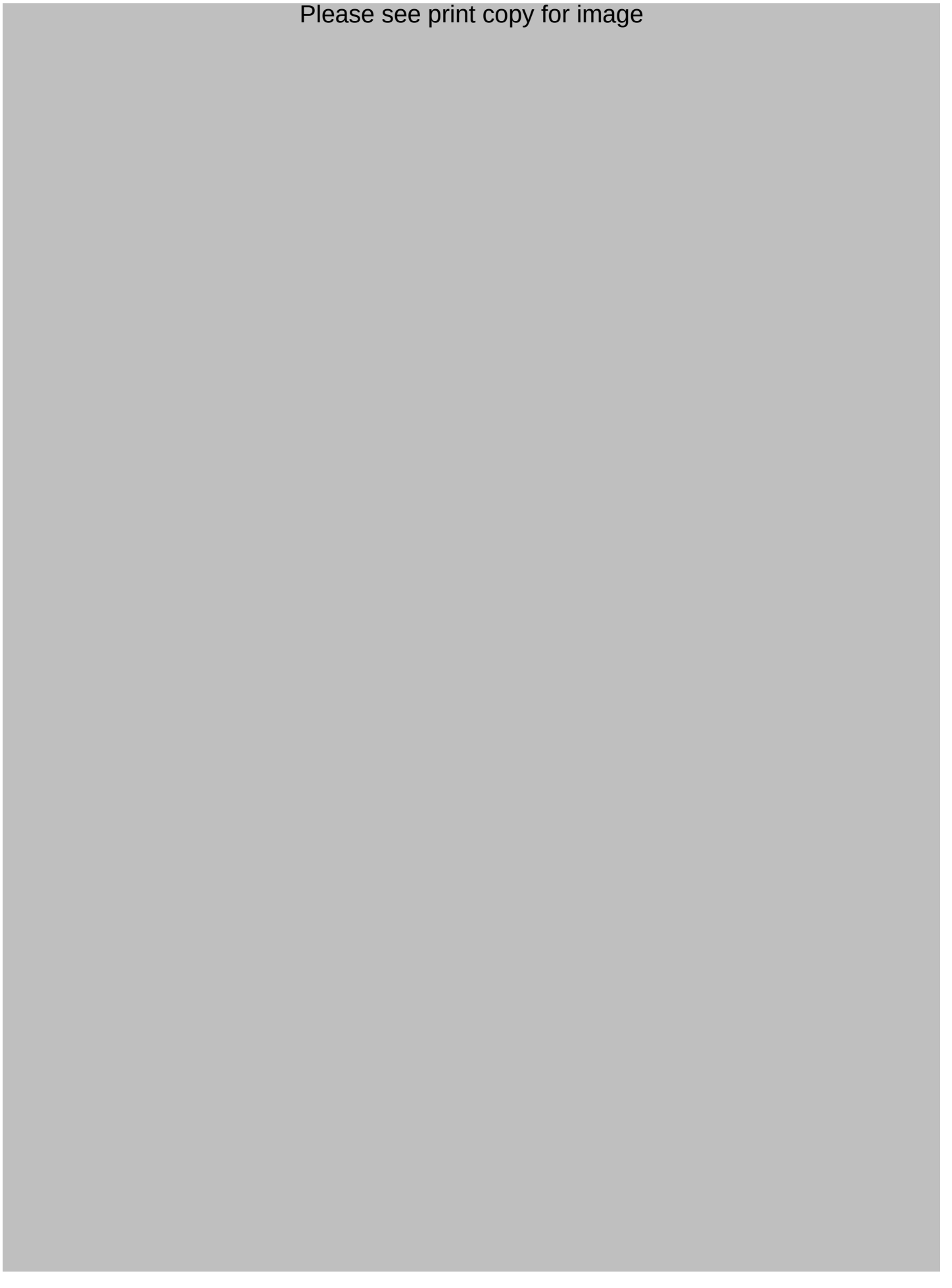
Please see print copy for image

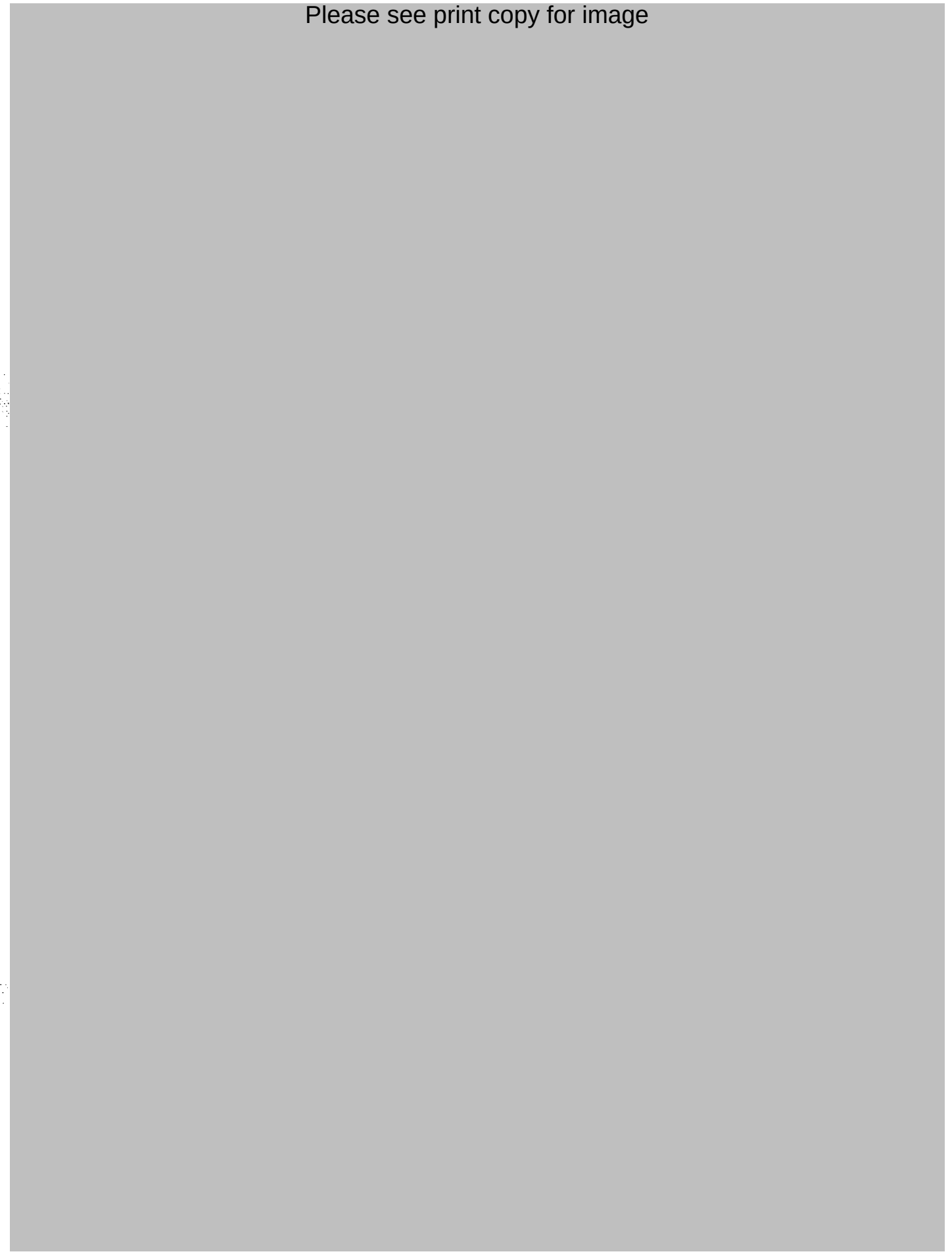
Please see print copy for image

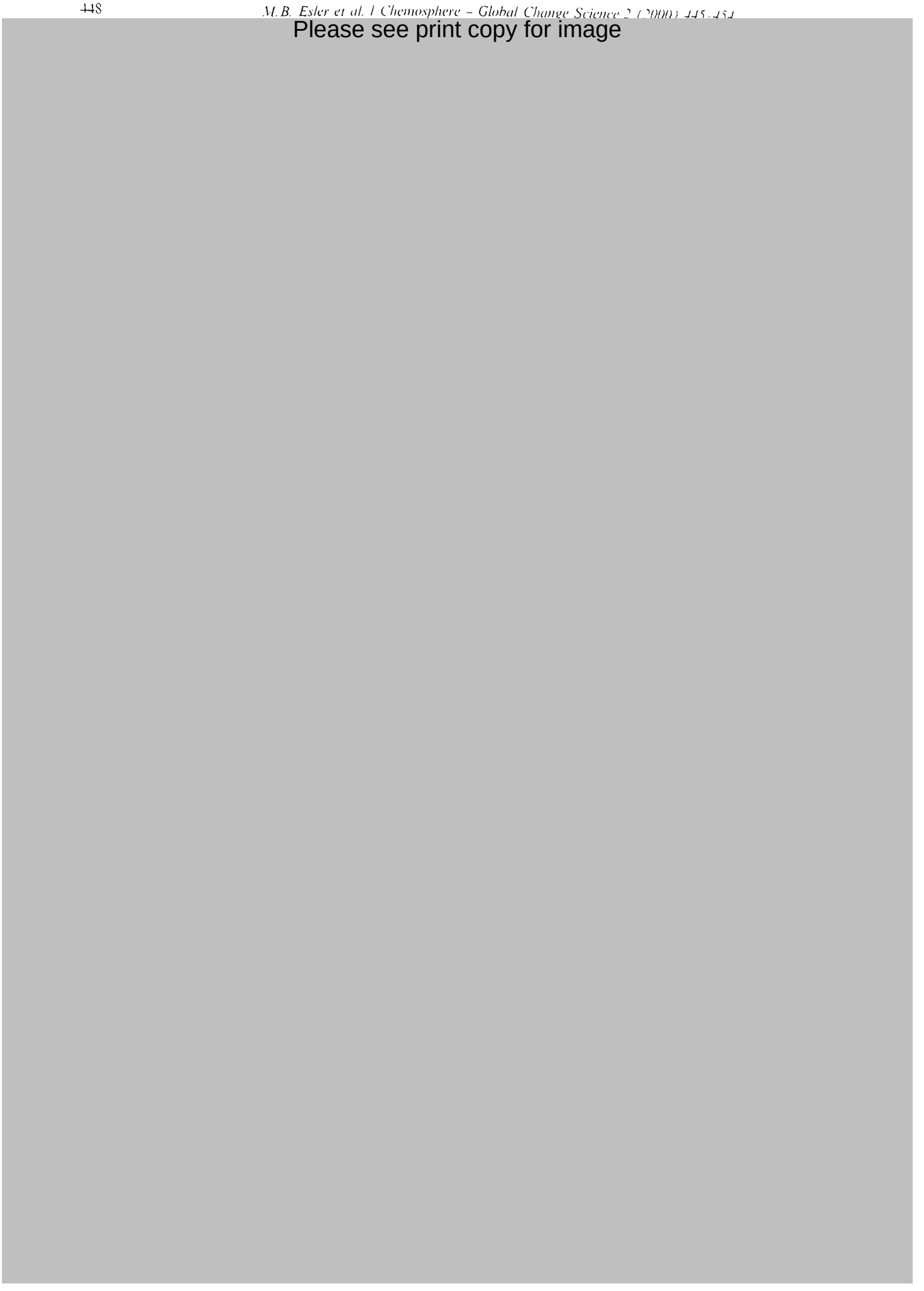
Please see print copy for image

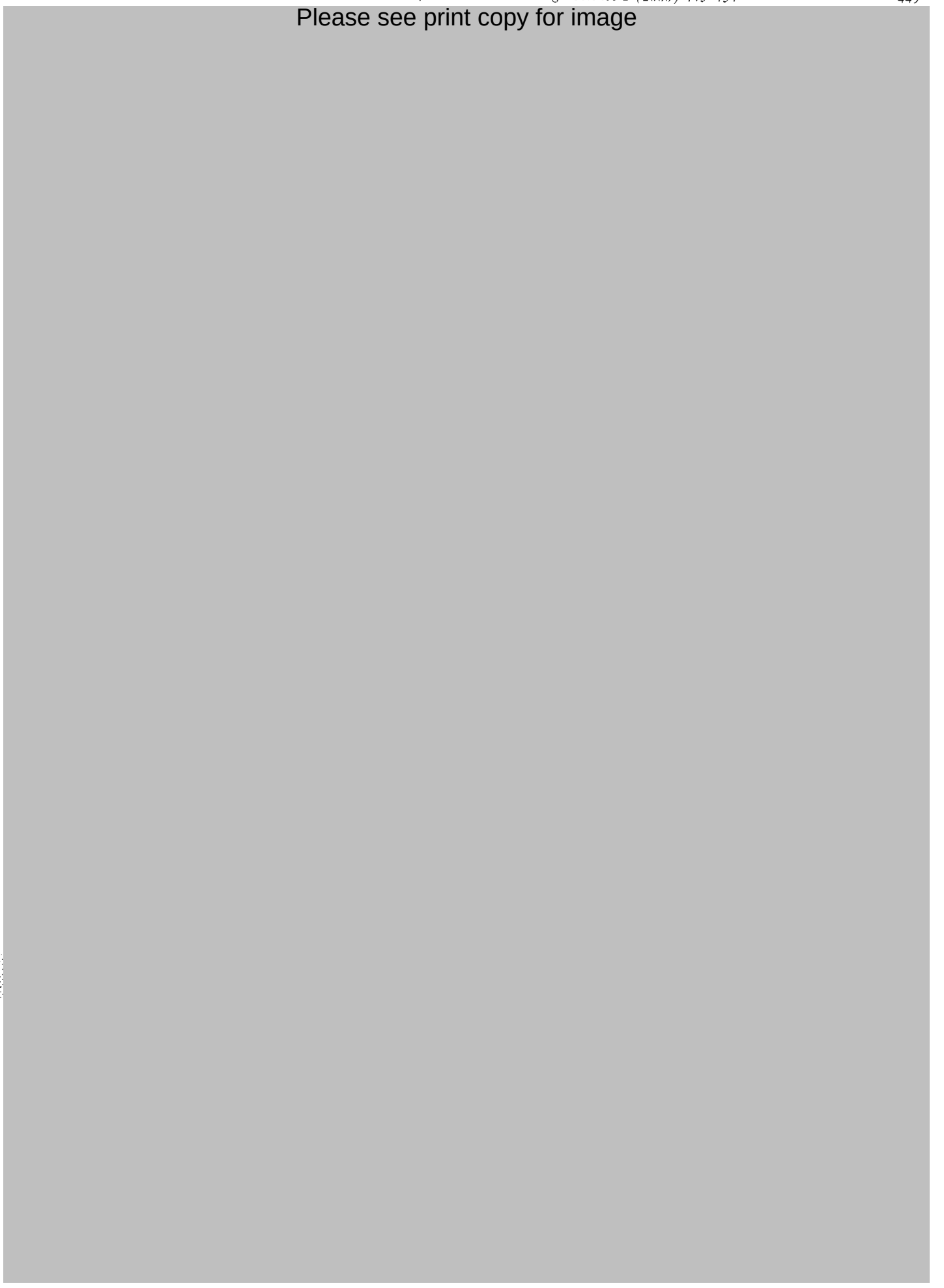
Please see print copy for image

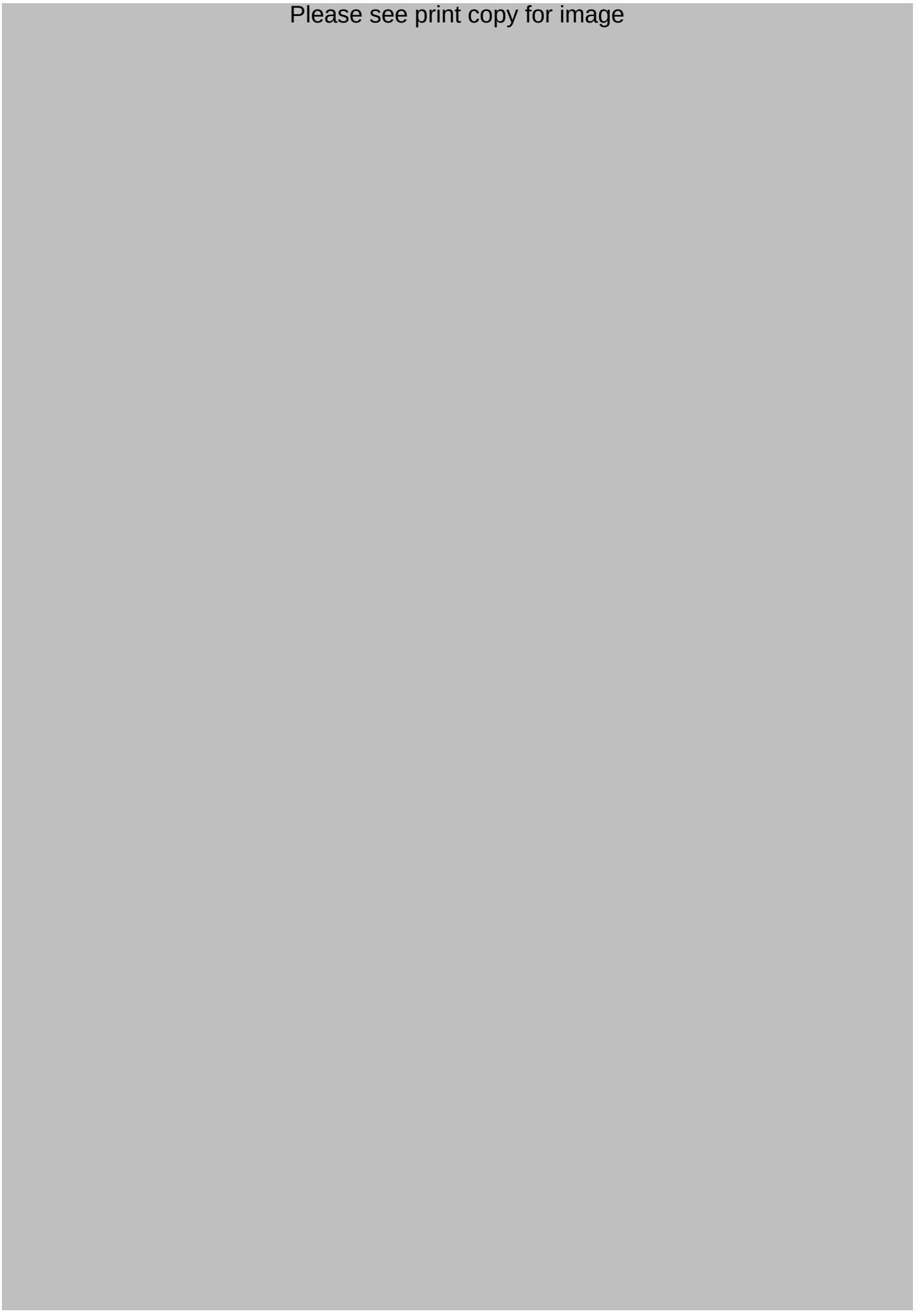
Please see print copy for image

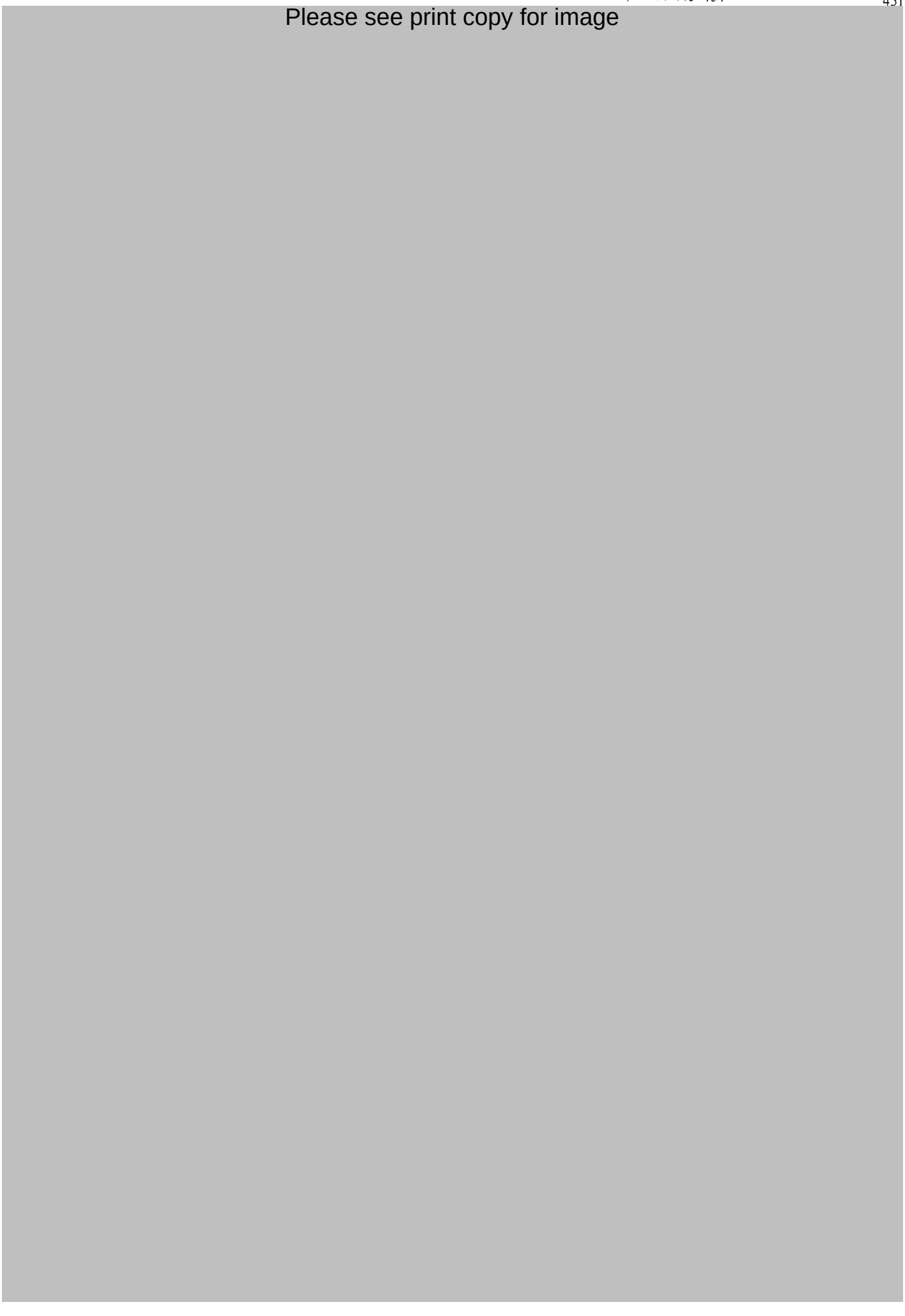
Please see print copy for image

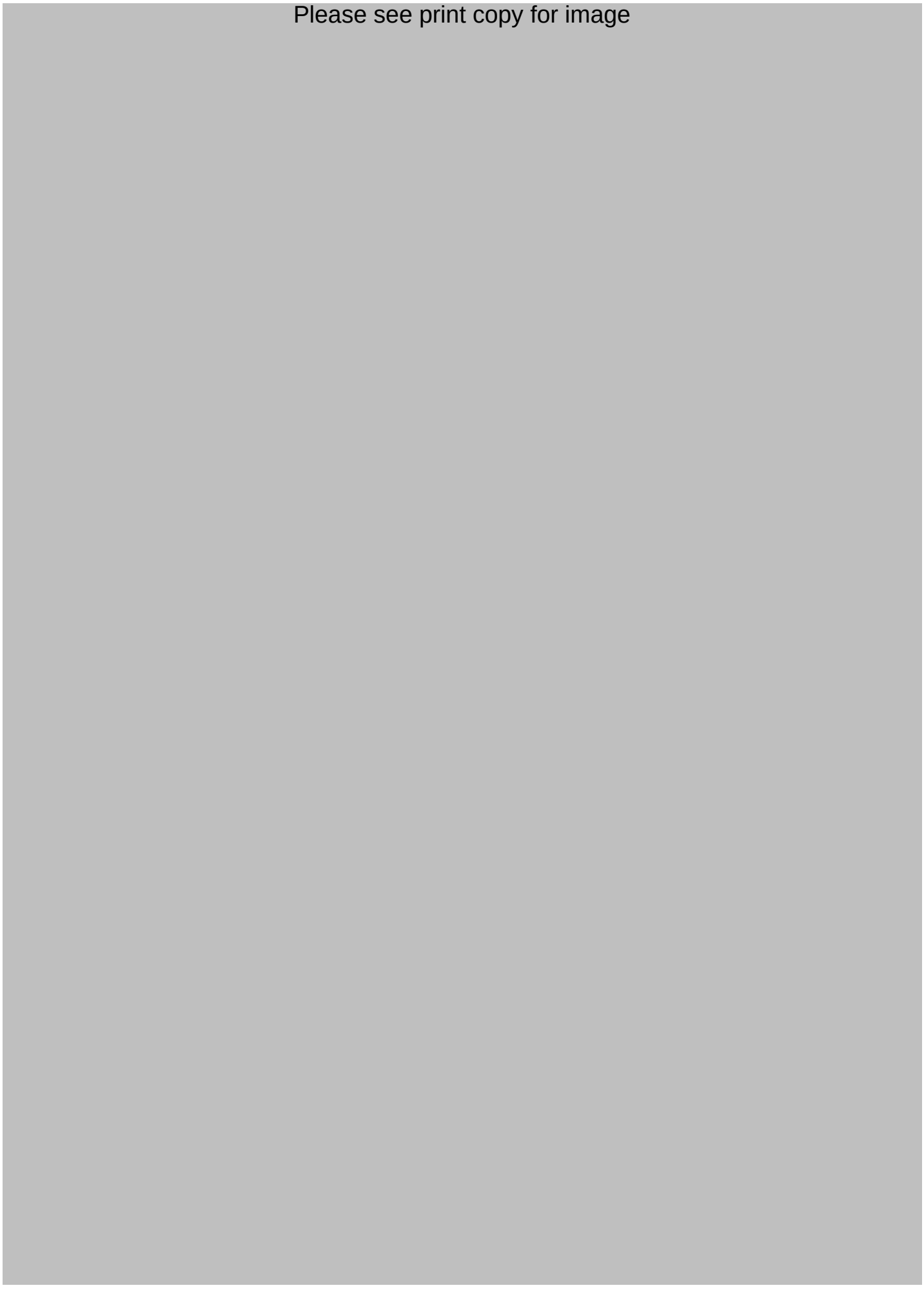
Please see print copy for image

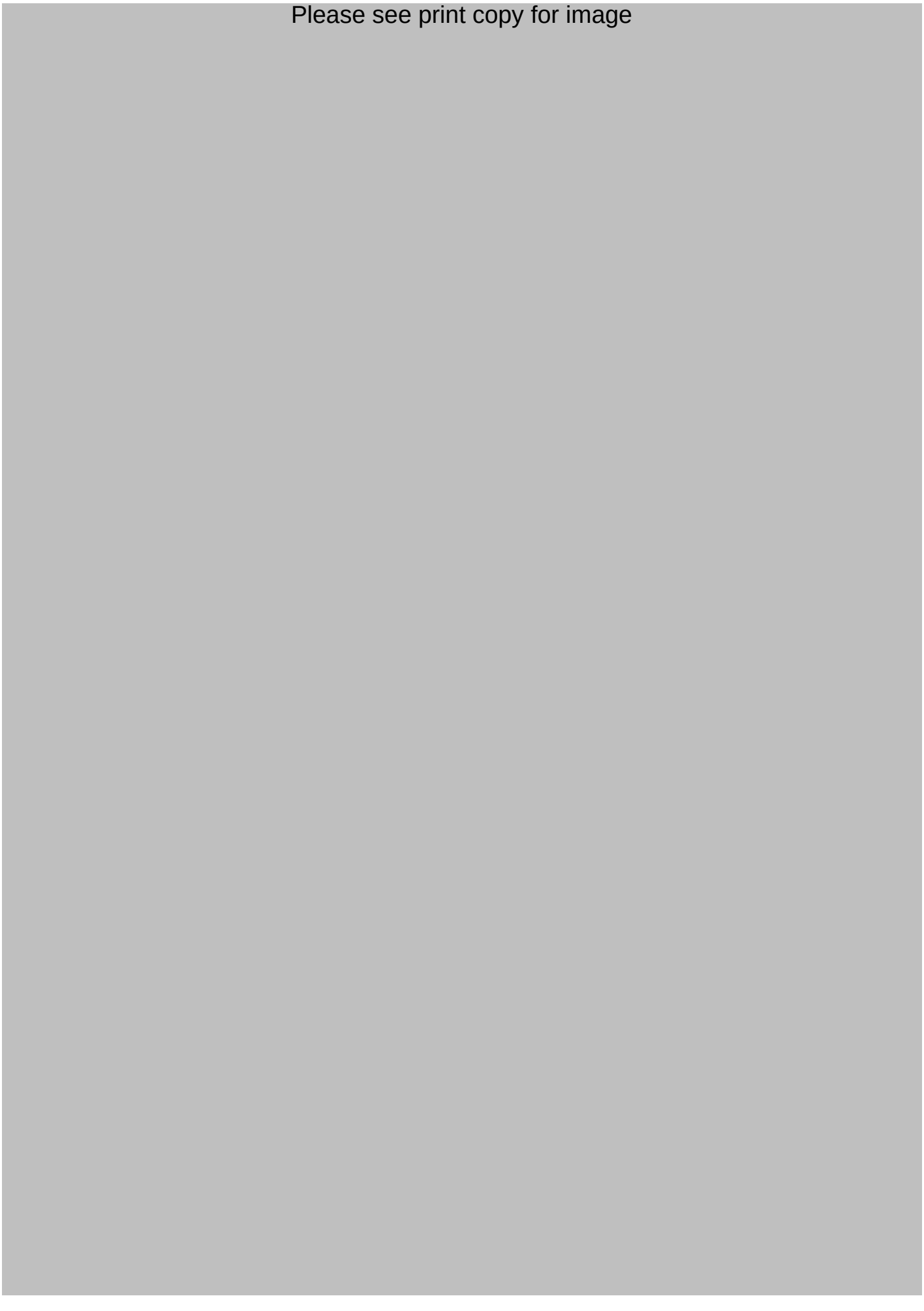
Please see print copy for image

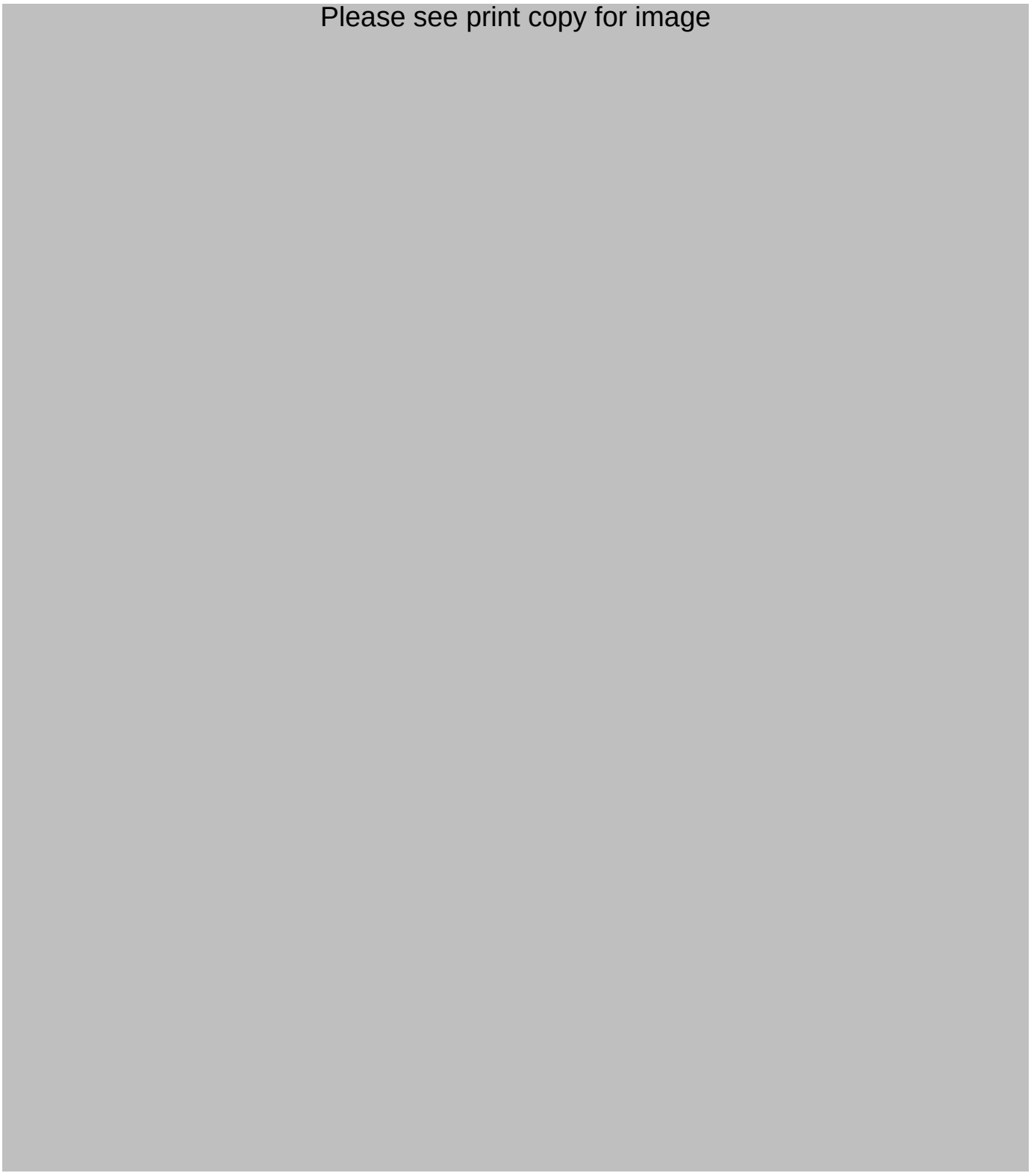
Please see print copy for image